



Universitat d'Alacant
Universidad de Alicante

BAND GAP CONTROL IN HYBRID TITANIA
PHOTOCATALYSTS

Marisa Rico Santacruz



Tesis

Doctorales

www.eltallerdigital.com

UNIVERSIDAD de ALICANTE

BAND GAP CONTROL IN HYBRID TITANIA PHOTOCATALYSTS



*Marisa Rico Santacruz
Molecular Nanotechnology Lab
Inorganic Chemistry Department
University of Alicante, 2014*

UNIVERSIDAD DE ALICANTE



Laboratorio de Nanotecnología Molecular
Departamento de Química Inorgánica

BAND GAP CONTROL IN HYBRID TITANIA PHOTOCATALYSTS

Memoria presentada por MARISA RICO SANTACRUZ
para aspirar al GRADO DE DOCTOR por la Universidad de Alicante

Directores del trabajo de investigación: Javier García Martínez y
Elena Serrano Torregrosa

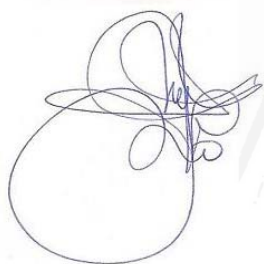
Alicante, 2014

Javier García Martínez, Profesor Titular de Química Inorgánica y responsable del Laboratorio de Nanotecnología Molecular del Departamento de Química Inorgánica de la Universidad de Alicante y Elena Serrano Torregrosa, Investigadora del Laboratorio de Nanotecnología Molecular del mismo Departamento

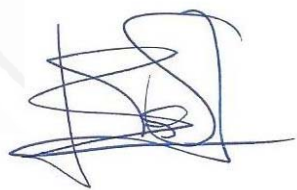
HACEN CONSTAR

que **Dña. Marisa Rico Santacruz**, Ingeniera Química por la Universidad Politécnica de Valencia, ha realizado en el Departamento de Química Inorgánica de la Universidad de Alicante, bajo nuestras dirección, el trabajo que lleva por título: "**Band control in hybrid titania photocatalysts**", el cual constituye su memoria para aspirar al Grado de Doctor por la Universidad de Alicante reuniendo, a nuestro juicio, las condiciones necesarias para ser presentada y defendida ante el tribunal correspondiente.

Y para que conste a los efectos oportunos, firmamos el presente documento en Alicante a 28 julio de 2014.



Dr. Javier García Martínez
Profesor Titular de Química Inorgánica



Dra. Elena Serrano Torregrosa
Investigadora Dpto. Química Inorgánica

Sueña, aunque el sueño parezca imposible.
Lucha, aunque el enemigo parezca invencible.
Aguanta, hasta que el dolor te inunde.
Corre, por donde no se debe.
Resiste y al final...

.... alcanzarás la estrella! ☆

DAISAKU IKEDA

Universitat d'Alacant
Universidad de Alicante

Para ella, para él



Universitat d'Alacant
Universidad de Alicante

Agradecimientos



Universitat d'Alacant
Universidad de Alicante

Dice el tópico que “todos los comienzos son duros” y en el caso de una tesis doctoral, el final tampoco iba a ser menos. Sin embargo, también se ha cumplido el dicho de “no será fácil pero merecerá la pena”. Si ha sido así, se debe en parte a las muchas personas que me han acompañado en esta etapa, las cuales han confiado en mí y me han apoyado de forma incondicional. Quiero expresar mi gratitud a:

A mis directores de tesis, el Dr. Javier García Martínez y la Dra. Elena Serrano Torregrosa por su orientación, seguimiento y dedicación en esta tesis pero sobretodo por su interés en mi formación como científica y como persona crítica. A Javier por su “don de palabra” y sus ideas innovadoras, con las que siempre acierta y a Elena, por su tiempo, motivación y paciencia, la cual está a prueba de bombas.

A mis compañeros de laboratorio: Ada, Daniel, Helga, Noe y Aida, ya que con ellos he compartido despacho, laboratorio, cafés, muchas horas de trabajo y también muy buenos ratos. Especialmente quiero agradecer a Noe su organización y sus listas interminables tras las reuniones, su música y su buen rollo que ha hecho desde que llegó, un laboratorio diferente mucho más animado. A Aida, la persona a la cual le estaré infinitamente agradecida por estar siempre ahí, tanto en lo laboral como en lo personal, por escucharme y tener siempre una sonrisa y una palabra de ánimo. Sabes que lo conseguiremos y si estás leyendo esto ya tienes la prueba.

A los becarios del departamento de Química Inorgánica, Física Aplicada y Óptica en especial a Laura y Zinab por los desayunos, los ratitos de descanso y los días de playa nublados. Al resto de compañeros del departamento tanto profesores como personal de laboratorio y administración, destacando a Esther, sin ella mi vida burocrática y económica habría sido un desastre.

A los compañeros de otros laboratorios, con los cuales hemos colaborado. Destaco al grupo de “Materiales Moleculares Organometálicos” de la Universidad de la Rioja: la Dra. Elena Lalinde, Dra. M^a Teresa Moreno, Patri, Julio, Santi, Nora y

en especial al Dr. Jesús Berenguer, “Chuchi”, y Ángel por su inestimable colaboración. Quiero agradecerles la buena acogida en su laboratorio, la simpatía con que siempre me han tratado, su ayuda sea la hora que sea y donde sea (bien en su despacho, skype o la cafetería si se tercia). También su buena disponibilidad a visitar la calle Laurel, una bodega o lo que surgiese, un placer haber disfrutado de todos y cada uno de los momentos vividos con vosotros.

No puedo olvidarme de los compañeros del grupo del grupo “Nano para biotecnología y electrónica molecular” de la Universidad de Palermo, así como al grupo de fotocatalisis “Schiavello-Grillone” de la Universidad de Palermo. Especialmente agradecerles a Elisa y Giuseppe su disposición y ayuda a integrarme en la sociedad palermitana y mostrarme los mejores platos de pasta de toda Sicilia. También a Carmen, Dani y Bea tres personajillos que me hicieron sentir en Palermo como en casa y eso os puedo asegurar que no es nada fácil.

A los Servicios Técnicos de Investigación (SSTTi) de la Universidad de Alicante, en especial a Ion, Sara, Alejandro, Jero, Fernando, Ana Paula y Mayte por sus medidas y a Cristina por las fotos de TEM.

A todas y cada una de las personas que han formado o entrado a formar parte de mi vida en estos años, durante mis viajes, mis congresos, pero en especial a mis amigas, “las de siempre”, las cuales aunque no entiendan muy bien cómo se puede tardar tanto en escribir una tesis o en corregirla, siempre tienen una palabra de ánimo.

Y como no a mis padres y hermanos, que de forma incondicional siempre han estado ahí, bien para celebrar los triunfos o para animarme si las cosas no salían como se esperaba. Es toda una satisfacción el sentir que mis logros son los suyos.

A todos ellos, muchas gracias

Resumen



Universitat d'Alacant
Universidad de Alicante

Resumen

La presente memoria refleja el resultado de la investigación realizada para aspirar al GRADO DE DOCTOR por la Universidad de Alicante en el marco del programa de DOCTORADO DE CIENCIA DE MATERIALES de la misma universidad, incluyendo la MENCIÓN DE DOCTORADO INTERNACIONAL.

El trabajo de investigación ha sido desarrollado en el Laboratorio de Nanotecnología Molecular, del Departamento de Química Inorgánica de la Universidad de Alicante.

El dióxido de titanio (titania) es un material blanco principalmente usado como pigmento en la industria de la pintura debido a su opacidad y alto índice de refracción.

Sin embargo, en 1972, Fujishima and Honda demostraron que la titania era mucho más que un aditivo para pigmentos. Estudiaron y confirmaron el potencial de este material semiconductor para descomponer el agua en hidrógeno y oxígeno en una celda electroquímica. A partir de ese momento, los estudios científicos basados en este semiconductor crecieron considerablemente debido a la amplia gama de aplicaciones medioambientales y energéticas en las que podría ser determinante, como son la fotocatalisis, la energía fotovoltaica, sensores y biomedicina, entre otros muchos.

1. OBJETIVO E INTRODUCCIÓN

La titania (TiO_2) destaca entre todos los semiconductores que pueden actuar como fotocatalizadores, ya que se trata de un material fotoactivo muy eficaz en el rango del ultravioleta (UV), barato, abundante, no tóxico, químicamente estable, biocompatible y que cuenta con una amplia variedad de aplicaciones medioambientales basadas en la captación de luz solar. Estas aplicaciones abarcan desde celdas solares hasta eliminación de compuestos orgánicos volátiles (VOx) o de óxidos de nitrógeno (NOx) en efluentes tanto líquidos como gaseosos o la generación de superficies autolimpiables, todas ellas basadas en su actividad fotocatalítica.

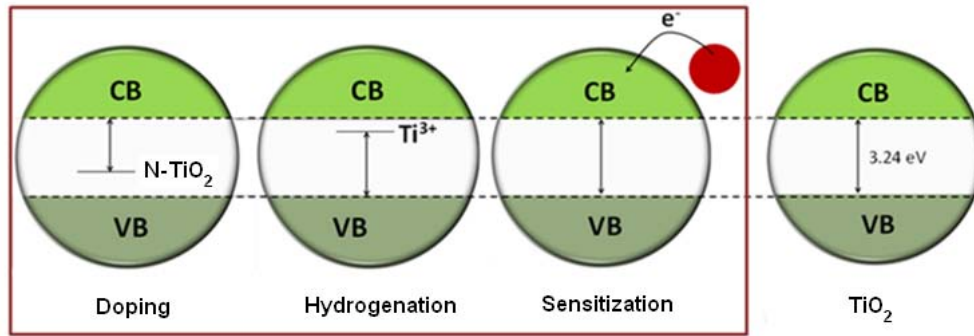
Sin embargo, la titania presenta un elevado *band gap* o diferencia energética entre sus bandas de valencia y de conducción (3,0 eV para la fase rutilo y 3,2 eV para la anatasa), correspondiente al rango del UV (aproximadamente 5% de la energía solar total), por lo que no absorbe la luz visible (aproximadamente el 45%

de la energía solar total), y en consecuencia su actividad fotocatalítica bajo luz solar es baja.

En términos de eficiencia energética, el reto consiste en extender el espectro de trabajo de la TiO_2 a la región de la luz visible para un mayor aprovechamiento de la energía solar.

Las estrategias existentes para mejorar la eficiencia fotocatalítica de los materiales basados en titania se pueden dividir en dos grupos, modificaciones asociadas con modificaciones en la morfología/porosidad de los materiales, como la disminución del tamaño de partícula, el aumento del área superficial y/o porosidad, o bien modificaciones químicas, mediante la incorporación de diversas funcionalidades en la estructura de la titania.

Las nanopartículas son la morfología más comúnmente empleada ya que permite controlar el diámetro de partícula y optimizar así el tamaño de los cristales, el área superficial o la tasa de recombinación. Por tanto, las estrategias empleadas en la actualidad para mejorar las propiedades fotocatalíticas de la titania se centran principalmente en modificaciones químicas de nanopartículas de titania. En concreto, las aproximaciones utilizadas hasta ahora para extender el espectro de trabajo de la TiO_2 a la región de la luz visible han sido: (1) el dopaje con iones metálicos y no metálicos en la estructura de la titania, siendo el nitrógeno el dopante más prometedor, (2) la reducción de la titania de Ti(IV) a Ti(III) mediante hidrogenación a elevadas temperaturas y (3) la sensibilización de la superficie de la titania mediante complejos de coordinación o colorantes (*dyes*) capaces de inyectar electrones en la banda de conducción de la titania generados a partir de la luz visible (esquema 1).



Esquema 1. Diferentes estrategias para mejorar la eficiencia fotocatalítica de la titania.

La primera estrategia se basa en la generación de estados intermedios (bien aceptores o bien donantes) por encima o por debajo de las bandas de valencia y conducción de la titania, respectivamente, mediante (i) la implantación de iones metálicos o dopaje con iones no metálicos en la red anatasa (dopaje) y (ii) la reducción del titanio mediante hidrogenación a elevadas temperaturas. A pesar de los esfuerzos realizados, los resultados están muy lejos de las eficiencias requeridas. En el caso de la hidrogenación, además, las propiedades finales dependen considerablemente del proceso de síntesis, que implica temperaturas muy elevadas, y además, requieren de la incorporación de metales preciosos, lo que encarece el material final limitando su uso.

La sensibilización de las titanias implica el uso de colorantes o compuestos de coordinación capaces de inyectar electrones en la banda de conducción de la titania sin modificar la estructura electrónica de la misma. Dicha sensibilización se realiza mediante procesos post-sintéticos, ya sea impregnación o *grafting*, de manera que el *dye* queda unido covalentemente a la superficie de la titania con el objeto de mejorar la transferencia de carga, con los sabidos problemas que ello implica en cuanto a baja homogeneidad, poca accesibilidad y sobre todo pérdida

del catalizador durante la reacción (*leaching*). Grätzell sintetizó la primera celda solar sensibilizada por colorante (DSSCs, por sus siglas en inglés) en 1991, con una eficiencia energética del 7,1%, la cual ha aumentado tan sólo hasta un 11.4% en 25 años.

De forma paralela también se han desarrollado estrategias basadas en la reducción de la tasa de recombinación de pares electrón-hueco. El método más eficaz, desarrollado hasta ahora para reducir esa tasa de recombinación y aumentar la eficiencia del fotocatalizador es el dopaje de la titania con cationes de metales de transición. La eficiencia del metal empleado dependerá de si sirve o no como mediador en la transferencia de carga así como centro de recombinación, lo cual está estrechamente relacionado con el método de preparación y la concentración de dopante, entre otros aspectos.

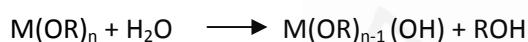
A pesar de los esfuerzos realizados, los resultados están muy lejos de las eficiencias requeridas. Ampliar el rango de aplicación de estos semiconductores al espectro visible (45% de la energía solar total) supondría utilizar más eficazmente la luz del sol para activar estos fotocatalizadores, un salto disruptivo en un área científica en la que se lleva trabajando más de 20 años, por ejemplo en el caso de la tecnología fotovoltaica.

Para la síntesis de nanopartículas son varios los métodos de síntesis que existen, tales como la precipitación química, la microemulsión, la cristalización hidrotermal, deposición en fase líquida y técnicas sol-gel. El proceso sol-gel es una de las técnicas más exitosas y ampliamente utilizadas para la preparación de materiales de diferentes óxidos metálicos de tamaño nanométrico, que se emplean posteriormente como catalizadores o como soportes para especies catalíticamente activas (nanopartículas, compuestos organometálicos, enzimas, etc).

El proceso sol-gel involucra la creación de una red sólida a través de sucesivas reacciones de policondensación en un medio líquido. Generalmente los precursores de la red sólida son alcóxidos del tipo $M(OR)_n$, donde M puede ser Si, Al, Ti, etc., y R un grupo alquilo (C_xH_{2x+1}). En el caso de la titania, la química sol-gel generalmente supone la hidrólisis y posterior condensación de un precursor de titania mediante los pasos de reacción básicos que se indican en el esquema 2.

Una vez iniciada la reacción de hidrólisis del alcóxido, sucesivas etapas de hidrólisis y condensación ocurren simultáneamente. De esta forma, la viscosidad de la disolución se va incrementando gradualmente, desde un sol (suspensión coloidal de partículas muy pequeñas, 1-100 nm) hasta formar la red rígida que constituye el gel.

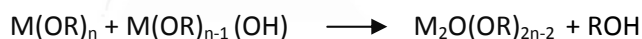
1. *Hidrólisis*



2. *Condensación:*

a. Reacciones parciales

i. Condensación con producción de alcohol



ii. Condensación con producción de agua



b. *Reacción global*



Esquema 2. Etapas de reacción en la formación de una red de titania mediante el proceso sol-gel.

Las condiciones de reacción tales como el tiempo de reacción, el pH, la proporción y concentración de los reactivos y la presencia de catalizadores,

determinan el desarrollo del proceso sol-gel, que puede resultar en cambios en la morfología y/o la estructura del sólido final.

Conscientes de las limitaciones de los métodos actuales para para mejorar la respuesta de luz visible de titanias, y las nuevas oportunidades ofrecidas por la técnica “Sol-gel Coordination Chemistry”, desarrollada en el Laboratorio de Nanotecnología Molecular de la Universidad de Alicante, la Tesis Doctoral aquí descrita, se basa en el uso de diferentes funcionalidades que pueden actuar como ligandos y coordinarse con el Ti (IV) del alcóxido de titanio, $Ti(OR)_4$.

Empleando como base la técnica sol-gel, en esta Tesis Doctoral se ha desarrollado una nueva metodología para la incorporación, en un solo paso, de diferentes funcionalidades, desde compuestos orgánicos hasta complejos metálicos y precursores de otros óxidos inorgánicos, en materiales mesoporosos basados en titania, para su posterior empleo como fotocatalizadores.

La metodología de síntesis propuesta implica la co-condensación del precursor de titania, *terc*-butóxido de titanio (IV) (TBOT), en presencia de las diferentes funcionalidades. De esta forma la hidrólisis del precursor ocurre simultáneamente a la incorporación de la funcionalidad, evitando así los problemas asociados a los métodos *post*-sintéticos ya que la funcionalidad queda incorporada dentro de la propia estructura de la titania, protegida por la misma, favoreciendo su utilización tras varios ciclos de reutilización con altos rendimientos. De esta forma, se obtienen materiales basados en titanias cuyo *band gap* ha sido modificado mediante la incorporación vía *in-situ* de diferentes funcionalidades en la red cristalina de dichas titanias durante su proceso de síntesis, así como el rango del espectro en el que son activas, desplazándolo hacia el visible. De esta forma, se generan titanias diferentes a las clásicas, con un *band gap* controlado y aptas para un uso más eficiente de la luz solar.

Con este objetivo se ha desarrollado y validado una metodología mediante la cual se incorporan a la estructura de la titania diferentes compuestos orgánicos (Capítulo 4), un complejo de Ru (II) (Capítulo 5) y dos precursores organosilíceos (Capítulo 6). La aplicabilidad de estos materiales se ha confirmado a lo largo de esta Tesis Doctoral mediante reacciones de degradación del colorante rodamina 6G bajo luz ultravioleta y luz solar, así como en la reacción de oxidación parcial de propileno, en el caso de las titanias organosilíceas.

La memoria del presente trabajo de investigación se ha estructurado en siete capítulos diferentes, cuya descripción viene resumida a continuación.

En el primer capítulo se define el objetivo propuesto del estudio de esta tesis Doctoral para a continuación describir los diferentes capítulos en los que la tesis Doctoral ha sido dividida, incluyendo un breve resumen de cada uno de los mismos.

El segundo capítulo ofrece una visión general de los semiconductores, en particular de los basados en titania, sus propiedades y estructura, sus posibles aplicaciones, desventajas y limitaciones así como el enfoque y la presentación de la química de sol-gel como una posible solución para superar tales limitaciones.

El objetivo del capítulo 3 es describir brevemente las diferentes técnicas empleadas para llevar a cabo la caracterización de los materiales preparados durante la presente investigación, haciendo especial hincapié en los aspectos más relevantes para este trabajo. Asimismo, se especifican los equipos y condiciones utilizados en cada caso así como los programas informáticos empleados para el análisis de los resultados obtenidos.

En el capítulo 4 se describe la modificación de titanias mediante la incorporación de dos compuestos orgánicos en la estructura de la misma durante el proceso de hidrólisis. Se han empleado dos compuestos orgánicos comerciales: 4,6-

dihidroxipirimidina y *p*-fenilendiamina, este último conocido por oscurecerse hasta dar coloración negra al oxidarse. Estos materiales fueron evaluados en la reacción de degradación de rodamina 6G bajo radiación ultravioleta y bajo luz visible. Se obtuvieron interesantes resultados en ambos casos, destacando especialmente la muestra de titanía con la *p*-fenilendiamina (TiO₂-PPD), la cual absorbe en todo el rango del visible y presenta una actividad fotocatalítica de hasta 3 veces superior a la titanía control, sintetizada en las mismas condiciones.

De forma similar, en el capítulo 5 se describe la síntesis de un material de titanía con un complejo de Ru (II) incorporado en su estructura. El complejo de Ru (II) elegido es similar al compuesto comercial, *dye* N3, empleado en celdas solares de tipo Grätzel (DSSCs). Como se describió en el capítulo 4, la incorporación se lleva a cabo mediante la formación de un enlace de coordinación entre los grupos carboxílicos terminales presentes en este complejo y el óxido de titanio durante la hidrólisis del precursor (TiO₂_IS). Con fines comparativos, se realizó también el *grafting* del complejo de Ru (II) sobre la superficie de la titanía (TiO₂_G), tal y como se emplea en las DSSCs. Todos los materiales se evaluaron en la reacción de degradación de rodamina 6G usando tanto irradiación UV como luz visible. Los resultados para la muestra TiO₂_IS son realmente prometedores obteniendo una mejora en la constante de fotoactividad considerable tanto bajo luz UV como con luz visible frente a la titanía control y a la titanía obtenida mediante *grafting*. TiO₂_IS, por tanto, se postula como una posible alternativa a las celdas solares de tipo Grätzel.

En el capítulo 6 se describe la síntesis de titanias híbridos obtenidas a partir de dos precursores de organosílice diferentes 1,4-bis (trietoxisilil) benceno (BTEB) y 1,2-bis (trietoxisilil) etano (BTEE), en condiciones suaves y en ausencia de surfactantes siguiendo la metodología empleada en capítulos anteriores. La

incorporación de los precursores organosilíceos en la titania se obtuvo a través de la hidrólisis y posterior condensación de un precursor de titanio en presencia del precursor organosilíceo. Los materiales sintetizados se evaluaron en la reacción de degradación de rodamina 6G bajo irradiación UV y en la reacción de epoxidación de propileno.

En los capítulos 4, 5 y 6 se incluyen los resultados obtenidos durante estancias y colaboraciones en los centros y con los grupos de investigación que se citan a continuación:

- Departamento de Química, Grupo de Materiales Moleculares Organometálicos de la Universidad de la Rioja.
- Grupo de fotocatalisis de la Universidad de Palermo, Italia.

Finalmente, el capítulo 7 contiene las conclusiones más relevantes que se pueden extraer de los resultados obtenidos en la investigación expuesta en la presente memoria de Tesis Doctoral. Asimismo se presentan las futuras líneas de investigación propuestas, basándose principalmente en la incorporación de otras funcionalidades en titania de cara a la validación del método de síntesis propuesto como de establecer el mecanismo de control del *band gap*. Se propone, además, la evaluación de los materiales sintetizados en fotocatalisis y celdas solares. Estos materiales tienen ámbitos de aplicación muy diversos como la degradación de contaminantes y materia orgánica, la eliminación de óxidos de nitrógeno o compuestos volátiles (materiales sintetizados en el capítulo 4) o su aplicación como alternativa a las celdas solares de Grätzel (materiales sintetizados en el capítulo 5) o catálisis (capítulo 6).

En cada uno de los capítulos presentados se incluye en la portada los artículos a los que han dado lugar los resultados que allí se ofrecen. Por último, en los anexos

se han incluido el listado de tablas, figuras, esquemas y abreviaturas utilizados en esta memoria.

2. CARACTERIZACIÓN DE LAS TITANIAS MESOPOROSAS

Las titanias sintetizadas a lo largo de esta memoria se caracterizaron mediante isotermas de adsorción/desorción de nitrógeno a 77 K (caracterización textural), difracción de rayos X (DRX) (estructura cristalina, tamaño del dominio cristalino y distancia entre planos), análisis elemental (AE) y espectroscopía de emisión con plasma de acoplamiento inductivo (ICP-OES) (composición química), resonancia magnética nuclear (RMN) y espectroscopía infrarroja (FTIR) y fotoelectrónica de rayos X (XPS) (incorporación de las funcionalidades en la estructura de la titania), espectroscopía de reflectancia difusa (DRUV) (cálculo de *band gap*), espectroscopía de ultravioleta-visible (UV-vis) (actividad de los fotocatalizadores) y microscopía electrónica de transmisión (TEM)(morfología).

Los análisis de resonancia magnética nuclear se han realizado en los Servicios Técnicos de la Universidad Rey Juan Carlos I en Madrid y las medidas de carbono orgánico total (COT) se llevaron a cabo en el Instituto del Agua y departamento de Ciencias Ambientales de la UA. Los ensayos sólido-gas en la reacción de oxidación del propileno y DRUV se han llevado a cabo en la Universidad de Palermo en Italia y los ensayos sólido-líquido en la reacción de degradación de la rodamina 6G (R6G) bajo luz visible en el grupo de Materiales Moleculares Organometálicos de la Universidad de La Rioja, ambos durante estancias pre-doctorales. El resto de las técnicas empleadas se han llevado a cabo en los Servicios Técnicos (SSTTi) de la Universidad de Alicante (UA).

El análisis y la interpretación de todos los resultados mostrados en esta memoria, así como las síntesis de todos los materiales descritos han sido llevados a cabo en el Laboratorio de Nanotecnología Molecular de la UA.

3. RESULTADOS Y CONCLUSIONES

Los resultados más relevantes que se pueden extraer de la investigación expuesta en la presente memoria de Tesis Doctoral se resumen a continuación.

3.1. Optimización del método de síntesis de la titania

La síntesis de titania mesoporosa, llevada a cabo mediante el método inicialmente propuesto por Wang y colaboradores (Mat. Sci. Eng. B, 2006, 128, 229), se ha optimizado de manera que la nueva síntesis permite la obtención de titanias mesoporosas en condiciones suaves sin necesidad de surfactantes.

Las titanias obtenidas presentan una estructura anatasa, elevadas áreas superficiales (250-300 m²/g), una estrecha distribución de poro (correspondiente a la distancia interparticular) y elevado volumen de mesoporos. La modificación en los parámetros de síntesis ha permitido controlar el tamaño de las nanopartículas en torno a 6 nm.

La incorporación controlada de funcionalidad en las nanopartículas de titania ha permitido la preparación de materiales híbridos de titania con diferentes funcionalidades, desde compuestos orgánicos, hasta compuestos metálicos y precursores de otros óxidos metálicos, directamente incorporadas en la estructura de la titania. Los materiales híbridos obtenidos presentan potenciales aplicaciones en fotocatalisis, como se confirmará a lo largo de la Tesis Doctoral.

3.2. Incorporación de compuestos orgánicos en la estructura de la titania

Se han sintetizado titanias con dos compuestos orgánicos incorporados en su estructura utilizando el método de síntesis comentado anteriormente, en el cual ambos compuestos quedan incorporados en la estructura de la titania durante la co-condensación y posterior hidrólisis del precursor de titania. En particular se han utilizado los compuestos comerciales: 4,6-dihidroxipirimidida (DHP) y la *p*-fenilendiamina (PPD) que dan lugar a titanias coloreadas: amarilla y negra, respectivamente (figura 1).

Los grupos -OH, -NH₂ y -COOH actúan como ligandos, coordinados con el Ti(IV) del alcóxido de titanio, Ti(OR)₄, para formar un compuesto de coordinación de Ti(IV) (figura 2, etapa i). El segundo paso es la hidrólisis y co-condensación a temperatura ambiente de dichos compuestos (figura 2, etapa ii), y su posterior cristalización en la estructura de anatasa (figura 2, la etapa iii). Se ha llevado a cabo la incorporación de 3 cantidades diferentes de ambos compuestos orgánicos. En todos ellos, la incorporación homogénea de ambos compuestos se ha confirmado mediante AE, FTIR y XPS, con rendimientos de incorporación en torno al 86%, lo que confirma la efectividad de la ruta sintética empleada.

Entre sus propiedades destacan unas buenas propiedades texturales con elevadas áreas superficiales (250-300 m²/g), estrecha distribución del tamaño de poro y tamaños de partícula en torno a 6 nm, similares a la titania control. Sin embargo, las propiedades ópticas de estos materiales híbridos son significativamente mejores en comparación a dicha titania control. En ambos casos se han obtenido titanias que presentan un *band gap* menor que la correspondiente titania control, sintetizada en las mismas condiciones.

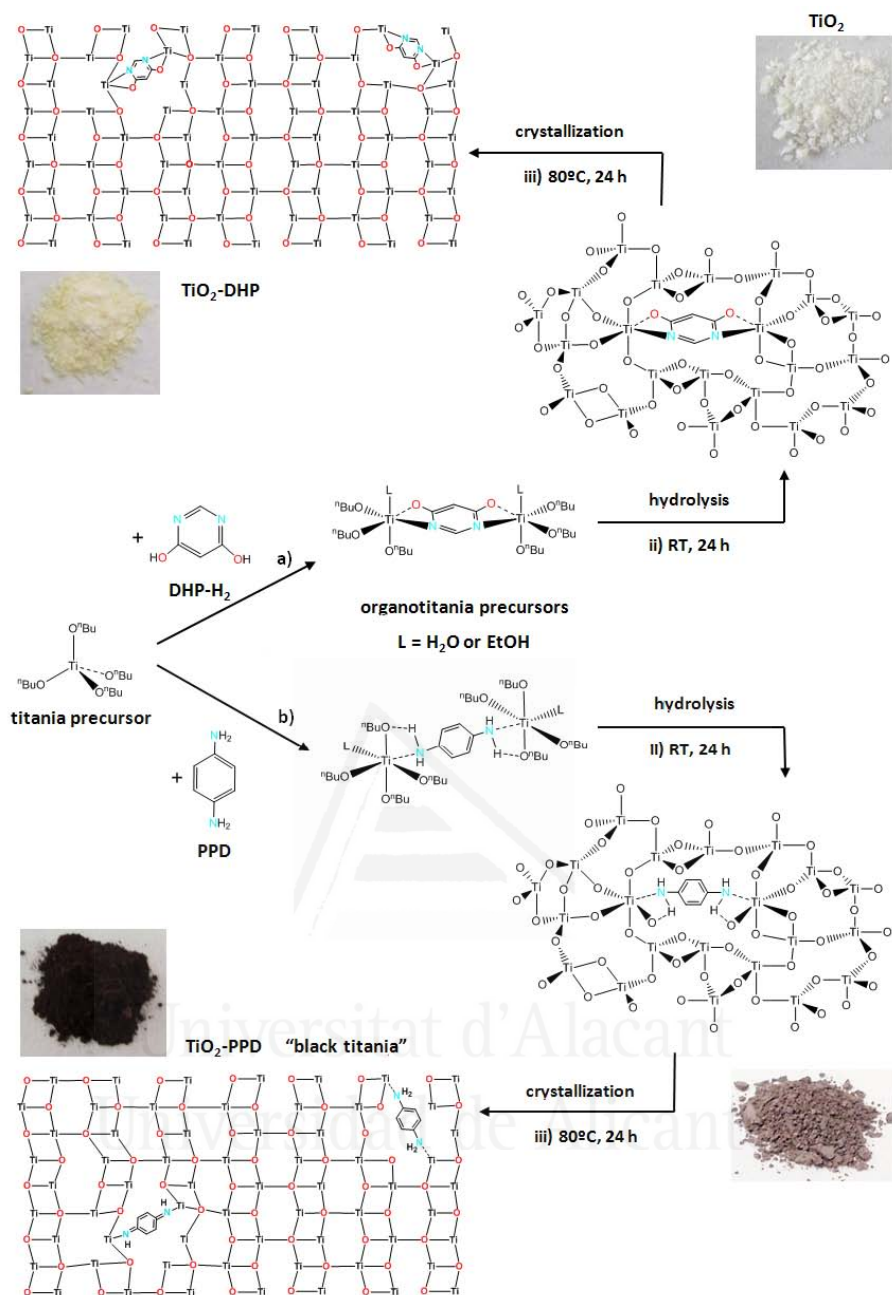


Figura 1. Esquema de la metodología propuesta para la preparación de la titania amarilla TiO₂-DHP y titania negra TiO₂-PPD.

La diferencia es mucho más acusada en el caso de la titania negra, con el compuesto PPD, debido a la oxidación parcial de la diamina, que confiere a este material la propiedad óptica de ser activo en todo el rango del visible dentro del espectro electromagnético (figura 3).

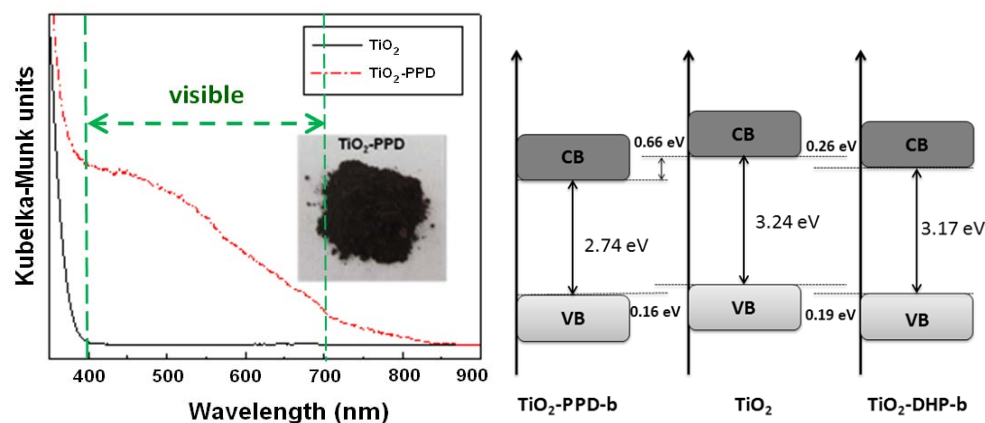


Figura 3. Espectros de DRUV de la titania control y la titania con fenilendiamina, activa en todo el rango del visible (izquierda) y esquema de densidad de estados (DOS) determinado a partir de medidas de DRUV y XPS.

La titania con el PPD incorporado, muestra un *band gap* de 2.74 eV frente al 3.24 eV de la titania control, lo que produce que este material presente una excelente actividad fotocatalítica en la reacción de degradación de rodamina 6G tanto bajo irradiación con luz UV como con luz visible, la cual se mantiene incluso tras 5 ciclos de reutilización (figura 4).

Este material constituye el primer ejemplo de uso de alcóxidos de titanio polimetálicos como precursores de organotitanias para la síntesis de titanias estables y activas en todo el rango del visible.

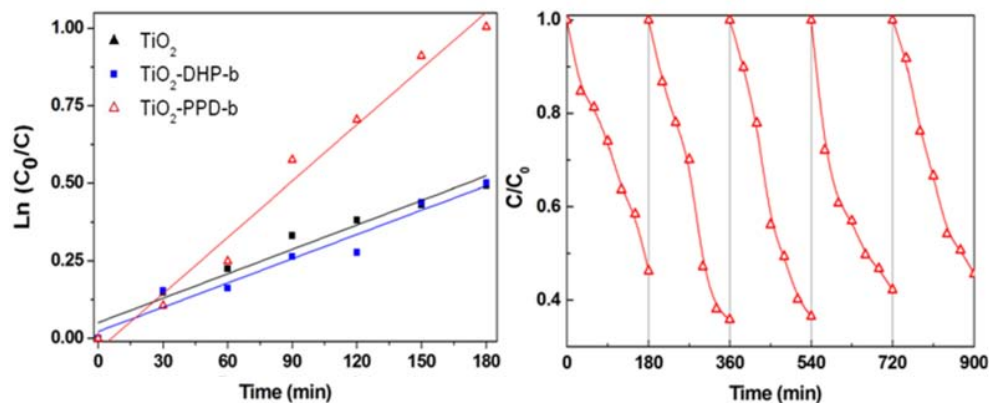
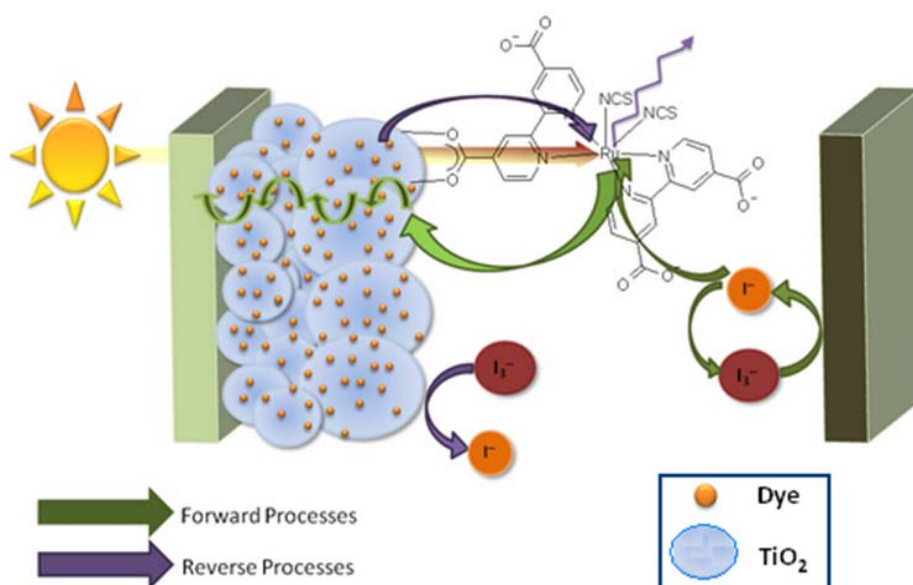


Figura 4. Representación de la constante de actividad (k') de las titanias con compuestos orgánicos incorporados frente a la titania control en la reacción de degradación de la rodamina 6G ($5 \cdot 10^{-5}$ M) bajo luz visible (izquierda). Ciclos de reutilización bajo las mismas condiciones (derecha).

3.3. Incorporación de compuestos metálicos en la estructura de la titania

De forma similar, se ha llevado a cabo la incorporación del complejo de Ru(II), conocido comercialmente como *Dye N3*, en la estructura de la titania. Dicha incorporación se lleva a cabo mediante la formación de un enlace de coordinación entre los cuatro grupos carboxílicos terminales presentes en este complejo y el óxido de titanio, durante la hidrólisis y posterior co-condensación del precursor de titanio ($\text{TiO}_2\text{-IS}$). Con fines comparativos, se realizó también la síntesis de una titania con el complejo de Ru(II) mediante *grafting*, un método tradicional (post-sintético), mediante el cual el complejo de Ru(II) queda anclado covalentemente sobre la superficie de la titania ($\text{TiO}_2\text{-G}$). Mediante esta técnica se han sintetizado las titanias usadas tradicionalmente en la celda solar de Grätzel (esquema 3).



Esquema 3. Diagrama esquemático de la celda solar de Grätzel.

La incorporación del complejo de Ru(II) en la titania ha sido confirmada en ambos casos mediante FTIR, XPS e ICP obteniendo un rendimiento de incorporación de 92% en el caso de la TiO₂_IS y de 60% en el caso de TiO₂_G.

El nuevo material TiO₂_IS presenta buenas propiedades texturales corroborando que la incorporación del complejo se ha realizado no sólo en la superficie del material, como es el caso de TiO₂_G, sino también en la estructura de la titania. En el material TiO₂_IS, la incorporación del complejo de Ru(II), provoca una disminución del band gap de hasta 2.82 eV (440 nm) frente a 3.24 eV (380 nm) de la titania control (TiO₂) o los 3.0 eV (410 nm) del material sintetizado mediante métodos tradicionales TiO₂_G (figura 5).

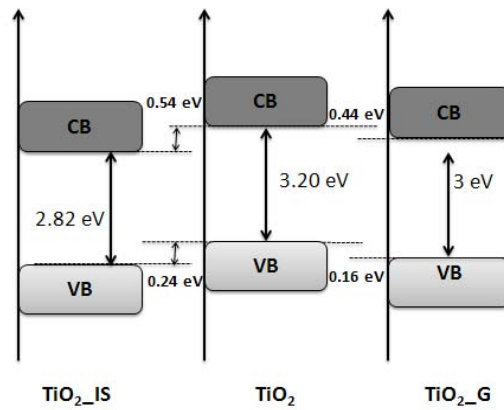


Figura 5. Esquema de la densidad de estados electrónicos de las titanias sintetizadas con el complejo de Ru(II), incorporado *in-situ* ($\text{TiO}_2\text{-IS}$) en comparación con la incorporación mediante *grafting* ($\text{TiO}_2\text{-G}$) y con la titania control TiO_2 .

Los resultados de la constantes de fotoactividad obtenidos en la reacción de degradación de rodamina 6G para la muestra $\text{TiO}_2\text{-IS}$ son hasta 4.5 veces más altos que los obtenidos para la titania control y 3 veces superiores a la titania $\text{TiO}_2\text{-G}$ (figura 6).

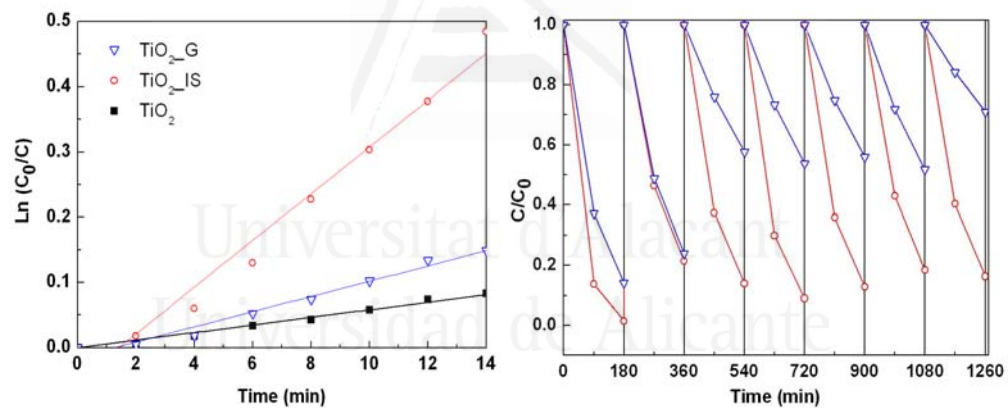


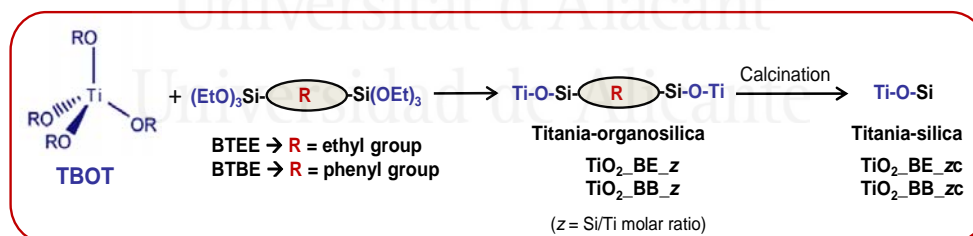
Figura 6. Representación de la constante de actividad (k') de las titanias con el complejo de Ru(II) frente a la titania control en la reacción de degradación de la rodamina 6G ($5 \cdot 10^{-5}$ M) bajo radiación ultravioleta (izquierda). Ciclos de reutilización bajo las mismas condiciones (derecha)

Cabe destacar la muestra TiO₂_IS, en la cual la efectividad permanece prácticamente constante tras 7 ciclos. En el caso de la titania TiO₂_G, sin embargo se observa claramente como la efectividad es menor y la pérdida de ésta aumenta con cada ciclo.

La ruta sintética empleada con la muestra TiO₂_IS se asocia con una mayor protección del complejo de Ru(II) en el interior de la estructura de la titania. Esta protección ayuda a obtener una mejor superposición entre el orbital LUMO del complejo de Ru(II) y la banda de conducción de la titania y, posiblemente, también ayuda a reducir la tasa de recombinación electrón-hueco que existe en este tipo de materiales. Todas estas mejoras conducen a un mejor aprovechamiento de la luz del sol y hacen de este material un candidato prometedor para su aplicación en celdas solares.

3.4. Incorporación de precursores organosilíceos en la estructura de la titania

Siguiendo la misma estrategia de síntesis, hemos obtenido nanopartículas híbridas de titania organosilíceas fotocatalíticamente activas mediante co-condensación de un precursor de titania, TBOT, con dos precursores diferentes organosilíceos: 1,4-bis (trietoxisilil)benceno (BTEB) y 1,2-bis (trietoxisilil)etano (BTEE), en ausencia de surfactantes (esquema 4).



Esquema 4. Procedimiento de síntesis de los materiales híbridos titania-organosilíce mediante co-condensación del precursor de titanio (TBOT), con diferentes cantidades de precursores organosilíceos (0.04–0.25 mol/mol TBOT).

A diferencia de lo descrito mayoritariamente en la bibliografía, los materiales híbridos de titania y organosilice sintetizados mediante esta metodología de síntesis no son una mera mezcla de sílice y titania, sino óxidos mixtos, como se pone de manifiesto por la existencia del enlace Si-O-Ti y la co-condensación de ambos precursores mediante FTIR, RMN y XPS. No se trata de óxidos mixtos perfectos ya que cuentan mayoritariamente con un enlace Ti-O-Ti, motivo por el cual mantienen su estructura anatasa.

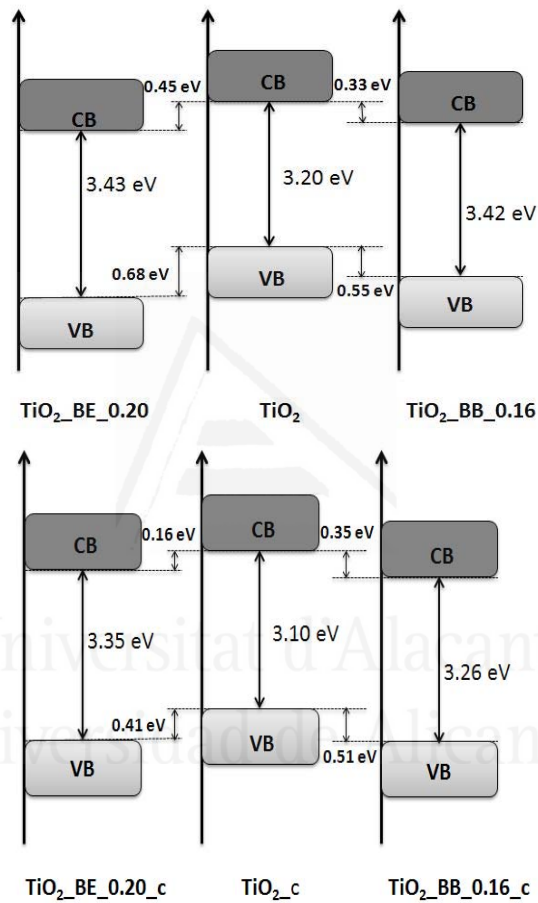


Figura 7. Representación de los diagramas de estados electrónicos de las muestras híbridas sin calentar (arriba) y calcinadas (abajo) con sus correspondientes valores de band gap.

A pesar del contenido en precursores organosilíceos, todas las muestras sintetizadas presentan áreas BET superficiales elevadas con valores similares a la titania control. Esto confirma la naturaleza mesoporosa de estas muestras y la incorporación de los grupos silíceos en la propia estructura de la titania y no entre las nanopartículas. La caracterización textural de las muestras después de la calcinación demuestra la alta estabilidad térmica de los materiales híbridos con contenido medio-bajo de precursor organosilíceo, a pesar de la ausencia de surfactante, que está probablemente asociado al cambio de coordinación en la superficie del Ti(IV) y al aumento de los enlaces Si-O-Ti tras la calcinación. Se observa un claro aumento del valor del band gap (figura 7) en todos los materiales híbridos debido al carácter aislante del Si.

La actividad fotocatalítica de estos materiales se comprobó como en casos anteriores en la reacción de degradación de la rodamina 6G, donde se confirmó que las muestras calcinadas presentan una mayor actividad que las que no lo están y la titania control tanto calcinada como la sin calcinar.

Este aumento en la fotoactividad se asocia con el cambio en la estructura electrónica de los materiales debido al cambio de coordinación del titanio y a la existencia del enlace Si-O-Ti presentes en todos los materiales.

A la vista de los resultados obtenidos en la reacción de degradación de la rodamina 6G, se estudió la actividad fotocatalítica de las muestras calcinadas en la reacción de oxidación parcial del propileno en fase gas. Los resultados obtenidos muestran como los materiales híbridos son más eficientes que la titania control en cuanto a formación de óxido de propileno (OP) se refiere. Específicamente, la muestra TiO₂_BB_0.16_c mostró, en los primeros minutos de la irradiación, un buen rendimiento en la reacción con una alta selectividad a OP.

3.5. Conclusiones generales

La metodología propuesta permite la incorporación de las funcionalidades (compuestos orgánicos, compuestos metálicos y precursores organosilíceos) en las titanias mesoporosas en un único paso, lo que conlleva un ahorro tanto en la economía del proceso, importante a la hora de escalar este proceso a escala industrial, como en su impacto ambiental debido al ahorro en tiempo y reactivos en la preparación de los mismos.

La excelente actividad fotocatalítica de todos los materiales sintetizados indica que la funcionalidad queda protegida por la red de titania cuando se incorpora directamente a su estructura. Esta protección evita los posibles inconvenientes que los materiales obtenidos por los métodos *post*-sintéticos suelen presentar, obteniéndose en todos los casos mayores valores de actividad fotocatalítica y menos pérdida de la funcionalidad a la disolución durante la reacción.

La incorporación de diferentes funcionalidades en los materiales presentados en esta memoria ha permitido validar una metodología de síntesis que podría ser aplicada a diferentes óxidos metálicos (ceria, alumina, etc) así como variar las diferentes funcionalidades a incorporar, con el fin de ampliar la aplicabilidad a otros campos. Cabe destacar que mediante esta metodología de síntesis es posible la obtención de titanias en las que se puede controlar su *band gap* mediante la funcionalidad incorporada, destacando particularmente el caso de la titania negra y la titania con el compuesto de rutenio incorporado vía *in-situ* debido a su actividad en todo el rango del visible. La funcionalidad influye decisivamente en las propiedades ópticas del material final lo que permite diseñar titanias para una aplicación en concreto con unos parámetros ópticos determinados.

Agradecimientos**Resumen****Table of contents**

Chapter 1: Abstract and objective	3
Chapter 2: Introduction	9
2.1. SEMICONDUCTORS ELECTRONIC STRUCTURE	9
2.1.1- Energy band diagrams in semiconductors	11
2.1.2- Light absorption	13
2.2. TITANIA AS PHOTOCATALYTIC MATERIAL	15
2.2.1 Structure and properties of titania	15
2.2.2 Photocatalysis process	19
2.2.3 Disadvantages and limitations	22
2.2.3.1 <i>Wide band gap</i>	22
2.2.3.2 <i>Recombination of photogenerated charge carriers</i>	23
2.2.4 Strategies for improving TiO ₂ photoactivity	24
2.2.4.1 <i>Traditional methods</i>	24
2.2.4.2 <i>Sol-gel process</i>	27
2.2.4.3 <i>Novel methods</i>	30
2.2.5 Applications	31
2.2.5.1 <i>Photocatalysis</i>	32
2.2.5.2 <i>Solar cells</i>	33
2.2.5.3 <i>Water splitting</i>	36
2.2.5.4 <i>Others</i>	38
2.2.5.4.1 <i>Pigments</i>	38
2.2.5.4.2 <i>Sensing</i>	39

2.2.5.4.3 <i>Antimicrobial coatings</i>	39
2.2.5.4.4 <i>Drug delivery</i>	40
2.3. REFERENCES	41
Chapter 3: Experimental Procedures	51
3.1. SYNTHESIS PROCEDURE	52
3.2. CHARACTERIZATION TECHNIQUES	53
3.2.1 Textural analysis. Gas adsorption	54
3.2.1.1. <i>Fundamentals</i>	54
3.2.1.2. <i>Equipment used and test conditions</i>	57
3.2.2. Thermogravimetric analysis	58
3.2.2.1. <i>Fundamentals</i>	58
3.2.2.2. <i>Equipment used and test conditions</i>	58
3.2.3. Structural and chemical composition. Molecular Spectroscopy techniques	59
3.2.3.1. <i>UV-vis spectroscopy</i>	59
3.2.3.1.1 <i>Fundamentals</i>	60
3.2.3.1.2 <i>Equipment used and test conditions</i>	60
3.2.3.2. <i>UV-vis diffuse reflectance spectroscopy</i>	60
3.2.3.2.1. <i>Fundamentals</i>	61
3.2.3.2.2. <i>Equipment used and test conditions</i>	62
3.2.3.3. <i>Nuclear magnetic resonance spectroscopy</i>	62
3.2.3.3.1. <i>Fundamentals</i>	62
3.2.3.3.2. <i>Equipment used and test conditions</i>	64
3.2.3.4. <i>X-ray diffraction</i>	64
3.2.3.4.1. <i>Fundamentals</i>	64
3.2.3.4.2. <i>Equipment used and test conditions</i>	67

3.2.3.5. <i>X-Ray fluorescence</i>	67
3.2.3.5.1. <i>Fundamentals</i>	68
3.2.3.5.2. <i>Equipment used and test conditions</i>	69
3.2.3.6. <i>X-ray photoelectron spectroscopy</i>	69
3.2.3.6.1. <i>Fundamentals</i>	69
3.2.3.6.2. <i>Equipment used and test conditions</i>	71
3.2.3.7. <i>Infrared spectroscopy</i>	71
3.2.3.7.1. <i>Fundamentals</i>	72
3.2.3.7.2. <i>Equipment used and test conditions</i>	73
3.2.3.8. <i>Inductively coupled plasma optical emission spectroscopy</i>	73
3.2.3.8.1. <i>Fundamentals</i>	73
3.2.3.8.2. <i>Equipment used and test conditions</i>	74
3.2.4. <i>Elemental analysis</i>	74
3.2.4.1. <i>Fundamentals</i>	75
3.2.4.2. <i>Equipment used and test conditions</i>	75
3.2.5. <i>Morphological study: Transmission electron microscopy</i>	75
3.2.5.1. <i>Fundamentals</i>	76
3.2.5.2. <i>Equipment used and test conditions</i>	77
3.2.6. <i>Solid-gas solid regime: Gas chromatography</i>	77
3.2.6.1. <i>Fundamentals</i>	77
3.2.6.2. <i>Equipment used and test conditions</i>	78
3.2.7. <i>Liquid-solid regime</i>	78
3.2.7.1. <i>Photocatalytic activity measurements</i>	78
3.2.7.2. <i>Total organic carbon (TOC)</i>	81
3.2.7.2.1. <i>Fundamentals</i>	81

3.2.7.2.2. <i>Equipment used and test conditions</i>	82
3.2.8. References	82
Chapter 4: Incorporation of organic compounds in the framework of mesoporous titania materials	89
4.1. INTRODUCTION	90
4.2. EXPERIMENTAL SECTION	92
4.2.1- Synthesis of the mesoporous organo-modified titanias	92
4.2.2- Physico-chemical characterization methods	93
4.2.3- Photocatalytic activity: liquid-solid regime	93
4.3. RESULTS AND DISCUSSION	94
4.3.1- Structural and physico-chemical characterization of the titanias with organic compounds incorporated into its structure	94
4.3.2- Optical properties	105
4.3.3- Liquid-solid regime photocatalytic activity of the organo-modified titania materials	109
4.3.3.1 <i>Photocatalytic activity under UV radiation</i>	110
4.3.3.2. <i>Photocatalytic activity under visible light</i>	116
4.4. CONCLUSIONS	120
4.5. REFERENCES	122
Chapter 5: Incorporation of a Ru(II) complex in the framework of mesoporous titania	129
5.1. INTRODUCTION	130
5.2. EXPERIMENTAL SECTION	135
5.2.1- Synthesis of <i>cis</i> -bis(isothiocyanato) bis(2,2'-bipyridyl-4,4'-dicarboxylato ruthenium(II) complex	135

5.2.2- Synthesis of the mesoporous Ru (II) complex titanias	135
5.2.3- Physico-chemical characterization methods	137
5.2.4- Photocatalytic activity: liquid-solid regime	138
5.3. RESULTS AND DISCUSSION	139
5.3.1- Structural characterization of the Ru(II) complex	139
5.3.2- Structural and physico-chemical characterization of the Ru(II) titania materials	141
5.3.3- Optical properties	147
5.3.4- Liquid-solid regime: photocatalytic activity of the Ru(II) titania materials	149
5.3.4.1 <i>Photocatalytic activity under UV radiation</i>	149
5.3.4.2. <i>Photocatalytic activity under visible light</i>	154
5.4. CONCLUSIONS	158
5.5. REFERENCES	160
Chapter 6: Incorporation of organosilica precursors in the framework of mesoporous titania	167
6.1. INTRODUCTION	168
6.2. EXPERIMENTAL SECTION	172
6.2.1-Synthesis of mesoporous titania-organosilicas	172
6.2.2- Physico-chemical characterization methods	173
6.2.3- Photocatalytic activity	174
6.2.3.1. <i>Liquid-solid regime</i>	174
6.2.3.2. <i>Gas-solid regime</i>	174
6.3. RESULTS AND DISCUSSION	175
6.3.1- Structural and physico-chemical characterization of the	

as-synthesized titania-organosilica materials	175
6.3.2- Structural and physico-chemical changes after calcination	186
6.3.3- Optical properties	190
6.3.4- Liquid-solid regime photocatalytic activity of the as-synthesized and calcined titania-organosilica samples.	195
6.3.5. Gas-solid regime photocatalytic activity of the calcined titania-organosilica samples	197
6.4. CONCLUSIONS	201
6.5. REFERENCES	202
Chapter 7: General Conclusions and future lines	209
7.1. GENERAL CONCLUSIONS	210
7.1.1. Incorporation of different organic compounds	212
7.1.2. Incorporation of metal complexes	213
7.1.3. Incorporation of organosilica precursors	214
7.2. FUTURE RESEARCH LINES	215
Chapter 8: Annex	222
1. LIST OF ABBREVIATIONS	223
2. LIST OF FIGURES	226
3. LIST OF SCHEMES	231
4. LIST OF TABLES	233

I. Abstract and objective



Universitat d'Alacant
Universidad de Alicante

I. Abstract and objective

Titanium dioxide (TiO_2) has historically been used as a white pigment in the paint industry due to its opacity and very high refractive index. However, in 1972, Fujishima and Honda confirmed that titanium dioxide was much more than an additive for pigments. They studied and demonstrated the potential of this semiconductor for splitting water into hydrogen and oxygen in a photo-electrochemical cell. Since that moment, the study of TiO_2 has intensified considerably owing to its wide range of promising environmental and energy related applications such as photocatalysis, solar energy conversion, sensing, self-cleaning coatings and biomedicine, among others.

Among all semiconductors that can act as photocatalysts, TiO₂ is notable for its high activity, thermal and chemical stability, low toxicity and low cost. However, TiO₂ possesses a great disadvantage, it has a wide *band gap* (3.2 eV in the anatase phase). Because of this, it can only work under ultraviolet radiation (UV) (<400 nm) for photoexcitation. This semiconductor cannot take up visible light from sunlight since the sunlight contains only 5–6% of UV radiation in its electromagnetic spectrum, meaning an external UV source is needed to maximize the photocatalytic activity of TiO₂ photocatalysts. Thus, it is necessary to overcome this shortcoming and improve the efficiency of this material by decreasing the *band gap* and making better use of the solar spectrum. Several strategies have been developed in recent years to overcome this limitation such as sensitization with dyes or doping with metals and no metals.

Sensitization has traditionally been done using post-synthetic methods, like *grafting*, where a dye is anchored to the substrate surface. This approach has several drawbacks such as pore blockage or low homogeneity in the dispersion. However, during the development of this Ph.D. Thesis the functionalities have been incorporated directly into the structure of the titania materials, through bottom-up synthetic techniques. More specifically, the synthesis method involves the co-condensation of a titania precursor in the presence of different functionalities. In this case, hydrolysis occurs at the same time as the functionality is being incorporated, thereby avoiding the problems mentioned above.

In summary, one of the main objectives of this Ph.D. Thesis is to decrease and control the *band gap* through the incorporation of different moieties into the structure of a synthesized titania material. The goal is to shift the range of the spectrum in which these hybrid materials are active, moving it towards the visible range and thus making a more efficient use of the solar light.

For this purpose a novel methodology has been proposed and developed. The technique allows the incorporation of different functionalities, such as organosilica precursors, organic compounds and Ru(II) complexes, into the framework of mesoporous titania. The radical novelty of this Ph.D. Thesis is that the proposed incorporation strategy will further the development of very cheap photoactive materials able to work using visible light. These highly efficient materials would serve as an alternative to current techniques of *band gap* control in semiconductors, in a wide range of applications. Specifically, the applicability of these materials was confirmed by several photocatalytic reactions such as the degradation of the colorant rhodamine 6G (R6G), under UV radiation and visible light, and the propylene epoxidation reaction.

The research work detailed herein has been structured into seven different chapters.

The first chapter outlines the different parts into which the Ph.D Thesis has been divided, giving a brief summary of each chapter that form it. The ultimate goal of the work is also defined.

Chapter 2 gives an overview of semiconductors, in particular titania materials, their properties and structure, possible applications, drawbacks and limitations. The sol-gel chemistry approach is proposed as a possible solution to overcome such limitations.

Chapter 3 outlines the fabrication techniques, equipment used and conditions of the experiments performed.

Chapter 4 describes of the modification of the titania materials by the incorporation of two organic compounds: 4,6-dihydropyrimidine (DHP) and *p*-phenylenediamine (PPD), that act as a bidentate ligand, into the framework of mesoporous titania. In both cases the incorporation is carried out by the formation

of a coordination bond between the hydroxyl/amine groups present in these compounds and the titania precursor during the hydrolysis of the titanium precursor. These materials were tested in the R6G degradation reaction using both UV radiation and visible light. Exciting results were obtained in both cases, especially with the sample containing *p*-phenylenediamine, obtaining one of the black titanias currently existing.

Chapter 5 involves the synthesis of a titania material with a Ru(II) complex incorporated directly into its structure, selected because of its common use in solar cells. As in chapter 4 the incorporation is carried out by formation of a coordination bond between the carboxylic terminal groups present in this Ru(II) complex and the titania, during the hydrolysis of the titanium precursor.

A titania material was also synthesized with the Ru(II) complex using traditional methods, i.e. *grafting*, for comparison purposes. Both the incorporated and the grafted materials were tested in the degradation of R6G using both UV radiation and visible light and promising results were obtained, making this material an optimal candidate for solar cells.

Chapter 6 deals with the synthesis of organosilica-titania materials obtained by the hydrolysis of two different organosilica precursors: 1,4-bis(triethoxysilyl) benzene (BTEB) and 1,2-bis(triethoxysilyl) ethane (BTEE), in mild conditions and in the absence of surfactant. The incorporation of organosilica precursors into the titania material was effected via co-hydrolysis and subsequent co-condensation of a titanium precursor with the organosilica precursor. The materials synthesized were evaluated in the R6G degradation reaction under UV radiation and the propylene epoxidation reaction.

Finally, Chapter 7 collects the general conclusions and future research lines.

II. Introduction



Universitat d'Alicante
Universidad de Alicante

II. Introduction

Nanocrystalline titania is attracting much attention worldwide due to its potential applications in environmental protection, solar energy conversion, sensing, biomedicine, photonic crystals and heterogeneous photocatalysis^[1], among others.

This chapter will introduce the semiconductor materials, focusing in particular on titania. The different structures and properties derived therefrom, as well as the drawbacks and limitations that this material presents, will be also discussed. A global vision of the titania market situation nowadays as well as possible strategies undertaken so far to help overcome its limitations, are discussed in this chapter.

2.1. SEMICONDUCTORS ELECTRONIC STRUCTURE

Semiconductors have played a fundamental role in the current technological revolution. A semiconductor behavior may vary from a conductor to an insulator depending on various factors such as the electric or magnetic field, pressure or the temperature of the environment in which it is found^[2]. In order to appreciate how semiconductors materials work and their applications, it is important to understand their basic electronic properties. Semiconductors are mainly classified into two categories: intrinsic and extrinsic^[2]. Intrinsic or pure semiconductors are those that are ideal, with no defects and no impurities. They show poor conductivity and have equal numbers of negative carriers (electrons) and positive carriers (holes). However, an extrinsic semiconductor is an improved intrinsic semiconductor with a small amount of impurities added by a process which alters the electrical properties of the semiconductor improving its conductivity.

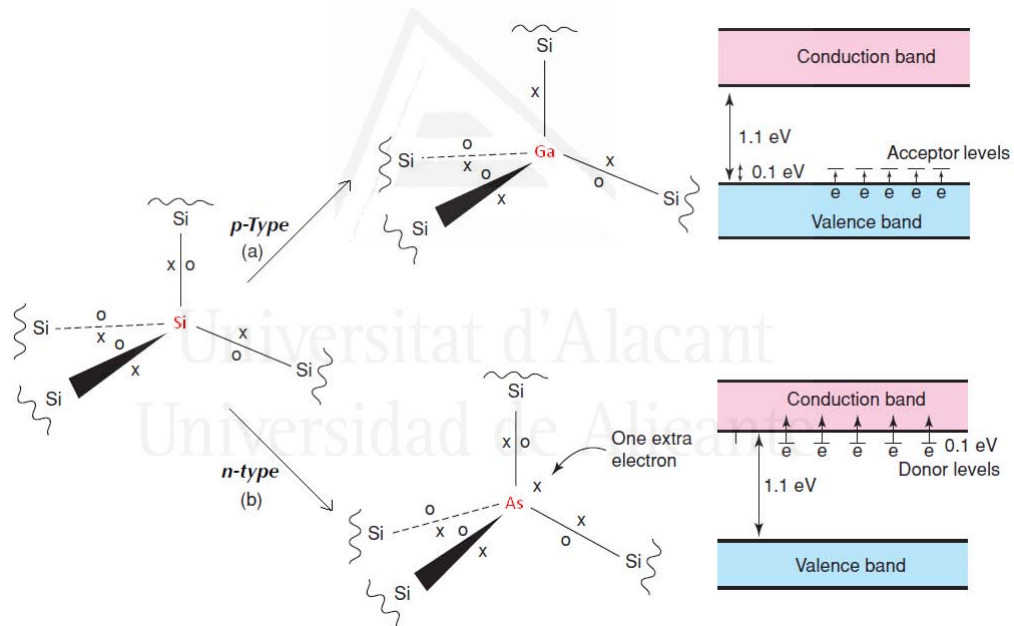


Figure 2.1. Extrinsic semiconductors: (a) *p*-type, gallium-doped silicon and (b) *n*-type, arsenic-doped silicon (adapted from ref. 2b).

The most common method of modifying the electronic properties of the semiconductors is doping, where an addition of 'foreign' atoms to the material takes place. The introduction of foreign atoms (impurities) into the semiconductor materials by the doping process vary their conductivity properties, producing two groups of semiconductors (figure 2.1), the negative charge conductor (n -type) and the positive charge conductor (p -type). Silicon and germanium are the most common intrinsic elemental semiconductors. The addition of a small percentage of foreign atoms with 5 valence electrons in the regular crystal lattice of an intrinsic semiconductor produces n -type semiconductors by contributing extra electrons. However, impurity atoms with 3 valence electrons produce p -type semiconductors by producing a hole or electron deficiency.

2.1.1. Energy band diagrams in semiconductors

When the atoms in a molecule interact, their atomic orbitals lose their individuality and become molecular orbitals, according to molecular orbital theory. The number of molecular orbitals created, is always equal to the number of combined atomic orbitals^[3].

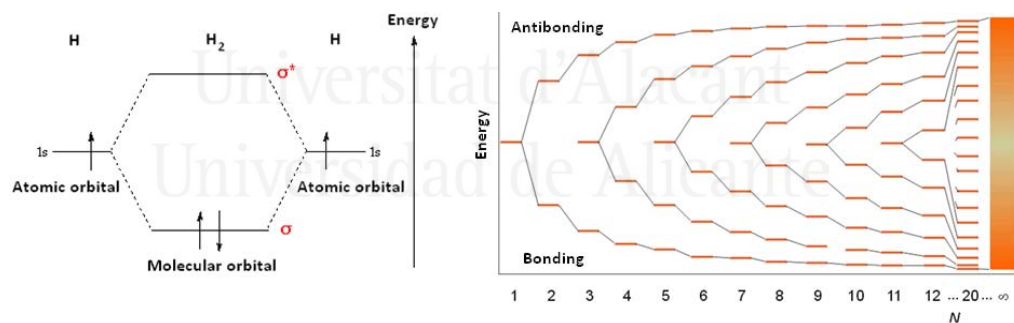


Figure 2.2. Molecular orbital diagram for the hydrogen molecule (left, adapted from ref.4) and band formation of molecular orbitals (right, adapted from ref.5)

The simplest case is the hydrogen formation (figure 2.2, left), where two atoms interact, each one with a single atomic orbital occupied by a single electron.

The molecular orbitals arise from the linear combination of atomic orbitals to form bonding (σ) and antibonding orbitals (σ^*). Bonding orbitals are at a lower energy than the antibonding orbitals, so they are the first to fill up. In a solid, the same principles can be applied. N atomic orbitals will combine to form N molecular orbitals, $N/2$ will be lowered in energy and $N/2$ will be raised in energy. As more and more atoms are brought together, the molecular orbitals extend larger and larger, and the energy levels of the molecule will become increasingly dense (figure 2.2, right). The collection of atoms will form a solid. In this situation, the energy levels are so close that they can be considered to form a band^[3].

The energy band diagrams contain multiple bands (completely-filled, completely-empty and also multiple partially-filled bands) which show the energy levels of the electrons in the material. Since the electronic properties of a semiconductor are dominated by the highest occupied molecular orbital (HOMO) and the lowest unoccupied molecular orbital (LUMO), it is therefore important to consider those bands, the valence (VB) and the conduction band (CB), respectively.

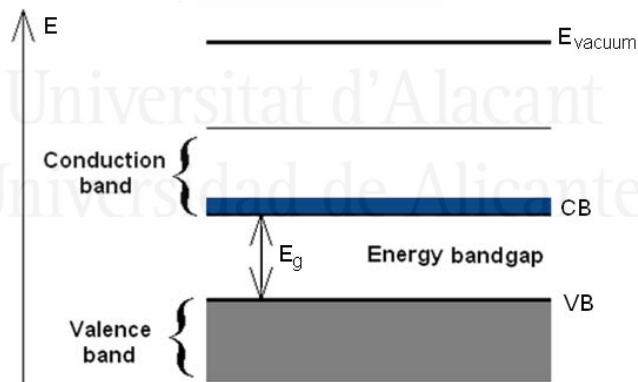
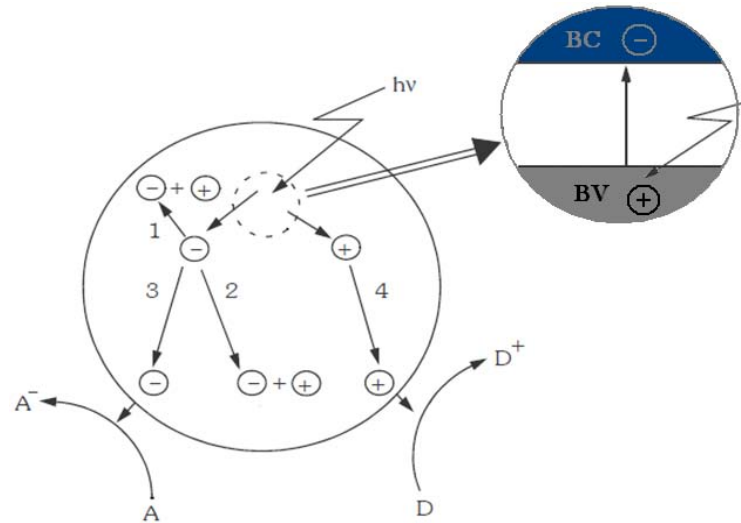


Figure 2.3. Scheme of a semiconductor energy band diagram where VB is the valence band edge, CB is the conduction band edge and E_g the band gap (adapted from ref.3).

The valence band is occupied by the electrons with the highest energy level of those which are still bonded to the bulk material. On the other hand, the conduction band is occupied by electrons which are free to move through the material. In semiconductors, there is an energy gap between the valence and conduction bands. This gap is associated with the amount of energy needed to transfer an electron from the valence to the conduction band (figure 2.3). Partially filled bands contain available energy levels at slightly higher energies as well as electrons which contribute to the electrical conductivity of the material. Completely filled bands do not contribute to the conductivity of the material. This is due to the electrons inability to gain energy since all energy levels are already full. For that reason, it can be assumed that only the valence electrons (the electrons in the outer shell) are of interest. The core electrons are tightly bound to the atom and are not allowed to freely move in the material.

2.1.2. Light absorption

If the energy of an incident photon on a semiconductor is higher than their band gap, absorption takes place. In the case of anatase phase (3.2 eV) and rutile (3.0 eV), this transition is in the UVA region, resulting in a sharp absorption band at 390-400 nm. Considering the electronic processes, the promotion of an electron to the conduction band results in a 'hole' in the valence band^[6]. The hole means a decrease in the electron density that was localised on that orbital, and usually assigned a positive charge to symbolize the loss of negative electron.



Scheme 2.1. Scheme of the mechanism produced by the electron-hole pair (adapted from ref.6).

The electron-hole pair generated (e^-h^+) forms an exciton (scheme 2.1) with a relatively short half-life, where the following mechanisms may occur^[7]:

1. The generated electron recombines with a surface defect
2. The electron recombines into the material (bulk).
3. The electron reaches the surface and reduces the adsorbed species A (acceptor).
4. The hole reaches the surface and oxidizes the adsorbed species D (donor).

Those photoelectrons that do not recombine and reach the material surface are able to exchange their charge with the species to degrade. Traps produced by surface defects act as intermediaries to prevent recombination and facilitate the transfer process.

2.2. TITANIA AS PHOTOCATALYTIC MATERIAL

Titania is a white powder, with titanium in oxidation state IV, i.e. (Ti(IV)). Its configuration is therefore $4s^2 3d^0$ and the white colour is explained by the lack of d-d or metal centered transitions. TiO_2 is a non-toxic, high photo-active, chemically stable, environmentally compatible and relatively inexpensive efficient photocatalyst.

Since the pioneering work by Honda and Fujishima, in which they reported the photoelectrochemical splitting of water using a TiO_2 anode^[8], TiO_2 has become the most widely investigated photocatalyst worldwide. At ambient temperatures, TiO_2 behaves as an *n*-type semiconductor due to oxygen vacancies in the TiO_2 lattice. This tendency for oxygen deficiency manifests itself in the formation of either oxygen vacancies or titanium interstitials; both of which are donor-type defects^[9]. Its ability to generate electron-hole pairs in the presence of suitable radiation (UV) has been used since the 70s to produce heterogeneous photocatalytic reactions^[10a].

Frank and Bard also reported the reduction of CN^- in water^[10b,c], which confirmed the potential use of this material for water and air purification through solar energy. Other relevant breakthroughs included Wang et al. who reported TiO_2 surfaces with self-cleaning abilities^[11] and Grätzel et al.^[12], who used nano TiO_2 as semiconductor material for efficient dye-sensitized solar cells.

2.2.1. Structure and properties of titania

Titanium is widely distributed over the surface of the Earth, being the ninth most abundant element on Earth (0.62% of the Earth crust). The naturally occurring titanium ores are ilmenite, rutile and brookite^[13]. Table 2.1 shows some of the physical and structural properties of the three main crystalline phases of titania.

Table 2.1. Physical and structural properties of the three common polymorphs of TiO₂^[13].

Property	Anatase	Rutile	Brookite
Melting point (°C)	1825	1825	1825
Boiling point (°C)	2500-3000	2500-3000	2500-3000
Mohr's Hardness	5.5	6.5-7	5.5-6
Refractive index	2.55	2.75	2.63
Crystal structure	Tetragonal	Tetragonal	Rhombic
Density (g/cm ³)	3.89	4.25	4.13

Titanium dioxide can exist in different polymorphs^[14]. Only three of them anatase, rutile and brookite are obtained at low pressures^[14c, 14d] and only anatase and rutile in its pure form^[15]. They can be readily synthesized in the laboratory as bulk structures and nanoparticles. The phase transformation sequence among these three titania polymorphs is size dependent, because their energies are sufficiently close that they can be reversed by small differences in surface energy.

Macrocrystalline rutile is thermodynamically stable relative to macrocrystalline anatase or brookite under ambient conditions. However, in particles with diameters below ca. 14 nm, anatase phase is more stable than rutile^[16], which can explain why anatase phase is obtained commonly when preparing titania nanoparticles.

Particularly, if particle sizes are equal, anatase is most thermodynamically stable at sizes less than 11 nm, brookite is most stable for crystal sizes between 11 and 35 nm, and rutile is most stable at sizes greater than 35 nm^[17]. If titania nanoparticles are heated, crystal growth leads to a phase transformation of both anatase and brookite to rutile. Anatase and brookite will transform to the thermodynamically stable rutile upon calcination at temperature exceeding

600°C^[9]. As previously reported, anatase phase could either transform directly to rutile, or to brookite and then to rutile^[17,18].

The activation energy of the anatase to brookite transformation is small (11.9 kJ/mol), thus the transformation can proceed at lower temperatures. However, for the brookite to rutile transformation, this energy is higher (163.8 kJ/mol), allowing the transformation only at higher temperatures^[17].

Brookite phase is the least common polymorph. There have not been much research reported about brookite and poor results (as compared with rutile and anatase phase) have been achieved with that phase^[19]. It can be due to its low stability and with the fact that it is the farthest phase from equilibrium under ambient conditions^[20].

The structure of TiO₂ comes from the octahedral coordination of Ti(IV). Each Ti(IV) atom is coordinated to six O²⁻ ions, being these oxygen ions attached to three titanium atoms with a trigonal configuration^[21]. Depending on the connections between individual octahedra, the three crystallographic forms discussed before appear (figure 2.4). Anatase can be regarded to be built up from edge-sharing octahedra, on the contrary, rutile is built up from corner-sharing octahedra. The structure of brookite is slightly complicated and contains edge-shared and corner-shared bonding. As a result, the anatase and rutile polymorphs crystallize in the tetragonal system while brookite in the rhombic one^[21].

For brookite, the atom distribution can be presented as a distorted octahedron with titanium atom almost in the center and two types of oxygen atoms in the vertices (figure 2.5). Unlike brookite, anatase and rutile structure only contain one type of oxygen atoms^[21] in all positions, with a high symmetry, being rutile more symmetric than anatase (figure 2.5).

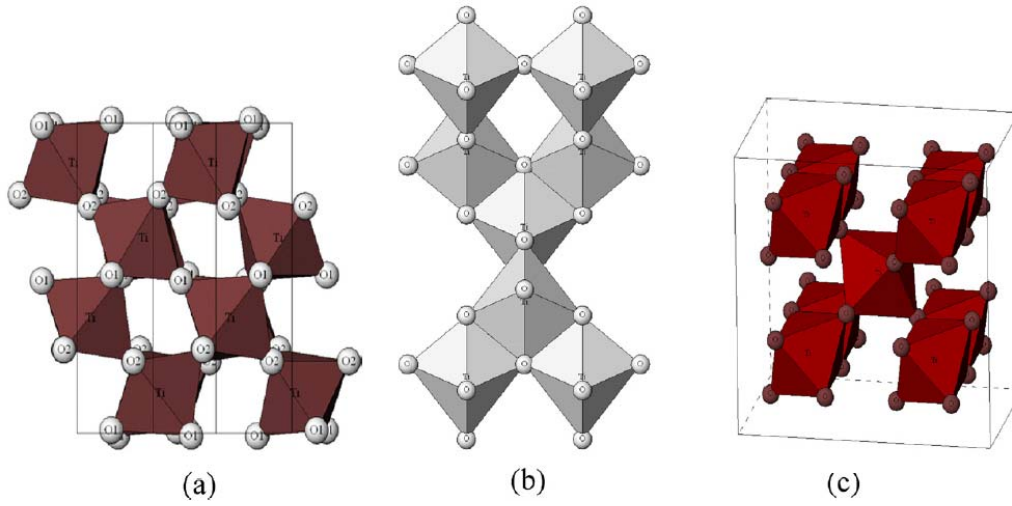


Figure 2.4. Representative crystalline structures of the three polymorphs of TiO₂: brookite (a), anatase (b) and rutile (c)^[9].

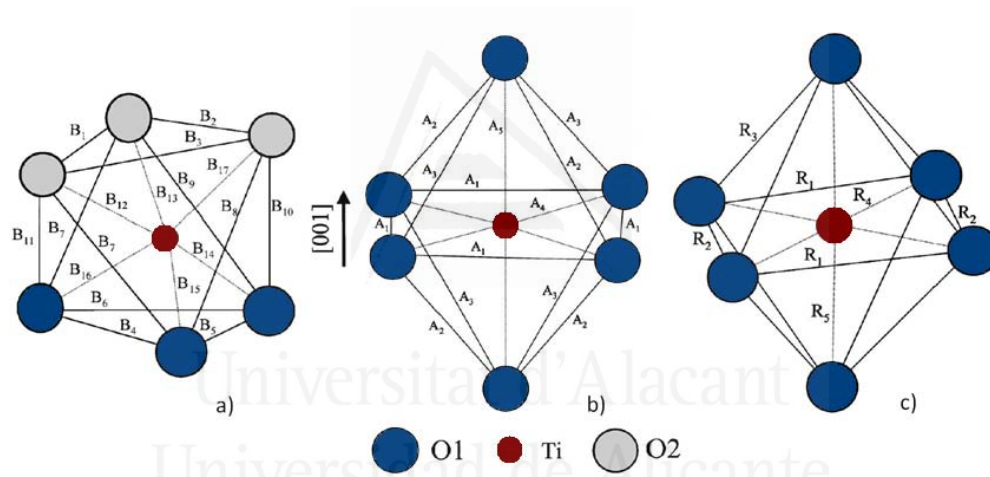


Figure 2.5. Representative octahedron of brookite (a), anatase (b) and rutile (c) crystalline structures where A, B and R represents the distances between the different ions (adapted from ref.21).

Although rutile phase has a higher refractive index (which is an important parameter for photonic crystals), anatase photocatalytic activity is higher than rutile^[22]. It can be related with a faster hole-electron recombination rate in the rutile than anatase, associated with a larger grain size and its lower capacity to adsorb species^[23], differences in morphology, synthesis conditions^[13b] and also to its lattice structure^[24].

A significant buckling degree associated with O-Ti-O bonds has been observed in anatase structure compared with rutile. Because of that the crystal symmetry is reduced, having as a result a larger unit cell dimension in the (001) direction^[22b]. The Ti-Ti distance in anatase phase is greater whereas the Ti-O distances are shorter than in rutile. In the rutile structures each octahedron is in contact with 10 neighbor octahedrons (two sharing edge oxygen pairs and eight sharing corner oxygen atoms) while in the anatase structure each octahedron is in contact with eight neighbors (four sharing an edge and four sharing a corner)^[24].

All these differences observed in lattice structures cause a variation in the mass density and electronic band structures between anatase and rutile phases. During the phase transition from anatase to rutile a change occurs in the symmetry. As a consequence, the ionic mobility that occurs during conversion results in an increased densification and coarsening of the TiO₂ nanoparticles^[25]. In order to get this densification in the rutile phase, a decrease in the mobility of the electrons involved in the photocatalysis is produced.

2.2.2. Photocatalysis process

Photocatalysis can be described as a process in which the acceleration of a reaction occurs when a semiconductor material, as for example TiO₂, interacts with a radiation to produce reactive oxidizing species which can lead to the

photocatalytic degradation of a pollutant. A TiO_2 semiconductor material presents an electronic band structure divided in two different bands, the valence band and the conduction band separated by a band gap which is in the order of 3.0-3.2 eV^[9]. The valence band and the conduction band consist of both the full 2p orbitals of oxygen and the empty 3d orbitals of titanium, which contribute to the both the bonding orbital and anti-bonding orbital and correspond respectively to the HOMO and the LUMO^[26] (figure 2.6).

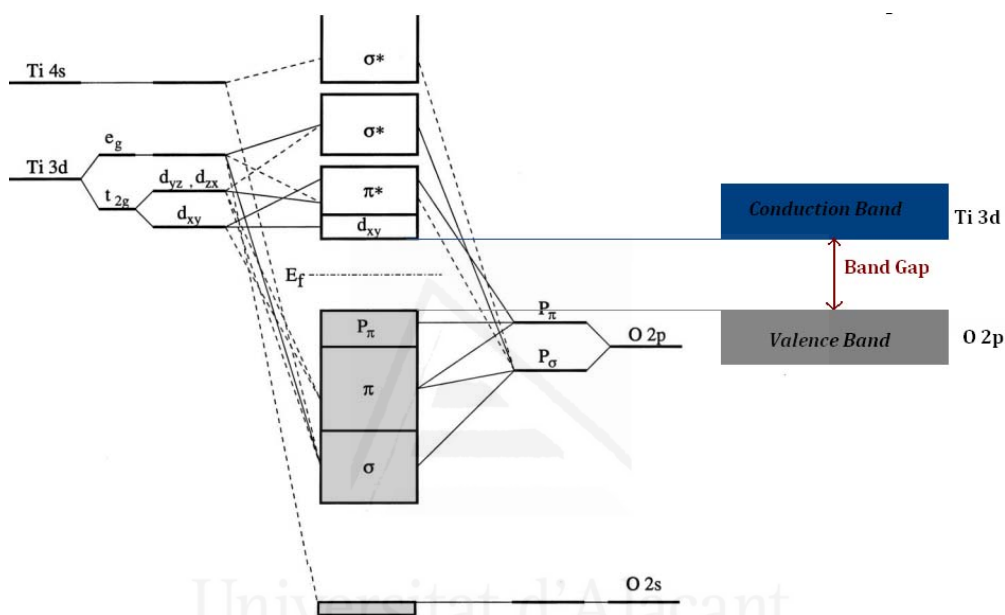
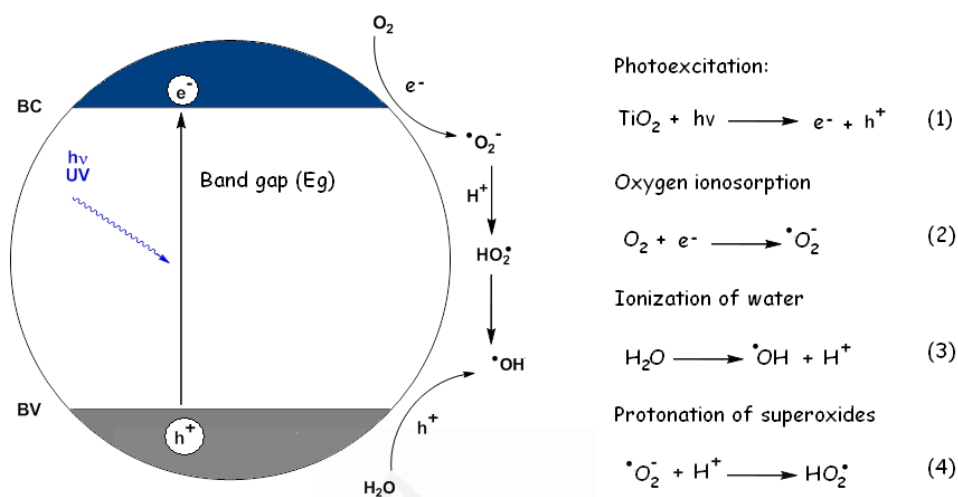


Figure 2.6. Molecular orbital bonding structure for anatase TiO_2 (adapted from ref.26c).

The basic photophysical and photochemical principles have been widely studied^[27]. Photocatalytic reaction is initiated when a photoexcited electron is promoted from the filled VB to the empty CB (scheme 2.2, left), due to the absorption of a photon with energy equal or exceed the energy difference between

the valence and conduction band (E_g), generating an electron-hole pair (e^-h^+). Anatase (3.2 eV) and rutile (3.0 eV) phases, require UV radiation ($\lambda < 384\text{nm}$)^[9].

The hole has the potential to oxidize water which results in the formation of H^+ and OH^\cdot radicals (equation 3).



Scheme 2.2. Schematic TiO_2 photoexcitation mechanism (left) and primary steps in the photocatalysis mechanism of TiO_2 under UV radiation (right) (adapted from ref.24).

Hydroxyl radicals (OH^\cdot) are themselves very powerful oxidizers, and can easily oxidize any organic species that happens to be nearby, ultimately to carbon dioxide and water. Meanwhile, the electron reduces the adsorbed oxygen to form the superoxide anion (equation 2, scheme 2.2) and they can subsequently react with protons (H^+) from water to form, again, an oxidizer radical (equation 2, scheme 2.2). This process is summarized in the scheme 2.2.

These pairs e^-h^+ can recombine, thus avoiding the photocatalytic process. It is immediate in the case of metals, but not in the semiconductors, where a time in the nanosecond range is needed, allowing the oxidation of the adsorbed molecules

on the surface of the titania by the holes^[28]. Rutile phase has a faster charge recombination rate than anatase, associated with a larger grain size and its lower capacity to adsorb species. Thus, in spite of the larger band gap of anatase phase compared with rutile, its higher density of localized states and consequent surface adsorbed hydroxyl radicals and its slower charge carrier recombination allow faster oxidation reactions and therefore photocatalysis^[23].

2.2.3. Disadvantages and limitations

Titanium dioxide could be considered one of the most researched semiconductor oxides in the field of environmental protection and energy applications but also it presents some critical limitations. The main ones are its wide band gap, which is associated with a poor response to visible light and its high electron-hole recombination rate.

2.2.3.1. Wide band gap

Although TiO₂ is the most popular photocatalyst material, it has not been applied yet widely in the field of water and air purification and energy generation control under natural solar light due to its low efficiency. UV radiation makes up only 4–5% of the solar spectrum, whereas approximately 40% of solar photons are in the visible region. The major drawback of pure TiO₂ is the large band gap (E_g = 3.0-3.2 eV) meaning it can only be activated upon irradiation with photons of light in the UV domain (≤384 nm), limiting the practical efficiency for solar applications. A shift in the optical response of TiO₂ from the UV to the visible spectral range would have a greater photocatalytic improvement in the energy efficiency of the material^[29].

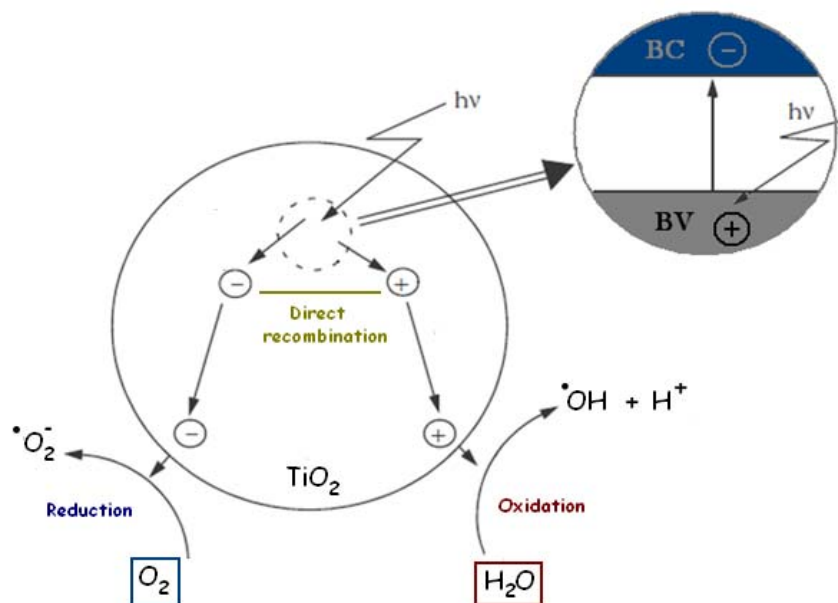
Existing visible light catalysts present several problems. As an example, CdSe or CdS are unstable under illumination and WO_3 and Fe_2O_3 have low activity^[30]. Thus, modification of TiO_2 materials in order to shift the absorption toward the visible light range is one of the main focuses of recent researches.

Furthermore, many efforts have been made to obtain nanostructured TiO_2 materials with large specific surface area. The nanostructured titania differs in its photophysical and photochemical surface properties when it is compared with its bulk counterparts due to the quantum size effect. It has been confirmed that TiO_2 nanoparticles will enhanced the photocatalytic properties of TiO_2 due to their larger active surface area and capability to avoid, or at least reduce the electron recombination rate. Moreover, the particle size of TiO_2 nanoparticles can alter the band gap width and the band bending at the interfaces, having this modification a significant impact on their photochemical properties^[31].

2.2.3.2. *Recombination of photogenerated charge carriers*

Recombination of photogenerated charge carriers is the major limitation in a semiconductor photocatalyst as it reduces the overall quantum efficiency^[32]. The recombination process (scheme 2.3) occurs when an excited electron returns to the valence band without reacting with the adsorbed species. It generates a dissipation of energy, non-radiative or radiative, as light or heat^[33].

The increase of photocatalytic activity in a titania nanoparticle is associated with a decrease in the particle size due to an increase in the specific surface area.



Scheme 2.3. Schematic electron-hole recombination in a TiO_2 nanoparticle (adapted from ref.34).

However a critical particle size exists, below which the wide band gap and the high probability for electron/hole surface recombination results in a loss of photoactivity^[34]. Zhang et al. have experimentally determined that about 10 nm was the optimal particle size for pure TiO_2 photocatalyst in the liquid-phase decomposition of chloroform^[34b].

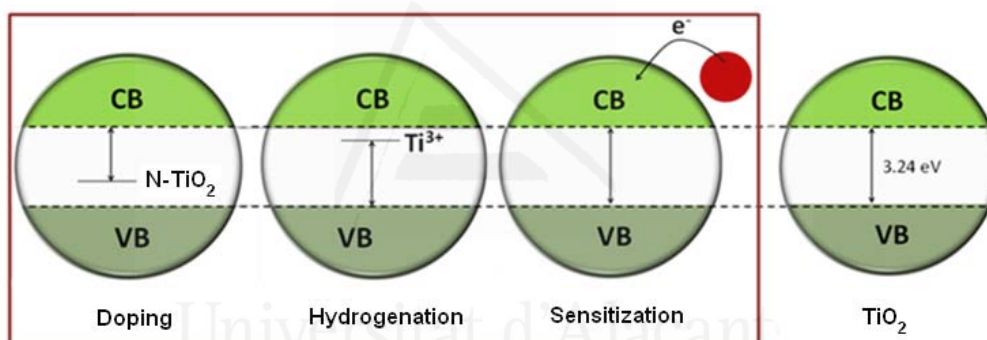
2.2.4. Strategies for improving TiO_2 photoactivity

2.2.4.1. Traditional methods

Several strategies can be adopted for improving the photocatalytic efficiency of TiO_2 materials. These strategies can be associated with morphological modifications, such as increasing surface area and porosity, or chemical modifications, by the incorporation of additional components in the TiO_2 structure.

Traditionally, the most common titania morphology has been nanoparticles, where the diameter is controlled to get small crystallite size, high surface area or reduced bulk recombination. Nowadays new strategies for improving TiO_2 photocatalytic properties are focusing on modify chemically its structure.

Typical strategies to increase the photocatalytic properties of titania are based on decreasing the band gap and extending the working range of these materials toward the region of visible light (about 45% of the total solar energy). The most successful have been (scheme 2.4): (1) the doping with metal ions or non-metal ions in the anatase structure^[35], being the nitrogen the most promising dopant^[36,37] (ii) the titanium reduction from Ti(IV) to Ti(III) by hydrogenation at elevated temperatures^[38,39] (self-doping) and (iii) the sensitization of titania surface by coordination compounds or dyes capable of injecting electrons into the conduction band by absorbing visible light^[40].



Scheme 2.4. Different strategies for improving TiO_2 photoactivity.

The first two strategies are based on generating intermediate states in the valence and conduction bands in the titania (either acceptors or donors). Despite these efforts, the results are far from the required efficiencies^[35].

In the case of the hydrogenation, the final properties are dependent of the synthesis process, which involves very high temperatures, and also require the incorporation of precious metals, which makes the final material more expensive, limiting its use^[39]. Still this technique suffers from important drawbacks including its reproducibility, high cost, charge-carrier recombination by the dopants and instability. Finally, the sensitization process is performed by post-synthetic methods as impregnation or *grafting*^[41], in order to improve the charge transfer, with the known problems involved as inhomogeneity, poor accessibility and leaching^[39,40]. Since the production of the first dye-sensitized nanocrystalline solar cell^[41b], conversion yields have only been increased from 7.1% to 11.4%. Therefore, it would be interesting the development of new synthesis strategies, which enable a better charge transfer dye integration into the semiconductor matrix. Thus, it would be possible to design higher efficiency solar cells.

Also strategies for increasing the photocatalytic properties of the titania, based on the reduction of the electron-hole recombination have been studied. Typically, the most common and effective method to reduce the charge recombination rates and increase photocatalyst efficiency is the doping of titania with transition metal cations^[42]. The relative efficiency of a metal ion dopant depends on whether it serves as a mediator of interfacial charge transfer or as a recombination center, which is related to the preparation method and the dopant concentration, among other things^[32].

For TiO₂ nanoparticles also several and different synthesis methods have been used, such as chemical precipitation^[43], microemulsion^[44], hydrothermal crystallization^[45], liquid phase deposition^[46] and sol-gel^[47]. Sol-gel processes is one of the most successful techniques (figure 2.7) and have been used extensively for preparing nanosized metallic oxide materials, which serve either as catalysts or as

supports for the catalytically active species (nanoparticles, organometallic compounds, enzymes, etc)^[48-50].

2.2.4.2. Sol-gel process

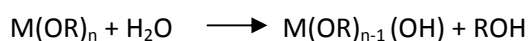
The IUPAC Gold Book defines the sol-gel process as “the process through which a network is formed from solution by a progressive change of liquid precursor(s) into a sol, to a gel, and in most cases finally to a dry network”^[51]. Sols are dispersions of colloidal particles and a gel is a rigid, interconnected network with pores of submicrometer dimensions or a polymer network with polymeric chains having average lengths greater than a micrometer^[52]. Thus, a versatile strategy for the synthesis of materials consists in the formation of a solid network starting from a liquid phase, usually a metal alkoxide precursor $M(OR)_n$ ($M=Si, Al, Ti, \text{etc.}$, where $R=(C_xH_{2x+1})$) is an alkyl group. Once the hydrolysis of the alkoxide starts in the aqueous phase, subsequent polycondensation reactions occur. The viscosity of the solution is gradually increased from a sol (colloidal suspension of very small particles 1 - 100 nm) to form a rigid gel network^[53].

The application of sol-gel process results in the formation of metal oxides around supramolecular structures, obtained by molecular self-assembly. Most literature on ordered mesoporous materials are based on silica, but, in recent years the synthesis of mesoporous oxides of titanium, aluminum, zirconium, niobium, tin, iron, manganese, among others^[54] have also described including the new family of organic-inorganic hybrid materials known as PMOs^[55,56].

In the sol-gel preparation, titanium alkoxide is first hydrolyzed (scheme 2.5, 1) by addition of water followed by polymerization of the hydrolyzed alkoxide through condensation of hydroxyl and/or alkoxy groups (scheme 2.5, 2). Condensation,

which usually includes a gelation, pulls together the gel particles of the gel, building up the metal oxide crystal^[57].

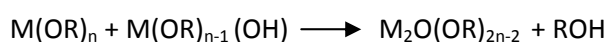
1. *Hydrolysis*



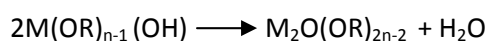
2. *Condensation:*

a. Partial reactions

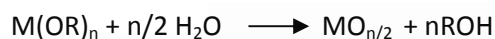
i. Dehydration



ii. Dealcoholation



b. *Overall reaction*



Scheme 2.5. Reaction steps in the formation of a titania network by sol-gel process^[567].

The polymerization process is particularly dependent on the pH. At lower pH levels, in acidic conditions, the hydrolysis proceeds slowly and the oxide tends to be formed by weakly crosslinked linear molecules.

However, under basic conditions, hydrolysis becomes the fastest step, being the condensation which determines the overall rate of reaction, resulting in larger particles and branched polymers. At intermediate pH (5-7), the rapid polymerization of the monomers leads to less organized phases. The reactivity of titanium alkoxides is considerably higher than for other alkoxides, for example silicon. Typically for the synthesis of mixed oxides such as titania-silica materials different acids are used to control the synthesis^[58].

Furthermore, the source and concentration of acids used in the synthesis have significant influence on the morphology, crystalline phase and particle size of titania^[59].

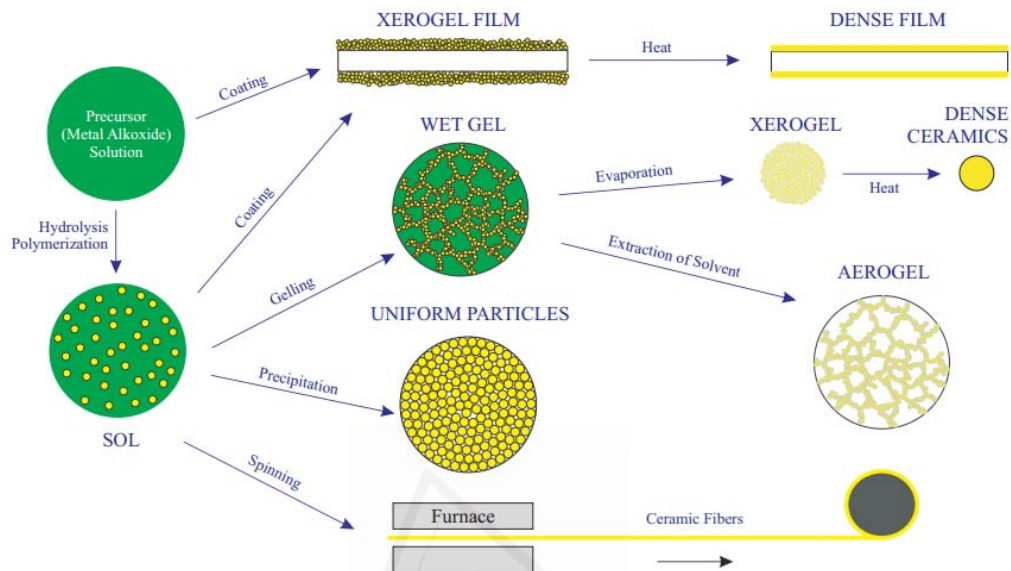


Figure 2.7. Synthesis options by sol-gel process^[60].

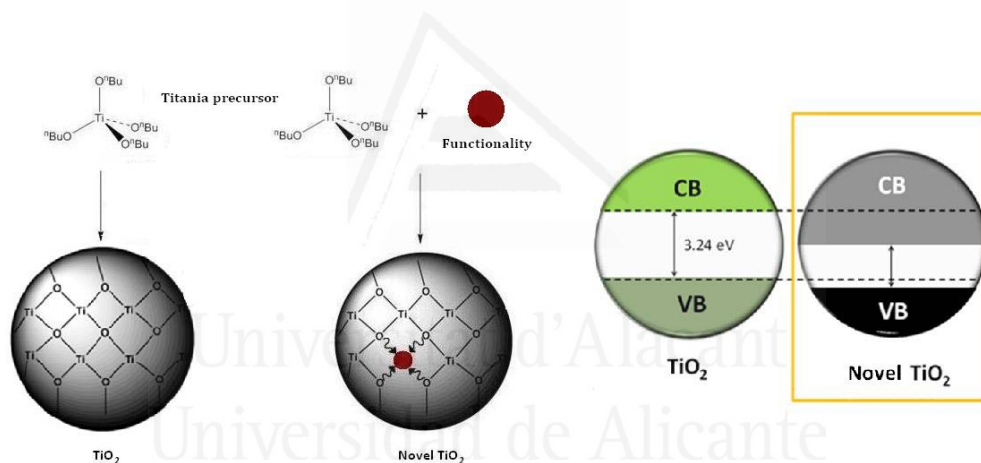
The use of surfactants is not needed to prepare mesoporous titania nanoparticles, as it is itself associated to the interparticular porosity between nanoparticles. In case of use a surfactant during the synthesis, it would be needed an additional calcination step for removing the organic molecules from the final materials.

Reaction conditions such as calcination temperature, reaction time, pH, the proportion and concentration of reactants and the presence of catalysts, determine the development of sol-gel process, which can result in changes in the morphology and/or the structure of the final solid. Calcination temperature is an important

factor to take into account because it can affect the microstructures as well as the properties of final TiO_2 nanoparticles. High calcination temperatures result in aggregation of particles and also could have associated a phase transformation of the materials.

2.2.4.3. Novel methods

The development of synthetic routes for the tailoring of efficient titania-based photocatalysts functionalized with coordination complexes has become an important goal in chemistry. Recently, there is an emerging approach, so-called sol-gel coordination chemistry reported for silica materials and based on co-condensation during the sol-gel preparation of the hybrid material of the corresponding complex or nanoparticle modified with terminal trialkoxysilane groups with a silica source and in the presence of an adequate surfactant^[61].



Scheme 2.6. Novel strategy for synthesize TiO_2 with the functionalities incorporated into its structure (left) and VB and CB position in the titania and novel titania materials (right)^[62].

The results herein described present the extension of this synthesis methodology to other metal oxides, titanium (scheme 2.6), getting the

incorporation of different chemical functionalities directly into the framework of the titania materials through the formation of a coordination bond between the terminal groups (amine groups, alcohol or carboxylic acid) present in the functionalities during the hydrolysis of the titanium precursor.

Using this strategy, novel hybrid mesoporous titania materials have been synthesized, as a method to obtain hybrid titania materials with controlled band gap and higher photocatalytic activities. This methodology leads to the obtention of new mesoporous hybrid titania materials, with the functionality incorporated homogeneously directly into the structure of the hybrid material, improving the stability of the functionality incorporated (which is protected by the titania network), reducing the leaching of the active phase and improving the photocatalytic properties of the hybrid titania. All these improvements are due to a decrease in the band gap and a better electron injection into the conduction band of the titania materials as a consequence of a good interaction between the LUMO of the dye or organic compound incorporated and the titania conduction band, favoring a rapid electron transfer to the conduction band of the titania and a low rate of recombination of electron-hole pair.

2.2.5. Applications

Over 96% of the worldwide use of titanium is in the oxide form, TiO_2 , thus creating a high demand for several applications. The development of new titania materials, is needed to provide enhanced performances and improvements with respect to the photochemical and photophysical properties of these materials.

Titania has been successfully applied in many different fields such as electronics, catalysis, sensing and biomedicine among others. Among its most important applications, energy conversion and photocatalysis can be highlighted. TiO_2 with

anatase structure has been used in the photoelectrodes of the dye-sensitized solar cell (DSSCs) and as photocatalysts to solve global energy and environmental problems.

The rutile phase is usually employed in corrosion and protective white coatings and paint, or in plastics, rubber, leather, sun-block lotion, and paper due to its high refractive index. For the brookite phase the applications are still limited. Each application requires a different morphology and properties of the titania materials. It is therefore very important to take into account the design and the synthesis conditions for the titania materials that are associated with morphological and structural changes in the final materials.

2.2.5.1. Photocatalysis

Titania photocatalysis also known as “Honda-Fujishima effect” was first unfolded by the pioneering research of Fujishima and Honda in 70’s^[63]. Photocatalysis can be described as a process in which light is used to activate a substance, the photocatalyst, which modify the rate of a chemical reaction without being involved itself in the chemical transformation. The photocatalyst creates an electron-hole pair as a result of exposure to UV radiation. The resulting free-radicals are very efficient oxidizers breaking down organic and inorganic pollutants^[64]. Already in 1977, Frank and Bard presented the decomposition of cyanide in the presence of aqueous TiO₂ suspensions^[65] and in 1980s, TiO₂ was also employed for detoxifications of several harmful compounds in air and water^[66]. Furthermore good results were also obtained using TiO₂ for photocatalytic reduction of CO₂^[67] or for water splitting by a photoelectrochemical cell^[63], among others (figure 2.8).

It can be ensured that TiO_2 photocatalysis has become a real and practical technology after the middle 90s. Nowadays competitive research studies on TiO_2 materials are still carried out worldwide based mostly on the development of new visible light sensitive photocatalysts to make a better use of sunlight for different applications. Thus, TiO_2 is playing and will continue to play an important role in the search of new renewable and clean energies and the protection of the environment, being a clear example of how basic scientific knowledge can be developed into a technological field and create a new industry.

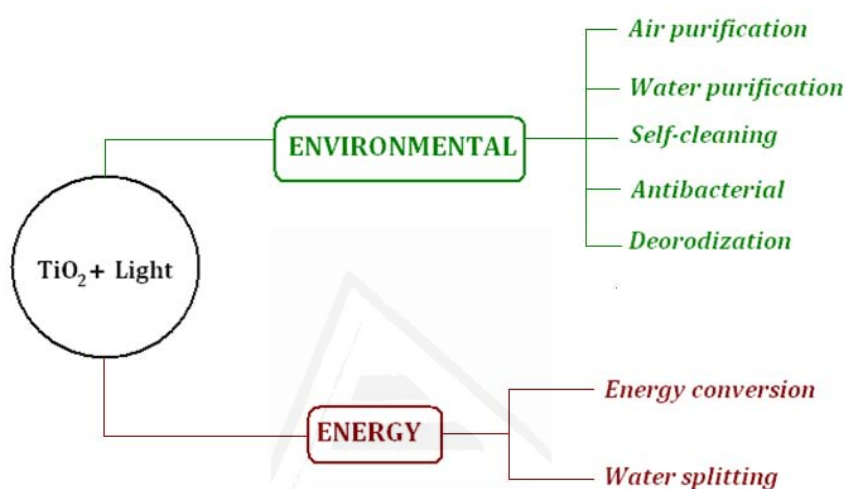
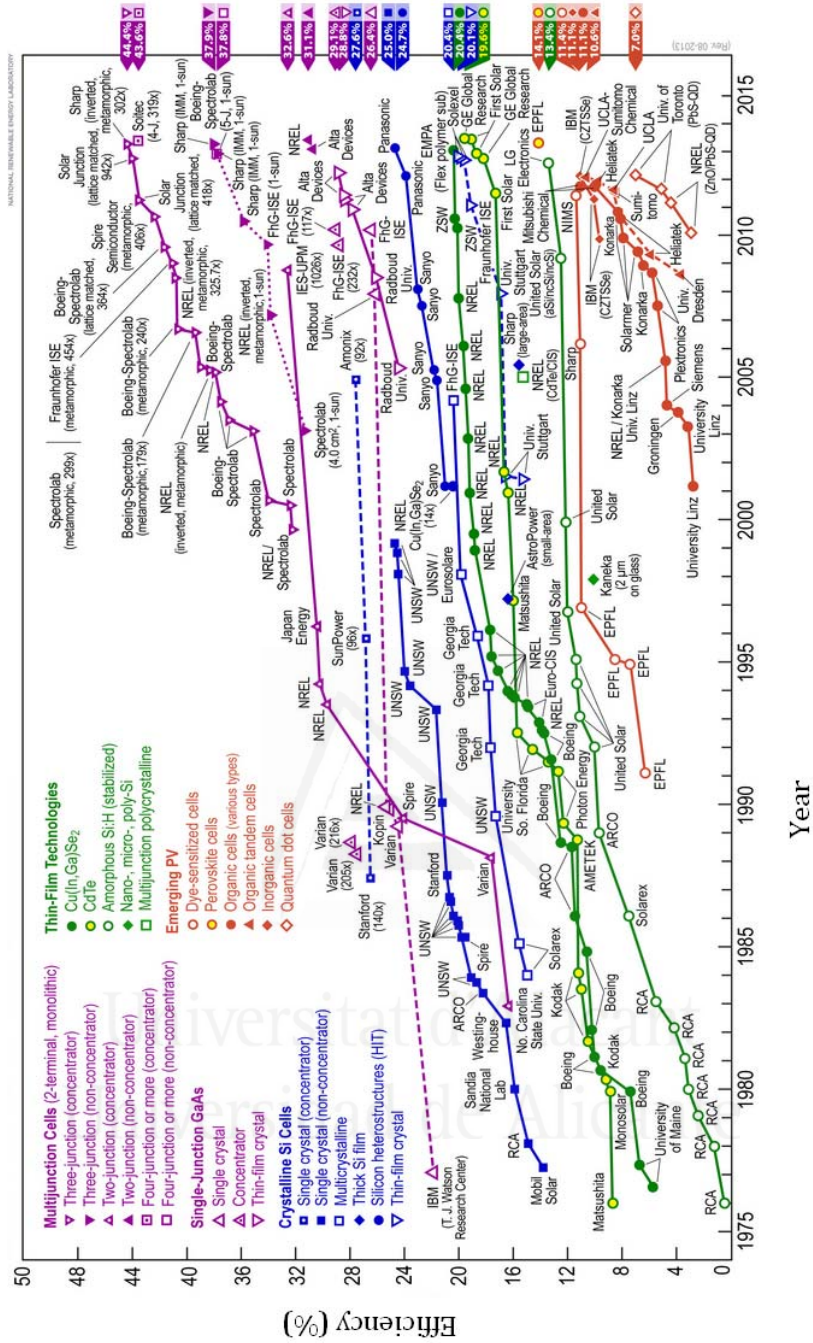


Figure 2.8. TiO_2 photocatalysis applications (adapted from ref. 68).

2.2.5.2. Solar cells

The development of sustainable and environment-friendly energy sources is needed due to the increase energy demand and the challenges of climate change. Sunlight is our largest energy resource by far. Many materials have been tested in order to obtain higher surface area, better photocatalytic properties and higher efficiency to traditional solar cells such as organic photovoltaic materials as conjugated polymers^[69,70], oligomers^[71], fullerene and fullerene derivatives^[72,73].



Scheme 2.7. NREL's latest chart of best research-cell efficiencies^[74].

The dye-sensitized nano-structured solar cell is a photoelectrochemical solar cell which delivers a competitive light-to-energy conversion efficiency together with promising stability. It was introduced by Grätzel and o'Regan in 1991^[75]. The scheme 2.7 provides an overview of the efficiencies for different solar cell types, including some emerging technologies like DSSC (14% of efficiencies), quantum dots (7%) and perovskite structures (14%) that although they are not very efficient yet, they prove to be a great promise in the solar field energy.

In terms of solar cell efficiency it is important to take into account that only solar cells with similar designs can be compared due to the big variety of solar cells varying in cost, complexity and mechanical properties among other parameters. Otherwise, other "commercial" parameters like price per kilowatt or applicability for a specific purpose should be considered in the first place because there is a gap between the research and the commercial solar cells. Thus, a research cell could be very efficient but difficult or even impossible to produce on a large scale. As an example multi-junction solar cells show the most efficiency (38-44%, scheme 2.6). The production of this type of cells on a large scale is still slow due their high costs.

These cells have several "*p-n* junctions", elementary "building blocks" that convert light to electricity. Each block is tuned to a different wavelength of light, reducing one of the largest inherent sources of losses, and therefore increasing the efficiency. However it implies a significant increase of complexity, and also costs. The commercial solar cells most used worldwide are still silicon-based solar cells (either single crystal or multicrystalline). In the case of multicrystalline silicon, it is easier to mass manufacture rather than single production and therefore cheaper. However it presents some disadvantages in relation to the material quality due to the presence of grain boundaries.

DSSCs that use nanocrystalline titanium dioxide as a semiconductor material are nowadays promising alternative photovoltaic devices, with high conversion efficiency, high quality materials and low cost making compared to silicon-based solar cells. TiO_2 has been one of the most popular photocatalysts, but its limited activity under visible light limits its practical applications in the photovoltaic field. However, heterogeneous TiO_2 photocatalysts sensitized by dyes^[76] extend its absorption beyond the UV range and it is become a promising substitute to the fossil fuels sources.

2.2.5.3. Water splitting

Water splitting can be described as a dissociation of water into hydrogen (H_2) and oxygen (O_2), using either artificial or solar light (figure 2.9). It has been widely investigated as a clean and renewable source of H_2 , due to both solar light and water are renewable.

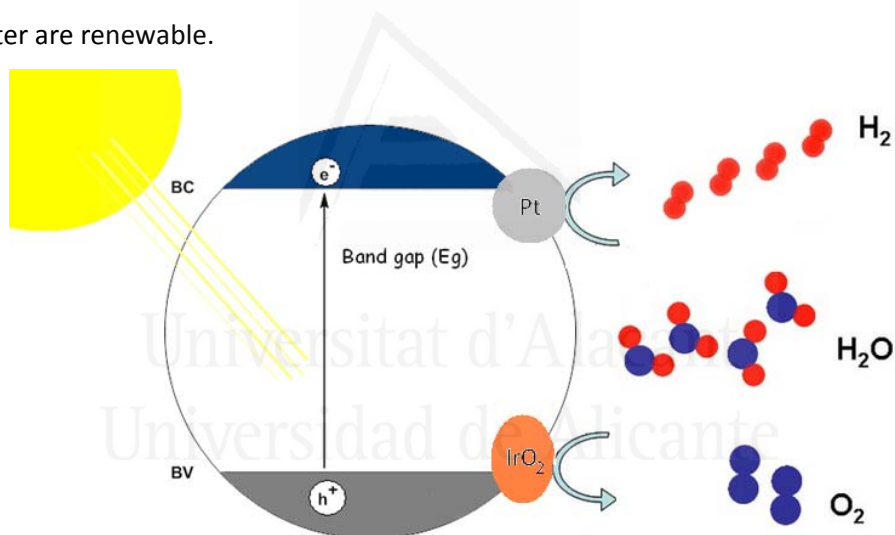
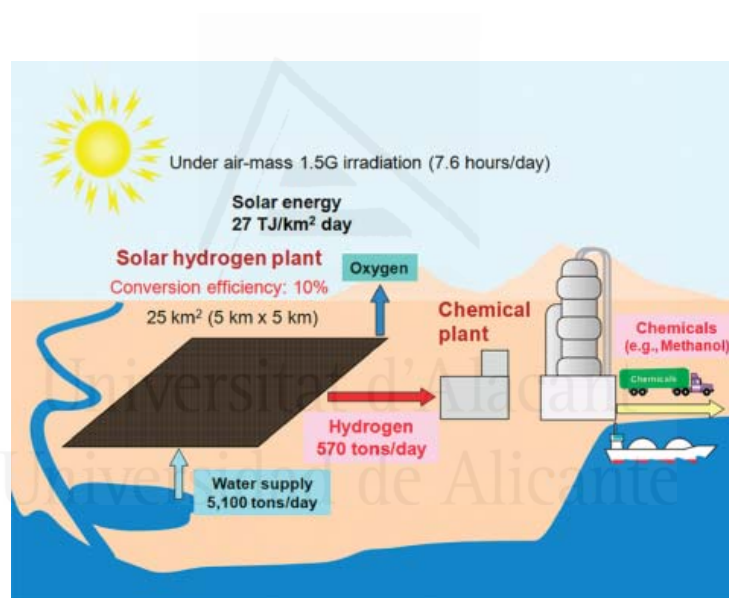


Figure 2.9. TiO_2 water splitting process employing a $\text{Pt}/\text{TiO}_2/\text{IrO}_2$ system where TiO_2 is used as light absorber, Pt as hydrogen evolution catalyst and IrO_2 as the oxygen evolution catalyst.

In recent years many efforts have made to design suitable photocatalysts to be used in the photocatalytic hydrogen production from water splitting without producing greenhouse gases^[77-79].

Several photocatalysts have been synthesized and tested in the water-splitting reaction. TiO_2 is the most common photocatalyst, although its activity is limited to UV radiation (band gap 3.0-3.2 eV). Also other oxide photocatalyst that act under UV radiation are $\text{Sr}_2\text{M}_2\text{O}_7$ ($M=\text{Nb}, \text{Ta}$), etc. Among non-oxide photocatalysts, CdS (band gap 2.4 eV) has been widely studied due to its activity under visible light, although it has associated photocorrosion problems in the absence of suitable sacrificial reagent^[78]. The major task is to develop photocatalyst with a sufficiently narrow band gap to harvest visible photons and stability against photocorrosion with a high solar energy conversion efficiency^[78].



Scheme 2.8. Scheme of a possible and future large-scale H_2 production via water splitting^[79].

Technical estimations show that in 2050, one-third of the energy will be supplied by 1000 solar plants with a solar energy conversion of 10%^[79]. Thus the main focus is to develop suitable photocatalysts for overall water splitting under solar light with a large absorption band, narrow band gap (2 eV should be desirable) and higher solar energy conversion efficiency.

2.2.5.4. Others

In addition to the applications discussed above, TiO₂ presents many others uses, that although are not the focus of this research work, will be briefly discussed in this section.

2.2.5.4.1. Pigments

TiO₂ most widely used application is as a pigment (figure 2.10), where it is used in powder form, exploiting its optical properties. It acts providing whiteness and opacity to several products such as paints and coatings, plastics, paper, inks, fibres and specialties as food and cosmetics. Titania is white and has a very high refractive index, exceeded only by diamond, making it an effective opacifier for pigments.

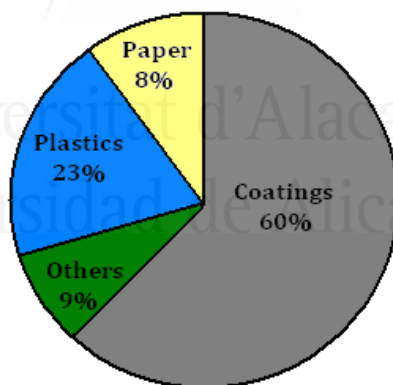


Figure 2.10. Schematic illustration of TiO₂ applications as a pigment (adapted from ref.80).

The refractive index determines the opacity that the material confers to the matrix in which the pigment is housed. The material is used as an opacifier in glass and porcelain enamels, cosmetics, sunscreens, paper, and paints being, one of the major advantages of the material its resistance to discoloration under UV radiation. Several researches confirm that the incorporation of TiO₂ in plastic and paper coatings achieves significant gains in brightness and opacity in the final materials due to the high light scatter ability of TiO₂ and the high refractive index contrast^[81].

2.2.5.4.2. Sensing

The technology for preparing TiO₂ with appropriate properties for its use as gas sensors are nowadays under permanent study^[82]. The gas-sensing mechanism of TiO₂ sensors can be explained by the adsorption of gas molecules on the TiO₂ surfaces and charge redistribution between the surfaces and the adsorbed molecules^[83]. These absorptions are associated with changes in the TiO₂ electronic structure and conductivity.

Particularly, for oxygen sensors in mild reducing atmospheres titania tends to lose oxygen and become *sub*-stoichiometric. When it is in this form the electrical resistivity of the material can be correlated to the oxygen content of the atmosphere to which it is exposed. Thus titania can be used to monitor the amount of oxygen (or reducing species) present in an atmosphere. Moreover, several researches have recently tested its sensor sensitivity for SO₂, H₂ and CO^[82a, 83] obtaining promising results.

2.2.5.4.3. Antimicrobial coatings

Infection control is of utmost importance in areas which require a high level of hygiene as hospitals, medical products, packaging food materials, or filters used in

air-conditioning systems. Thus, titania materials can have another interesting application in thin coatings, exhibiting self-cleaning and disinfecting properties under exposure to UV radiation with safety, economic and environmental advantages. These properties make TiO_2 a promising candidate for applications such as medical devices, food preparation surfaces, air conditioning filters, and sanitary ware surfaces. Moreover, titania nanoparticles seem to be a very good option for antimicrobial additives. The reason is mostly due to their size, which is similar to the size of the cells and particles and can pass through the membrane easily^[84-86]. More and more experiments in this field are being done and the proof is the great results obtaining for TiO_2 as effective antibacterial agents for coating on the high density polyethylene films^[85] and silver coated TiO_2 nanoparticles with a great inhibitory effect on bacteria as *E. Coli* and *S. Aureus*^[86].

2.2.5.4.4. Drug delivery

Nowadays, a growing interest in application of TiO_2 materials for biomedical applications exists, although the synthesis is not easy for that application. The research is focused on disinfection and the killing of cancer cells using photocatalytic chemistry with TiO_2 ^[87]. Although progress in this field is slow, some studies have already demonstrated that TiO_2 nanoparticles with properties as biocompatibility, ease of functionalization and high payload of therapeutic agents could be an excellent drug delivery platform^[88].

2.3. REFERENCES

- [1] (a) L. Saadoun, J. A. Ayllon, J. Jimenez-Becerril, J. Peral, X. Domenech, R. Rodriguez-Clemente, *Mat. Research Bull.*, 2000, **35**, 193; (b) A. Fujishima, T.N. Rao, A. Donald, *J. Photoc.: Photochem. Rev.*, 2000, **1**, 1; (c) T. Aarthi, G. Madras, *Ind. Eng. Chem. Res.*, 2007, **46**, 7; (d) A.L. Linsebigler, G. Lu, J.T. Yates, *Chem. Rev.*, 1995, **95**, 735.
- [2] a) M.L. Cohen, J.R. Chelikowsky, *“Electronic structure and optical properties of semiconductors”*, Springer, Berlin, 1988 ; b) A.R. West, *“Solid State Chemistry and its applications”*, John Wiley & Sons (2nd Edition), Chichester , 2014.
- [3]a) R.J. Singh, *“Solid-State Physics”*, Pearson Education India, New Delhi, 2011; b) B. Van Zeghbroeck, *“Principles of Semiconductor Devices”*, 2011 (http://ecee.colorado.edu/~bart/book/book/chapter2/ch2_3.htm) (Accessed on January, 2014)
- [4] W. Locke, *“Introduction to molecular orbitals theory”*, ICSTM Department of Chemistry, UK, 1996, (www.ch.ic.ac.uk/vchemlib/course/mo_theory/main.html) (Accessed on May, 2014)
- [5] H.J. Deiseroth, *“Lecture: Solid State Chemistry”*, 2006 (http://www.chemie-biologie.uni-siegen.de/ac/be/lehre/teil1_mit_rem_mini.pdf) (Accessed on May, 2014)
- [6] A. Linsebigler, G. Lu, J. T. Yates, *Chem. Rev.*, 1995, **95**, 735.
- [7] A. Mills, S. Le Hunte, *J. Photochem. Photobiol. A: Chemistry*, 1997, **108**, 1.
- [8] A. Fujishima, K. Honda, *Nature*, 1972, **238**, 37.
- [9] M. Pelaez, N.T. Nolan, S. Pillai, M.K. Seery, P. Falaras, A.G. Kontos, P.S.M. Dunlop, J. W.J Hamilton, J.A. Byrne, K. O’shea, M.H. Enterazi, D.D. Dionysiou, *App. Catal. B: Environ.*, 2012, **125**, 331.

- [10] a) J.H. Carey, J. Lawrence, H.M. Tosine, *Bull. Of Environ. Cont. & Toxicol.*, 1976, **16**, 697; b) S.N. Frank, A.J. Bard, *Journal of the Am. Chem. Soc.*, 1977, **99**, 303; c) S.N. Frank, A.J. Bard, *J. Phys. Chem.*, 1977, **81**, 1484.
- [11] R. Wang, K. Hashimoto, A. Fujishima, M. Chikuni, E. Kojima, A. Kitamura, *Nature*, 1997, **388**, 431.
- [12] B. O'Regan, M. Gratzel, *Nature*, 1991, **353**, 737.
- [13] a) T. Brock, M. Groteklaes, "*European Coatings Handbook*", Hanover, 2000; b) J. Kumar, A. Bansal, *Mat. Sci. Forum*, 2013, **764**, 130.
- [14] a) J. Tang, S. Endo, *J. Am. Ceram. Soc.*, 1993, **76**, 796; b) H. Sato, S. Endo, M. Sugiyama, T. Kikegava, O. Shimomura, K. Kusaba, *Science*, 1991, **251**, 786; c) J. Akimoto, Y. Gotoh, Y. Oosawa, N. Nonose, T. Kumagai, K. Aoki, H. Takei, *J. Solid. State Chem.*, 1994, **113**, 27; d) R. Marchand, L. Brohan, M. Tournoux, *Mater. Res. Bull.*, 1980, **15**, 1129.
- [15] Zheng, Y.; Shi, E.; Chen, Z.; Li, W.; Hu, X. *J. Mater. Chem.*, 2001, **11**, 1547.
- [16] H. Zhang, J.F. Banfield, *J. Mater. Chem.* 1998, **8**, 2073.
- [17] H. Zhang, J.F. Banfield, *J. Phys. Chem. B*, 2000, **104**, 3481.
- [18] T. Mitsuhashi, O.J. Kleppa, *J. Am. Ceram. Soc.*, 1979, **62**, 356.
- [19] a) A. Pottier, C. Chaneac, E. Tronc, L. Mazerolles, J.J. Jolivet, *Mater. Chem.*, 2001, **11**, 1116; b) H. Kominami, M. Kohno, Y. Kera, *J. Mater. Chem.*, 2000, **10**, 1151.
- [20] X. Nie, S. Zhuo, G. Maeng, K. Sohlberg, *Int. J. Photoen.*, 2009, **2009**, 294042.
- [21] X. Bokhimi, A. Morales, M. Aguilar, J.A. Toledo-Antonio, F. Pedraza, *Int. J. Hydrogen Energy*, 2001, **26**, 1279.
- [22] a) J-Y. Park, C. Lee, K-W. Jung, D. Jung, *Bull. Korean Chem. Soc.*, 2009, **30**, 2; b) Y. Liang, S. Gan, S. A. Chambers, E. I. Altman, *Phys. Rev. B*, 2001, **63**, 235402.
- [23] D.A.H. Hanaor, C.C. Sorrell, *J. Mater. Sci.*, 2011, **46**, 855.

- [24] A. Ahmad, G. H. Awan, S. Aziz, "Pakistan Engineering Congress, 70th annual Session Proceedings", 2000.
- [25] a) H. Z. Zhang, J.F. Banfield, *J. Mater. Chem.*, 1998, **8**, 2073; b) H.Z. Zhang, J.F. Banfield, *J. Phys. Chem. B*, 2000, **104**, 3481.
- [26] a) Z. Wang, Y. Liu, B. Huang, Y. Dai, Z. Lou, G. Wang, X. Zhang, X. Qin, *Phys. Chem. Chem. Phys.*, 2014, **16**, 2758; b) S. Agrawal, N.J. English, K.R. Thampi, J.M.D. Macleeroy, *Phys. Chem. Chem. Phys.*, 2012, **14**, 12044; c) R. Asahi, Y. Taga, W. Mannstadt, A. Freeman, *J. Phys. Rev. B*, 2000, **61**, 7459.
- [27] a) J. Zhao, X. Yang, *Build. Environ.*, 2003, **38**, 645; b) N.T. Dung, N.V. Khoa, J.M. Herrmann, *Inter. J. Photoenergy*, 2005, **7**, 11; c) J. Kumar, A. Bansal, *Mat. Sci. Forum*, 2013, **764**, 130.
- [28] P. Pizarro, Ph.D Thesis: "Desarrollo de materiales basados en TiO_2 mesoestructurado con aplicaciones fotocatalíticas", Rey Juan Carlos, Madrid, 2000.
- [29] Y. Liu, X. Chen, J. Li, C. Burda, *Chemosphere*, 2005, **61**, 11.
- [30] K. Kobayakawa, Y. Murakami, Y. Sato, *J. Photochem. Photobiol. A: Chem.*, 2005, **170**, 177.
- [31] M.H. Razali, M.N. Ahmad-Fauzi, R.M. Abdul, S. Sreekantan, *Adv. Mat. Research*, 2013, **772**, 365.
- [32] a) W. Choi, A. Termin, M.R. Hoffmann, *J. Phys. Chem. B*, 1994, **98**, 13669; b) M. Zhong, J. Shia, W. Zhanga, H. Hana, C. Lia, *Mat. Sci. Eng. B*, 2011, **176**, 1115.
- [33] J. Liqiang, Q. Yichun, W. Baiqi, L. Shudan, J. Baojiang, Y. Libin, F. Wei, F. Honggang, S. Jiazhong, *Solar En. Mat. & Solar Cells*, 2006, **90**, 1773.
- [34] a) B. Faure, G. Salazar-Alvarez, A. Anhiyaz, I. Villaluenga, G. Berriozabal, Y. Miguel, L. Bergström, *Sci. Technol. Adv. Mater.*, 2013, **14**, 023001; b) C. Wang, Z. Zhang, J. Ying, *Nanost. Mater.*, 1997, **9**, 583; c) Z. Zhang, C. Wang, R. Zakaria, J. Ying, *J. Phys. Chem. B*, 1998, **102**, 10871.

- [35] a) R. Asahi, T. Morikawa, T. Ohwaki, K. Aoki, Y. Taga, *Science*, 2001, **293**, 269; b) S.U.M. Khan, M. Al-Shahry, W.B. Ingler, *Science*, 2002, **297**, 2243; c) X. Chen, C. Burda, *J. Am. Chem. Soc.*, 2008, **130**, 5018; d) J.H. Park, S. Kim, A.J. Bard, *Nano Lett.*, 2006, **6**, 24; e) T. Umebayashi, T. Yamaki, H. Itoh, K. Asai, *Appl. Phys. Lett.*, 2002, **81**, 454; f) S. Hoang, S. Guo, N.T. Hahn, A.J. Bard, C.B. Mullins, *Nano Lett.*, 2012, **12**, 26; g) M.R. Hoffmann, S.T. Martin, W. Choi, D.W. Bahnemann, *Chem. Rev.*, 1995, **95**, 69; h) Y.H. Hu, *Angew. Chem. Int. Ed.*, 2012, **51**, 12410.
- [36] A. Fujishima, X. Zhang, D.A. Tryk, *Surf. Sci. Rep.*, 2008, **63**, 515.
- [37] A.V. Emeline, V.N. Kuznetsov, V.K. Rybchuk, N. Serpone, *Int. J. Photo.*, 2008, 258394.
- [38] a) X. Chen, L. Liu, P.Y. Yu, S.S. Mao, *Science*, 2011, **331**, 746; b) G. Wang, H. Wang, Y. Ling, Y. Tang, X. Yang, R. C. Fitzmorris, C. Wang, J. Z. Zhang, Y. Li, *Nano Lett.*, 2011, **11**, 3026; c) Z. Zheng, B. Huang, J. Lu, Z. Wang, X. Qin, X. Zhang, Y. Dai, M. Whangbo, *Chem. Commun.*, 2012, **48**, 5733; d) Z. Wang, C. Yang, T. Lin, H. Yin, P. Chen, D. Wan, *Adv. Funct. Mater.*, 2013, **23**, 5444; e) Z. Wang, C. Yang, H. Yin, P. Chen, D. Wan, F. Xu, F. Huang, J. Lin, X. Xie and M. Jiang, *Energ. Environ. Sci.*, 2013, **6**, 3007.
- [39] a) L.G. Devi, R. Kavitha, *Appl. Cat. B: Environ.*, 2013, **140**, 559; b) H. Zhang, Y. Zhao, S. Chen, B. Yu, J. Xu, H. Xu, L. Hao, Z. Liu, *J. Mater. Chem. A*, 2013, **1**, 6138; c) S. Majunder, D. Paramanik, V. Solanki, B.P. Bag, S. Varma, *Appl. Phys. Lett.*, 2011, **98**, 053105; d) W. Zhou, H. Fu, *Chem. Cat. Chem.*, 2013, **5**, 885; e) A.E. Shalan, M.M. Rashad, Y. Yu, M. Lira-Cantú, M.S.A. Abdel-Mottaleb, *Electroch. Acta*, 2013, **89**, 469; f) J. Yu, Q. Li, S. Liu, M. Jaroniec, *Chem. Eur. J.*, 2013, **19**, 2433.
- [40] a) S. Afzal, W.A. Daoud, S.J. Langford, *ACS Appl. Mater. Interf.*, 2013, **5**, 4753; b) A. Hagfeldt, M. Grätzel, *Acc. Chem. Res.*, 2000, **33**, 269.

- [41] a) L.G. Devi, R. Kavitha, *App. Catal. B: Environm.*, 2013, **140**, 559; b) A. Hagfeldt, M. Grätzel, *Acc. Chem. Res.*, 2000, **33**, 269.
- [42] a) C. Adán, A. Bahamonde, M. Fernández-García, A. Martínez-Arias, *App. Catal. B: Environ.*, 2007, **72**, 11; b) N. Riaz, F.K. Chong, B.K. Dutta, Z.B. Man, M.S. Khan, E. Nurlaela, *Chem. Eng. J.*, 2012, **185**, 108; c) N. Riaz, F.K. Chong, Z.B. Man, M.S. Khan, B.K. Dutta, *Ind. & Eng. Chem. Res.*, 2012, **52**, 4491.
- [43] A. Scolan, C. Sanchez, *Chem. Mater.*, 1998, **10**, 3217.
- [44] M. Lal, V. Chhabra, P. Ayyub, A. Maitra, *J. Mater. Res.*, 1998, **13**, 1249.
- [45] M. Wu, G. Lin, D. Chen, G. Wang, D. He, S. Feng, R. Xu, *Chem. Mater.*, 2002, **14**, 1974.
- [46] J.G. Yu, H.G. Yu, B. Cheng, X.J. Zhao, J.C. Yu, W.K. Ho, *J. Phys. Chem. B*, 2003, **107**, 13871.
- [47] C.C. Wang, J.Y. Ying, *Chem. Mater.*, 1999, **11**, 3113.
- [48] J.R.H. Ross, *"Heterogeneous Catalysis. Fundamentals and Applications"*, Elsevier, Amsterdam, 2012.
- [49] a) I.E. Wasch, C.A. Roberts, *Chem. Soc. Rev.*, 2010, **39**, 5002; b) D.P. Debecker, P.H. Mutin, *Chem. Soc. Rev.*, 2012, **41**, 3624 .
- [50] R.S. Sonawane, S.G. Hegde, M.K. Dongare, *Mater. Chem. Phys.*, 2002, **77**, 744.
- [51] *"IUPAC. Compendium of Chemical Terminology, 2nd ed. (the "Gold Book")"*. Compiled by A. D. McNaught and A. Wilkinson. Blackwell Scientific Publications, Oxford, 1997. XML on-line corrected version: [http:// goldbook.iupac.org](http://goldbook.iupac.org) (2006-) created by M. Nic, J. Jirat, B. Kosata; updates compiled by A. Jenkins. ISBN 0 – 9678550 –9 –8. DOI:10.1351/goldbook. (Accessed on September 2013)
- [52] L.L. Hench, J.K. West, *Chem. Rev.*, 1990, **90**, 33.
- [53] A. Fernández-González, L. Guardia, *An. Quím.*, 2007, **103**, 14.
- [54] J.Y. Ying, C.P. Mehnert, M.S. Wong, *Angew. Chem. Int. Ed.*, 1999, **38**, 56.

- [55] S. Inagaki, S. Guan, Y. Fukushima, T. Ohsuna, O. Terasaki, *J. Am. Chem. Soc.*, 1999, **121**, 9611.
- [56] T. Asefa, M.J. MacLachlan, N. Coombs, G.A. Ozin, *Nature*, 1999, **402**, 867.
- [57] C. Su, B.Y. Hong, C.M. Tseng, *Catal. Today*, 2004, **96**, 119.
- [58] a) R.J. Davis, Z. Liu, *Chem. Mater.*, 1997, **9**, 2311; b) R.A. Aziz, I. Sopyan, *Ind. J. Chem.*, 1997, **48A**, 951.
- [59] K.Y. Chen, C.S. Chen, *J. Northern Taiwan*, 2011, ISSN-1819-0278.
- [60] Chemat Scientific, "Sol-Gel Technology and products", (http://www.chemat.com/chemattechnology/files/Chemat_Sol-Gel_Brochure-101509.pdf) (Accessed on May, 2014)
- [61] E. Serrano, N. Linares, J. Berenguer, J. Garcia-Martinez, *Chem. Cat. Chem.*, 2013, **5**, 844.
- [62] M. Rico-Santacruz, A.E. Sepúlveda, E. Serrano, J.R. Berenguer, E. Lalinde, J. García-Martínez, Spanish Patent 201300536, 2013.
- [63] A. Fujishima, K. Honda, *Nature*, 1972, **238**, 37.
- [64] B. Kraeutler, A.J. Bard, *J. Am. Chem. Soc.*, 1978, **100**, 5958.
- [65] S.N. Frank, A.J. Bard, *J. Am. Chem. Soc.*, 1977, **99**, 303.
- [66] a) M.A. Fox, M.T. Dulay, *Chem. Rev.*, 1993, **93**, 341; b) M.R. Hoffman, S.T. Martin, W. Choi, D.W. Bahnemann, *Chem. Rev.*, 1995, **95**, 69.
- [67] T. Inoue, A. Fujishima, S. Konishi, K. Honda, *Nature*, 1979, **277**, 637.
- [68] K. Nakata, A. Fujishima, *J. Photochem. Photobiol. C: Photochem. Rev.*, 2012, **13**, 169.
- [69] J. Gong, J. Liang, K. Sumathya, *Renew. Sustain. Energ. Rev.*, 2012, **16**, 5848.
- [70] a) M.R. Narayan, *Renew. Sustain. Energ. Reviews*, 2012, **16**, 208; b) J.H. Snook, L.A. Samuelson, J. Kumar, Y. Kim, J.E. Whitten, *Org. Elect.*, 2005, **6**, 55.
- [71] D. Matthews, P. Infelta, M. Grätzel, *Solar En. Mat. Solar Cells*, 1996, **44**, 119.

- [72] B. O'Regan, M. Grätzel, *Nature*, 1991, **353**, 737.
- [73] T. Stergiopoulos, S. Karakostas, P. Falaras, *J. Photochem. Photobiol. A*, 2004, **163**, 331.
- [74] Mathias, "NERL sets New World Record with two junction solar cells" (www.energyinformative.org/nrel-efficiency-record-two-junction-solar-cell) (Accessed on January, 2014)
- [75] B. o'Regan, M. Grätzel, *Nature*, 1991, **335**, 737.
- [76] a) H. Qin, S. Wenger, M. Xu, F. Gao, X. Jing, P. Wang, S.M. Zakeerudin, M. Grätzel, *J. Am. Chem. Soc.*, 2008, **130**, 9202; b) F. Gao, Y. Wang, D. Shi, J. Zhang, M. Wang, X. Jing, R. Humphry-Baker, P. Wang, S.M. Zakeeruddin, M. Grätzel, *J. Am. Chem. Soc.*, 2008, **130**, 10720; c) S. Földner, R. Mild, H.I. Siegmund, J.A. Schroeder, M. Gruber, B. König, *Green Chem.*, 2010, **12**, 400.
- [77] A. Kudo, *Catalysis Surveys from Asia*, 2003, **7**, 1.
- [78] R. Sasikala, S.R. Bharadwaj, *Chem. Div.*, 2012, **325**, 10.
- [79] K. Maeda, K. Domen, *J. Phys. Chem. Lett.*, 2010, **1**, 2655.
- [80] Dupont "A brief overview of TiO₂ Pigments compared with TiO₂ materials", 2010, (www.dtsc.ca.gov/TechnologyDevelopment/Nanotechnology/upload/Whiting_-_TiO2_Uses.pdf) (Accessed on January, 2014).
- [81] S.E. Sherbiny, F. Morsy, M. Samir, O.A. Fouad, *Appl Nanosci.*, 2014, **4**, 305.
- [82] a) G.S. Devi, T. Hyodo, Y. Shimizu, M. Egashira, *Sens. Actuators B*, 2002, **87**, 122; b) S. Boyadzhiev, V. Georgieva, M. Rassovska, *J. Phys.: Conference Series*, 2010, **253**, 012040; c) K.D. Benkstein, S. Semancik, *Sens. Actuators B*, 2006, **113**, 445.
- [83] J. Nisar, Z. Topalian, A.D. Sarkar, L. Österlund, R. Ahuja, *Appl. Mater. Interfaces*, 2013, **5**, 8516.
- [84] V. Jasková, L. Hochmannová, J. Vytlasová, *Int. J. Photoenergy.*, 2013, ID 795060.

[85] N. Saraschandraa, M. Pavithrab, A. Sivakumara, *Appl. Sci. Res.*, 2013, **5**, 189.

[86] a) J. Keleher, J. Bashant, N. Heldt, L. Johnson, Y. Li, *World J. Microbiol. Biotech.*, 2002, **18**, 133; b) P.Wu, J.A. Imlay, J. Shang, *Biomat.*, 2010, **31**, 7526.

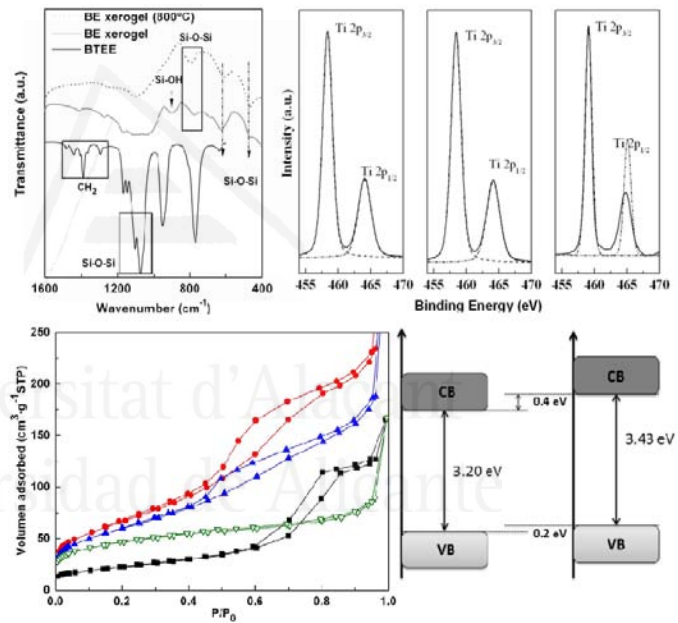
[87] D.M. Blake, P.C. Maness, Z. Huang, E.J. Wolfrum, J. Huang, *Sep. Purif. Meth.*, 1999, **28**, 1.

[88] K.C.W. Ku, Y. Yamauchi, C.Y. Hong, Y.H. Yang, Y.H. Liang, T. Funatsu, M. Tsunoda, *Chem. Comm.*, 2011, **47**, 5232.



Universitat d'Alacant
Universidad de Alicante

III. Experimental procedures



III. EXPERIMENTAL PROCEDURES

This chapter describes the basics of the experimental procedures and techniques used for the synthesis and characterization of the used titania materials. The specifications of the equipment and conditions used for the characterization of each system as well as the mathematical models used in the interpretation of the obtained results are also described.

Universitat d'Alacant
Universidad de Alicante

3.1. SYNTHESIS PROCEDURE

The procedure reported by Y. Wang et al.^[1] was adapted for the synthesis of mesoporous titania with surfactant. In a typical synthesis, 5 g (14.7 mmol) of titanium precursor were mixed with 4.6 g (7.36 mmol) of Triton X-100 in 35.37 ml of absolute ethanol under magnetic stirring. Following, 123.5 g (6.86 mol) of water were added drop-wise causing the precipitation of the solid. The molar ratio of the synthesis gel was kept equal 1TBOT: 0.5 Triton X-100: 41.3 EtOH: 467 H₂O. The mixture was then reacted at room temperature during 24 h under vigorous magnetic stirring, followed by a treatment in an oven at 80 °C for 24 hours (h). The obtained solid product was washed with water, ethanol and acetone, successively, filtered and dried in an oven at 100 °C for 8 h. The surfactant was removed by ethanol extraction (1.0 g catalyst/40 ml solvent) at room temperature for 6 h. Samples without surfactant were prepared following the same procedure.

Table 3.1. Textural parameters and surfactant incorporated of the mesoporous titania prepared with and without surfactant.

Sample	Molar ratio of the synthesis gel	Surf. ^a (wt%)	d_p ^b (nm)	V_p ^c (cm ³ /g)	A_{BET} ^d (m ² /g)
TiO ₂ with surf.	1TBOT: 0.5 Triton X-100: 41.3 EtOH: 467 H ₂ O	12 (85)	5.7 (2-9)	0.31	235
TiO ₂ without surf.	1TBOT: 0 Triton X-100: 41.3 EtOH: 467 H ₂ O	---	5.6 (2-9)	0.29	245

^aWeight loss measured between 200 °C and 400 °C from TGA scans corresponding to the surfactant incorporated. Values in brackets indicate the theoretical surfactant added. ^bAverage mesopore diameters, estimated from the adsorption branch of the nitrogen isotherm using the BJH method. ^cMesopore volume from the isotherms at relative pressure of 0.95 (see section 3.2.1). ^dBET surface area, estimated by multipoint BET method using the adsorption data in the relative pressure (P/P_0) range of 0.05–0.30 (see section 3.2.1).

Table 3.1 shows the molar ratio of the synthesis gel, the textural parameters as well as the surfactant amount incorporated into the sample prepared with surfactant. As shown in table 3.1, only a 12 w% of the surfactant added during the synthesis is finally incorporated into the titania structure. Interestingly, both TiO₂ samples prepared with and without surfactant show Type IV isotherms, typical of mesoporous materials, with similar textural properties. The pore size, calculated from adsorption isotherm is 5-6 nm, and it can be associated with the interparticle mesoporosity of titania materials^[2]. This mesoporosity is independent of the surfactant used because it is an interparticle mesoporosity (due to typical configuration adopted by nanoparticles). Surfactant therefore only fills, the gaps between particles, hence there are no differences between the samples synthesized with and without surfactant. Thus, all the hybrid titania materials, herein presented, will be synthesized without surfactant with the same synthesis conditions described in this section.

3.2. CHARACTERIZATION TECHNIQUES

Elemental analysis (EA) and inductively coupled plasma optical emission spectrometry (ICP-OES) measurements were carried out in order to study the chemical composition of the materials. The structure of the materials was confirmed by X-ray diffraction (XRD). Fourier transform infrared spectroscopy (FTIR), nuclear magnetic resonance (NMR) and X-ray photoelectron spectroscopy (XPS) were used to analyse the incorporation of the functionalities into the titania materials. Porosity of synthesized titanias was analysed by adsorption/desorption isotherms of N₂ at 77K. The morphology of the titania materials was analyzed using transmission electronic microscopy (TEM) and the photocatalytic activity of the

materials was evaluated in the degradation reaction of rhodamine 6G (R6G), followed using UV-vis spectroscopy (UV-vis) and total organic carbon (TOC).

N₂ isotherms, TEM, XRD, FTIR, EA, XPS and ICP tests have been conducted at the Technical Services (SSTi) of the University of Alicante (UA) and NMR measurements has been obtained from the Technical Services of the University Rey Juan Carlos I (Madrid, Spain). TOC measurements were done at the Water Institute of the UA (Alicante, Spain).

Assays of gas-solid regime and diffuse reflectance spectroscopy were in the University of Palermo (Palermo, Italy) during a pre-doctoral stay. Assays of liquid-solid regime and the correspondingly UV-vis spectroscopy analyses have been performed at the Molecular Nanotechnology Lab of the UA as well at the University of La Rioja (Logroño, Spain) during several pre-doctoral stays.

The analysis and interpretation of all results presented in the present work, as well as the synthesis of all hybrid materials described have been carried out at Molecular Nanotechnology Lab of the UA by the author of this work.

3.2.1. Textural analysis. Gas adsorption

Analysis of nitrogen adsorption/desorption isotherms was carried out to obtain the pore size distribution, volume of mesoporosity and surface area of the hybrid titania materials.

3.2.1.1. Fundamentals

The study of the adsorption of gas molecules on a solid surface is a widely used technique for the characterization of porous materials^[3] in terms of specific surface area, pore size distribution and pore volume. Two types of adsorption are known: physisorption (physical adsorption) and chemisorption (chemical adsorption)^[4-5].

The first one is due to weak gas-solid interactions (Van der Waals forces), while the chemisorption is due to chemical bonds between the adsorbate and the adsorbent. The origin of the adsorption phenomenon is the imbalance forces existing on the atoms of the external surface of the particles (figure 3.1). When a clean surface solid (orange) is exposed to a gaseous atmosphere (red), in the internal part of the material all the chemical bonds are completed but not on the surface.

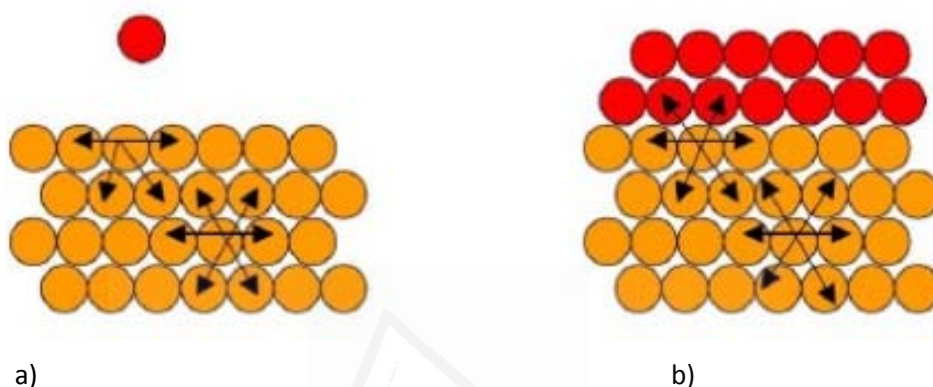


Figure 3.1. Representation of cohesive forces: in a solid (a) and in a solid where a gas has been adsorbed (b)^[6].

The representation of the amount of gas adsorbed by a solid versus the relative pressure of the gas, at constant temperature, is called adsorption isotherm. The existence of common characteristics among some solids isotherms with similar surface properties has resulted in the classification of six different types of isotherms^[7]. The titania materials synthesized in this study show a Type IV isotherm, typical of mesoporous materials with pore sizes between 2 and 50 nm^[8].

The specific surface area was determined using the BET method which is based on the number of adsorbed molecules required to form a monolayer and the area occupied by a molecule.

The name comes from the initials of the researchers who developed it: Brunauer, Emmett and Teller^[9]. At low relative pressures, the BET equation is linearly as is shown in equation (1):

$$x/n^a(1-P/P_0) = (1/n_m^a) + (P/P_0)((C-1)/C \cdot n_m^a) \quad (1)$$

where:

- n^a : amount of adsorbed gas
- P/P_0 : relative pressure of gas (adsorbate)
- n_m^a : amount of gas adsorbed in the monolayer
- C : BET constant related to the heat of adsorption of the monolayer, it can be expressed as $C = \exp(E_1 - E_2) / RT$, where E_1 is the heat of adsorption of the monolayer and E_2 the adsorption heat for subsequent layers.

From the BET equation, the specific area of the adsorbent can be calculated through the area of a molecule of adsorbate. The range of partial pressure P/P_0 in which the BET representation results in a straight line dependent on the system and the operating temperature, in the present work the range used is $0.05 < P/P_0 < 0.3$.

Pore size distribution was determined by the BJH method (Barret, Joyner and Halenda)^[10], applied to the adsorption branch of the nitrogen isotherm at 77 K. BJH method has been traditionally used for characterization of mesoporous solids, although this method slightly underestimates the size of the pore by considering a hemispherical meniscus at liquid-vapor interface and a well-defined surface tension.

The pore size distributions calculation of for mesoporous materials is based on the Kelvin equation^[11] (equation 2):

$$\text{Log} (P/P_0) = - 2\varphi \text{Vol} / 8.316 \cdot 10^7 \cdot 2.303 T r_k = - 4.14 / r_k \quad (2)$$

where:

- P/P_0 : relative gas pressure
- φ : surface tension of liquid nitrogen
- Vol : molar volume of liquid nitrogen
- T : absolute temperature (K)
- r_k : capillary radius, that can be expressed as the difference between the pore radius (r_p) and the thickness of the adsorbed layer (t), $r_p = r_k + t$,
 $t = 3.5400 \cdot [-5.0000 / \ln (P/P_0)] \cdot 0.3330$.

The BJH model is a modification of the Kelvin equation, which is based on filling, by multilayer, an adsorbent with cylindrical pores. The BJH calculation model divides the isotherm in several intervals. Average pressure between each interval provides the thickness of the adsorbed layer (t) and the average radius of $r_p = r_k + t$ pores.

3.2.1.2. Equipment used and test conditions

Porous texture of the titania materials synthesized in chapters 4-6 was characterized by N_2 adsorption/desorption isotherms at 77 K in an AUTOSORB-6 apparatus. The titania samples were previously degassed for 4 h at 373 K at 5×10^{-5} bars. BET surface area was estimated by using multipoint BET method, using the adsorption data in the relative pressure (P/P_0) range of 0.05–0.30.

The pore size distribution was calculated from the adsorption branch of the N₂ adsorption isotherms using the BJH method. As expected, for all the titania materials the micropore volume estimated from the *t*-plot method, was determined to be zero and thus the mesopore volume can be directly read from the isotherms at a relative pressure of 0.95.

3.2.2. Thermogravimetric analysis

Thermogravimetric analysis (TGA) was used to determine the surfactant content, before and after extraction, in the control titania and the content of organic groups anchored titania in chapter 4.

3.2.2.1. Fundamentals

TGA is a technique in which the mass of a substance is monitored as a function of temperature or time, where the sample is subjected to a controlled temperature program in a controlled atmosphere. The sample's mass can vary during the course of a reaction by gaining or losing mass^[12]. A TGA consists of a sample pan that is supported by a precision balance. That pan resides in a furnace and is heated or cooled during the experiment. The mass of the sample is monitored during the experiment. A sample purge gas controls the sample environment inside the furnace.

3.2.2.2. Equipment used and test conditions

The analysis were carried out in a TG-ATD METTLER TOLEDO, model TGA/SDTA851e/SF/1100 in the temperature range 25-900°C (10°C·min⁻¹) in a N₂:O₂ 4:1 atmosphere.

3.2.3. Structural and chemical composition. Molecular spectroscopy techniques.

Spectroscopic techniques are based on the interaction phenomena between the electromagnetic radiation with matter. These phenomena can be carried out by energy absorption or emission through electron transition between quantum levels.

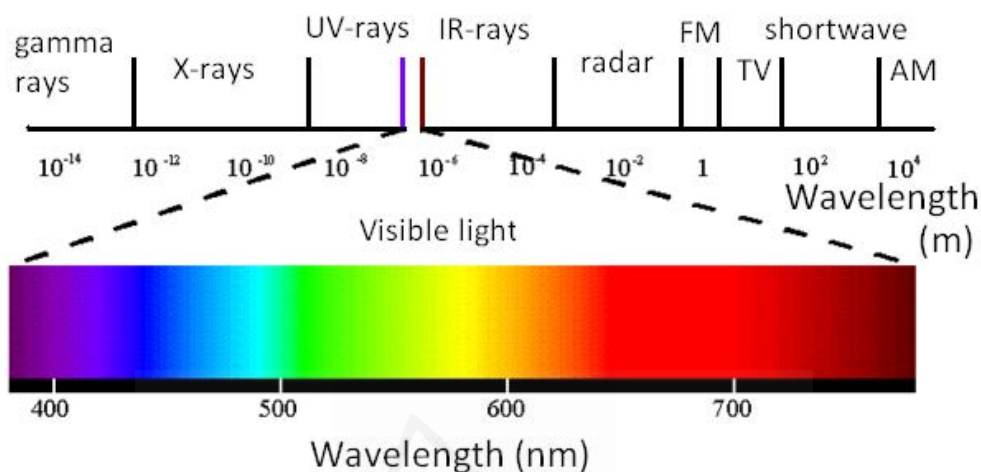


Figure 3.2. Wavelengths in the electromagnetic spectrum^[13].

Each particular interaction will produce a characteristic electromagnetic spectrum. Depending on the energy of the generated waves, these can be in the range of: X-ray, ultraviolet-visible (UV-vis), infrared (IR), etc (figure 3.2).

3.2.3.1. UV-vis spectroscopy

UV-visible spectroscopy (UV-vis) technique has been used in the present investigation to evaluate the degradation of the rhodamine 6G by the synthesized titanias in chapters 4-6.

3.2.3.1.1. Fundamentals

This technique is based on the absorption of UV-vis light by a molecule. The interaction of ultraviolet and/or visible radiation with matter causes electronic transitions (promotion of electrons from the ground state to a high energy state) releasing the excess energy as heat^[14,15]. The ultraviolet region falls in the range between 190-380 nm and the visible region between 380-750 nm. Electromagnetic absorption radiation in the UV-vis range by molecules can be used for identifying compounds. For a quantitative analysis, the Beer's law, which relates the intensity of incoming light to the intensity of outgoing light after the absorption occurs, can be used in diluted solutions. The Beer-Lambert law states that, under certain conditions, the absorbance of a solution is directly proportional to the concentration of the absorbing species in the solution and the path length^[16].

3.2.3.1.2. Equipment used and test conditions

The equipment used was a Jasco V-650 UV-vis spectrophotometer. Spectra were registered in the 700-300 nm wavelength range, with a resolution of 0.5 nm, at intervals of 2 min. *In-situ* monitorization of the reaction was followed using a UV Ultramini tauchsonde (Hellma Analytics, 661.622-UV).

3.2.3.2. UV-vis diffuse reflectance spectroscopy

One of the most widely use method to estimate the band gap of a semiconductor is based on the results of diffuse reflectance spectroscopy (DRUV) measurements. In this work, DRUV spectra measurements are used to calculate the band gap value of all the synthesized titania materials (chapters 4-6).

3.2.3.2.1. Fundamentals

DRUV measures the characteristic reflectance spectrum produced when a sample is irradiated. The primary mechanisms are absorption and scattering, both of which vary with wavelength to produce the reflectance spectrum, which is recorded. This spectrum provides information about the optical properties and structure of the sample^[17].

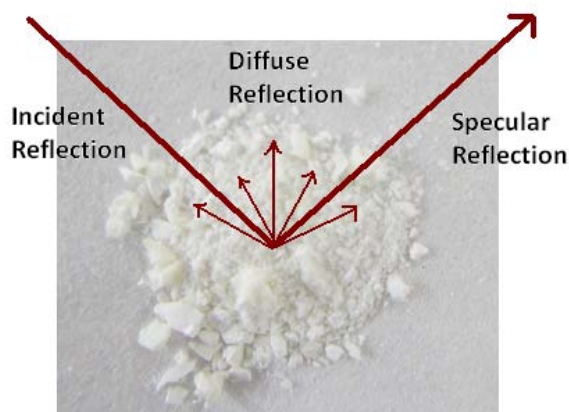


Figure 3.3. Schematic illustration about how diffuse reflectance works.

DRUV is very closely related to UV-vis spectroscopy. Both of these techniques use UV-vis radiation to excite valence electrons to empty orbitals. The difference between both techniques is that in UV-vis spectroscopy the relative change of transmittance of light is measured when it passes through a sample/medium, whereas in diffuse reflectance, the relative change in the amount of reflected light off of a surface is measured.

DRUV is mainly used when the materials of the reflective surface are weak absorbers and when the penetration of the radiation is large relative to the wavelength used for radiation.

3.2.3.2.2. Equipment used and test conditions

DRUV spectra were carried out in air at room temperature in the 800-200 nm wavelength range using a Shimadzu UV-2401 PC spectrophotometer with BaSO₄ as the reference material. For the estimation of the band-gap the reflectance data was converted into the equivalent absorption coefficient using the Kubelka-Munk formalism according to equation 3:

$$F(R') = - (1-(R')^2)/2R' \quad (3)$$

where R' is the reflectance value obtained directly from the spectrophotometer. Band gap calculations are based on the $[F(R')h\nu]^{n/2}$ versus photon energy ($h\nu$) plot. As previously reported, for indirect band gap materials such as titania, the intercept of the tangent to the $(F(R')h\nu)^{1/2}$ versus ($h\nu$) plot gives a good estimation of the band gap energy^[18-21].

3.2.3.3. Nuclear magnetic resonance spectroscopy

Nuclear magnetic resonance spectroscopy (NMR) has been used to confirm the incorporation of the organosilica precursors into the titania materials and to analyze the environment and type of bonds presented on these synthesized hybrid materials.

3.2.3.3.1. Fundamentals

NMR can be applied to investigate the chemical environment of certain nuclear isotopes, the coordination number, the local symmetry and connectivity. NMR spectroscopy studies the behavior of atomic nuclei with spin different from zero under the influence of an external magnetic field (odd number of protons or

neutrons, or both of them). Such cores are magnetically active and have a rotation movement, about an axis that makes them behave like tiny magnets. This situation occurs in ^1H , ^{13}C , ^{19}F , ^{29}Si and ^{31}P atoms [22,23].

In absence of magnetic field, the nuclear spins are randomly oriented. However, when a sample is placed in a magnetic field, the nuclei with positive spin are oriented in the same direction as the field, in a state of minimum energy called α spin state, whereas nuclei with negative spin are oriented towards opposite to the magnetic field in a higher energy state called β spin state.

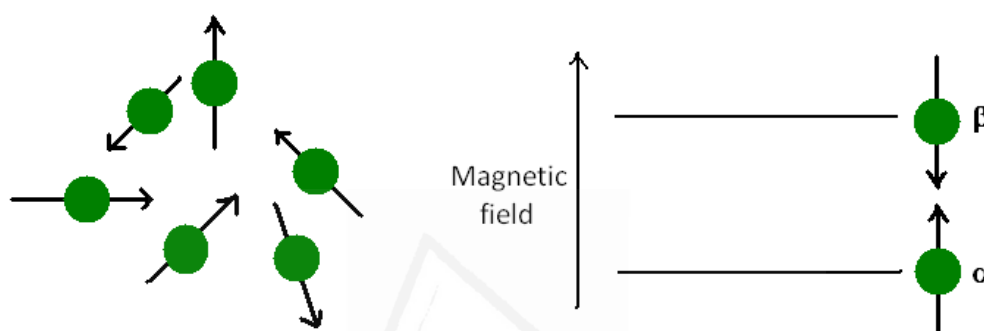


Figure 3.4. Schematic illustration of the nuclear spins in absence of magnetic field (left) and under a magnetic field (right).

There are more nuclei in the α spin state than β but, although the difference is not very significant, it is enough to establish the basis for NMR spectroscopy. The energy difference between the two spin states α and β depends on the intensity of the applied magnetic field H_0 .

When a sample is irradiated, the nuclei in the spin state α are promoted to the status of β spin. When the nuclei return to their initial state they emit signals whose frequency depends on the energy difference (ΔE) between the states of α and β spin. NMR spectrometer detects these signals and records them as a plot of

intensity versus frequency, which is called NMR spectrum. Equation 4 shows the dependence between the signal frequency and magnetic field strength H_0 (measured in Tesla, T):

$$\Delta E = h\gamma H_0/2\pi \quad (4)$$

where γ is the gyromagnetic radius and its value depends on the type of core that is being irradiated.

3.2.3.3.2. Equipment used and test conditions

^{29}Si MAS NMR spectra were recorded on a Varian-Infinity Plus Spectrometer at 400 MHz operating at 100.52 MHz proton frequency (4 μs 90° pulse, 4000 transients, spinning speed of 6 MHz, contact time 3 ms, pulse delay 1.5 s). The relative amount of the different structural units is derived from the integrated areas of the single peaks after the fit of the signal by using a combination of Lorentzian/Gaussian curves.

3.2.3.4. X-ray diffraction

The X-ray diffraction technique (XRD) was used to determine the crystalline structure and to estimate the crystalline domain size and spacing between planes of all synthesized hybrid materials described in chapters 4-6.

3.2.3.4.1. Fundamentals

XRD is the result of the interaction of an X-ray electromagnetic wave with the electron cloud of the atoms in a crystal^[24-26]. X-rays have wavelengths of the order of a few angstroms (10⁻¹⁰ m = 1 Å), so it can be used to study the position of atoms in crystalline solids.

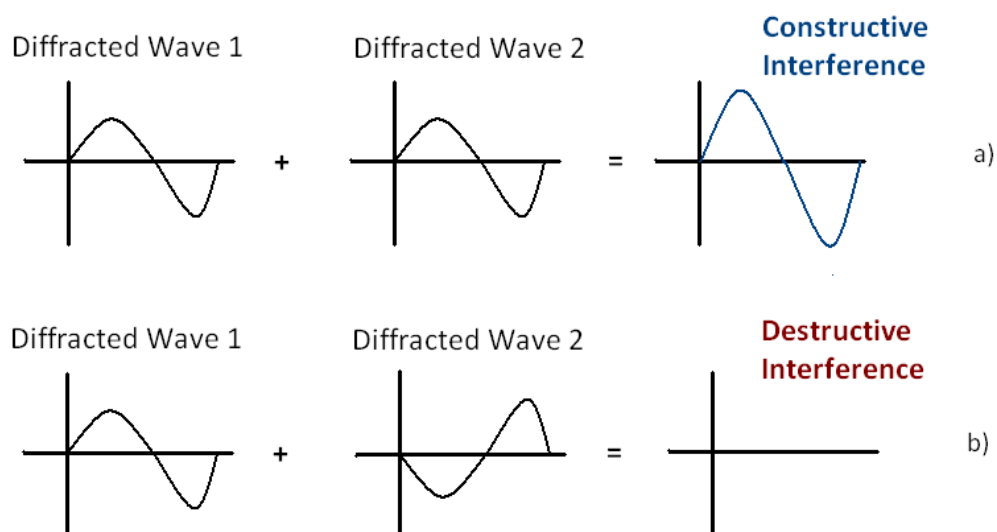


Figure 3.5. Types of interference when crystalline solids are exposed to X-rays: constructive (a) and destructive (b).

When crystalline solids are exposed to X-ray radiation, an interference occurs between the waves scattered by the atoms. There are two types of interferences depending on how the waves overlap one to another. Destructive interference occurs when the waves are out of phase. Constructive interference occurs when the waves are moving in phase with each other and this phenomenon results in diffraction patterns (figure 3.5).

The angle at which a beam of X-rays of a particular wavelength diffracts from a crystalline surface was discovered by William H. Bragg and W. Lawrence Bragg and is known as Bragg's Law (equation 5):

$$n\lambda = 2d_{hkl} \cdot \sin \theta \quad (5)$$

where :

- λ = wavelength (of the X-ray)
- θ = scattering angle
- n = value representing the order of the diffraction peak.
- d_{hkl} = inter-plane distance of i.e atoms, ions, molecules

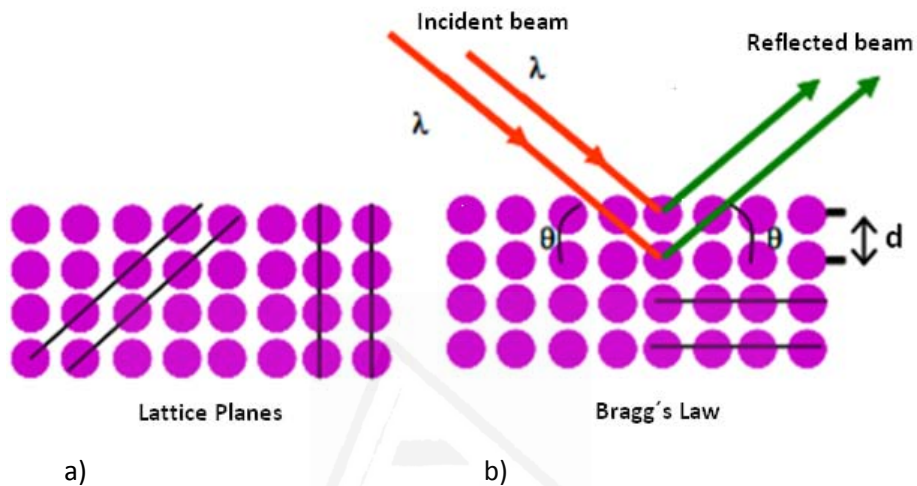


Figure 3.6. Bragg's law of diffraction: illustration of how X-rays interact with crystal lattice. Two-dimensional description of the X-ray reflection beam from two parallel crystalline planes separated by a distance d_{hkl} .

The spacing d of each family of planes (hkl), can be obtained using Bragg's law (figure 3.6 and equation 5), from the value of the detection angle. The Miller indices (hkl) are used to specify directions and planes in lattices or in crystals.

By plotting the intensity of radiation diffracted by the sample as a function of the angle of the incident beam, a diffractogram which is a distinguishable feature of each crystalline solid can be obtained^[27].

The Scherrer equation is a formula that relates the size of particles or crystallites in a solid to the width of the X-ray diffraction peak, in radians, at a height half-way between background and the peak maximum. With the Scherrer equation (equation 6) it was possible to determine the crystallite size of all titania materials (chapters 4-6) synthesized in this work:

$$D^{XRD} = K \cdot \lambda / \beta \cos \theta \quad (6)$$

where:

- D^{XRD} : size of the ordered crystalline domains
- K : dimensionless shape factor (0.9 for titania nanoparticles^[28])
- λ : X-ray wavelength
- β : line at half the maximum intensity in radians
- θ : is the Bragg angle

3.2.3.4.2. *Equipment used and test conditions*

XRD analysis was carried out in a Bruker D8-Advance diffractometer with Göebel mirror and a X-ray generator KRISTALLOFLEX k 760-80F (operating at 40 kV and 40 mA), using a CuK α radiation ($\lambda = 1.54056 \text{ \AA}$). The samples were scanned from 20° to 60° (2 θ), at a scanning velocity of 0.05°/min.

3.2.3.5. *X-ray fluorescence*

X-ray fluorescence (XRF) was used to determine the Si/Ti ratio of the hybrid titanias described in chapter 6.

3.2.3.5.1. Fundamentals

XRF is a powerful local quantitative and qualitative analytical tool for elemental analysis of materials^[29]. When a sample is irradiated with a source of high intensity X-rays, fluorescent X-rays will be emitted from the sample at specific energy levels to those elements.

In detail, when a primary X-ray excitation source hits a sample, the X-ray can either be adsorbed by the atom or scattered through the material. By the photoelectric effect, the X-ray absorbed by the atom, transfers all of its energy to an inner level electron. The electrons ejected can create vacancies (figure 3.7) if the X-ray used had sufficient energy and these vacancies present an unstable condition for the atom. Thus, when the atom returns to its stable condition, electrons from the outer shells are transferred to the inner shells and in the process give off a characteristic X-ray (secondary X-rays or fluorescent emission) whose energy is the difference between the two binding energies of the corresponding shells^[29]. The characteristic X-rays are denoted as K, L, M or N in accordance with the shells they originated from. Each element produces X-rays at a unique set of energies. This therefore allows to determine the elemental composition of a sample.

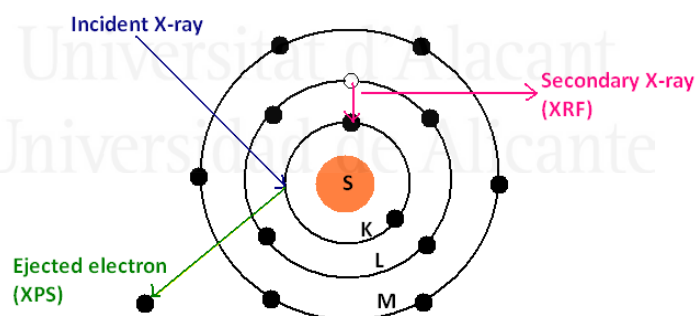


Figure 3.7. Representation of the different phenomena that can result from the excess of energy when a sample is irradiated with a X radiation.

3.2.3.5.2. *Equipment used and test conditions*

XRF spectra were taken using a sequential X-ray spectrometer Philips Magix Pro fitted with a rhodium tube and beryllium window. All samples were prepared as pressed pellets. Data were analysed using the SuperQ Manager software.

3.2.3.6. *X-ray photoelectron spectroscopy*

In the present work, X-ray photoelectron spectroscopy (XPS) has been used to calculate the position of the valence band of the synthesized titania and to determine the composition and titanium electronic states in the synthesized materials. These results can be associated with the bonds created between titania and the different functionalities, confirming the presence of them and their incorporation into the framework of titania (chapters 4-6).

3.2.3.6.1. *Fundamentals*

The principle of XPS is based on the photoelectric effect^[30-31], already described in the XRF. A surface is irradiated in vacuum with X-rays, being the most common $AlK\alpha$ or $MgK\alpha$. When an x-ray photon hits and transfers its energy to a core-level electron, an electron is emitted from its initial state with a kinetic energy dependent on the incident X-ray and binding energy of the atomic orbital from which it originated. The intensity and energy of the emitted photoelectrons are analysed to identify and determine the concentrations of the elements present in a sample. These photoelectrons come from a depth of <10 nm, since all the photoelectrons emitted at higher depths in the sample are trapped in the various excited states of the material. Therefore, the information obtained is related with this depth and the applications of this technique are restricted to a chemical analysis of the material surface^[32].

XPS measurements are carried out following the equation 7 that is based on the work of Ernest Rutherford^[33]. The energy of an X-ray, with known wavelength, and the work function (ϕ) of the spectrometer are known and the kinetic energy of the emitted electrons is measured. Thus, the electron binding energy of each of the emitted electrons can directly be determined using equation 7.

$$E_{\text{Binding}} = E_{\text{Photon}} - E_{\text{Kinetics}} - \phi \quad (7)$$

where:

- E_{Binding} : is the binding energy of the electron
- E_{Photon} : is the energy of the X-ray photons used (AlK α or MgK α)
- E_{Kinetics} : is the kinetic energy of the electron measured by the instrument
- ϕ : is the work function of the spectrometer (independent of the material). Instrumental correction factor that accounts for the few eV of kinetic energy given up by the photoelectron as it becomes absorbed by the instrument's detector.

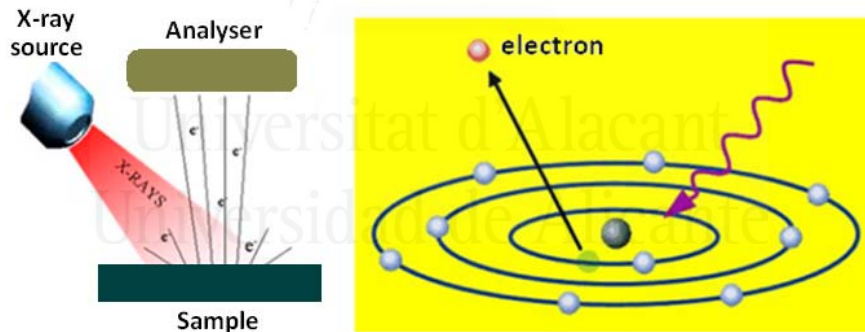


Figure 3.8. Irradiated surface with a source of high-energy photons that causes the emission of electrons (left) and photon which imparts its energy to an electron of an internal electronic level (right) (adapted from ref. 34).

In a typical XPS spectrum, the number of electrons detected is represented versus the binding energy of these electrons. Thus, the characteristic peaks correspond to the electron configuration of the electrons inside the atoms (1s, 2s, 2p, etc.) and the number of electrons detected for each peak is directly related to the amount of that element present in the irradiated area.

Taking into account that the binding energy is unique for a given element and the number of photoelectrons is proportional to the concentration of each element in a surface, XPS can provide information about surface atomic composition and the oxidation state of the elements.

3.2.3.6.2. Equipment used and test conditions

XPS measurements were carried out in a VG-Microtech Multilab instrument, using MgK α radiation (1253.6 eV) and a pass energy of 50 eV. The pressure during data acquisition was $5 \cdot 10^{-7}$ Pa.

A careful deconvolution of the spectra was made and the areas under the peaks were estimated by calculating the integral of each peak after subtracting a Shirley background (in which the background intensity at any given binding energy is proportional to the intensity of the total peak area above the background in the lower binding energy peak range) and fitting the experimental peak to a combination of Lorentzian/Gaussian lines (30/70). Binding energies were referenced to the C1s line at 284.6 eV^[35].

3.2.3.7. Infrared spectroscopy

In this research work, Fourier transform infrared spectroscopy (FTIR) has allowed to identify the chemical nature of the synthesized titanias. More specifically, it has been used to confirm the structure integrity of the organic

compounds (chapter 4), the metal complex (chapter 5) and the organosilica precursors (chapter 6) and to confirm its incorporation into the titania network by comparing their FTIR spectra with those of the hybrid materials containing those groups.

3.2.3.7.1. *Fundamentals*

Infrared spectroscopy is a type of molecular vibrational spectroscopy which analyses molecular vibrations. To understand the basis of this spectroscopy is useful to know the principles of simple harmonic motion where the chemical bond between two atoms can be considered as a simple harmonic oscillator. The bond is the spring and the two atoms or groups of atoms connected by the bond, would be the masses. Each atom has a different mass and the single, double or triple bonds have different stiffness, so each combination of atoms and bonds has a characteristic harmonic frequency. There are six different ways in which the molecules can vibrate: symmetric and antisymmetric stretching, scissoring, rocking, wagging and twisting^[36]. Each of these vibrations can occur in any molecule, but all of them at different frequencies, which enables to identify them. At any temperature above absolute zero, all small simple harmonic oscillators that constitute a molecule are vibrating. Infrared light is in the same frequency range as the vibration of the molecule so, the basis of operation of this technique consists in the interaction of a beam of infrared radiation with the sample^[37]. If a molecule is radiated, the molecule will absorb those frequencies of light which are exactly equal to the frequencies of the different harmonic oscillators that takes place in the molecule. Most classical analytical infrared spectroscopy applications take place in the mid-IR (650-4000 cm⁻¹).

In this way, it is possible to determine the chemical functional groups present in a given material by comparing the obtained vibration frequencies with those described in the literature^[38].

The infrared spectrum of a sample is recorded, therefore, considering the amount of infrared light that transmits a sample after being illuminated by an infrared beam, thereby determining, how much energy is absorbed for each wavenumber. This can be done with a monochromatic beam, which changes the wavenumber in time, or by Fourier transform (FTIR), used in this investigation, which allows measuring all wavenumbers simultaneously. Currently, there are several tabulated spectra of substances, making it relatively easy to identify the groups present in a sample.

3.2.3.7.2. Equipment used and test conditions

FTIR spectra were recorded on a Nicolet Nexus FT-IR Spectrometer. The spectra were taken with a 2 cm^{-1} resolution in a wavenumber range from 4000 to 400 cm^{-1} . All samples were prepared as KBr pellets.

3.2.3.8. Inductively coupled plasma optical emission spectroscopy

In the present investigation the inductively coupled plasma optical emission spectroscopy (ICP-OES) has been used to determine the content of ruthenium in the hybrid titanias synthesized in chapter 5.

3.2.3.8.1. Fundamentals

ICP-OES is an analytical technique that allows a quantitative determination of metals at trace and ultratrace levels, starting from aqueous samples^[39]. In practice, an aqueous sample is introduced into a nebulizer system which forms an aerosol.

Such aerosol is led to the ionization region, consisting of a plasma generated by subjecting a stream of argon gas to the action of an oscillating magnetic field induced by a high frequency current. It may reach temperatures of 8000 K, such that the atoms in the sample are ionized. Upon returning to the ground state, these ions or excited atoms emit radiation of a wavelength, characteristic of each element. This radiation passes through an optical system that separates the radiation as a function of its wavelength. Then a sensor measures the intensity of each radiation which is related with the concentration of each element in the sample^[40].

3.2.3.8.2. Equipment used and test conditions

The analysis of the materials described in chapter 5 was carried out in a Perkin Elmer, 7300 DV with a power of 1300W and a liquid flow of 1ml/min.

The samples were pretreated in a Milestone, model START-D, and digest using a microwave working at a maximum power of 1000 W and a maximum operating pressure of 100bar. Prior to the analysis, 0.3 g of the mesoporous titanias were mineralized by microwave digestion in 8 ml of HCl (35-38 vol%) with a 10 min ramp to 220 °C temperature, maintaining this temperature 15 min. Then water is added to the above solution until 25 ml.

3.2.4. Elemental analysis

Elemental analysis (EA) was carried out to determine the amount of organic moieties incorporated into the titanias prepared in chapter 4.

3.2.4.1. Fundamentals

EA is a technique widely used to determine the amount of carbon, hydrogen, nitrogen and heteroatoms (halogens, sulfur) present in a sample^[41] (usually expressed as percentage by mass). This technique is based on the complete oxidation of the sample by combustion in pure oxygen at temperatures of approximately 1000 °C. Different gas products CO₂, H₂O and N₂, are transported by the carrier gas (He) and then selectively separated in specific columns to be then thermally desorbed. Finally, gases pass separately by a thermal conductivity detector which gives a signal proportional to the concentration of each of the individual components of the mixture. The weights of these products of combustion are used to calculate the composition of the sample.

3.2.4.2. Equipment used and test conditions

The elemental analysis of the samples produced was performed using a ThermoFinnigan elemental analyzer model FLASH 1112. Powder samples were placed on tin capsules with V₂O₅ to aid in combustion. The combustion was carried out at 900 °C with He as a carrier gas. In each case, different patterns can be used to calibrate the equipment, depending on the nominal quantity of each element in the sample. In particular for these samples, the SOIL10% pattern was used (C: 10.03%, N₂: 0.45%, H₂: 1.30%).

3.2.5. Morphological study: Transmission electron microscopy

The morphology and structure of all mesoporous titania materials synthesized and described herein (chapters 4-6) was investigated by transmission electron microscopy (TEM).

3.2.5.1. Fundamentals

Historically, electron microscopes were developed to overcome the limited resolution of optical microscopes. The amplifier power of an optical microscope is limited by the wavelength of visible light. Electron microscopes, however, use an electron beam to illuminate the sample and as the electrons have a smaller wavelength than light, 0.05 \AA versus 4000 \AA , these microscopes can be used to study, much smaller structures^[42]. Currently, TEM is a standard characterization technique in materials science^[43].



Figure 3.9. Transmission electron microscope used in SSTTi (UA).

TEM microscopy consists of irradiating a thin sample with an electron beam of uniform density current (energy in the range of 100 to 200 keV)^[43]. Part of these electrons are transmitted, others are scattered and other produce interactions that result in different phenomena as light emission, Auger and secondary electrons, X-rays, etc.

In this technique, transmission/scattering of electrons are used for obtaining images, the electron diffraction to obtain information about the crystal structure, and the X-ray emission to determine the elemental composition of the local regions in the sample (EDX spectroscopy)^[44].

By using an electron beam on a thin sample (thickness less than 100 nm) high spatial resolution images can be obtained. Currently the resolution that can be achieved in transmission electron microscopy is 0.1 nm. Atoms with higher atomic number scatter electrons more efficiently and at higher angles of deflection than light atoms, therefore heavy elements have a greater contrast in TEM images.

3.2.5.2. Equipment used and test conditions

The equipment used was a JEM-2010 microscope (JEOL, 200 kV, 0.14 nm of resolution). Samples for TEM studies were prepared by dipping a sonicated suspension of the sample in ethanol. The digital analysis of the TEM micrographs was performed using Gatan Digital MicrographTM 1.80.70 for GMS 1.8, being the particle size estimated as an average of the size of 100 particles.

3.2.6. Solid-gas regime: Gas chromatography

3.2.6.1. Fundamentals

Gas chromatography (GC) is a physical method, based on the principle of selective retention of different compounds of a mixture, where it is possible to identify and determine the amounts of the different elements present in a sample.

In gas chromatography, the sample (normally a fluid) is volatilized and injected into the head of a chromatography column. Passing through the stationary phase (chromatographic column) at different speeds, the different compounds are

separated. After that, the compounds pass through a detector which generates a signal dependent on the concentration and type of compound.

Retention time is often used for qualitative analysis due to is unique for each compound given certain conditions (same carrier gas flow and temperature ramp)^[45]. In quantitative applications, the concentration or amount of each analyte present can be obtained integrating the areas of each compound or measuring its height, with a calibrated pattern.

3.2.6.2. Equipment used and test conditions

Substrate and intermediates concentrations of the solid-gas propylene epoxidation reaction (chapter 6) were measured by a GC-17A Shimadzu gas chromatograph equipped with a HP-1 column and a flame ionization detector (FID), whereas carbon dioxide was analyzed by a Carboxen column in an HP6890 gas chromatograph equipped with a thermal conductivity detector (TCD).

3.2.7. Liquid-solid regime

3.2.7.1. Photocatalytic activity measurements

The photocatalytic activity of the synthesized materials was evaluated in liquid-solid regime. The absorbance of R6G solutions was measured under UV radiation in a photochemical reactor system equipped with a 125W medium-pressure Hg lamp with a maximum emission at 365 nm (figure 3.10).

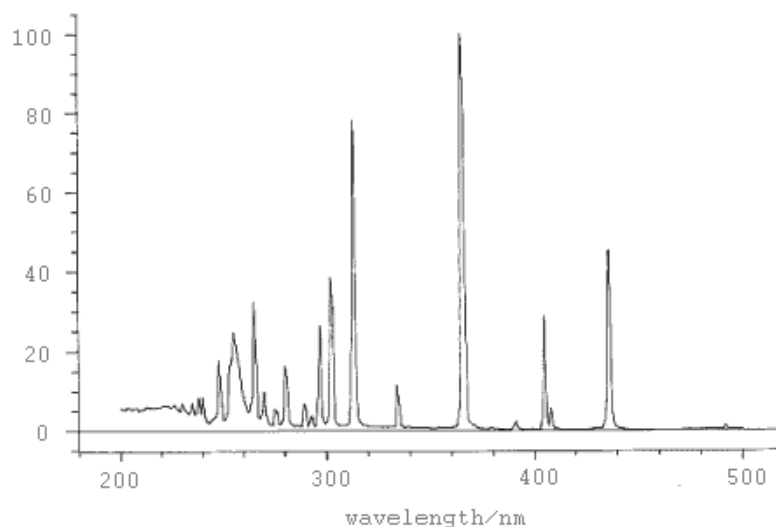


Figure 3.10. Emission spectrum for the medium pressure mercury lamp used in these photocatalytic reactions of rhodamine 6G^[46].

The lamp is located in a cooled, double-walled quartz, immersion well, inside of a borosilicate reaction vessel, where reaction takes place. The reaction vessel allows for the introduction of a UV Ultramini tauchsonde (Hellma Analytics, 661.622-UV) that allows the *in-situ* monitoring of the degradation reaction on a UV-vis spectrophotometer (figure 3.11).

The system is located inside a black photochemical safety reaction cabinet. For a typical degradation test, a R6G aqueous suspension ($5 \cdot 10^{-5}$ M, 100 ml) with 0.15 g/l of synthesized catalyst was stirred during 30 min in order to achieve the adsorption/desorption equilibrium of the dye on the catalyst surface. Afterwards, this suspension was irradiated with UV light and the bleaching of the solution was monitored by absorbance measurements on a UV-vis spectrophotometer.

For the experiments under visible light, a similar procedure was followed ($5 \cdot 10^{-5}$ M, 200 ml with 0.4 g/l of synthesized catalyst) but using a 400W medium-pressure Hg lamp located in a double-walled Pyrex immersion well, cooled with a 2M solution of NaNO_2 (UV cutoff filter >400 nm) to remove the UV radiation. To further investigate the mechanism of the R6G degradation process under visible light using the photocatalyst described in chapters 4 and 5, controlled experiments have been carried out to determine the dominant active species involved in the photocatalytic reactions. The experimental procedure was similar to that described before, but using aqueous solutions of R6G ($5 \cdot 10^{-5}$ M) with triethanolamine (TEOA, $5 \cdot 10^{-2}$ M) or isopropanol ($i\text{PrOH}$, $5 \cdot 10^{-2}$ M), which were used to scavenge photogenerated holes (h^+) or hydroxyl radicals ($\cdot\text{OH}$), respectively^[47].



Figure 3.11. Image of the photochemical reactor system of the Molecular Nanotechnology Lab (UA), equipped with a 125W medium-pressure Hg lamp and a UV sonde, that allows to monitor *in-situ* reactions.

3.2.7.2. Total organic carbon (TOC)

Total organic carbon (TOC) was used in order to determine the total organic carbon content in all titania materials (chapters 4, 5 and 6) and thus, to determine the bleaching and/or degradation of rhodamine 6G.

3.2.7.2.1. Fundamentals

TOC content can be measured directly or alternatively, subtracting the inorganic carbon content from the total carbon content, being this the most common method^[48]. This strategy is based on the total combustion of the samples by heating them at elevated temperatures (700 °C) in an oxygen-rich environment (figure 3.12). The concentration of total carbon (TC) in the sample is obtained through comparison with a standard calibration curve. Furthermore, by subjecting the oxidized sample to the sparging process, the inorganic carbon (IC) in the sample is converted to carbon dioxide. The TOC concentration is then calculated by subtracting the IC concentration from the obtained TC concentration.

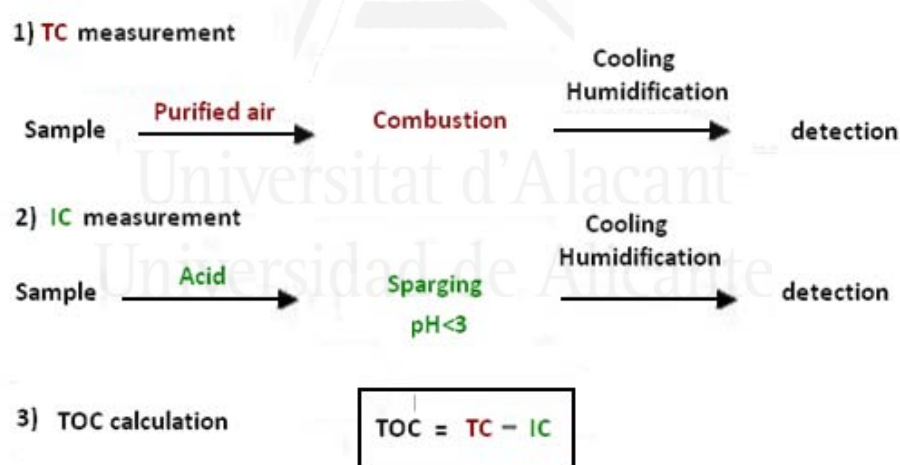


Figure 3.12. Schematic diagram showing TOC measurement.

3.2.7.2.2. Equipment used and test conditions

A total organic carbon analyzer Shimadzu, TOC-5000A was used in order to determine the total organic carbon content in all titania materials. Rhodamine 6G with different concentrations was used as a standard calibration curve to quantitatively determination of TOC contents of the samples.

3.3. REFERENCES

- [1] Y. Wang, Z.H. Jiang, F.J. Yang, *Mat. Sci. Eng. B*, 2006, **128**, 229.
- [2] a) T. Fröschl, U. Hörmann, P. Kubiak, G. Kucerova, M. Pfanzelt, C.K. Weiss, R.J. Behm, N. Hüsing, U. Kaiser, K. Landfesterd, M. Wohlfahrt-Mehrens, *Chem. Soc. Rev.*, 2012, **41**, 5313; b) H. Chen, K. Dai, T. Peng, H. Yang, D. Zhao, *Mat. Chem. Phys.*, 2006, **96**, 176.
- [3] (a) F. Rouquerol, J. Rouquerol, K. Sing, “*Adsorption by Powders & Porous Solids, Principles, Methodology and Application*”, Academic Press, London, 1999. (b) J.B. Condon, “*Surface Area and Porosity Determinatons by Physisorption, Measurements and Theory*”, Elsevier, Amsterdam, 2006.
- [4] S.J. Gregg, K.S.W. Sing, “*Adsorption, Surface Area and Porosity*”, Academic Press, New York, 1967.
- [5] J.O. Ross, “*Adsoption*”, Ed. Jonh Wiley & Sons, New York, 1982.
- [6] A. Gómez, Ph.D Thesis, “*Nuevos materiales mesoporsos como soportes para catálisis heterogénea. Control de su morfología y aplicación en procesos catalíticos asistidos por microondas*”, Universidad de Alicante, Alicante, 2011.
- [7] J. Rouquerol, “*Characterization of Porous Solids III*”, Elsevier Science Publishers, Amsterdam, 1994.
- [8] K.S.W.Sing, D.H. Everett, R.A.W. Haul, L. Moscou, R.A. Pierotti, J. Rouquerol, Siemieniowska T., *Pure Appl. Chem.*, 1985, **57**, 603.

- [9] S. Brunauer, P.H. Emmett, E. Teller, *J. Am. Chem. Soc.*, 1938, **60**, 309.
- [10] L.G. Joyner, E.P. Barret, R. Skold, *J. Am. Chem. Com.*, 1951, **73**, 3155.
- [11] E.P. Barret, L.G. Joyner, P.P. Halenda, *J. Am. Chem. Soc.*, 1951, **73**, 373.
- [12] C. Duval, *"Inorganic Thermogravimetric Analysis"*, Elsevier, Amsterdam, 1953
- [13] H.J. Pain, *"The physics of vibrations and waves"*, John Wiley & Sons, 6th Edition, London, 2005.
- [14] W.W. Wendlandt, H.G. Hecht, *"Reflectance Spectroscopy"*, Wiley Interscience, New York, 1966.
- [15] G. Kottim, *"Reflectance Spectroscopy"*, Springer, New York, 1969.
- [16] D.F. Swinehart, *J. Chem. Educ.*, 1962, **39**, 333.
- [17] G. Körtum, W. Braun, G. Herzog, *Angew. Chem. Int. Ed.*, 1963, **2**, 333.
- [18] P. Kubelka, *J. Opt. Soc. Am.*, 1948, **38**, 448.
- [19] D. Reyes-Coronado, G. Rodriguez-Gattorno, M.E. Espinosa-Pesqueira, C. Cab, R. Coss, G. Oskam, *Nanotechnology*, 2008, **19**, 14605.
- [20] a) S. Valencia, J.M. Marin, G. Restrepo, *Open Mater. Sci. J.*, 2010, **4**, 9; b) N. Serpone, D. Lawless, R. Khairutdinov, *J. Phys. Chem.*, 1995, **99**, 16646.
- [21] L. Zhao, J. Yu, *J. Coll. Int. Sci.*, 2006, **304**, 84.
- [22] K.J. MacKenzie, M.E. Smith, *"Multinuclear Solid-State NMR of Inorganic Materials"*, Pergamon Materials Series Volume 6, Elsevier, Oxford, 2002.
- [23] K.C. Wong, *J. Chem. Educ.*, 2014, DOI: 10.1021/ed500324w
- [24] M. Rodríguez, *"La Difracción de los Rayos X"*, Ed. Alhambra Universidad, Madrid, 1982.
- [25] J. Bermúdez, *"Métodos de Difracción de Rayos X. Principios y Aplicaciones"*, Editorial Pirámide, Madrid, 1981.
- [26] a) Y. Waseda, A. Muramatsu, *"Morphology control of materials and nanoparticles"*, Springer, Heidelberg, 2004.

- [27] P.W. Atkins, *“Physical Chemistry”*, Oxford University Press, 1995.
- [28] S.J.S. Qazia, A.R. Rennie, J.K. Cockcroft, M. Vickers, *J. Coll. Interf. Sci.*, 2009, **338**, 105.
- [29] a) B. Beckhoff, B. Kanngießer, N. Langhoff, R. Wedell, H. Wolff, *“Handbook of Practical X-Ray Fluorescence Analysis”*, Springer, Heidelberg, 2006; b) R.E. Van Grieken, A. A. Markowicz, *“Handbook of X-Ray Spectrometry”*, Marcel Dekker Inc., New York, 2002.
- [30] E.P. Bertin, *“Introduction to X-Ray Spectrometric Analysis”*, Plenum Press, New York, 1978.
- [31] A.K. Cheetham, P. Day, *“Solid State Chemistry”*, Oxford University Press, New York, 1987.
- [32] J.F. Moulder, W.F. Stickle, P.E. Sobol, K.D. Bomben, *“Handbook of X-ray Photoelectron Spectroscopy”*, Perkin-Elmer Corp., Eden Prairie, Minnesota, 1992.
- [33] a) D. Briggs, *“Surface Analysis of Polymers by XPS and static SIMS”*, Cambridge University Press, New York, 1998; b) L. C. Feldman and J. W. Mayer, *Fundamentals of Surface and Thin Film Analysis*, North Holland-Elsevier, New York, 1986.
- [34] J.F. Watts, J. Wolstenholme, *“An Introduction to Surface Analysis by XPS and AES”*, Ed. John Wiley & Sons Ltd, New York, 2003.
- [35] A. Einstein, *Ann. Phys.*, 1905, **17**, 132.
- [36] P. Larkin, *“Infrared and raman spectroscopy, principles and spectral interpretation”*, Elsevier, Oxford, 2011.
- [37] K. Nakamoto, *‘Infrared and Raman Spectra of Inorganic and Coordination Compounds’*, Ed. John Wiley & Sons, New York, 1978.
- [38] M.L. Hair, *‘Infrared Spectroscopy in Surface Chemistry’*, Ed. Marcel Dekker Inc. New York, 1967.
- [39] J.M. Mermet, *J. Anal. At. Spectrom.*, 2005, **20**, 11.

[40] a) J.M. Mermet, *J. Anal. At. Spectrom.*, 2005, **20** 11; b) Technical Services of the University of Alicante (<http://ssti.ua.es/en/scientific-instrumentation/analysis-unit.html>) (Accessed on February 2014).

[41] Technical Services of the University of Alicante (www.ssti.ua.es/en/scientific-instrumentation/x-ray-unit/elemental-analysis) (Accessed on May 2014).

[42] R. González, *'The electronic microscopy in the scientific research'*, Publications Service of the University of Alcalá de Henares, Madrid, 1999.

[43] K.E. Sickafus, *"Encyclopedia of Materials Characterization: Surfaces, Interfaces, Thin Films; TEM - Transmission Electron Microscopy"*, Manning Publications, Greenwich, 1992.

[44] D.B. Williams, C.B. Carter, *"Transmission Electron Microscopy"*, Springer, New York, 1996.

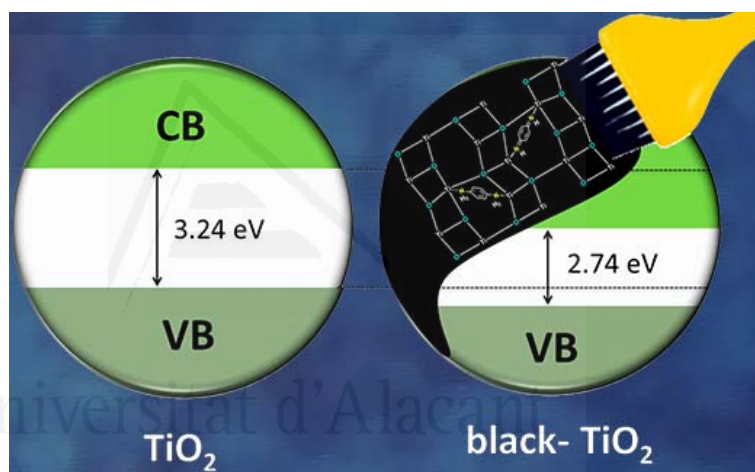
[45] V. Bárta, S. Wičar, G.J. Scherpenzeel, P.A. Leclercq, *J. Chromatography A*, 1986, **370**, 219.

[46] www.photochemicalreactors.com (Accessed on September 2013).

[47] J. Yu, Q. Li, S. Liu, M. Jaroniec, *Chem. Eur. J.*, 2013, **19**, 2433.

[48] I. Bistutti, I. Hilke, M. Raessler, *Trend. Anal. Chem.*, 2004, **23**, 10.

IV. Incorporation of organic compounds in the framework of mesoporous titania materials



M. Rico, E. Serrano, A.E. Sepulveda, J.R. Berenguer, E. Lalinde, J. Garcia-Martínez, "Organotitanias: a versatile approach for band gap reduction in titania-based materials" *J. Mater. Chem. C*, 2014 (sent for publication).

M. Rico-Santacruz, A.E. Sepúlveda, E. Serrano, J.R. Berenguer, E. Lalinde, J. García-Martínez, *Spanish Patent 20130535*, 2013.

IV. Incorporation of organic compounds in the framework of mesoporous titania

The reduction of the band gap of titania is critically important to fully utilize its photocatalytic properties. Two main strategies, i.e. doping and partial reduction of Ti(IV), are the alternatives available up to date. Herein it is shown a new synthetic strategy, where novel organotitania materials, with photocatalytic activities significantly better than the control titania have been prepared by co-condensation of a titanium precursor, TBOT, with two different organic compounds 4,6-dihydroxypyrimidine (DHP) and *p*-phenylenediamine (PPD). This new strategy allows the homogeneous incorporation of organic moieties within the crystal structure of titania, obtaining yellow and black titanias. The black ones show an enhanced photocatalytic activity under visible light, becoming a promising material in environmental applications such as decomposition of NO_x reduction of volatile organic contaminants and CO₂ from the atmosphere.

4.1. INTRODUCTION

Semiconductor nanoparticles and nanostructures have been extensively studied as building blocks for light harvesting systems with applications in the design of dye-sensitized solar cells (DSSCs), solar water splitting and the purification of air and water^[1]. As it was described in chapter 2, titania, due to its large band gap (3.0 eV for rutile and 3.2 eV for anatase phases), only harvests about 5% of the solar radiation (UV), which is the major limitation for this material. Because of this, search on titania-based materials with a smaller band gap to enable light absorption in the 400-900 nm (visible and near-IR) spectral range, is of prime importance for improving their efficiency and applicability.

Visible light-activated titanias have been prepared by partially reducing Ti(IV) (self-doping), metal-ion implantation and non-metal doping^[2,3]. Along this line, a remarkable interest has been devoted to the so-called “black titanias”, dark colored materials able to absorb a wide range of wavelengths^[4a,5a]. Very recently, black TiO₂ materials have been prepared by different methods based on the partial reduction of Ti(IV) to Ti(III)^[5,6] using hydrogen at high temperatures and pressure or metals such as Al or Zn^[7].

For example Chen et al.^[5a] reported the preparation of black TiO₂ by treatment in hydrogen at 20 bar and 200 °C for 5 days. All these methods present drawbacks as using hydrogen at high pressure and elevated temperatures. Moreover, a challenge encountered in the design of these titania-based materials is the predictability of their structural and electronic photocatalytic properties, because they have been found to be largely dependent on the synthetic conditions and procedures, which normally include high temperature treatments^[4b-d,8]. For all these reasons, a facile and low cost synthesis method is needed to produce black titania materials with a large solar absorption wavelength range.

As stated in Chapter 2, the band gap of titania-based materials can be also modified by sensitizing TiO₂ with appropriated organic or coordination compounds that act as dyes, able to inject electrons into the CB upon absorption of visible (or near IR) light. This sensitization is normally a post-synthetic procedure (impregnation or *grafting*^[4c,9]), thus suffering the inherent problems associated with these methods, already commented.

In these sensitized systems, it has been stated that the electronic transference is more efficient when the charge-transfer dye is covalently attached to the surface of a semiconductor substrate^[9c]. This could be due to the fact that the properties of these materials depend not only on the inorganic semiconductor or the charge-transfer dye, but also on the interface between both phases. For that reason, it would be highly desirable new low-cost and reproducible synthetic pathways for the preparation of efficient hybrid photocatalyst based on titania, in which the charge-transfer dyes are more closely integrated in the semiconductor matrix.

Recently, Prof. Schubert synthesized titanium coordination compounds [Ti(OR)_a(L)_b]_n, being L an organic ligand, pointing out the possibility of using them as precursors in the preparation of hybrid materials by sol-gel processing^[10]. Inspired by this work, and taking into account the previous experience of our research group in the design of hybrid periodic mesoporous metal complex-silica^[11], we explore the possibility of synthesize [Ti(OR)_a(L)_b]₄ coordination compounds, containing adequate functionalized organic ligands (L), as precursors for the design of functional hybrid mesoporous organotitanias for photocatalytic applications.

In this chapter, the successful synthesis of novel mesoporous organotitania materials with anatase structure and excellent photocatalytic activity is reported.

It should be noted that, compared with the extensive research carried out on mesoporous organosilicas, the introduction of functionalities into titania-based materials using organic or coordination compounds remains essentially unexplored^[12].

4.2. EXPERIMENTAL SECTION

4.2.1. Synthesis of the mesoporous organo-modified titanias

The synthesis of hybrid mesoporous organotitanias is herein described, by co-condensation of tetrabutyl orthotitanate (TBOT) with different amounts of 4,6-dihydropyrimidine (DHP) and *p*-phenylenediamine (PPD) (6 – 24 wt%). The synthesis is carried out using only water and ethanol as solvents and without the concurrence of surfactants (scheme 4.1). Mesoporous organotitanias were synthesized following a similar procedure to that described in Chapter 3 for the synthesis of the control titania. The details are proprietary^[13].

In a typical synthesis, the organic compounds were firstly dissolved in absolute ethanol during 2 h at 40 °C under magnetic stirring. Following, 5 g (14.7 mmol) of TBOT were added to that solution and the mixture was magnetically stirred during 40 min at room temperature. Finally, 123.5 g (6.86 mol) of water were added drop-wise causing the precipitation of the solid. The mixture was then kept at room temperature during 24 h under vigorous magnetic stirring, followed by a treatment at 80 °C for 24 h in a drying oven. The obtained solid product was washed with water and acetone, successively, filtered and dried in an oven at 100 °C for 8 h. The molar ratio of the synthesis gel was 1TBOT: *x* Org: 41.3 EtOH: 467 H₂O, where *Org* refers to organic compound, being *x* varied between 0.05 and 0.2.

4.2.2. Physico-chemical characterization methods

The incorporation of both organic compounds in the titania samples was evaluated by TGA and FTIR and XPS spectroscopies and the content of both organic compounds in the final titania materials, was analyzed by elemental analysis.

XRD analysis was carried out in order to study the crystalline structure of the titania materials and TEM was used to analyse their morphology, porosity and crystallinity. The particle size was estimated as an average of the size of 100 particles by TEM and using the Gatan software package.

Porous texture parameters (mesoporosity volume, surface area and pore diameter) were characterized by N₂ adsorption at 77 K and the results were analyzed using the software package AUTOSORB.

DRUV spectra were carried in order to determinate the band gap of the titania materials. The XPS spectra of these materials were obtained in the -10 to 2 eV region to calculate the position of the maximum of their valence bands. Both techniques were combined to determine the conduction band position of the titania materials and to obtain the density of states (DOS) scheme.

All the equipment and experimental conditions used are described with more detail in Chapter 3.

4.2.3. Photocatalytic activity: liquid-solid regime

Photocatalytic activity of the synthesized titania materials was evaluated by following the reduction in the absorbance band (bleaching) of R6G (R6G) solutions ($5 \cdot 10^{-5}$ M, 100 ml) under both UV radiation and visible light in a photochemical reactor system equipped with a medium-pressure Hg lamp (more details are described in Chapter 3). The study of the photocatalytic activity of all titania materials under visible light was performed during a pre-doctoral stay in the

“Organometallic Molecular Materials” group in the University of La Rioja (Spain) under the supervision of Dr. Jesús R. Berenguer Marín.

The samples irradiated with UV light were studied with a total organic carbon analyzer to determinate the TOC content of the synthesized samples before and after bleaching of the sample (more details in Chapter 3). A calibration curve using R6G with different concentrations was used for determining TOC contents of samples.

4.3. RESULTS AND DISCUSSION

4.3.1. Structural and physico-chemical characterization of the titanias with organic compounds incorporated into its structure

Mixing of the ethanolic solutions of the organic compounds with TBOT leads to the formation of titanium-alkoxide complexes as shown in scheme 4.1. Room temperature hydrolysis of these mixtures for 24 h affords to obtain a gel, white for DHP and pale-grey for PPD (figure 4.1), which crystallizes in an anatase phase by heating the suspension at 80 °C for other 24 h, (scheme 4.1).

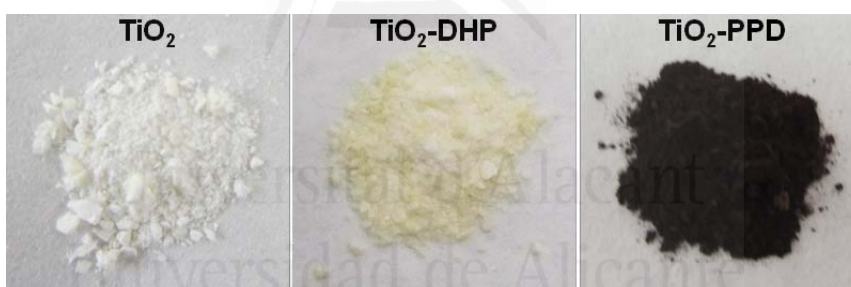
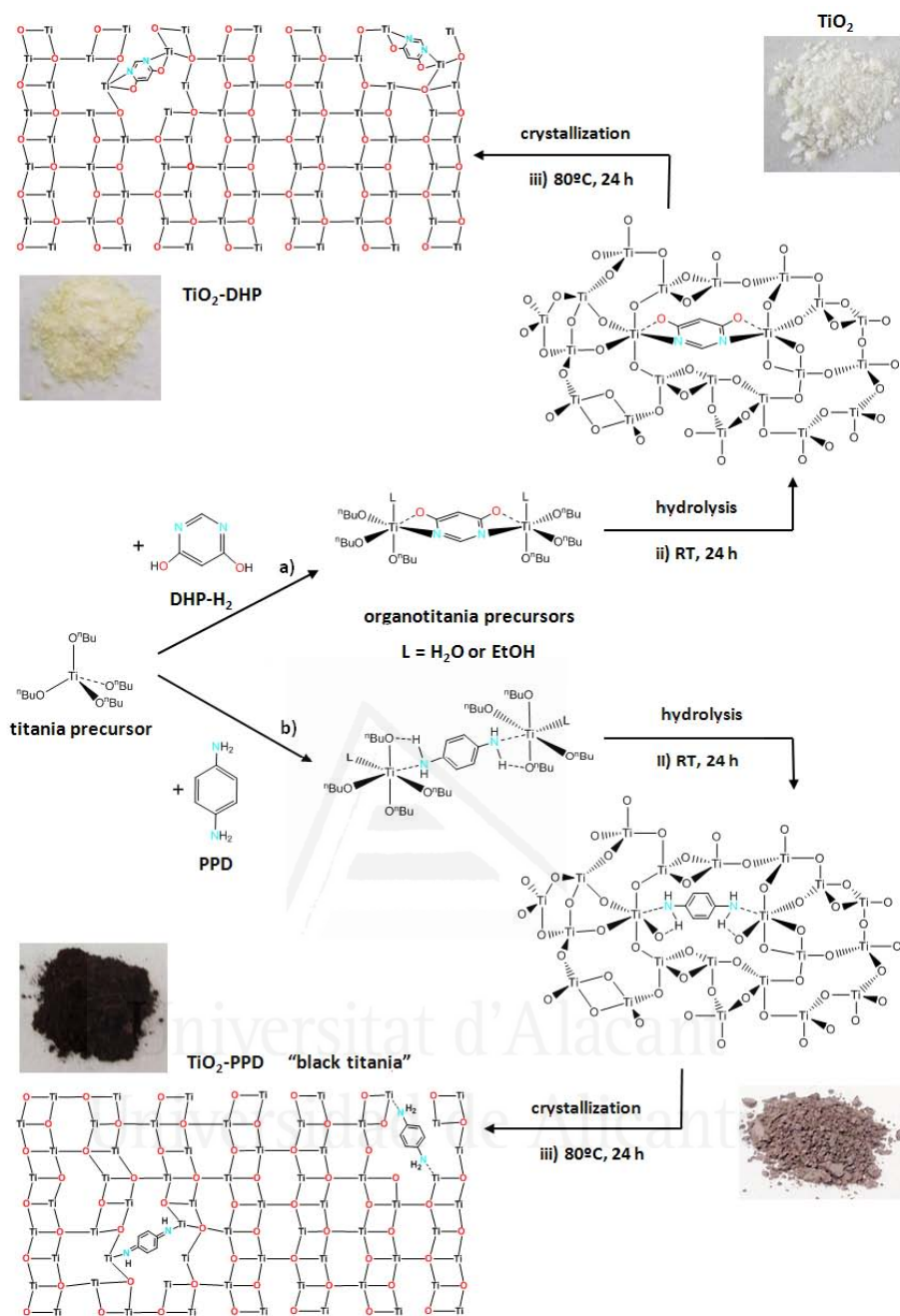


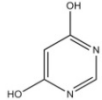
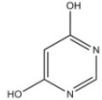
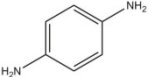
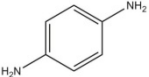
Figure 4.1. Comparison of the colour of control titania, a pale yellow titania ($\text{TiO}_2\text{-DHP-b}$) and a black titania ($\text{TiO}_2\text{-PPD-b}$).



Scheme 4.1. Synthesis methodology to incorporate the organic compounds: a) 4,6-dihydroxypyrimidine (DHP) and b) *p*-phenylenediamine (PPD) in the mesoporous titania^[14].

The resulted coloured samples are denoted TiO₂-DHP-x and TiO₂-PPD-x, where x indicates the nominal wt% of organic compound incorporated (x = a, b and c for 6, 12 or 24 wt%, respectively). Table 4.1 lists the structure and name of the organic compounds used as well as the molar ratio of the synthesis gel, wt% of organic compound and the nomenclature used for samples.

Table 4.1. Nomenclature of the organotitanias synthesized indicating the name and chemical formula of the incorporated organic compound as well as the nominal and experimental organic compound content.

Sample	Org. compound name /formula	Org/TBOT molar ratio	Nom. Org. Cont. (wt %)	Org. cont. ^a (wt%)	Org. cont. ^b (wt%)	Inc. Yield ^c (%)
TiO ₂ -DHP-a	4,6-dihydroxypyrimidine*	0.05	6.4	3.9	1.7	61 (26)
TiO ₂ -DHP-b		0.10	12.1	5.1	2.7	42 (22)
TiO ₂ -DHP-c		0.20	21.7	5.0	3.8	23 (18)
TiO ₂ -PPD-a	<i>p</i> -phenylenediamine	0.05	6.3	5.2	3.5	83 (56)
TiO ₂ -PPD-b		0.10	11.9	4.6	4.7	39 (40)
TiO ₂ -PPD-c		0.20	21.3	9.2	8.5	43 (40)

^aOrganic content as determined by elemental analysis from the C content, ^bOrganic content as determined by TGA, ^cIncorporation yield calculated by elemental analysis. Values in brackets represent the incorporation yield by TGA. *98% of purity

The homogeneous incorporation of the organic compounds into the structure of mesoporous titania was confirmed using EA, TGA, FTIR and XPS analyses (figures 4.2, 4.3 and 4.4, respectively) thus indicating the effectiveness of the synthetic route herein described for both compounds. Besides the higher complexing capacity of the tetradentate DHP in comparison with the bidentate PPD ligand, both elemental and thermogravimetric analysis show better incorporation yields for the PPD ligand in the

organotitania materials. EA indicates a threshold of DHP and PPD incorporation of ca. 5 wt% except for TiO₂_PPD_c titania sample with the higher organic content (column 5, table 4.1). Similar values were obtained by TGA as with the PPD ligand, being a little smaller in the TiO₂-PPD-a sample but not in the case of DHP ligand, where the yield difference is more significant (column 6, table 4.1). Both techniques results confirmed the incorporation of the organic compounds into the titania. Higher results obtained with EA analysis from the C content can be associated with the measurement of residual alcohol molecules presented in the samples, which is not considered in the TG analysis.

FTIR spectra of both organotitania materials show bands characteristic of each of the organic moieties (figure 4.2). In the spectrum of TiO₂-DHP, it is clearly observed one absorption at 1410 cm⁻¹, corresponding to the $\delta(\text{CH})$ associated with the ring of the pyrimidine and absorptions due to $\nu(\text{C}=\text{C})_{\text{arom}}$ (1620, 1550 cm⁻¹).

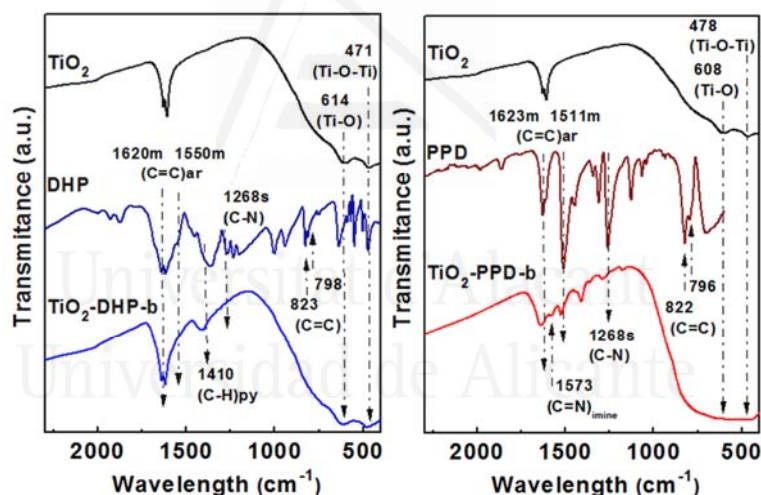


Figure 4.2. FTIR spectra of organotitanias (12 wt% organic compounds), as compared with the control TiO₂ and the organic compounds. The bands characteristics of the incorporation of the organic compounds are denoted by arrows.

The spectrum of TiO₂-PPD (figure 4.2, right) shows also several absorptions due to $\nu(\text{C}=\text{C})_{\text{arom}}$ (1623, 1511 cm⁻¹) and the corresponding one to $\nu(\text{C}-\text{N})$ at 1268 cm⁻¹. Also, an absorption assignable to $\nu(\text{C}=\text{N})_{\text{imine}}$ is observed at 1573 cm⁻¹^[15], indicating the presence of oxidized PPD, which probably are the responsible of the dark colour, as discussed below. Absorptions associated to Ti-O-C^[16], at around 1067 cm⁻¹, can be only distinguished as weak bands in TiO₂-PPD sample, probably due to the broad absorption corresponding to Ti-O and Ti-O-Ti bonds.

As shown in figure 4.3, XPS spectra of N1s peak of both organotitanias (TiO₂-DHP-b and TiO₂-PPD-b) show a broad band with a maximum at ca. 399 eV, which can be deconvoluted in two peaks (400.5 and 399 eV, for TiO₂-PPD, and 400.2 and 398.8 eV for TiO₂-DHP).

The assignment of XPS peaks in nitrogen-containing titania is still under debate and different hypothesis are discussed^[9a,17]. Normally, the assignment of N1s peaks in the XPS spectra can be classified into different categories. At ca. 400 eV is usually ascribed to adsorbed molecular nitrogen as well as nitrogen species in a higher oxidation state, for example nitrogen species containing NC, C-N=C or NCO bonds or interstitial NH species. As expected, peaks characteristics of substitutional nitrogen, at ca. 396 eV^[18], were never observed in our samples. These results strongly support the formation of a coordination compounds between DHP or PPD with Ti of the anatase structure^[19]. Anionic doping is difficult to carry out because of the larger size of the organic compounds in comparison with oxygen anion. Both ligands are larger than the interstitial space of titania lattice. According to the proposed methodology, the incorporation of the DHP and PPD takes place through the formation of coordination compounds that, after hydrolysis, led to a modified titania lattice, which is associated with a decrease in the crystalline domain of these materials (table 4.2).

The two bands of N1s XPS spectra in figure 4.3 can be thus tentatively ascribed with the presence of two types of nitrogen species in the anatase structure (such as coordinated and uncoordinated N atoms in TiO₂-DHP and TiO₂-PPD, and also oxidized species derived for the black titanias). XPS spectra of N 1s region of the control TiO₂ shows peaks associated to adventitious N₂^[17,18], which disappear after the etching of sample.

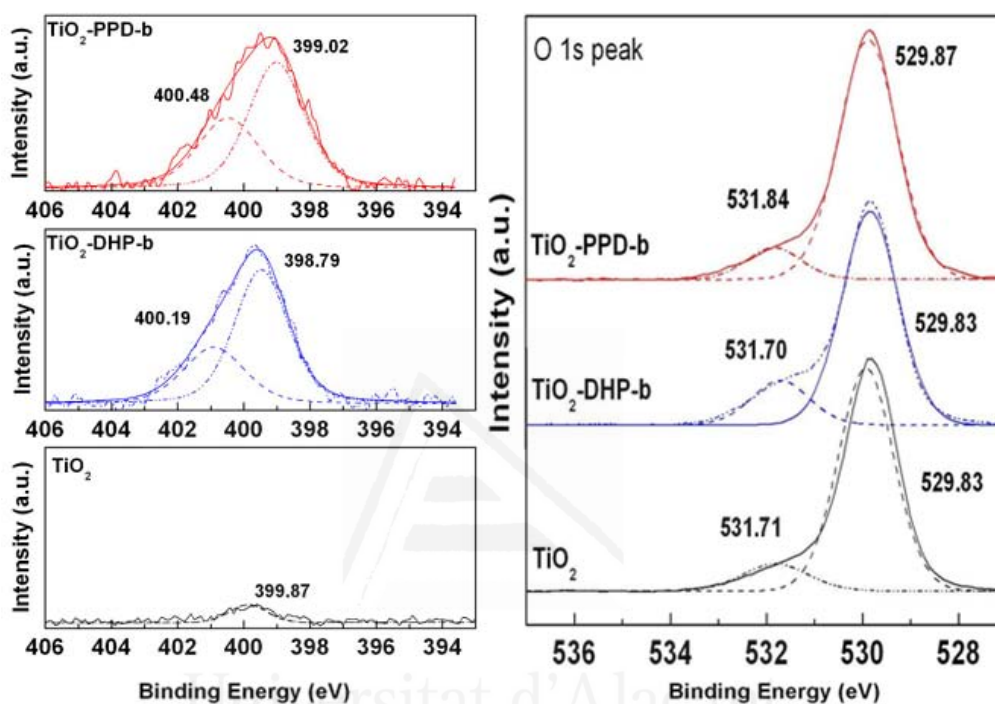


Figure 4.3. N 1s XPS spectra of hybrid TiO₂-DHP-b and TiO₂-PPD-b organotitanias (left) and O 1s XPS spectra (right) of hybrid TiO₂-PPD-b organotitania as compared with those of control TiO₂.

XPS spectra for both types of organotitanias display symmetric Ti(2p) features, 2p_{3/2} and 2p_{1/2}, corresponding to Ti(IV) octahedral coordination sites^[20] (figure 4.4, left). These bands do not show additional lower binding energy components

associated to the presence of reduced Ti(III) centres, which is rather common in non-metal atom doped titanias^[9a].

Also, both samples have Ti 2p and O 1s binding energies similar than those of control titania, confirming the octahedral coordination of Ti and also that the incorporation of the organic compounds do not affect the structure of the titania materials. The O1s XPS spectra exhibit two components, one centered at 529.8 eV corresponding to lattice oxygen in TiO₂ and the other centered at 531.7 eV for TiO₂ and TiO₂-DHP-b and 531.8 for TiO₂-PPD-b, assigned to surface hydroxyls^[21] (figure 4.3, right).

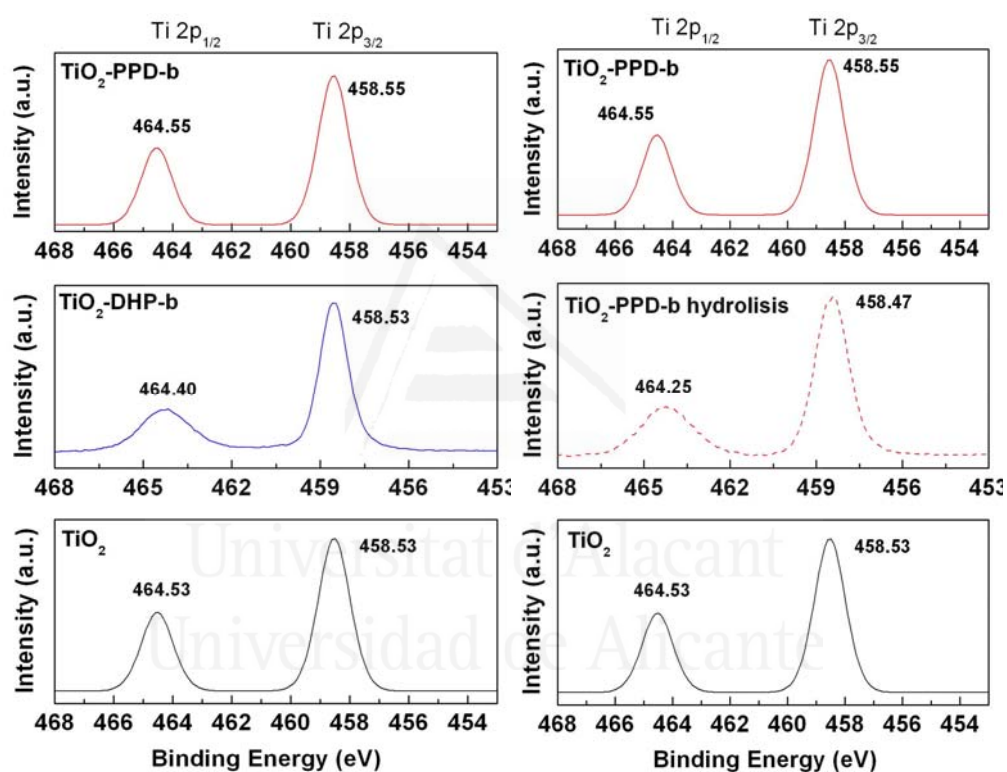


Figure 4.4. Ti 2p XPS spectra of the synthesized organotitanias (left) and Ti 2p XPS spectra of the TiO₂-PPD-b, before (hydrolysis) and after the crystallization (right) as compared with those of control TiO₂.

In addition, figure 4.4 (right) shows the Ti(2p) spectra of the TiO₂_PPD_b after the hydrolysis and before the crystallization (TiO₂-PPD-b hydrolysis) as compared with control TiO₂ and TiO₂-PPD-b after the crystallization. All the spectra present similar energy bands, associated with the octahedral coordination of the Ti(IV) in the samples. Thus, Ti octahedral coordination is maintained throughout the whole synthesis process of the titania materials.

Table 4.2. Textural and structural parameters of the mesoporous organotitania materials synthesized as compared to the control titania.

Sample	Org. cont. (wt%) ^a	d_p^b (nm)	V_p^c (cm ³ /g)	A_{BET}^d (m ² /g)	$D^{XRD, e}$ (nm)	$\Phi^{TEM, f}$ (nm)	$d_{101}^{XRD, g}$ (nm)	$d_{101}^{TEM, h}$ (nm)
TiO ₂	---	5.6 (2-9)	0.29	245	6.4	8.7	0.35	0.37
TiO ₂ -DHP-a	3.9 (1.7)	4.6 (2-9)	0.26	260	5.7	8.8	0.35	0.38
TiO ₂ -DHP-b	5.1 (2.7)	3.8 (1-9)	0.21	258	5.5	8.5	0.35	0.38
TiO ₂ -DHP-c	5.0 (3.8)	3.4 (1-9)	0.20	218	5.7	9.1	0.35	0.38
TiO ₂ -PPD-a	5.2 (3.5)	6.1 (2-10)	0.27	210	6.0	8.9	0.35	0.37
TiO ₂ -PPD-b	4.6 (4.7)	6.0 (2-11)	0.27	210	5.6	8.7	0.35	0.38
TiO ₂ -PPD-c	9.2 (8.5)	6.1 (2-11)	0.31	225	5.6	9.9	0.35	0.38

^aOrganic content as determined by elemental analysis from C content. Values in brackets indicate the organic content as determined by thermogravimetric analysis. ^bAverage mesopore diameters were estimated from the adsorption branch of the nitrogen isotherm using the BJH method. ^cMesopore volume from the isotherms at relative pressure of 0.95 (see Chapter 3). ^dThe BET surface area was estimated by multipoint BET method using the adsorption data in the relative pressure (P/P_0) range of 0.05–0.30. ^eDomain size of the particle calculated from XRD using the Scherrer equation. ^fParticle size from an average of 100 particles was calculated by TEM using the Gatan software package. ^gAnatase spacing (d_{101}) calculated using Bragg equation. ^hAnatase spacing (d_{101}) calculated from TEM from an average of 10 particles using Gatan software package (see Chapter 3).

Nitrogen adsorption/desorption isotherms of the TiO_2 -DHP and TiO_2 -PPD organotitanias are shown in figure 4.5. For comparison purposes, the isotherm of the control TiO_2 is also included. Based on these isotherms, the textural parameters of the samples were calculated and listed in table 4.2. The novel organotitania materials (TiO_2 -DHP and TiO_2 -PPD) show Type IV isotherms, in all cases very similar to the control TiO_2 . This is indicative of the mesoporous nature of these samples, being the textural properties similar to the control titania. Furthermore, no significant effect was observed of neither the ligand amount incorporated (quite similar in all materials) nor the type of ligand, in good agreement with the incorporation of the organic compounds in the framework of the titania and not between the titania nanoparticles.

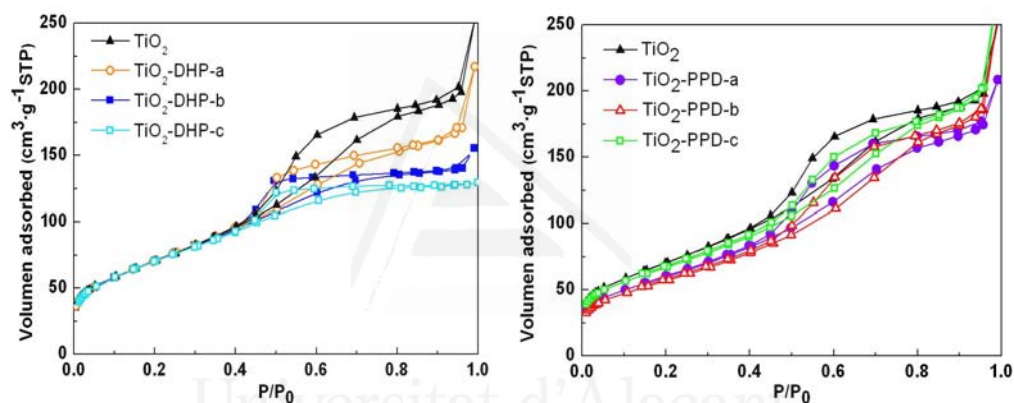


Figure 4.5. Nitrogen adsorption/desorption isotherms at 77 K of TiO_2 -DHP (left) and TiO_2 -PPD (right) organotitanias, as compared to control TiO_2 .

The XRD spectra of these titania materials (figure 4.6) are typical of the anatase structure ($2\theta = 25.3^\circ$, 37.8° and 48.05°)^[22]. Also a slightly decrease in the crystalline domain of the organotitanias synthesized is observed, compared to the control TiO_2 . The crystal domain decrease can be explained by considering the incorporation of

the organic compounds into the structure, which partially alters the crystalline structure of the materials (table 4.2). This fact could be associated with the enhancement of the photochemical properties of these materials, specially with PPD.

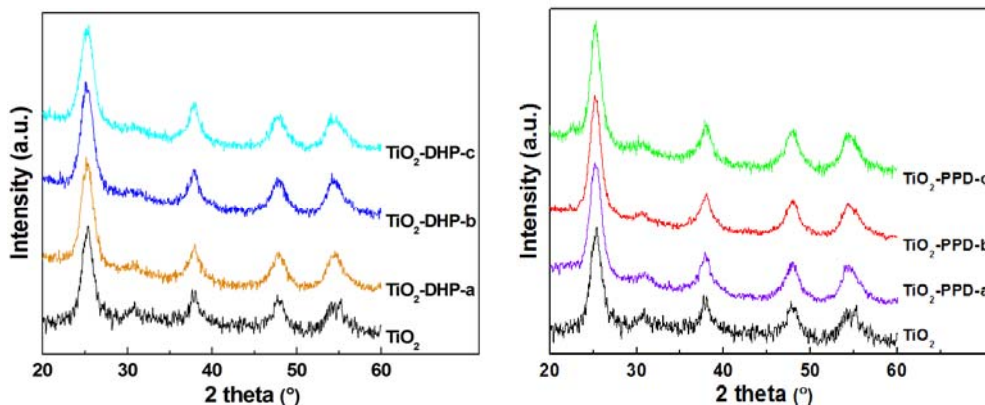


Figure 4.6. Normalized XRD patterns of the TiO_2 -DHP (left) and TiO_2 -PPD (right) organotitanias, as compared to control TiO_2 .

The mesoporous nature and the crystalline structure of these materials were also analysed by TEM (figure 4.7). The lattice spacing was obtained using the Gatan software package. The obtained value was 0.37-0.38 nm, in agreement with the distance between (101) crystal planes of the anatase phase (ca. 0.35 nm) calculated by XRD. The close agreement between crystallite size determined by XRD and the particle size calculated by TEM, confirms not only the lack of significant agglomeration of titania nanoparticles (also supported by TEM images), but also the effective and homogeneous incorporation of both DHP and PPD during the formation of the gel.

As a consequence, the crystallization of the titania structure takes place during the incorporation of the organic compounds modifying the crystalline lattice, but maintaining similar textural properties to those of the control titania, with only a slight decrease in the crystalline domain.

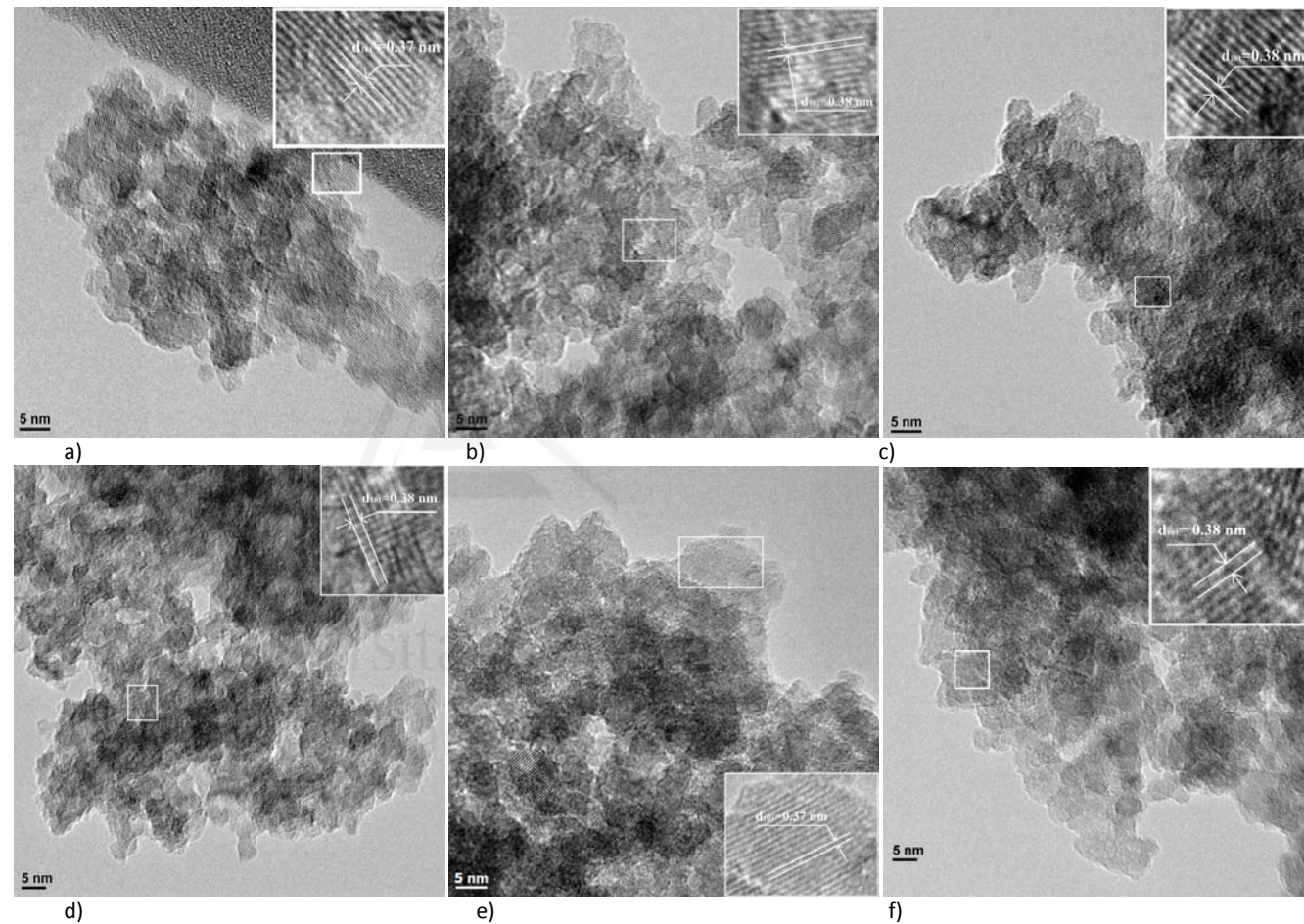


Figure 4.7. TEM micrographs of: TiO₂ (a), TiO₂-DHP-a (b), TiO₂-DHP-b (c), TiO₂-DHP-c (d), TiO₂-PPD-a (e) and TiO₂-PPD-b (f). Spacing of lattice image was determined by using Gatan software and, in all cases, corresponds to d_{101} spacing of anatase crystalline phase.

The particle size determined by XRD slightly decreases from 6.4 nm, in the control titania, up to 5.5-5.7 nm in the hybrid organotitanias, while a constant value of ca. 8.7 nm was determined by TEM for all the synthesized samples. This supports the presence of the organic compounds between the anatase structure (distorting or interrupting it) and not in the surface. Indeed, contrary to that observed by TEM by other authors for titania sensitized by carbonaceous species^[23], no evidences of a core-shell structure has been detected after a careful examination of the samples by TEM.

4.3.2. Optical properties

The optical characterization of these samples was carried out by XPS and DRUV. As previously reported, for indirect band gap materials such as titania, the intercept of the tangent to the $(F(R')h\nu)^{1/2}$ with $(h\nu)$ gives a good estimation of the value of the band gap^[24]. The $(F(R')h\nu)^{1/2}$ versus photon energy $(h\nu)$ plots are shown in figure 4.8a, which can be used to determine the optical band gap by extrapolation of the base line and the absorption edge in the UV-vis spectra. The maximum of the valence band measured by XPS is shown in figure 4.8b and a schematic illustration of the density orbital states (DOS) in the figure 4.8c.

The band gap of the control TiO₂ has been estimated to be 3.24 eV, in good agreement with bulk anatase TiO₂^[25]. The only difference of the DRUV spectra of the yellow titania TiO₂-DHP in relation to the control TiO₂ is a slight red-shift in the absorption band edge related to the indirect band gap transition (3.17 vs. 3.24 eV). By contrast, the DRUV spectra of the black titania (TiO₂-PPD) show two absorption band edges. The low energy feature covering the visible with a tail to ca. 900 nm is associated to transitions from the final species generated by the oxidation of part of the PPD, whereas the higher energy one is related to the indirect band gap transition

of TiO_2 . Interestingly in this black titania, the energy of the indirect band gap is found strongly red-shifted (2.74 eV), lying into the visible range (453 nm), and the HOMO-LUMO gap associated to the partial oxidized PPD decreases to 1.24 eV, which makes it suitable for photocatalytic applications under visible light.

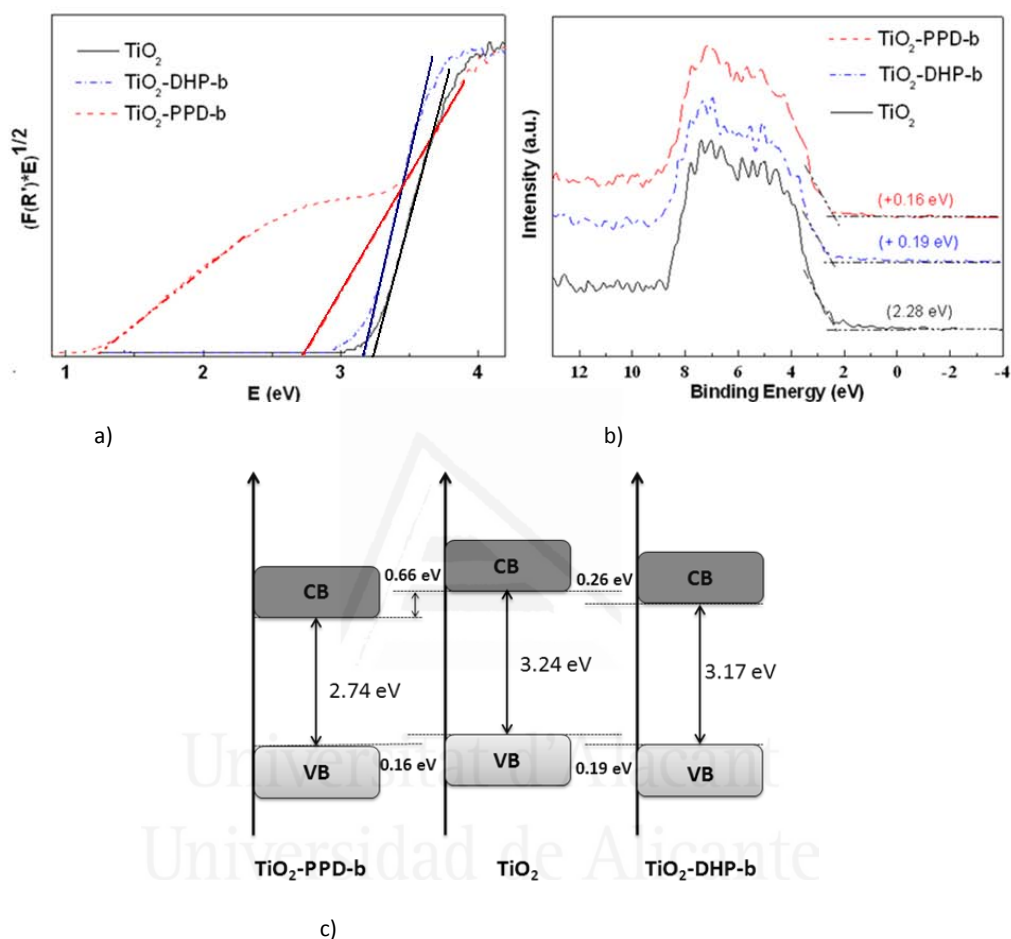


Figure 4.8. Valence band XPS spectra (a) and plot of the transformed Kubelka-Munk function versus the energy of light adsorbed (b). Schematic illustration of the DOS (c) of the organotitania $\text{TiO}_2\text{-DHP-b}$ and $\text{TiO}_2\text{-PPD-b}$ samples as compared with the control TiO_2 .

As shown in figure 4.8b, the XPS spectra of the control titania shows the edge of the maximum energy at 2.28 eV, similar to that found for other titanias^[5a], thus the conduction band minimum (CB) should occur at ca. -0.96 eV. Although not shown, voltamperometry measurements gave similar results for the conduction band minimum position.

Despite of having used the same synthesis conditions, while the TiO₂-DHP-x organotitanias are pale-yellow solids, this method yields black organotitanias in the case of PPD (figure 4.1). It is known that DHP reacts with titanium alkoxides Ti(OR)₄ to yield alcoxy-titanium (μ -dihydroxypyrimidinate) complexes^[26] similar to the dimetallic organotitania precursor proposed in scheme 4.1.a, which is able to co-condensate with the rest of the TBOT precursor in the first hydrolysis step.

The case of the *p*-phenylenediamine is more complex. There is a good number of described dimetallic or polymeric amine adducts of stoichiometry [Ti₂(OR)₈(NH₂R')₂]^[27], showing hydrogen bonds between the -NH group and a neighboring OR ligand. Nevertheless, as far as we know, in none of the described examples the nitrogen atom of the amine is bonded to a C sp² atom. In fact, all the attempts to obtain either dimetallic or polymeric complexes by reaction of TBOT with the appropriated amount of PPD have been fruitless, and only unreacted precursors have been obtained. However, although rather weak, some interaction between PPD and the titanium atoms of TBOT must exist in order to stabilize the ligand homogeneously dispersed along the TBOT mixture, probably supported by hydrogen bonds (scheme 4.1.b).

At this point, it must be noted the different behaviour of the PPD in aqueous suspension or in the TBOT mixture. It is well known that PPD is prone to autoxidation in aqueous media to give dark materials, which have been used as typical ingredient in hair dyes or in a large variety of coloured products, like textiles, cosmetic, black

rubber or even temporary tattoos. This oxidation produces first the highly reactive *p*-phenylenequinone diimine (NH=C₆H₄=NH, PPQD), which further undergoes self-conjugation reactions to form a mixture of dimers and trimers^[28,29]. Notwithstanding, during the formation of the “black titania”, after the hydrolysis at room temperature, (step ii, scheme 4.1b) a pale-grey (almost white) gel is formed, thus indicating the existence of an effective protection against the oxidation of the PPD in the synthesis gel. In fact, darkening of the material, and thus the partial oxidation of the PPD present in the gel, happens along with the crystallization (step iii, scheme 4.1b).

The extension of the oxidation cannot be stated, which probably leads to mixture of organic derivatives (OPPD, oxidized *p*-phenylenediamine, figure 4.9), but it is reasonable to assume that if the PPD molecules are protected during the formation of the gel and homogeneously dispersed in the mixture, it should be difficult for them to oligomerize during the oxidation process. For this and taking into account FTIR analyses, it is tentatively proposed that the organic species present in the black organotitanias are mainly molecules of PPD and PPQD.

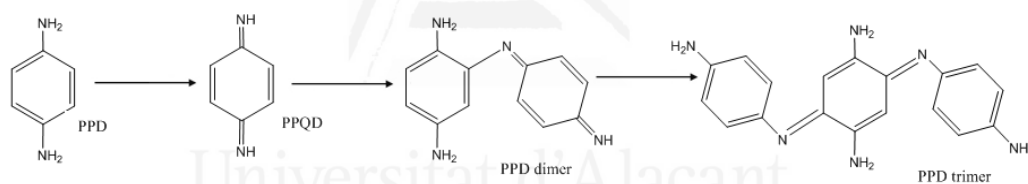


Figure 4.9. Oxidative process of the organic compound *p*-phenylenediamine (PPD).

To further study this phenomenon, TiO₂_PPD sample was prepared in different reducing or oxidizing media to modify the extension of the oxidation process of PPD. For instance, the presence of NaBH₄, which does not react with PPD in the conditions tested, leads to the obtention of a white solid with anatase structure, but the incorporation of organic moieties fell down drastically to negligible levels.

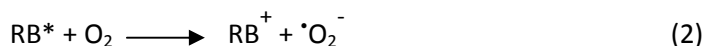
Nevertheless, bubbling of air during the synthesis process yielded a similar black titania than that obtained carrying out the reaction in Ar atmosphere with deoxygenated water.

Finally, prolonged refluxing of the black titania in EtOH or in aqueous solution of NaBH₄ (24 to 48 h) only produces a slight decolouration of the material, which shows the enhanced hydrothermal stability of the organic species, probably due to their incorporation into the solid titania matrix.

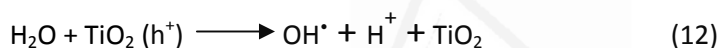
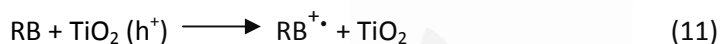
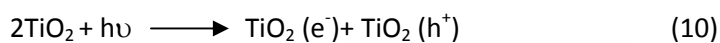
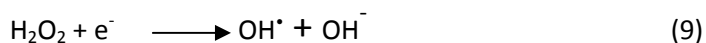
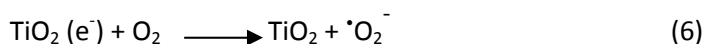
Therefore it can be concluded that it is possible to obtain modified titania materials, where the value of the band gap has been modified by the incorporation of organic compounds, particularly PPD, so that they are active in the whole visible range, opening the possibility to make a better use of the sunlight spectrum.

4.3.3. Liquid-solid regime photocatalytic activity of the organo-modified titania materials

To test the photocatalytic activity of the different titania materials prepared, a R6G aqueous solution ($5 \cdot 10^{-5}$ M, 100 ml) was degraded by the catalysts (0.15 g/l) under two different types or radiation: UV and visible light. R6G is commonly used as model organic dye, due to its importance as dye pollutant from the textile industry in environmental pollution and its degradation mechanism has been extensively studied^[30]. The blank reaction showed that the dye scarcely degraded in the absence of catalyst under the test conditions. The reaction mechanism in the absence of TiO₂ and the presence of oxygen includes the following reactions^[30]:



Irradiation with UV radiation or visible light produces the excitation of the rhodamine (equation 1), followed by the reduction of O₂ generating radicals ([•]O₂⁻), which reacts with a proton producing OOH[•] (equations 2 and 3). In presence of TiO₂, under UV or visible light, the following reactions occur^[30]:



When TiO₂ is present in the R6G degradation reaction, the reaction 2 is very slow as compared to reaction 5, in which the excited dye reacts with titania injecting electrons into the TiO₂ conduction band, TiO₂(e⁻). This observation confirms that the presence of TiO₂ in the reaction enhances considerably the photoactivity for the degradation of R6G^[30].

4.3.3.1. Photocatalytic activity under UV radiation

The photocatalytic activity under UV radiation of both organotitanias is enhanced up two-three fold higher than the control titania (table 4.3, figure 4.13a), despite of showing similar textural and structural properties.

After irradiating for ca. 3 h, R6G is completely bleached and no signal was observed by UV-vis spectroscopy for both hybrid titanias (figure 4.10). Contrarily, more than 12 h are needed to bleach the dye using control TiO_2 . The characteristic absorption peak at 525 nm of R6G practically disappears with the concomitant decoloration of the solution (figure 4.10).

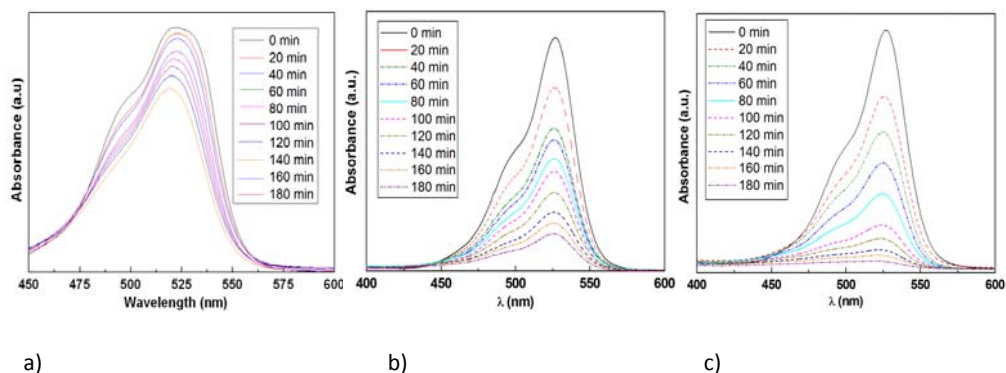


Figure 4.10. UV-vis absorption spectra of the degradation reaction of an aqueous solution of R6G ($5 \cdot 10^{-5}$ M) under UV radiation using as photocatalysts: TiO_2 (a), TiO_2 -DHP-b (b) and TiO_2 -PPD-b (c).



Figure 4.11. Photographs of the different samples taken along the degradation reaction of an aqueous solution of R6G ($5 \cdot 10^{-5}$ M) under UV radiation using TiO_2 -PPD-b as photocatalysts.

In the dye degradation reaction under UV radiation, no blue-shift of the absorption maximum peak to 498 nm was observed (figure 4.10) suggesting that the

final formed species in solution presumably do not contain aromatic conjugated rings, that usually absorb in this region^[30]. Watanabe et.al^[31] described that blue-shift in the absorption maximum is associated to the N-deethylation of R6G to rhodamine (figure 4.12), the major intermediate in the degradation reaction of R6G. At the end of the reaction, the cationic dye radical is degraded to carbon dioxide and water and a colourless solution is obtained.

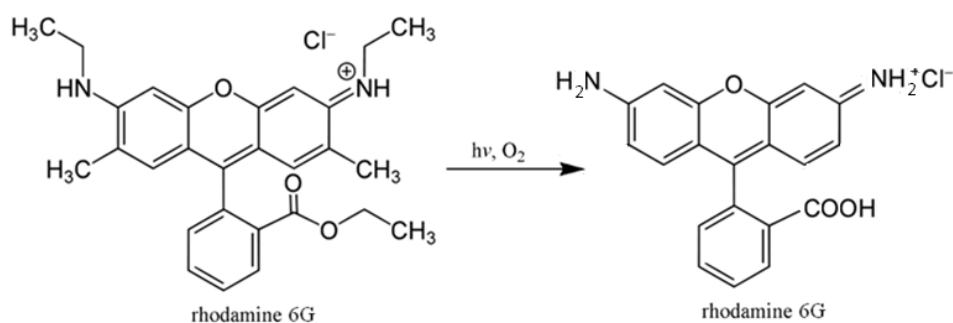


Figure 4.12. N-deethylation reaction of R6G to rhodamine^[30].

The rhodamine intermediate was not detected by UV-vis spectroscopy when UV radiation was used, only a decrease in R6G concentration was found. The degradation of R6G without a detectable rhodamine intermediate was also reported by Wu and Zang^[32]. Moreover, the absence of the rhodamine intermediate peak (blue-shift) does not necessarily mean that the N-deethylation does not take place and the fact is that no additional peaks appearing in the UV-vis spectra during the degradation, suggesting that the dye is completely degraded and not only photobleached^[30].

The degradation results as the $(\ln C_0/C)$ vs. the irradiation time in which C_0 and C represent the initial and the current dye concentration measured during the first 14 min. of the runs are shown in figure 4.14a. All experimental results can be adjusted by a linear equation indicating that the process follows a pseudo-first order kinetic.

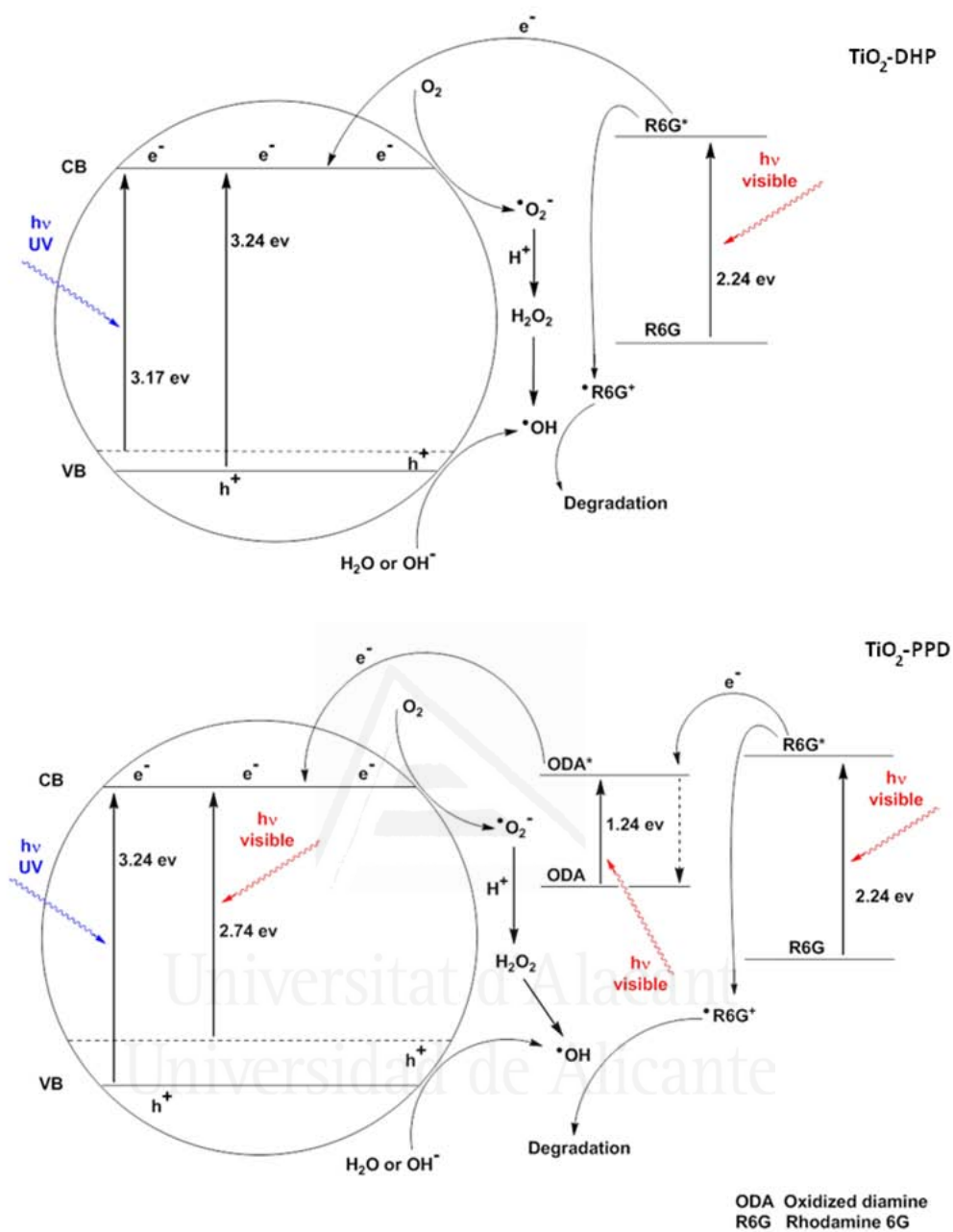


Figure 4.13. Representation of the proposed photocatalytic mechanism for the rhodamine 6G degradation reaction using $\text{TiO}_2\text{-DHP}$ and $\text{TiO}_2\text{-PPD}$ titania as photocatalysts.

UV radiation in semiconductors produces the formation of a hole-electron pair (*the hole way*). While holes are scavenged by hydroxyl groups (or H₂O molecules) present on the surface of the titania material (equation 12), electrons are transferred to the conduction band of the semiconductor and subsequently trapped by the absorbed O₂ (equation 6) leading, in both cases, to the formation of OH[•] radicals, which promotes the degradation of the organics (figure 4.13)^[33]. In this context, the good photocatalytic response of the organotitanias could be attributed both to the smaller domain size of particle (from 6.4 nm in TiO₂ to *ca.* 5.5 nm in both organotitanias), which may reduce the recombination rate of the charge carriers and the decrease in the band gap value. In the case of PPD ligand, strongly red-shifted into the visible range (453 nm), can be also ascribed with the HOMO-LUMO gap associated to the oxidized organic moieties.

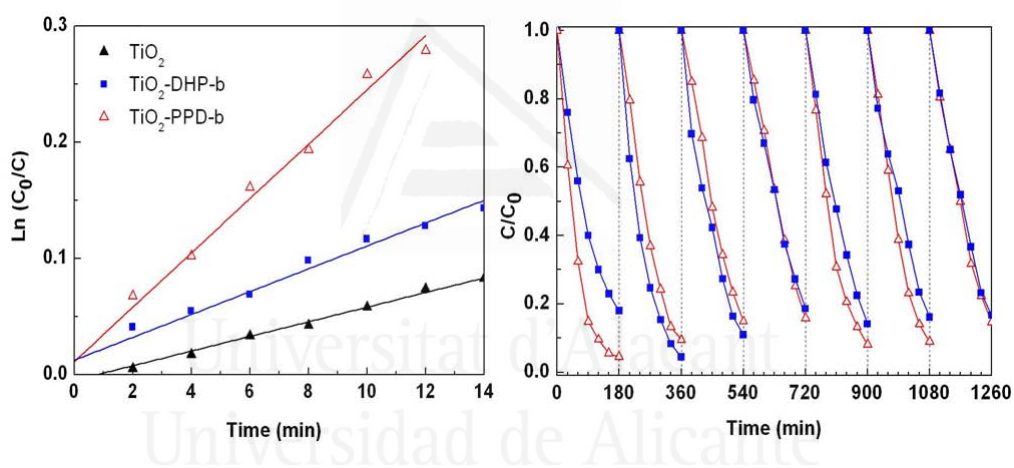


Figure 4.14. Representation of the pseudophotocatalytic constant (k') of the of the organotitania samples: $\text{TiO}_2\text{-DHP-b}$ and $\text{TiO}_2\text{-PPD-b}$ as compared with control titania, TiO_2 , in the degradation reaction of an aqueous solution of R6G ($5 \cdot 10^{-5}$ M) under UV radiation (left). Cycling tests under the same conditions (right).

Table 4.3. Constant values of the photocatalytic activity under UV radiation, regression coefficients and conversions at different times of the organotitania samples as compared with the control TiO₂.

Samples	E_g^a (eV)	$k' \cdot 10^3^b$ (min ⁻¹)	R^{*c}	%Conversion ^d			$k'/k'_{TiO_2}^e$
				1h	2h	3h	
TiO ₂	3.24	7.2 ± 1.9 (6.3)	0.990	31.1	52.8	67.7	---
TiO ₂ -DHP-b	3.17	12.3 ± 2.4 (9.8)	0.986	43.6	66.5	84.2	1.7
TiO ₂ -PPD-b	2.74	20.0 ± 3.4 (23.4)	0.987	75.7	94.0	98.5	2.8

^aBand gap energies calculated from the intercept of the tangent to the $(F(R')h\nu)^{1/2}$ versus $(h\nu)$ plot. ^b1st order reaction rate pseudophotocatalytic constant of the degradation of an aqueous solution of R6G ($5 \cdot 10^{-5}$ M) obtained as the average of a minimum of three runs. Values in brackets indicate the k value used for the determination of the degree of conversion. ^cRegression coefficient for the same degradation reaction as paragraph b). ^dDegree of conversion (%) achieved by samples after 1 h, 2 h and 3 h of reaction. ^eRatio between the average k' values of the as-synthesized organotitanias as compared with the average k' value determined for control TiO₂.

The TOC measurements carried out in the absence of UV radiation indicated that, after 30 min under stirring, the amount of R6G adsorbed on the TiO₂-DHP-b catalyst surface was negligible while rhodamine relative concentration diminished up to $C/C_0 = 0.81 \pm 0.06$ and 0.69 ± 0.04 for control titania and TiO₂-PHD-b, respectively. Thus the values used for the estimation of mineralization were those measured after 30 min of stirring in absence of light. After 3h of UV radiation, carbon concentration decreased by ca. 40% of the initial concentration when hybrid organotitanias are used as photocatalysts thus indicating a partial R6G degradation. No R6G is left in the reaction mixture but it seems that there is still some carbon species in solution such as aldehydes or carboxylic acids. This observation points out that the reaction time for the complete degradation of R6G is longer than for the bleaching of R6G.

The results of cycling tests of the photocatalytic activity of black and yellow organotitanias using the same conditions are shown in figure 4.14b. Once each cycle is completed, an amount of R6G is added to the solution to reach the initial concentration of $5 \cdot 10^{-5}$ M. Both hybrid titanias show >80% efficiency even after 7

cycles. So, these results confirm the incorporation of the organic compounds directly into the structure of the mesoporous titania materials, protecting them and preventing their loss during cycles of reuse. Moreover, the obtained results validate the novel methodology of incorporation of functionalities into the titania materials herein described because of the significant enhancement of the photocatalytic properties of these materials as compared with control titania.

4.3.3.2. Photocatalytic activity under visible light

To test the photocatalytic activity of the mesoporous organotitanias under visible light, a similar procedure with the degradation reaction of R6G was used (figure 4.16). For this purpose the same methodology used for the UV radiation experiment was followed. The difference was that a filter of 2 M NaNO_2 , which is able to remove the radiation with wavelength $< 400\text{nm}$ in the cooling water, was used to avoid the wavelengths under 400nm .

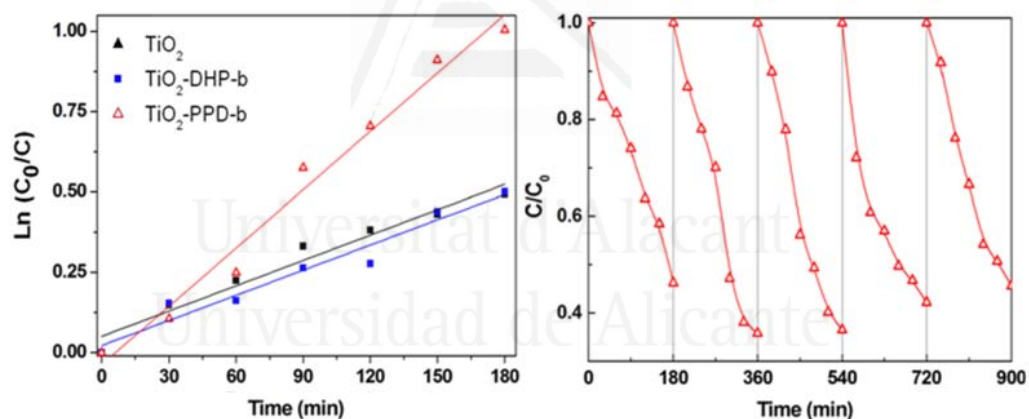


Figure 4.15. Representation of the pseudophotocatalytic constant (k') of $\text{TiO}_2\text{-DHP-b}$ and $\text{TiO}_2\text{-PPD-b}$ as compared with control titania, in the degradation reaction of an aqueous solution of R6G ($5 \cdot 10^{-5}$ M) under visible light (left). Cycling tests under the same conditions (right).

The blank reaction under visible light showed that the dye was scarcely degraded in the absence of a catalyst. While the yellow TiO_2 -DHP-b showed similar activities than the control titania, the black TiO_2 -PPD-b exhibits more than two-fold enhanced activity, obtaining decomposition rates of about 60% after 3 h of irradiation (see table 4.4 and figure 4.15).

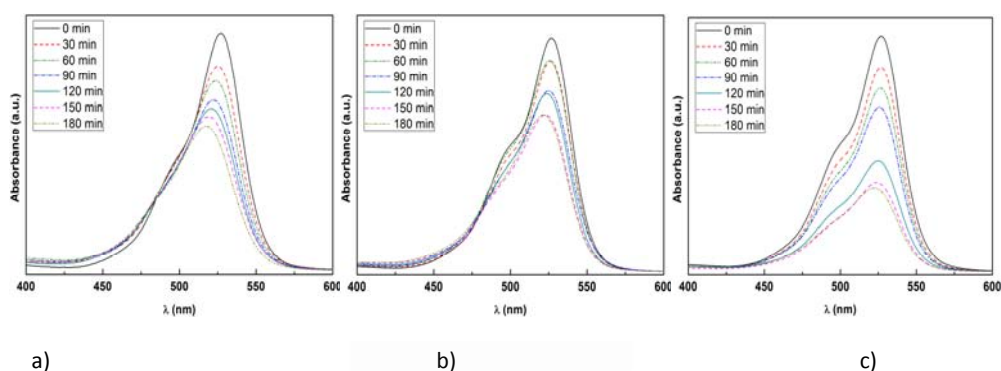


Figure 4.16. UV-vis absorption spectra of the degradation reaction of an aqueous solution of R6G ($5 \cdot 10^{-5}$ M) under visible light using as photocatalysts: TiO_2 (a), TiO_2 -DHP-b (b) and TiO_2 -PPD-b (c).

In figure 4.16, a blue-shift is observed in the absorbance peaks for both titania materials with organic compounds incorporated. The blue shift was observed only when the degradation was carried out under visible light and not when UV radiation was used. This suggests a selective stepwise deethylation process, which occurs before the degradation of the R6G. Chen et al.^[34] described that visible light-induced photocatalytic degradation of dye proceeds on the surface of catalysts rather than in the bulk solution and active oxygen species preferentially attack the molecular portion that connects directly to the surface of catalysts. This can be explained by taking into account that the R6G can inject an electron from its excited state into the semiconductor and itself become a positively charged radical, generating active

oxygen species which would lead to the degradation of the organics substrates, inducing the deethylation, promoting this process.

TiO₂-PPD showed the best photocatalytic performance under visible light. For that reason, only the cycling tests results of the sample TiO₂-PPD-b are shown (figure 4.15b). This sample shows 60% efficiency and did not decline even after being reused five times. These results confirm the incorporation of the organic compounds directly into the structure of the mesoporous titania materials and the stability of the materials after long working hours, exhibiting a negligible degradation during the photocatalytic oxidation of R6G. Moreover, this black titania manages to overcome the limitation of the efficiency range in the UV range of control titania, increasing its efficiency in the visible range and enabling a most effective use of solar light. There are very few black titania cases in the literature, hence the importance of the black titania synthesized by this methodology. This material becomes a promising material in applications such as certain environmental decomposition of NO_x. Currently the black material herein described is being tested to remove NO_x in a gas steam.

The different behaviour under UV radiation and visible light for the same degradation process is likely based on the difference in the active oxygen species generation mechanism^[32]. Under visible light, only R6G (or its deethylation products) can absorb the photons, then the rhodamine excited state molecule transfers the LUMO electron to the conduction band of TiO₂, where the conductive electron reacts with pre-adsorbed oxygen molecules to produce active oxygen species.

Under UV radiation, however, TiO₂ itself absorbs the photons and then it directly reacts with H₂O, O₂ and OH- groups to produce active oxygen species. In that case the adsorption of R6G is not very significant because the TiO₂ directly is able to produce active oxygen species^[32].

It should be noted that, in the case of the photodegradation of R6G under visible light using TiO₂ and TiO₂-DHP-b, the filtration of radiation with wavelength shorter than 400 nm precludes *the hole way*.

Nevertheless, due to its band gap of 2.24 eV (experimentally obtained and similar as described in the literature^[35]), the R6G molecules are excited by visible light, generating cationic *R6G⁺ (equation 1) radicals and electrons. As it has been previously noted, these electrons can be transferred to the CB of titania because of the R6G LUMO energy is higher than the titania CB in about 1.4 eV (*the dye way*), acting TiO₂ only as an electron mediator in the decomposition of the R6G, in accordance with their similar observed photocatalytic activity (figure 4.13)^[4b].

Table 4.4. Constant values of the photocatalytic activity under visible light, regression coefficients and conversions at different times of the organotitania samples as compared with control TiO₂.

Samples	E_g^a (eV)	$k' \cdot 10^3^b$ (min ⁻¹)	R^{*c}	%Conversion ^d			$k'/k'_{TiO_2}^e$
				1h	2h	3h	
TiO ₂	3.24	2.5 ± 0.7 (2.63)	0.9640	20.2	31.7	39.0	---
TiO ₂ -DHP-b	3.17	2.4 ± 0.7 (2.61)	0.9563	15.0	24.3	39.5	1.0
TiO ₂ -PPD-b	2.74	5.6 ± 1.2 (6.1)	0.9842	22.1	50.6	63.4	2.3

^aBand gap energies calculated from the intercept of the tangent to the $(F(R')h\nu)^{1/2}$ versus $(h\nu)$ plot. ^b1st order reaction rate pseudophotocatalytic constant of the degradation of an aqueous solution of R6G ($5 \cdot 10^{-5}$ M) obtained as the average of a minimum of three runs. Values in brackets indicate the k value used for the determination of the degree of conversion. ^cRegression coefficient for the same degradation reaction as paragraph b). ^dDegree of conversion (%) achieved by samples after 1 h, 2 h and 3 h of reaction. ^eRatio between the average k' values of the as-synthesized organotitanias as compared with the average k' value determined from the control TiO₂.

By contrast, the improved photoactivity under visible light of the black titania can be due to the synergistic combination of its reduced band gap and the redox properties of the aromatic oxidized dyes (OPPD) or even of the R6G (*the dye way*) (figure 4.13).

To gain a better understanding of the degree of contribution of each of these two mechanisms to the activity of the photocatalyst, the influence of some scavengers in the process was studied.

Additional experiments with typical scavengers were carried out to get deeper knowledge on this process. It was observed that while the addition of isopropanol ($i\text{PrOH}$), as a hydroxyl radical scavenger, only caused a slight decrease in the photodegradation rate. However, no significant catalytic degradation activity was found by the addition of triethanolamine (TEOA) as a hole scavenger (figure 4.17). These results seem to suggest that the dominant mechanism is *the hole way*, at least in the experimental conditions used^[4b].

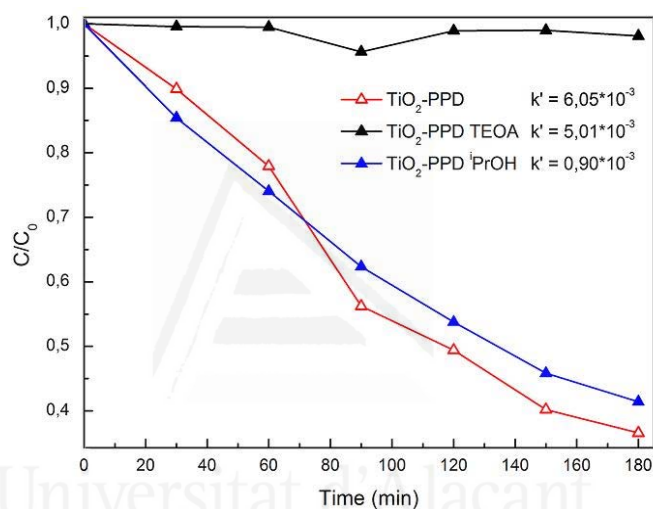


Figure 4.17. Variation of the concentration along the time in the photodegradation reaction of aqueous solutions of R6G ($5 \cdot 10^{-5}$ M) by $\text{TiO}_2\text{-PPD-b}$ in the absence or presence of different scavengers ($i\text{PrOH}$ or TEOA, $5 \cdot 10^{-2}$ M) under visible light.

4.4. CONCLUSIONS

A new synthetic approach to reduce the band gap of titania materials has been developed by using an environmentally-friendly one-pot synthesis method to

produce a novel organotitania materials with two organic compounds, 4,6-dihydropyrimidine and *p*-phenylenediamine, homogeneously incorporated into the anatase framework by complexing both ligands with the Ti(IV) atom during the condensation of the titania precursor, TBOT. Coloured mesoporous organotitanias were obtained without the concurrence of surfactants using mild conditions. Nevertheless, while these materials are pale-yellow solids for DHP, in the case of PPD this method yields black titanias, due to the partial oxidation of the diamine to mixtures of diimine fragments. The homogeneous incorporation of the organic moieties into the structure of titania has been confirmed using EA, TGA, FTIR and XPS analyses, with incorporation yields up to 86% thus indicating the effectiveness of this synthetic route. These hybrid materials show textural and structural properties similar to those of control TiO₂. However, it was shown that they have a smaller band gap and a lower maximum VB, which has a remarkable impact in its photocatalytic performance. By using *p*-phenylenediamine, a black titania has been obtained with a remarkable reduction of its band gap (from 3.24 to 2.74 eV), exhibiting outstanding photocatalytic activity under visible light.

The formation of these hybrid titanias, particularly, the black titania not only allows for the extension of the spectral response for these materials, but also for band gap engineering, providing a novel direction for the development of new photocatalysts active under visible light for environmental applications, able to maintain their effectiveness after several cycles of reuse.

This titania material is one of the few black titanias reported so far and it has been developed with well defined environmental applications in the treatment of NO_x and CO₂ and nowadays it is being implemented. Currently, further work is being performed to clarify the relationship between the structure of the organic moiety and the band gap of the final organotitania.

4.5. REFERENCES

- [1] a) J.H. Heo, S.H. Im, J.H. Noh, T.N. Mandal, C.S. Lim, J.A. Cahng, Y.H. Lee, H.J. Kim, A. Sarkar, M.K. Nazeeruddin, M. Grätzel, S.I. Seok, *Nature Photonics*, 2013, **7**, 486; b) B.E. Hardin, H.J. Snaith, M.D. McGehee, *Nature Photonics*, 2012, **6**, 162; c) W.Y. Teoh, J.A. Scott, R. Amal, *J. Phys. Chem. Lett.*, 2012, **3**, 629; d) P.V. Kamat, *J. Phys. Chem. C*, 2012, **116**, 11849.
- [2] a) X. Chen, C. Burda, *J. Am. Chem. Soc.*, 2008, **130**, 5018; b) X. Chen, S.S. Mao, *Chem. Rev.*, 2007, **107**, 2891; c) S.U.M. Khan, M. Al-Shahry, W.B. Ingler, *Science*, 2002, **297**, 2243.
- [3] a) R. Asahi, T. Morikawa, T. Ohwaki, K. Aoki, Y. Taga, *Science*, 2001, **293**, 269; b) W. Choi, A. Termin, M.R. Hoffmann, *J. Phys. Chem.*, 10094, **98**, 13669; c) M. Anpo, M. Takeuchi, *J. Catal.*, 2003, **216**, 505; d) F. Zuo, L. Wang, T. Wu, Z. Zhang, D. Borchardt, P. Feng, *J. Am. Chem. Soc.*, 2010, **132**, 11856.
- [4] a) Z. Wang, C. Yang, H. Yin, P. Chen, D. Wan, F. Xu, F. Huang, J. Lin, X. Xie, M. Jiang, *Energ. Environ. Sci.*, 2013, **6**, 3007; b) J. Yu, Q. Li, S. Liu, M. Jaroniec, *Chem. Eur. J.*, 2013, **19**, 2433; c) H. Zhang, Y. Zhao, S. Chen, B. Yu, J. Xu, H. Xu, L. Hao, Z. Liu, *J. Mater. Chem. A*, 2013, **1**, 6138; d) S. Majunder, D. Paramanik, V. Solanki, B. P. Bag, S. Varma, *Appl. Phys. Lett.*, 2011, **98**, 053105.
- [5] a) X. Chen, L. Liu, P. Y. Yu, S.S. Mao, *Science*, 2011, **331**, 746; b) X. Jiang, Y. Zhang, J. Jiang, Y. Rong, Y. Wang, Y. Wu, C. Pan, *J. Phys. Chem. C*, 2012, **116**, 22619.
- [6] W. Wang, Y.R.Ni, C.H. Lu, Z.Z. Xu, *RSC Adv.*, 2012, **2**, 8286; b) J.B. Lu, Y. Dai, H. Jin, B.B. Huang, *Phys. Chem. Chem. Phys.*, 2011, **13**, 18063.
- [7] Z. Zheng, B. Huang, X. Meng, J. Wang, S. Wang, Z. Lou, Z. Wang, X. Qin, X. Zhang, Y. Dai, *Chem. Commun.*, 2013, **49**, 868.
- [8] W. Zhou, H. Fu, *Chem. Cat. Chem.*, 2013, **5**, 885.

- [9] a) L.G. Devi, R. Kavitha, *App. Catal. B: Environm.*, 2013, **140**, 559; b) S. Afzal, W.A. Daoud, S.J. Langford, *ACS Appl. Mater. Interfaces*, 2013, **5**, 4753; c) A. Hagfeldt, M. Grätzel, *Acc. Chem. Res.*, 2000, **33**, 269.
- [10] U. Schubert, *J. Mater. Chem.*, 2005, **15**, 3701.
- [11] a) N. Linares, A.E. Sepúlveda, J.R. Berenguer, E. Lalinde, J. Garcia-Martinez, *Micro. Mesopor. Mat.*, 2012, **158**, 300; b) M. Rico, A.E. Sepúlveda, S. Ruiz, E. Serrano, J.R. Berenguer, E. Lalinde, J. Garcia-Martinez, *Chem. Commun.*, 2012, **48**, 8883.
- [12] a) R. Nafria, P. Ramírez de la Piscina, N. Horms, J.R. Morante, A. Cabot, U. Diaz, A. Corma, *J. Mater. Chem. A*, 2013, **1**, 14170; b) C. Maurer, B. Baumgartner, S. Pabisch, J. Akbarzadeh, H. Peterlik, U. Schubert, *Dalton Trans.*, 2014, **43**, 950.
- [13] M. Rico-Santacruz, A.E. Sepúlveda, E. Serrano, J.R. Berenguer, E. Lalinde, J. García-Martínez, Spanish Patent 201300536, 2013.
- [14] M.Rico, E.Serrano, A.E. Sepúlveda, J.R. Berenguer, E.Lalinde, J. Garcia-Martinez, *Organotitanias: a versatile approach for band gap reduction in titania based materials*, *J. Mater. Chem. C*, 2014 (Sent)
- [15] E. Pretsch, P. Bühlmann, C. Affolter, "Structure determination of organic compounds – Tables of spectra data", Edition 4th, Springer, Berlin, 2000.
- [16] a) D.C.L. Vasconcelos, V.C. Costa, E.H.M. Nunes, A.C.S. Sabioni, M. Gasparon, W.L. Vasconcelos, *Mat. Sci. Appl.*, 2011, **2**, 1375; b) R. Urlaub, U. Posset, R. Thull, *J. Non-Cryst. Sol.*, 2000, **265**, 276; c) F.N. Castellano, J.M. Stipkala, L.A. Friedman, G.J. Meyer, *Chem. Mater.*, 1994, **6**, 2123.
- [17] a) V. Etacherri, M.K. Seery, S.J. Hinder, S.C. Pillai, *Inorg. Chem.*, 2013, DOI: dx.doi.org/10.1021/ic3001653; b) C.D. Valentin, G. Pacchioni, A. Selloni, *Chem. Mater.* 2005, **17**, 6656; c) D. Valentin, E. Finazzi, G. Pacchioni, A. Selloni, S. Livraghic, M.C. Paganini, E. Giamello, *Chem. Phys.* 2007, **339**, 44; d) W. Mao, H. Ma, B. Wag, *J.*

Hazard. Mater. 2009, **167**, 707; e) R. Beranek, H. Kisch, *Photochem. Photobiol. Sci.*, 2008, **7**, 40.

[18] H. Irie, S. Washizuka, N. Yoshino, K. Hashimoto, **Chem. Commun.**, 2003, 1298.

[19] M. Senna, N. Myers, A. Aimable, V. Laporte, P. Bogen, *J. Mater. Res.*, 2013, **28**, 3.

[20] D. Zhao, C. Chen, W. Yang, H. Ji, W. Ma, L. Zang, J. Zhao, *J. Phys. Chem. C.*, 2008, **112**, 5993.

[21] J. Bu, J. Fang, F. Shi, Z. Jiang, W. Huang, *Chinese J. Chem. Phys.*, 2010, **23**, 1.

[22] Y. Wang, Z.H. Jiang, F. Yang *Mat. Sci. Eng. B*, 2006, **128**, 229.

[23] N.G. Moustakas, V. Likodimo, F. Katsaro, N. Boukos, D. Tsoutsou, A. Dimoulas, G.E. Romanos, D.D. Dyonysiou, P. Falaras, *Appl. Cat. B: Environ.*, 2013, **130-131**, 14.

[24] a) P. Kubelka, *J. Opt. Soc. Am.*, 1948, **38**, 448; b) D. Reyes-Coronado, G. Rodriguez-Gattorno, M.E. Espinosa-Pesqueira, C. Cab, R. Coss, G. Oskam, *Nanotechnology*, 2008, **19**, 14605; c) N. Serpone, D. Lawless, R. Khairutdinov, *J. Phys. Chem.*, 1995, **99**, 16646; d) L. Zhao, J. Yu, *J. Coll. Int. Sci.*, 2006, **304**, 84.

[25] R. Thapa, S. Maiti, T.H. Rana, U.N. Maiti, K.K. Chattopadhyay, *J. Mol. Catal. A: Chem.*, 2012, **363**, 223.

[26] T.J. Boyle, M.A. Rodriguez, T.M. Alam, *Dalton Trans.*, 2003, 4598.

[27] U. Schubert, *J. Mater. Chem.*, 2005, **15**, 3701.

[28] S. Jahn, H. Faber, R. Zazzeroni, U. Karst, *Rapid Commun. Mass. Spectrom.*, 2012, **26**, 1453.

[29] M. Dolinsky, C.H. Wilson, M.S. Wisneski, F.X. Demers, *J. Soc. Cosmetic Chem.*, 1968, **19**, 411.

[30] P. Wilhelm, D. Stephan, *J. Photochem. Photobiol. A: Chem.*, 2007, **185**, 19.

[31] T. Watanabe, T. Takizawa, K. Honda, *J. Phys. Chem.*, 1977, **81**, 1845.

[32] J.M. Wu, T.W. Zhang, *J. Photochem. Photobiol. A*, 2004, **162**, 171.

[33] T. Aarathi, G. Madras, *Ind. Eng. Chem. Res.*, 2007, **46**, 7.

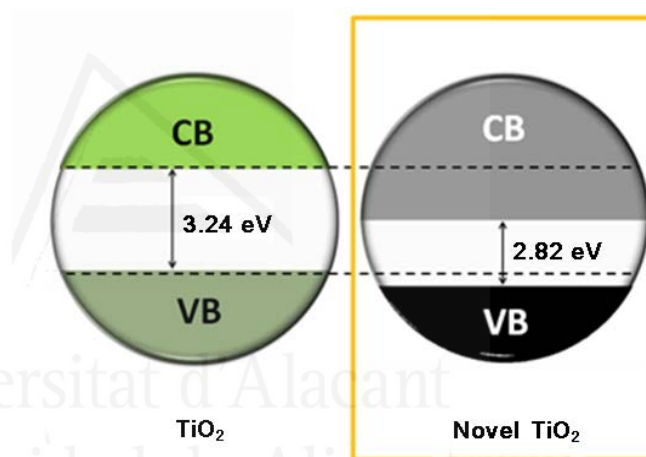
[34] F. Chen, J. Zhao, H. Hidaka, *Int. J. Photoen.*, 2003, **5**, 209.

[35] a) D.P. West, M.D. Rahn, C. Im, H. Bässler, *Chem. Phys. Lett.*, 2000, **326**, 407; b) L. Bahadur, P. Srivastava, *Solar En. Mat. & Solar Cells*, 2003, **79**, 235.



Universitat d'Alacant
Universidad de Alicante

V. Incorporation of a ruthenium complex in the framework of mesoporous titania materials



M. Rico, A.E. Sepúlveda, E. Serrano, J.R. Berenguer, E. Lalinde, J. Garcia-Martinez "Promising ruthenium modified titanias as solar cells" (in preparation).

M. Rico-Santacruz, A.E. Sepúlveda, E. Serrano, J.R. Berenguer, E. Lalinde, J. García-Martínez, *Spanish Patent 20130535*, 2013.

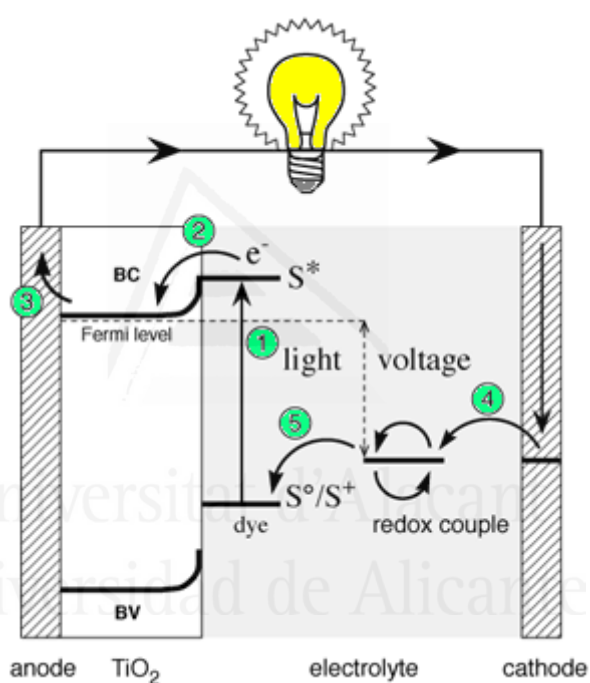
V. Incorporation of a Ru(II) complex in the framework of mesoporous titania

A novel titania material containing a Ru(II) complex in its structure, which acts as a dye (molecular antenna), has been synthesized by direct co-condensation of a titania precursor, tetrabutylortotitanate (TBOT) with the Ru(II) complex, in mild conditions and in the absence of surfactant. This novel synthetic strategy yields the homogeneous incorporation of the Ru(II) complex within the crystal structure of the titania which causes a significant reduction of its band gap. This novel material, which presents excellent textural, structural and optical properties, was tested in the degradation of rhodamine 6G (R6G) under UV radiation as well as visible light showing an excellent photocatalytic activity, higher than for dye sensitized titania obtained by traditional methods (*grafting*) and the control titania. The enhancement of its photocatalytic properties are likely due to a significantly decrease in the band gap of the material, a better overlap between the LUMO of the dye and the conduction band of TiO₂, and an improved use of the solar spectrum. This novel Ru(II) complex titania (TiO₂_IS) is a promising alternative to the traditional dye-sensitized solar cells.

5.1. INTRODUCTION

Dye-sensitized solar cells (DSSCs) have attracted significant attention due to the increasing demand of energy, high prices of fossil fuel and the environmental problems associated. DSSCs that used nanocrystalline titanium dioxide as a semiconductor are nowadays promising photovoltaic devices, with high conversion efficiencies, high quality materials and low cost making compared to silicon-based solar cells.

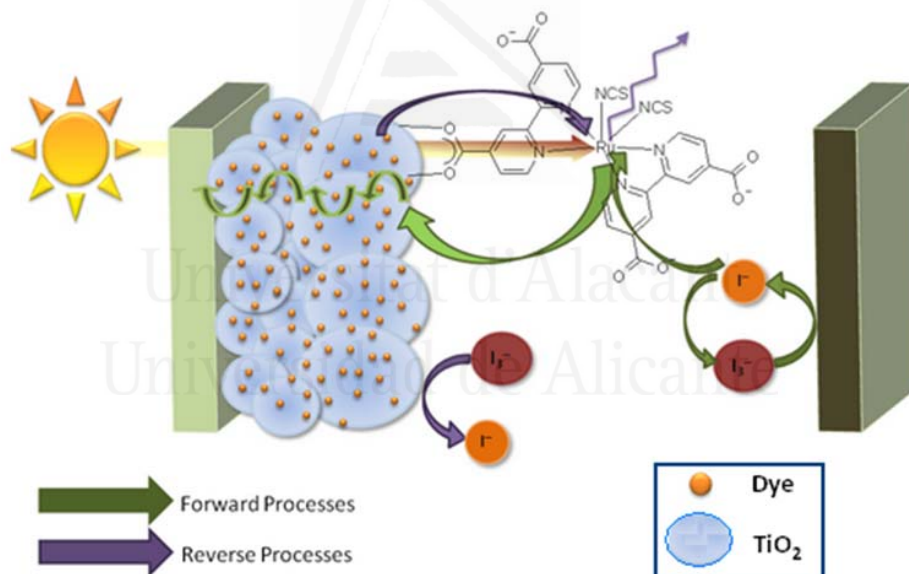
A solar cell device (scheme 5.1) consists of a semiconductor (typically TiO_2) with a dye monolayer on its surface and connected to other electrode via a liquid electrolyte or a solid hole conducting material.



Scheme 5.1. Energetic schema of a dye-sensitized solar cell where S^0 is the initial state, S^* the excited state and the S^+ the oxidized state of the dye (adapted from ref.1)

The dye absorbs visible light exciting an electron from the Highest Occupied Molecular Orbital (HOMO) into the Lowest Unoccupied Molecular Orbital (LUMO). The excited electron is then injected into the conduction band (CB) of the titania, travelling to a conducting glass electrode. A rapid regeneration of the dye by the electrolyte prevents back transfer of the electron or degradation of the dye. Finally, the electron reaches the counter electrode where it regenerates the redox couple and the process can start again^[2-4].

The polypyridyl-type complexes of Ru(II) are the most efficient charge transfer sensitizers employed, due to their high ability to inject electrons generated from the visible light^[5-9]. Particularly, dye N3 (*cis*-bis(isothiocyanato) bis(2,2'-bipyridyl-4,4'-dicarboxylato ruthenium(II) complex) synthesized and incorporated in a photochemical cell by Grätzel et al. (scheme 5.2), with a 10% solar-to-electric conversion yield^[5-10] and its analog N179 (double protonated) with 11.1%^[11], are still the most common dyes used nowadays as sensitizers in DSSCs devices^[9].



Scheme 5.2. Schematic diagram of the Grätzel solar cell (adapted from ref.12)

Later on, Grätzel and co-workers synthesized and tested more than 800 different dyes but no one has reached the good results obtained with the dye N3^[6]. Less research work has been conducted on the application of dye sensitization in photocatalytic oxidation processes. TiO₂ is inactive for the degradation of common pollutants under visible light due to its wide band gap (3.2 eV), limiting its application only under UV radiation. Extension of the photocatalytic properties of TiO₂ by photosensitization via surface adsorbed organic dyes and coordination metal complexes has received increasing research attention^[13,14].

The strategies used to extend the working range of titania materials to the visible light region (45% energy from solar light) so far have been based on the incorporation of ruthenium (metal) into the titania material^[15] or by sensitization using ruthenium complexes capable of injecting electrons into the conduction band of the titania. Until now several studies devoted to the titania modification with different ruthenium complexes have been carried out. The addition is traditionally achieved by impregnation and/or immersion of TiO₂ in a solution with the ruthenium complex to be incorporated^[16-21] or by covalent bonding between the carboxylic groups of the metal complex with the TiO₂ surface^[22].

However these incorporation techniques present several drawbacks in the final material in terms of inhomogeneity and poor distribution of the dye into the titania surface. All of them in addition to those associated with the titania materials.

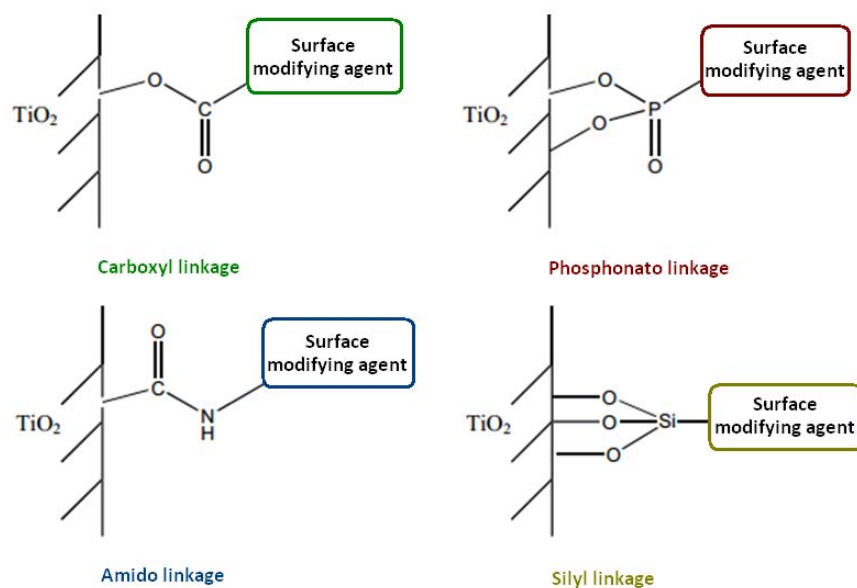
Dye N3 can be synthesized with different ligands such as –NSC and Cl⁻, among others. The dye with –NSC groups shows the best optical properties associated directly with the contribution of the isothiocyanato group on the redox properties, light absorption and an increase of the charge injection efficiency^[6].

However, besides the excellent results obtained using the dye N3, its long term stability after several cycles has raised concern due to a possible desorption of the dye from the TiO₂ layer^[23].

As previously reported, the photocatalytic properties of the hybrid materials are superior to the control titania, which are likely to be due to the reduction of the band gap energy of the TiO₂ (improving absorption in the visible region) and avoiding the electron-hole recombination due to the modification of the titania material^[24]. Mahmoud and co-workers obtained an enhancement of the photocatalytic activity of Ru-TiO₂ samples with a Ru loading ranging from 0.2w% to 0.8w%, prepared by the impregnation method, for the degradation of 2-chlorophenol, reaching a degradation of 53% under visible light as a consequence of an increment of the formation of electron capture traps^[24]. Chan et. al. tested the efficiency of dyes N3 and N179 in the removal of volatile organic compounds (VOCs) from indoor pollution sources under a low intensity ultraviolet LED, obtaining a 95% degradation of toluene after 2 h for both dyes^[18b].

Despite the attractive possibilities of the photosensitization and its ability to improve degradation reactions in the visible range, reports on successful photocatalytic titania systems with high photocatalytic activities are scarce and remains practically unexplored. It may be due, among other limitations, to the difficulty of establishing a stable anchorage of the charge-transfer photosensitizer with the titania material^[25]. Numerous ways of anchoring dyes onto the TiO₂ surface such as covalent attachment, electrostatic interaction, hydrogen bonding and hydrophobic interactions have been studied in the last years^[26], being the covalent attachment the most widely approach adopted^[25].

Carboxyl, phosphonato, amido and silyl functionalities (scheme 5.3) have been demonstrated to bond with TiO₂ with high efficiencies^[25].



Scheme 5.3. Schematic diagram of the most common covalent anchoring groups for surface modification of TiO_2 photocatalyst (adapted from ref.25).

Therefore, the development of an optimal efficient visible light system, based on TiO_2 , with a better and more stable anchorage of the charge-transfer dyes with the titania material is needed. Herein an environmental friendly method is described to incorporate ruthenium complexes, directly into the framework of mesoporous titania (bulk) and not only on its surface. This methodology avoids the disadvantages previously mentioned, maintaining the textural properties of unmodified titania while drastically improving their photocatalytic applications. The synthesized materials were evaluated as photocatalysts in liquid-solid regime for the degradation of the commercial R6G dye under UV radiation and visible light obtaining an important improvement in their photocatalytic activity as compared with the control TiO_2 and the $\text{TiO}_2\text{-G}$, synthesized for comparison purposes.

5.2. EXPERIMENTAL SECTION

5.2.1. Synthesis of *cis*-bis(isothiocyanato) bis(2,2'-bipyridyl-4,4'-dicarboxylato) ruthenium(II) complex

The synthesis and characterization of the complex *cis*-bis(isothiocyanato) bis(2,2'-bipyridyl-4,4'-dicarboxylato) ruthenium(II) (figure 5.1), similar to the commercial dye N3, was performed by Dr. Angel E. Sepúlveda San Pedro and Dr. Jesús R. Berenguer Marín, from the "Organometallic Molecular Materials" group of the University of La Rioja (Spain). The Ru(II) complex was synthesized following the procedure described previously in the literature^[27].

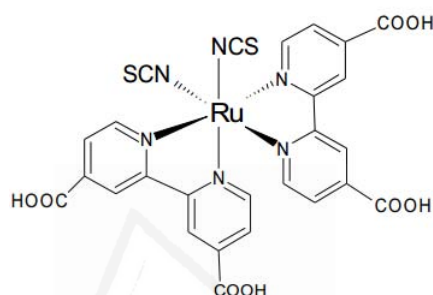
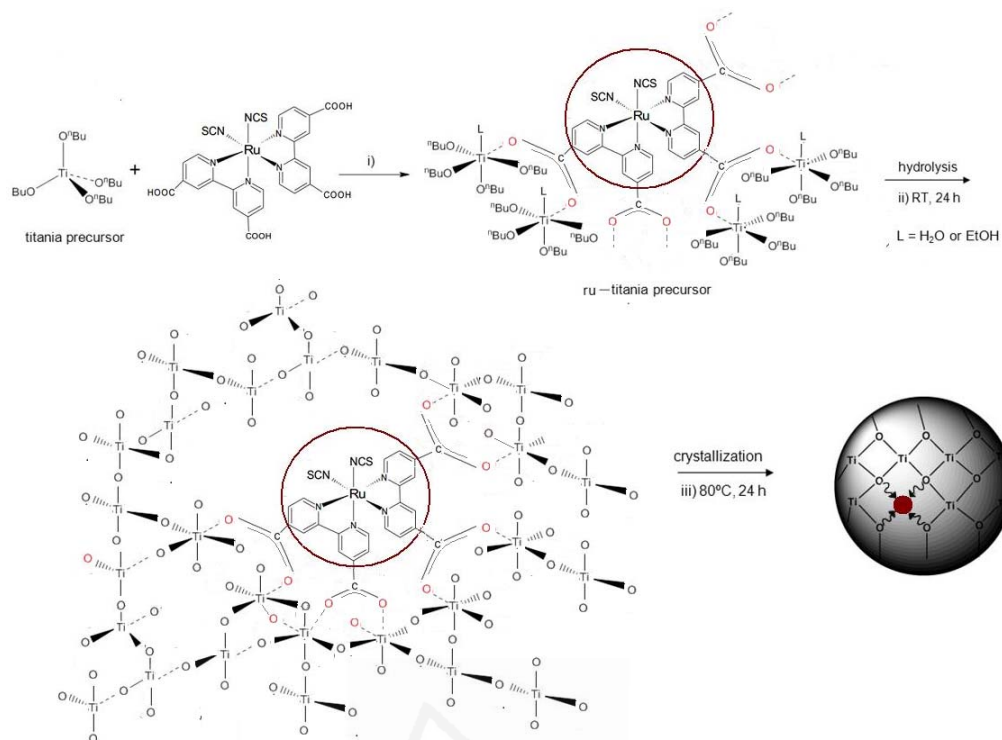


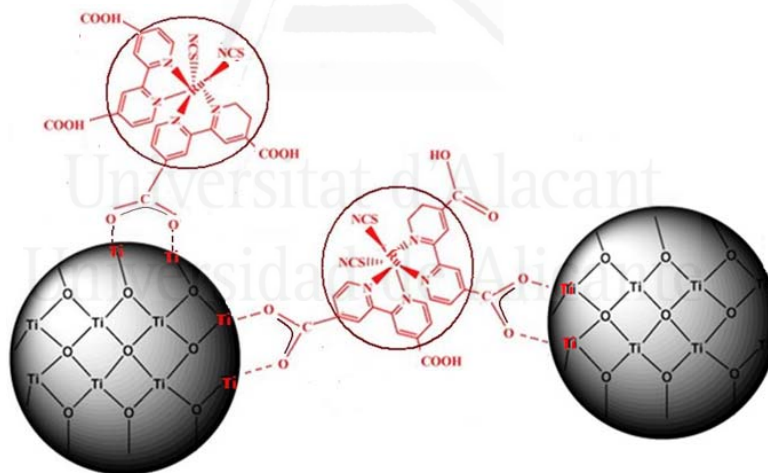
Figure 5.1. Chemical structure of the Ru(II) complex *cis*-bis(isothiocyanato) bis(2,2'-bipyridyl-4,4'-dicarboxylato) ruthenium (II).

5.2.2. Synthesis of the mesoporous Ru (II) complex titanias

Samples were synthesized following our procedure developed for the synthesis of mesoporous titania, already described in Chapter 3. The details are proprietary^[28].



Scheme 5.4. Synthesis methodology to incorporate the Ru(II) complex by the *in-situ* methodology ($\text{TiO}_2\text{-IS}$)^[28].



Scheme 5.5. Ru(II) complex covalently bonded to the titania surface by *grafting*($\text{TiO}_2\text{-G}$).

Titania samples with the Ru(II) complex incorporated in their structure were synthesized by two different methods. The sample denoted as TiO₂_IS was prepared by an *in-situ* sol-gel method (scheme 5.4) which gets the incorporation of the Ru(II) complex directly into the framework of the titania through the formation of a coordination bond between the carboxylic acids present in the complex during the hydrolysis of the titania precursor. TiO₂_G was synthesized by *grafting* (scheme 5.5) for comparative purposes. In this case, the Ru(II) complex was covalently bonded to the titania surface. For the synthesis of TiO₂_G, 1.17 g of TiO₂ (14.65 mmol) were added to a solution of 40 mg of Ru (II) complex (0.05 mmol) in 35 ml of MeOH. The mixture was stirred for 30 minutes. After this, the mixture was heated to reflux overnight. The obtained purple solid was filtered off, washed with EtOH and acetone, and dried, following a similar procedure with TiO₂_IS and control TiO₂.

TiO₂_IS was prepared by co-condensation of tetrabutylorthotitanate (TBOT) with the Ru(II) complex ($5 \cdot 10^{-5}$ mol/mol TBOT) by using only water and ethanol as solvents and without the need of surfactants. The Ru(II) complex needed to be previously dissolved in an ethanol solution overnight under magnetic stirring. The molar ratio of the synthesis gel was 1TBOT: $5 \cdot 10^{-5}$ Ru(II) complex: 41.3 EtOH: 467 H₂O.

5.2.3. Physico-chemical characterization methods

The incorporation the Ru(II) complex in the titania samples (TiO₂_IS and TiO₂_G) was evaluated by FTIR and XPS spectroscopies and the incorporation yield of the Ru(II) complex in the final titania materials was analyzed by ICP-OES.

XRD analysis was carried out in order to study the crystalline structure of the titania materials and TEM was used to study the morphology and crystallinity of the samples. Furthermore, it was possible to calculate the particle size by TEM using the Gatan software package, being estimated as an average of the size of 100 particles.

Porous texture parameters (mesoporosity volume, surface area and pore diameter) were characterized by N₂ adsorption/desorption isotherms at 77 K and the results were interpreted using the software AUTOSORB.

DRUV spectra were carried out in order to determine the band gap of the titania materials following the methodology described in Chapter 3. XPS in the region from -10 to 2 eV was used to calculate the position of the maximum of the valence band of the titanias. Both techniques were combined to determine the position of the conduction band of the titania materials and to draw the density of states (DOS) scheme.

All the equipment and test conditions used are described with more detail in Chapter 3.

5.2.4. Photocatalytic activity: liquid-solid regime

The photocatalytic activity of the titania materials was evaluated in liquid-solid regime reaction. The reaction followed was the degradation of R6G under UV radiation and visible light, as in Chapter 4 (more details about conditions and equipment used are described in Chapter 3). Moreover, total organic carbon measurements were carried out in order to determine the TOC content before and after the dye solutions bleaching.

For photocatalytic activity under visible light, a 2M NaNO₂ cooling solution was used as a filter to exclude UV radiation (under 400 nm). The study of the photocatalytic activity of the synthesized titanias under visible light was performed during a pre-doctoral stay in the "Organometallic Molecular Materials" group at the University of La Rioja (Spain) under the supervision of Dr. Jesús R. Berenguer Marín.

5.3. RESULTS AND DISCUSSION

5.3.1. Structural characterization of the Ru(II) complex

The characterization of the Ru(II) complex was carried out at the University of La Rioja. The UV-vis absorption spectrum (figure 5.2) of the Ru(II) complex in ethanol shows the typical bands associated with that type of compounds, two main bands at 539 and 408 nm that are assigned with to metal-to-ligand charge transfer (MLCT) and other band at 322 nm, which can be associated with intraligand (π - π^*) charge-transfer transitions^[27].

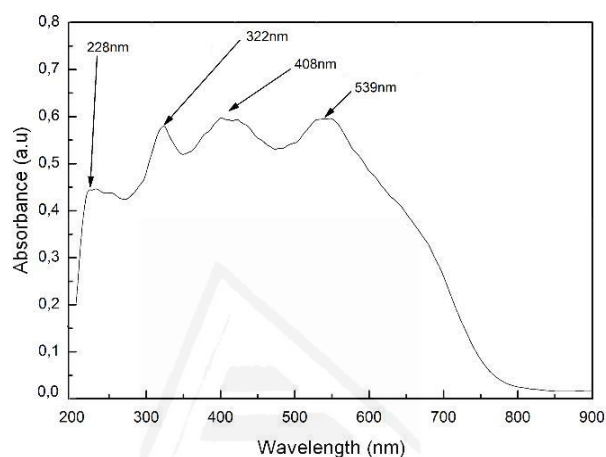


Figure 5.2. Absorption spectra of the Ru(II) complex *cis*-Bis(isothiocyanato) bis(2,2'-bipyridyl-4,4'-dicarboxylato ruthenium(II)).

¹H NMR spectrum shows six peaks in the aromatic region due to two different "dcbpy" (dcbpy = 4,4'-dicarboxy-2,2'-bipyridine) ring protons, in which two pyridine rings are in *trans* position to the NCS ligands and the remaining two are in *trans* position to each other (figure 5.3). The downfield-shifted proton resonances can be assigned to pyridine rings *trans* to each other and the high-field proton resonances to pyridine rings *trans* to the NCS ligand^[27,29].

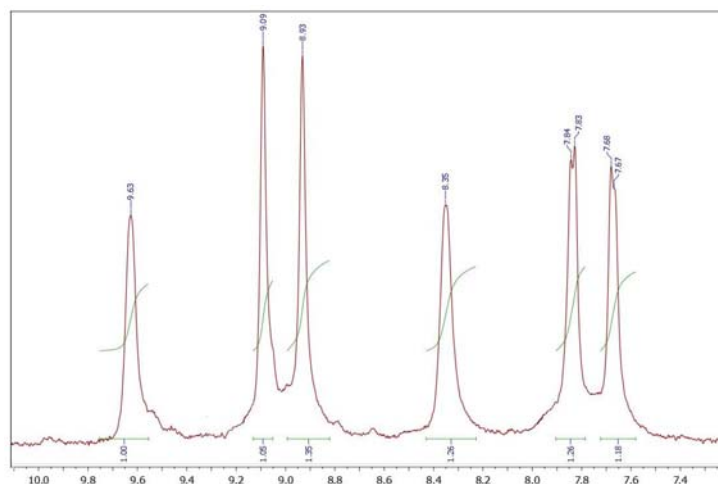


Figure 5.3. ^1H RMN spectra of the Ru(II) complex *cis*-Bis(isothiocyanato) bis(2,2'-bipyridyl-4,4'-dicarboxylato) ruthenium(II).

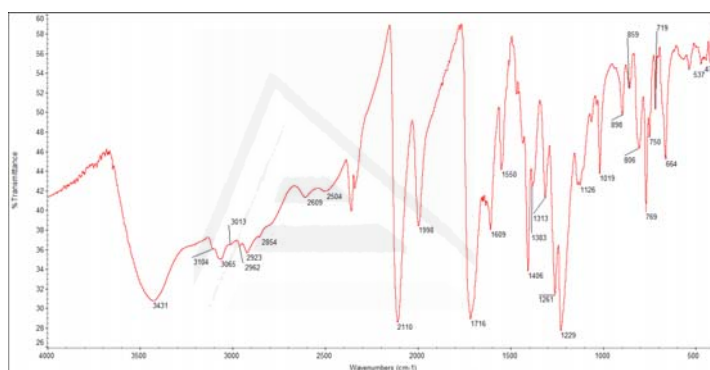


Figure 5.4. FTIR spectra of the synthesized Ru(II) complex *cis*-Bis(isothiocyanato) bis(2,2'-bipyridyl-4,4'-dicarboxylato) ruthenium(II).

The FTIR spectra of the Ru(II) complex is shown in figure 5.4. A broad band can be observed at 3431 cm^{-1} , characteristic of associated hydroxyl groups. C-H stretching vibrations of the heteroaromatic pyridines^[27,30] appear at 3104 , 2962 , 2923 and 2854 cm^{-1} , the intense absorption band at 2110 cm^{-1} is attributed to the SCN stretch mode

of N-bonded SCN ligand^[27, 31] and the band at 1716 cm⁻¹ to the carbonyl group of the ligand^[27].

According with the obtained results, it can be confirmed that the Ru(II) complex synthesized is the complex cis-bis(isothiocyanato)bis(2,2'-bipyridyl-4,4'-dicarboxylato ruthenium(II)), as shown in figure 5.1, which is similar to the commercial Ru(II) complex dye N3^[32].

5.3.2. Structural and physico-chemical characterization of the Ru (II) titania materials

The homogeneous incorporation of the Ru(II) complex into TiO₂ (TiO₂_IS and TiO₂_G materials) has been confirmed using ICP, FTIR and XPS.

Table 5.1. Textural and structural parameters of the mesoporous titania materials with the Ru (II) complex, as compared to the control titania.

Sample	d_p^a (nm)	V_p^b (cm ³ /g)	A_{BET}^c (m ² /g)	Metal ^d (w%)	$D^{XRD, e}$ (nm)	$\Phi^{TEM, f}$ (nm)	$d_{101}^{XRD, g}$ (nm)	$d_{101}^{TEM, h}$ (nm)
TiO ₂	5.6 (2-9)	0.29	245	---	6.4	8.7	0.35	0.37
TiO ₂ _IS	6.0 (3-11)	0.31	200	0.49 (0.53)	6.4	7.2	0.35	0.38
TiO ₂ _G	6.0 (3-11)	0.35	240	0.32 (0.53)	6.1	7.3	0.35	0.38

^aAverage mesopore diameters were estimated from the adsorption branch of the nitrogen isotherm using the BJH method. ^bMesopore volume from the isotherms at relative pressure of 0.95 (see Chapter 3). ^cThe BET surface area was estimated by multipoint BET method using the adsorption data in the relative pressure (P/P_0) range of 0.05–0.30. ^dCalculated by ICP-OES analysis (see Chapter 3). Values in brackets represent the theoretical values. ^eDomain size of the particle calculated from XRD using Scherrer equation. ^fParticle size from an average of 100 particles calculated from TEM using Gatan software (see Chapter 3). ^gAnatase spacing (d_{101}) calculated using Bragg equation. ^hAnatase spacing (d_{101}) calculated from TEM from an average of 10 particles using Gatan software (see Chapter 3).

The amount of the Ru(II) complex in the TiO₂_IS material, determined by ICP-OES (see table 5.1), is ca. 92%, higher than the observed for the *grafting* material TiO₂_G, indicating the effectiveness of the synthetic method herein described.

The FTIR spectra of the samples are shown in figure 5.5. Also the FTIR spectra of the Ru(II) complex and the control TiO₂ sample, synthesized in the same conditions, are shown for comparison purposes. As it was expected, FTIR spectra of both hybrid titania materials (TiO₂_IS and TiO₂_G), show the characteristic bands of the Ru(II) complex.

The bands below 750 cm⁻¹, correspond to the Ti-O bonds in titania materials. The Ti-O-Ti asymmetric stretching mode appears at 615 and 474 cm⁻¹. A broad band at 3400 cm⁻¹ is characteristic of associated hydroxyl groups from water and overlaps with the C-H stretching vibrations of the heteroaromatic pyridines expected about 3100 cm⁻¹^[30]. Vibrations associated with carboxylate groups coordinated as a bidentate bridging to the surface (1366 cm⁻¹ for symmetric ($\nu_s(-COO)$) and 1539 cm⁻¹ for asymmetric ($\nu_{as}(-COO)$) can be observed in both hybrid materials^[33].

The band around 2100 cm⁻¹ corresponds to the thiocyanate anions^[30]. For monodentate groups, the $\nu(OC=O)$ should be close to 1670 cm⁻¹ but overlaps in both titania materials with the peak at 1618 cm⁻¹ associated with the binding vibration of H-O bond from terminal groups in TiO₂^[34]. However, it can be observed that the band at this wavelength, for both hybrid materials, is wider than for the control TiO₂, suggesting the existence of the $\nu(OC=O)$ and an ester-type linkage in the TiO₂.

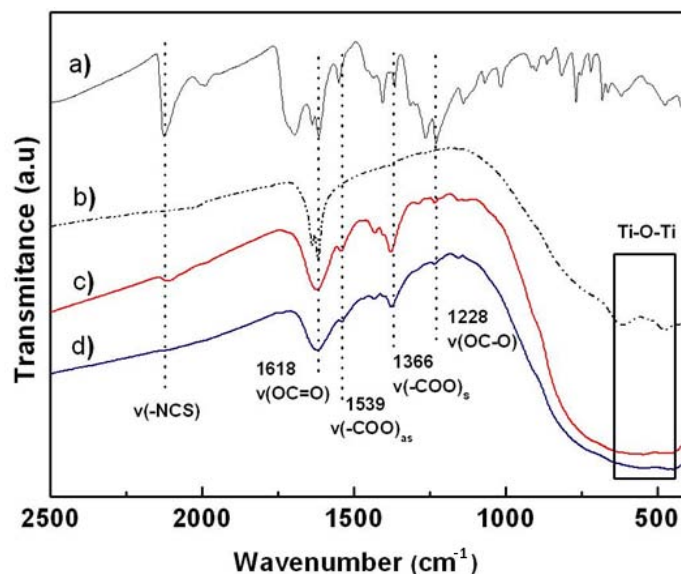


Figure 5.5. FTIR spectra of the ruthenium titania materials: TiO₂_IS (c), TiO₂_G (d) as compared with the FTIR spectra of the Ru(II) complex (a) and control TiO₂ (b).

Weak peaks at 1228 cm⁻¹ can be observed in both hybrid materials. They are associated with $\nu(\text{OC-O})$ stretching vibrations due to the presence of monodentate and free carboxylic groups.

Surface characterization of the samples was evaluated by XPS measurements. XPS spectra of hybrid titania samples and the control TiO₂ are shown in figure 5.6. Spectra in the Ti2p region of the TiO₂ control shows two signals at around 458 eV and 464 eV (figure 5.6, left), typical of Ti(IV) 2p_{3/2} and Ti(IV) 2p_{1/2} states respectively, where Ti is in an octahedral coordination^[35].

Samples TiO₂_IS and TiO₂_G do not show any shift or shape changes in Ti 2p peaks, which confirms that the incorporation of the Ru(II) complex in the hybrid titania materials does not affect neither the anatase structure of the titania nor the Ti coordination.

The O1s XPS spectra (figure 5.6, right) of all samples were deconvoluted using symmetric Gaussian curves. For control TiO₂ the characteristic main peak at 529,7 eV is attributed to the oxygen in the metal oxide (Ti-O-Ti bonds)^[37] while the additional one at 531.6 eV is related to the oxygen in a surface hydroxyl (Ti-OH species) and carboxylic groups^[37-39]. Hybrid materials present their O 1s peaks at similar binding energies.

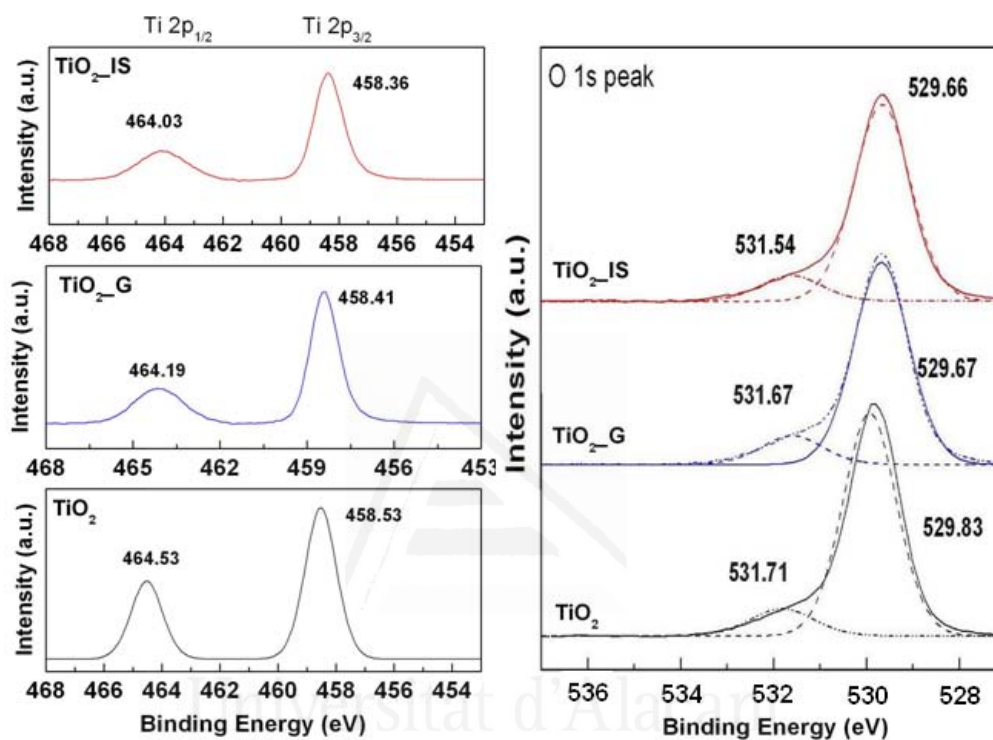


Figure 5.6. XPS spectra in the Ti2p (left) and O1s (right) regions of TiO₂-IS and TiO₂-G samples as compared with control TiO₂.

The presence of ruthenium on the spectrum cannot be clearly observed due to the small amount incorporated (4 wt%). This can be explained by considering that the

typical peaks of Ru 3p are hidden under the Ti 2p peaks and similarly Ru 3d_{3/2} peak, at 287.8 eV, is hidden under one of the C1s peaks^[35,38,40].

Regarding the textural properties of synthesized titanias, all the materials show Type IV isotherms with a similar shape, indicative of the mesoporous nature of these samples. The textural properties for the materials with the Ru(II) complex were similar to the control titania, showing high surface areas and similar pore diameter (ca 6 nm) in all cases, thus proving the effectiveness of the synthetic route herein proposed and the accessibility of reactive sites of these materials for photocatalytic applications (table 5.1).

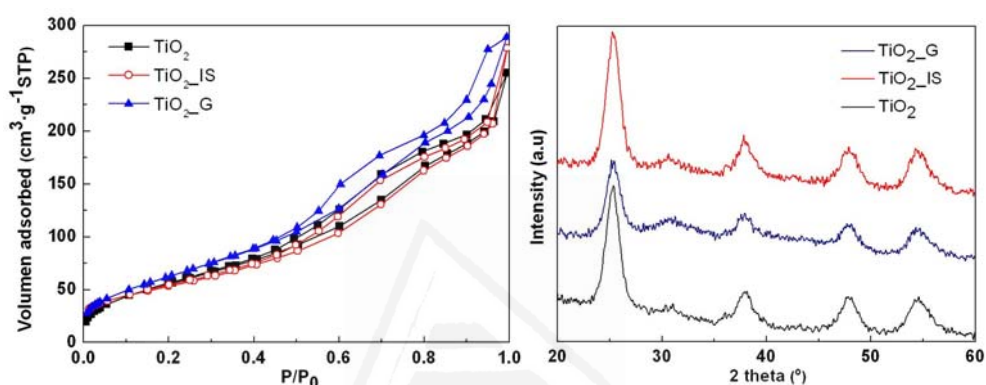


Figure 5.7. Representative nitrogen adsorption isotherms (left) and XRD patterns (right) for the materials with the Ru(II) complex, TiO₂-IS and TiO₂-G as compared to the control mesoporous titania TiO₂.

The XRD spectra of all titania materials (figure 5.7, right) are characteristic of the anatase phase ($2\theta = 25.3^\circ$, 37.8° and 48.05°), consistent with the photocatalytic results obtained. The broad XRD peaks indicate that the titania materials synthesized are nanoparticles, with a crystalline domain size around 6 nm range, determined by the Scherrer equation (table 5.1).

The crystalline domain size determined by XRD for the hybrid materials is also similar to the obtained for the control TiO_2 thus the incorporation of the Ru(II) complex does not affect the crystallinity of the TiO_2 (table 5.1). Unlike Chapter 4, the similar value in the crystalline domain of the Ru(II) complex titanias as compared with control titania material can be associated with the small amount of Ru(II) complex incorporated (0.5 wt% metal basis).

Likewise, the d_{101} spacing does not present variations, showing similar values for the titania materials with the Ru(II) complex incorporated as compared with control TiO_2 (table 6.1).

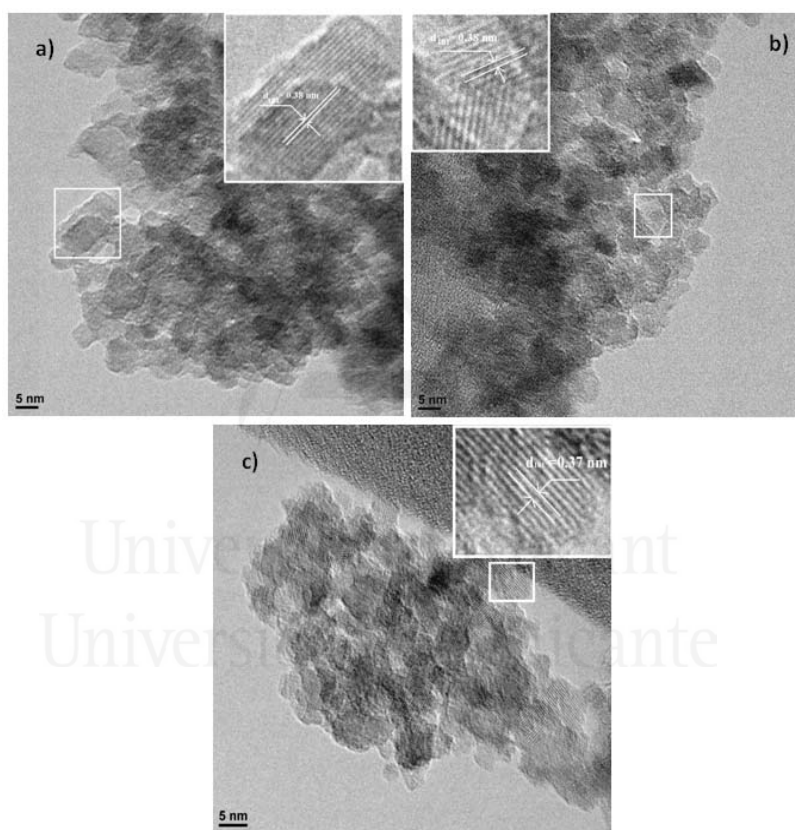


Figure 5.8. Representative TEM images of the materials with the Ru(II) complex: $\text{TiO}_2\text{-IS}$ (a) and $\text{TiO}_2\text{-G}$ (b) as compared with control TiO_2 (c).

TEM analysis of hybrid titanias (TiO₂_IS and TiO₂_G) shows the crystalline lattice of these materials and their typical interparticle mesoporosity (figure 5.8). The distance between the (101) crystal planes of the anatase phase are in agreement with the values obtained by using the Gatan software package (table 5.1). The similar crystalline domain size value determined by XRD and the particle size by TEM in all the samples confirms that there is no significant agglomeration of titania nanoparticles and that all materials, despite their small size have a high degree of crystallinity.

5.3.3. Optical properties

The optical properties of all the titania samples were studied by XPS and DRUV measurements, as it was described in the previous chapter. The band gaps can be calculated by extrapolation of the base line and the absorption band edge in the UV-vis spectra (figure 5.9a). The position of the valence bands (VB), measured by XPS, are shown in figure 5.9b and the density of states (DOS) in figure 5.9c. Band gap of the control TiO₂ has been estimated to be 3.24 eV, in good agreement with bulk anatase TiO₂^[41] as well as the edge of the maximum energy at about 2.28 eV, is similar than for other titania samples^[39a].

TiO₂_IS band gap decreases significantly up to 2.82 eV and also the valence band maximum energy (0.24 eV, figure 5.9c) which means that the minimum of the CB is 0.42 eV lower than the control titania. However, the incorporation of the Ru(II) complex by *grafting* (TiO₂_G) does not significantly alter the band gap of the titania sample, which decreases up to 3 eV. In a similar way, the valence band maximum energy lightly slightly red-shifts toward the vacuum level at approximately 0.16 eV which implies than the conduction band minimum should occur at c.a. -0.52 eV. In

both hybrid titania materials, two absorption band edges can be observed (figure 5.9a), one associated with the Ru(II) complex and the other with the titania material.

Specifically, the low energy feature covering the visible range has been assigned to a metal-ligand charge transfer (MLCT) transition from the d orbitals (Ru(II)) to π^* orbitals localized at a bipyridine ligand, whereas the higher energy one is associated with the indirect band gap transition^[42].

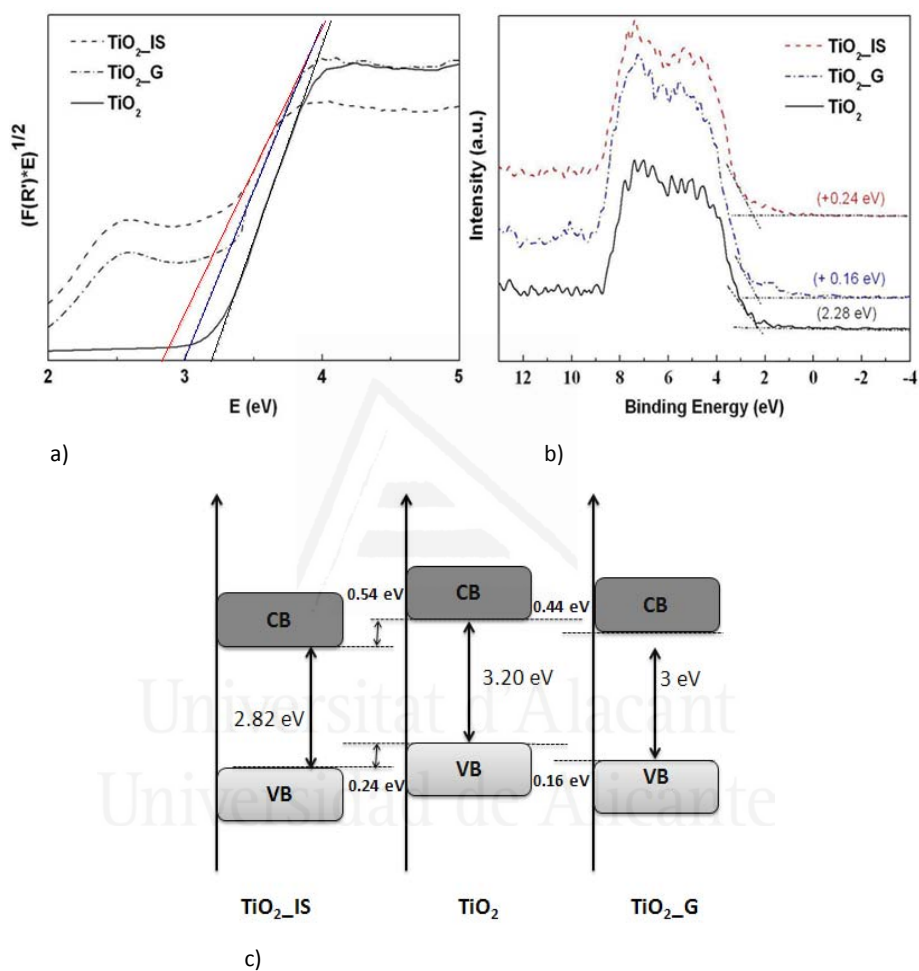


Figure 5.9. Plot of the transformed Kubelka-Munk function versus the energy of light adsorbed (a), valence band XPS spectra (b) and schematic illustration of the DOS (c) of the Ru(II) complex titania materials as compared with the control TiO_2 .

The photoexcitation of the dye generates the oxidation of Ru(II) to Ru(III) and the formation of a bipyridine radical anion. The carboxylate groups of the bipyridine ligands in the TiO₂_IS sample, homogeneously bonded in all the TiO₂ structure, can lead to a better overlap between the accepting metal d orbitals of the TiO₂ and the N3 carboxylate π^* orbitals. This fact may facilitate a rapid electron transfer from the bipyridine radical anion^[42] to the CB of the titania material, which could be associated with a higher photocatalytic activity, as it can be confirmed experimentally.

A reduction of the band gap in the TiO₂_IS material can be clearly observed, corroborating the incorporation of the Ru(II) complex directly into the framework of the titania and a good interaction (better than for TiO₂_G) between the LUMO of the dye incorporated and the CB of the titania, favoring the rapid transfer of the electron to the CB of the titania and a low rate of recombination of electron-hole pair.

5.3.4. Liquid-solid regime: photocatalytic activity of the Ru(II) titania materials

To test the photocatalytic activity of the titania materials containing the Ru(II) complex, a R6G aqueous solution ($5 \cdot 10^{-5}$ M, 100 ml) was degraded by the catalysts (0.15 g/L) under two different types of irradiation: UV radiation and visible light (for more details see Chapter 3).

As stated in Chapter 4, blank reaction showed that the R6G scarcely degraded in the absence of catalyst under the test conditions used and the presence of control TiO₂ considerably enhances the photoactivity for the degradation of R6G.

5.3.4.1. Photocatalytic activity under UV radiation

The total bleaching of the dye takes place after ca. 3 h of irradiation in the case of titanias with Ru(II) complex against the more than 12 h needed for the control titania. The characteristic absorption peak at 525 nm of R6G practically disappears

with concomitant decoloration of the solution (figure 5.10). In the dye degradation experiment under UV radiation, no blue-shift of the absorption maximum peak, associated with the N-deethylation is observed (figure 5.10). Blue-shift in the absorption maximum is associated with the N-deethylation of R6G to rhodamine^[43], the major intermediate in the degradation of R6G.

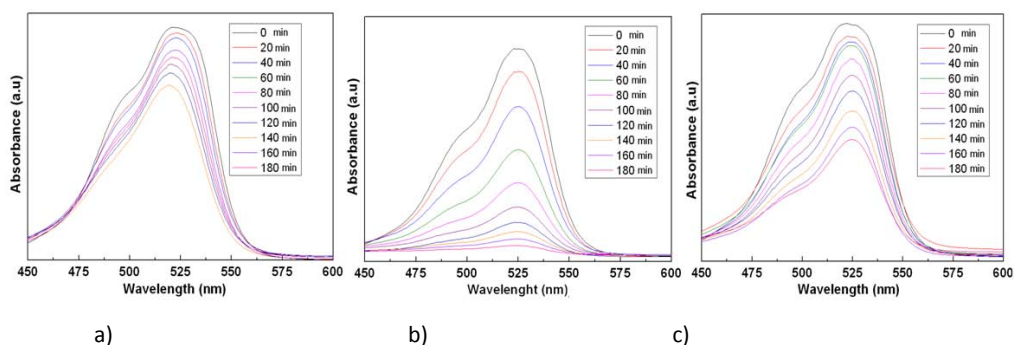


Figure 5.10. UV-vis absorption spectra of the degradation reaction of an aqueous solution of R6G ($5 \cdot 10^{-5}$ M) under UV radiation using as photocatalysts: TiO_2 (a), $\text{TiO}_2\text{-IS}$ (b) and $\text{TiO}_2\text{-G}$ (c).

During the reaction, the cationic dye radical is degraded to carbon dioxide and water and a colourless solution is obtained. TOC measurements carried out on the solutions before and after irradiation in the presence of the catalysts indicated only a partial degradation of the total organic dissolved carbon (up to ca. 50%) at least when the total dye bleaching was reached, which can confirm that the Ru(II) complex incorporation in the titania material gives rise to an enhancement of the photocatalytic bleaching of the dye solutions.

After 3 h of irradiation, no rhodamine could be detected by UV-vis spectroscopy and the carbon concentration decrease, as was determined by TOC analysis. This suggests that no rhodamine 6G is left in the reaction mixture, although after the decolourization of the dye, there is still some organic carbon species left such as, aldehydes and/or carboxylic acids.

During the degradation of rhodamine no additional peaks are present in the UV-vis spectra of the solutions containing the TiO₂ based catalysts, which suggests that the dye is completely degraded and not only photobleached^[44].

Table 5.2. Constant values of the photocatalytic activity under UV radiation, regression coefficients and conversions at different times of the titanias with the Ru (II) complex as compared with the control titania, TiO₂.

Samples	E_g^a (eV)	$k' \cdot 10^3^b$ (min ⁻¹)	R^{*c}	%Conversion ^d			$k'/k'_{TiO_2}^e$
				1h	2h	3h	
TiO ₂	3.24	7.2 ± 1.9 (6.30)	0.9897	31.1	52.8	67.7	---
TiO ₂ _IS	2.82	31.6 ± 5.0 (35.80)	0.9683	87.7	98.6	99.8	4.4
TiO ₂ _G	3.00	11.0 ± 1.6 (11.66)	0.9739	49.6	75.0	87.6	1.6

^aBand gap energies calculated from the intercept of the tangent to the $(F(R')h\nu)^{1/2}$ versus $(h\nu)$ plot. ^b1st order reaction rate pseudophotocatalytic constant of the degradation of an aqueous solution of R6G ($5 \cdot 10^{-5}$ M) obtained as the average of a minimum of three runs. Values in brackets indicate the k value used for the determination of the degree of conversion. ^cRegression coefficient for the same degradation reaction as paragraph b). ^dDegree of conversion (%) achieved by samples after 1 h, 2 h and 3 h of reaction. ^eRatio between the average k' values of the as-synthesized organotitanias as compared with the average k' value determined from the control TiO₂.

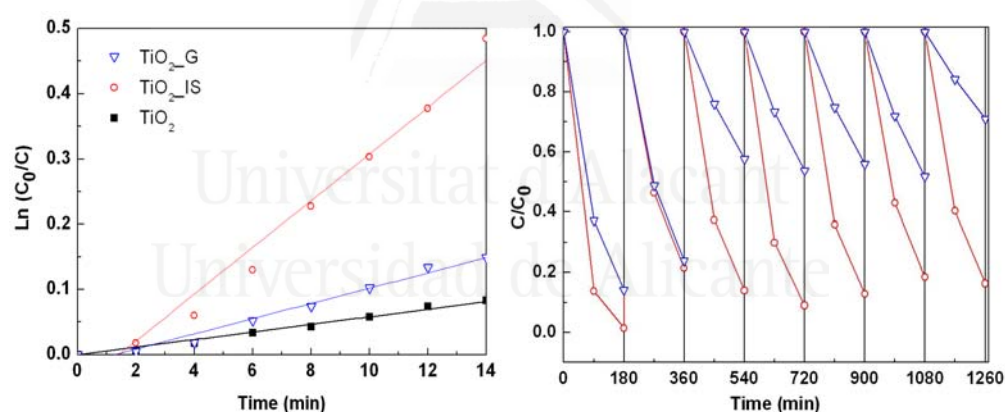


Figure 5.11. Representation of the pseudophotocatalytic constant (k') of the TiO₂_IS and TiO₂_G samples as compared with control TiO₂, in the degradation reaction of an aqueous solution of R6G ($5 \cdot 10^{-5}$ M) under UV radiation (left). Cycling tests under the same conditions (right).

Figure 5.11 (left) shows the $\ln(C_0/C)$ vs the irradiation time measured during the first 14 min of the degradation of R6G. All experimental results can be adjusted by a linear equation indicating that the process follows a pseudo-first order kinetic. The photocatalytic activity of the Ru(II) complex titania samples is considerably higher than the photocatalytic activity of control titania (figures 5.10 and 5.11, left and table 5.2), especially for the sample $\text{TiO}_2\text{-IS}$. The photocatalytic activity of $\text{TiO}_2\text{-IS}$ is 4.5 times better than control TiO_2 and almost 3 times better than the sample in which the Ru(II) complex is only on the surface ($\text{TiO}_2\text{-G}$).

These results are consistent with the decrease of the band gap in the Ru(II) complex materials (figure 5.9c), which is more accused in the $\text{TiO}_2\text{-IS}$. The electron transfer to the titania is favored due to the excitation of the Ru(II) complex, which generates an electron from the LUMO of the dye which is transferred directly to the conduction band of TiO_2 as schematically show in figure 5.12.

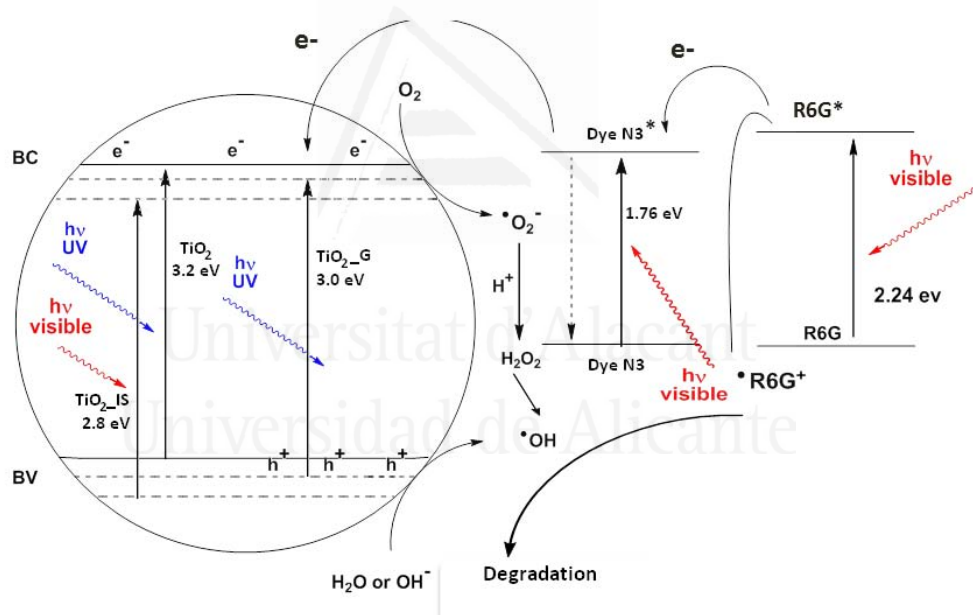


Figure 5.12. Schematic representation of the injection electrons from the dye to the titania materials in the synthesized samples.

The incorporation of the dye into the structure of titania in the TiO₂_IS material gets a better overlap between the dye and the titania, enhancing in the photocatalytic properties of the final material as compared to TiO₂_G and obviously to the control TiO₂.

Under UV radiation, the degradation mechanism is based on *the hole way* (figure 5.12). While the positive holes are scavenged by the hydroxyl groups (or H₂O molecules) present in the surface, the electrons are transferred to the conduction band of the semiconductor and subsequently trapped by the absorbed O₂ leading, in both cases, to the formation of [•]OH radicals, which promote the degradation of the organics (figure 5.12)^[45].

In the TiO₂_IS sample, the incorporation of Ru(II) complex into the structure of titania is directly associated with the reduction of its band gap and with the enhancement of its photocatalytic properties due to a better interaction between the LUMO of the dye and the CB of the titania. This makes possible a faster electron charge transfer to the conduction band of the titania and a decrease in the electron-hole recombination rate. Furthermore the higher decrease in the band gap (2.82 eV) for the sample TiO₂_IS can be associated with the incorporation of the dye directly into the framework and not on the surface, as occurs for TiO₂_G with a smaller decrease (3 eV). All results obtained can tentatively assume that the enhancement of the photocatalytic properties of the TiO₂_IS can be attributed to a synergetic effect between the high decrease in the band gap of this material and the faster electron injection of the electrons into the CB of the titania due to the Ru(II) complex situated into its framework (bulk), favouring a low rate of recombination.

TiO₂_IS titania material shows almost 90% efficiency even after 7 cycles and conversely, the efficiency of sample TiO₂_G observed is decreasing until 20% over cycles. It can confirm that the Ru(II) complex in the TiO₂_IS material is further

protected being incorporated into the structure of the titania and presents a more stable anchorage resulting in greater efficiency despite subjecting it to several cycles of reuse.

5.3.4.2. Photocatalytic activity under visible light

Figure 5.13 shows the results of the visible light photocatalytic activity of titania samples containing Ru(II) complexes as compared with the control TiO₂ (see Chapter 4 for the details).

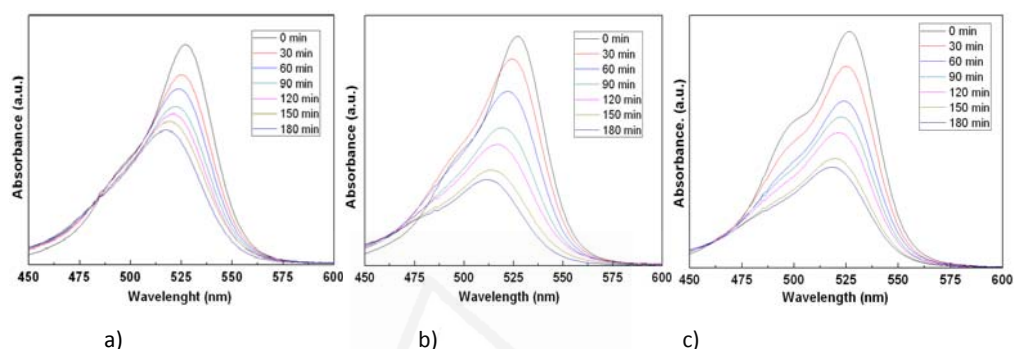


Figure 5.13. UV-vis absorption spectra of the degradation reaction of an aqueous solution of R6G ($5 \cdot 10^{-5}$ M) under visible light using as photocatalysts: TiO₂ (a), TiO₂-IS (b) and TiO₂-G (c).

A blue-shift in the absorbance peaks is observed during the reaction time for the titanias with and without Ru(II) complex, associated with a highly selective stepwise deethylation process of R6G, which occurs before the destruction of the dye.

Under visible light, the active oxygen species attack primarily and easily the R6G areas that connect directly with the surface of the titania than the bulk material inducing a photocatalytic degradation of the R6G on the surface of the photocatalyst. This phenomenon can be explained considering that when rhodamine is irradiated with light in the visible range, is able to inject an electron from its excited state into the CB of the titania, becoming a positively charged radical which generates active

oxygen species. This species may be responsible for inducing the deethylation process in the degradation of R6G under visible light.

In view of these results, the same degradation reaction can be due to two different mechanisms, depending on the kind of light that is irradiated, UV or visible. R6G is able to absorb photons in the visible range and inject electrons from its LUMO to the CB of the titania which generates differences in the active oxygen presents^[46]. However under UV radiation, TiO₂ directly absorbs the photons and the adsorption by the R6G is not significantly important^[46].

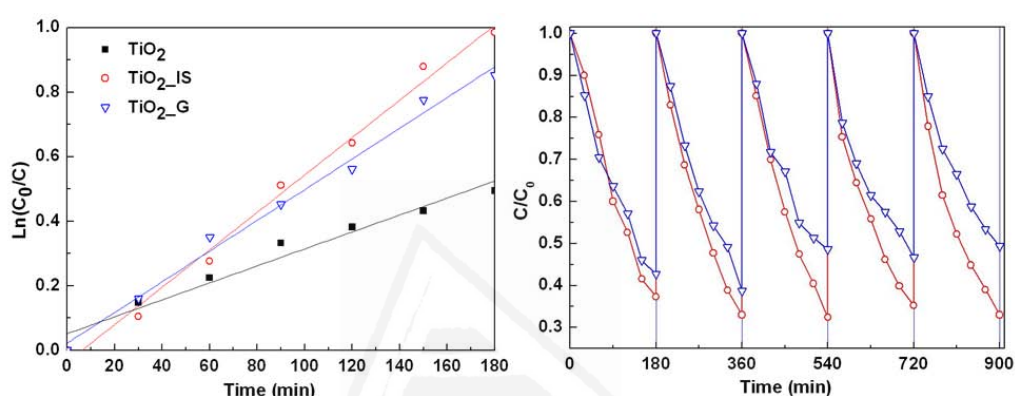


Figure 5.14. Representation of the pseudophotocatalytic constant (k') of the TiO₂-IS and TiO₂-G samples as compared with control TiO₂, in the degradation reaction of an aqueous solution of R6G ($5 \cdot 10^{-5}$ M) under visible light (left). Cycling tests under the same conditions (right).

The photocatalytic activity of the Ru(II) complex-containing titanias, represented in figure 5.14, is enhanced up more than two times in comparison with the control titania sample, being slightly higher in the case of TiO₂-IS. The difference between the photocatalytic activities of the samples TiO₂-IS and TiO₂-G is not very accused since degradation under visible light occurs mainly in the surface of the titania material, where both samples are very similar.

Table 5.3. Constant values of the photocatalytic activity under visible light, regression coefficients and conversions at different times of the titanias with the Ru(II) complex as compared with the control titania, TiO₂.

Samples	E_g^a (eV)	$k' \cdot 10^3^b$ (min ⁻¹)	R^{*c}	%Conversion ^d			$k'/k'_{TiO_2}^e$
				1h	2h	3h	
TiO ₂	3.24	2.5 ± 0.7 (2.63)	0.9640	20.2	31.7	39.0	---
TiO ₂ _IS	2.82	5.8 (5.8)	0.9898	26.8	48.3	63.5	2.2
TiO ₂ _G	3.00	4.7 (4.7)	0.9881	26.2	44.3	58.0	1.7

^aBand gap energies calculated from the intercept of the tangent to the $(F(R')h\nu)^{1/2}$ versus $(h\nu)$ plot. ^b1st order reaction rate pseudophotocatalytic constant of the degradation of an aqueous solution of R6G ($5 \cdot 10^{-5}$ M) obtained as the average of a minimum of three runs. Values in brackets indicate the k' value used for the determination of the degree of conversion. ^cRegression coefficient for the same degradation reaction as paragraph b). ^dDegree of conversion (%) achieved by samples after 1 h, 2 h and 3 h of reaction. ^eRatio between the average k' values of the as-synthesized organotitanias as compared with the average k' value determined from the control TiO₂.

From the photodegradation of R6G under visible light using TiO₂_IS and TiO₂_G, it can be concluded that the filtration of radiation with wavelength shorter than 400 nm precludes *the hole way*.

Described in Chapter 4, the R6G molecules can be excited by visible light due to its band gap of 2.24 eV, generating cationic R6G⁺ radicals and electrons. These electrons can be transferred to the conduction band of titania because of R6G LUMO energy is higher than the titania CB, following *the dye way* mechanism, acting TiO₂ only as an electron mediator in the decomposition of the R6G^[3b].

However, the Ru(II) complex plays an important role in the photocatalytic process under visible light because the position of its band gap in the visible range is adequate for generating excited electrons and injecting them into the CB of the titania. It can be worth mentioning that the photocatalytic activity of the TiO₂_IS is slightly higher than for TiO₂_G (table 5.3).

Since the Ru(II) complex is present in both samples, what makes the difference is its location in the structure of titania bulk (TiO₂_IS) and a more stable bond between the carboxylic groups and the titania.

As in the case of UV radiation, several cycles were studied for both samples containing Ru(II) complex in order to test the stability and efficiency of these materials. Sample TiO₂_G shows better results as compared with itself under UV radiation (see figure 5.14, right). However, its efficiency after several cycles of reuse decreases in that case around 50%, meanwhile TiO₂_IS sample continues showing a high efficiency (about 70%) after 5 cycles such as in the UV radiation test.

TiO₂_IS shows a higher stability as compared with TiO₂_G due to the Ru (II) complex is protected by the structure of the titania and moreover leaching is not observed. Thus it has been achieved the objective of synthesizing a titania material with a significant improvement in its photocatalytic properties, high stability after several cycles of reuse and lower band gap, thus improving its photocatalytic properties and enabling a better use of sunlight.

To gain a better understanding of the mechanisms involved, different scavengers, such as isopropanol (¹PrOH) and triethanolamine (TEOA), were added to the system and influence were studied. The addition of ¹PrOH, as a hydroxyl radical scavenger, caused the same effect in the photodegradation rate as the addition of TEOA as a hole scavenger (figure 5.15). These results suggest that the both mechanisms, *the hole and electron way* have the same significance in the photocatalytic process under visible light, at least in the experimental conditions used.

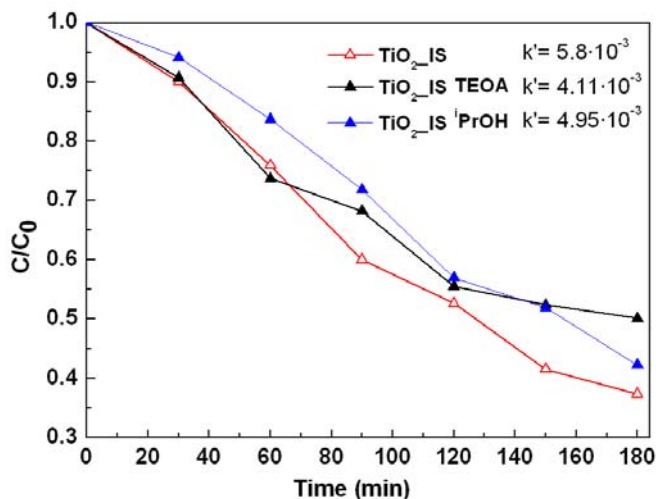


Figure 5.15. Variation of the concentration along time in the photodegradation reaction of aqueous solutions of R6G ($5 \cdot 10^{-5}$ M) by $\text{TiO}_2\text{-IS}$ in the absence or presence of different scavengers $i\text{PrOH}$ or TEOA, $5 \cdot 10^{-2}$ M) under visible light.

The high photocatalytic activity of the sample $\text{TiO}_2\text{-IS}$ under visible light, even after several cycles, confirms the possibility to synthesize a very stable material, able to work under different radiation conditions including visible light. This expands the application of these materials to areas such as environmental applications, particularly degradation of air pollutants under visible light or water purification without the need for expensive treatments.

5.6. CONCLUSIONS

A novel titania material with a Ru(II) complex, similar to the commercial dye N3, incorporated in its framework, that acts as a charge-transfer dye, has been synthesized by direct co-condensation of a titanium precursor, TBOT, in mild conditions and in the absence of surfactant ($\text{TiO}_2\text{-IS}$).

The methodology used to incorporate organic compounds that act as ligand during the hydrolysis of the titania precursor has been extended to other functionalities with promising results.

The incorporation of the Ru(II) complex into the structure of the titania has been confirmed by FTIR, XPS and ICP-OES with a high yield incorporation and without disturbing the XRD diffraction pattern of these materials (anatase). Moreover the sample have high BET surface area, indicating the mesoporous nature of this sample, also confirmed by N₂ adsorption isotherms. The optical properties of the final sample have been improved with the incorporation of the complex. The band gap has decreased significantly and the range in which they are active has been extended from the UV to visible range, thus improving its photocatalytic properties and enabling a better use of solar light.

These results have been confirmed by the photocatalytic degradation test of R6G in liquid-solid regime by using both UV radiation and visible light. Photoreactivity experiments showed that the R6G degradation rate is faster using the sample TiO₂_IS with respect to TiO₂_G and the control TiO₂. This observation is likely due to the incorporation of the Ru(II) complex directly into the structure of the titania (bulk), getting a more stable anchorage, a better overlap between the Ru(II) complex and the CB of the titania and a significant decrease in its band gap, from 3.2 eV to 2.82 eV.

It is worth mentioning that the Ru (II) complex is protected by its incorporation in the structure of TiO₂ (bulk), sample TiO₂_IS, which also allows for a more stable anchorage, as the recycling and leaching studies have shown. Under irradiation with visible light, although both samples, TiO₂_IS and TiO₂_G, show similar photocatalytic activities, in the TiO₂_IS sample the Ru (II) complex is more protected which results in greater efficiency despite subjecting it to 5 cycles of reuse.

In view of the stated above, this new material can be considered as a possible alternative to existing solar cells due to their higher efficiency and more efficient use of sunlight as well as in the field of photocatalysis in specific reaction such as oxidation and partial oxidation of alcohols or certain pollutants.

5.6. REFERENCES

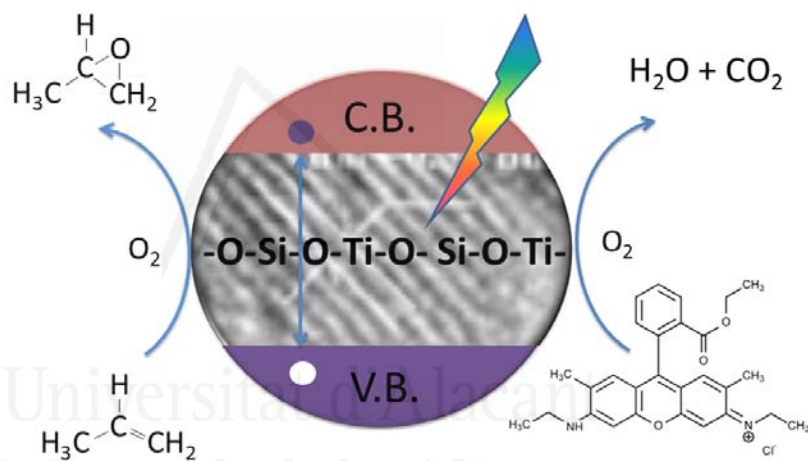
- [1] O.Kohle, M. Graetzel, A.F. Meyer and T.B. Meyer, *Adv. Mat.*, 1997, **9**, 904. (www.solaronix.com/technology/dyesolarcells) (Accessed on 14th January 2014)
- [2] J. Gong, J. Liang, K. Sumathya, *Renew. Sustain. Energ. Rev.*, 2012, **16**, 5848.
- [3] a) M.R. Narayan, *Renew. Sustain. Energ. Reviews*, 2012, **16**, 208; b) J.H. Snook, L.A. Samuelson, J. Kumar, Y. Kim, J.E. Whitten, *Org. Elect.*, 2005, **6**, 55.
- [4] D. Matthews, P. Infelta, M. Grätzel, *Solar Energy Mat. Solar Cells*, 1996, **44**, 119.
- [5] B. O'Regan, M. Grätzel, *Nature*, 1991, **353**, 737.
- [6] T. Stergiopoulos, S. Karakostas, P. Falaras, *J. Photochem. Photobiol. A*, 2004, **163**, 331.
- [7] M. Grätzel, *Nature*, 2001, **414**, 338.
- [8] A. Mishra, M.K. Fisher, P. Bauerle, *Angew. Chem. Int. Ed. Engl.*, 2009, **48**, 2474.
- [9] P. Liu, J.J. Fu, M.S. Guo, X. Zuo, Y. Liao, *Comp. Theor. Chem*, 2013, **1015**, 8.
- [10] M.K. Nazeeruddin, A. Kay, I. Rodicio, R. Humphry-Baker, E. Müller, P. Liska, N. Vlachopoulos, M. Grätzel, *J. Am. Chem. Soc.*, 1993, **115**, 6382.
- [11] a) M.K. Nazeeruddin, F. Angelis, S. Fantacci, A. Selloni, G. Viscardi, P. Liska, S. Ito, B. Takeru, M. Gratzel. *J. Am. Chem. Soc.*, 2005, **127**, 16835; b) F. Gao, Y. Wang, J. Zhang, D. Shi, M. Wang, R. Humpry-Baker, P. Wang, S.M. Zakeeruddin, M. Grätzel, *Chem. Commun.*, 2008, **23**, 2635.
- [12] M. Seery, "Dye-sensitized solar cells" (<http://photochemistry.wordpress.com/2009/08/17/dye-sensitised-solar-cells-dssc>) (Accessed on 14th January 2014)

- [13] C.P. Chen, X.Y. Qi, B.M. Zhou, *J. Photochem. Photobiol. A*, 1997, **109**, 155.
- [14] Y. Cho, W. Choi, C.H. Lee, T. Hyeon, H.I. Lee, *Environ. Sci. Technol.*, 2001, **35**, 966.
- [15] M. Senthilnathan, D.P. Ho, S. Vigneswara, H.H. Ngo, H.K. Shon, *Separ. Purif. Technol.*, 2010, **75**, 415.
- [16] H. Rensmo, S. Södergren, L. Patthey, K. Westermarck, L. Vayssieres, O. Kohle, P.A. Brühwiler, A. Hagfeldt, H. Siegbahn, *Chem. Phys. Lett.*, 1994, **274**, 51.
- [17] A. Islam, H. Sugihara, L. Singh, K. Hara, R. Katoh, Y. Nagawa, M. Yanagida, Y. Takahashi, S. Murata, H. Arakawa, *Inorg. Chim. Acta*, 2001, **322**, 7.
- [18] a) Y. Hsu, H. Zheng, T. Suen, J. Lin, K. Ho, *Solar Energ. Mat. Sol. Cells*, 2005, **87**, 357; b) C.H. Lee, J.L. Shie, C.Y. Tsai, Y.T. Yang, C.Y. Chang, *J. Clean Energ. Tech.*, 2013, **1**, 2.
- [19] S. Wu, C. Chen, J. Chen, J. Li, Y. Tung, K. Ho, C. Wu, *Dyes Pigments*, 2010, **84**, 95.
- [20] T. Funaki, M. Yanagida, N. Onozawa-Komatsuzaki, Y. Kawanishi, K. Kasuga, H. Sugihara, *Solar Energ. Mat. Sol. Cells*, 2009, **93**, 729.
- [21] C. Sahin, T. Dittrich, C. Varlikli, S. Icli, M. Lux-Steiner, *Solar Energ. Mat. Sol. Cells*, 2010, **94**, 686.
- [22] M. Yanagida, T. Yamaguchi, M. Kurashige, G. Fujihashi, K. Hara, R. Katoh, H. Sugihara, H. Arakawa, *Inorg. Chim. Acta*, 2003, **351**, 283.
- [23] a) K.Y. Liu, C.L. Hsu, S.H. Chang, J.G. Chen, K.C. Ho, K.F. Lin, *J. Polym. Sci. Part A: Polym. Chem.*, 2010, **48**, 366; b) K.Y. Liu, C.Y. Ko, K.C. Ho, K.F. Lin, *Polymer*, 2011, **52**, 3318.
- [24] R.A. Elsalamony, S.A. Mahmoud, *Arabian J. Chem.*, 2012, Article in Press (DOI: 10.1016/j.arabjc.2012.06.008)
- [25] A.K.M. Fung, B.K.W. Chiu, M.H.W. Lam, *Water Res.*, 2003, **37**, 1939.
- [26] K. Kalyanasundaram, M. Grätzel, *Coord. Chem. Rev.*, 1998, **77**, 347.

- [27] Md. K. Nazeeruddin, S.M. Zakeeruddin, R. Humphry-Baker, M. Jirousek, P. Liska, N. Vlachopoulos, V. Shklover, C.H. Fischer, M. Grätzel, *Inorg. Chem.*, 1999, **38**, 6298.
- [28] M. Rico-Santacruz, A.E. Sepúlveda, E. Serrano, J.R. Berenguer, E. Lalinde, J. García-Martínez, *Spanish Patent 20130535*, 2013.
- [29] Md. K. Nazeeruddin, S.M. Zakeeruddin, R. Humphry-Baker, S.I. Gorelsky, A.B.P. Lever, M. Grätzel, *Coord. Chem. Rev.*, 2000, **208**, 213.
- [30] W.K. Seok, A.K. Gupta, S.J. Roh, W. Lee, S.H. Han, *Bull. Korean Chem. Soc.*, 2007, **28**, 8.
- [31] K.J. Hwang, S.J. Yoo, S-S. Kim, J.M. Kim, W.G. Shim, S.I. Kim, J.W. Lee, *J. Nanosc. Nanotech.*, 2008, **8**, 4976.
- [32] www.sigmaaldrich.com/catalog/product/aldrich/703206?lang=es®ion=ES (Accessed on April 2014).
- [33] F. Schiffmann, J.V. Vondele, J. Hutter, R. Wirz, A. Urakawa, A. Baiker, *J. Phys. Chem. C*, 2010, **114**, 8398.
- [34] J. Zhu, D. Yang, J. Geng, D. Chen, Z. Jiang, *J. Nanopart. Res.*, 2008, **10**, 729.
- [35] a) V. Saxena, A.K. Chauhan, J. Singh, D.K. Aswal, S.K Gupta, "Absorption mechanism of N719 dye on carboxylic acid treated anatase TiO₂ surface"; b) D. Zhao, C. Chen, W. Yang, H. Ji, W. Ma, L. Zang, J. Zhao, *J. Phys. Chem. C.*, 2008, **112**, 5993.
- [36] Y. Fu, H. Du, S. Xhang, W. Huang, *Mater. Sci. Eng.*, 2005, **403**, 25.
- [37] a) G.W. Simmons, B.C. Beard, *J. Phys. Chem.*, 1987, **91**, 1143; b) P. Stefanov, M. Shipochka, P. Stefchev, Z. Raicheva, V. Lazarova, L. Spassov, *J. Phys. Conf. Ser.*, 2008, **100**, 012039; c) H. Chermette, P. Pertosa, *Chem. Phys. Lett.*, 1980, **69**, 2; d) M. Oku, H. Matsuta, K. Wagatsuma, Y. Waseda, S. Kohiki, *J. Elec. Spect. Rel. Phen.*, 1999, **105**, 211; e) A.E. Bocquet, T. Mizokawa, K. Morikawa, A. Fujimori, *Phys. Rev. B*, 1996, **53**, 3.

- [38] A.O.T. Patrocínio, E.B. Paniago, R.M. Paniago, N.Y. Murakami, *Appl. Surf. Scienc.*, 2008, **254**, 1874.
- [39] a) X. Chen, L. Liu, P.Y. Yu, S.S. Mao, *Science* 2011, **331**, 746; b) E. McCafferty, J.P. Wightman, *Surf. Interface Anal.*, 1998, **26**, 549.
- [40] M. Balaraju, V. Rekha, B.L.A. Prabhavathi Devi, R.B.N. Prasad, P.S. Prasad, N. Lingaiah, *Appl. Catal. A*, 2010, **384**, 107.
- [41] R. Thapa, S. Maiti, T.H. Rana, U.N. Maiti, K.K. Chattopadhyay, *J. Mol. Catal. A: Chem.*, 2012, **363–364**, 223.
- [42] a) L.C.T. Shoute, G.R. Loppnow, *J. Am. Chem. Soc.*, 2003, **125**, 15636; b) N. Onozawa-Komatsuzaki, M. Yanagida, T. Funaki, K. Kasuga, K. Sayama, H. Sugihara, *Sol. Energ. Mat. & Sol. Cells*, 2011, **95**, 310.
- [43] T. Watanabe, T. Takizawa, K. Honda, *J. Phys. Chem.*, 1977, **81**, 1845.
- [44] P. Wilhelm, D. Stephan, *J. Photochem. Photobiol. A:Chem.*, 2007, **185**, 19.
- [45] Aarthi, T.G. Madras, *Ind. Eng. Chem. Res.*, 2007, **46**, 7.
- [46] F. Chen, J. Zhao, H. Hidaka, *Int. J. Photoen.*, 2003, **5**, 209.

VI. Incorporation of organosilica precursors in the framework of mesoporous titania materials



M. Rico, E. Serrano, G. Marcí, E.I. García-López, J. Garcia-Martinez, "Synthesis, characterization and photocatalytic applications of mesoporous organosilane-modified titanias" (in preparation).

VI. Incorporation of organosilica precursors in the framework of mesoporous titania

Mesoporous titania-organosilica nanoparticles with anatase structure have been prepared by direct co-condensation of a titania precursor, tetrabutylortotitanate (TBOT), with two different organosilica precursors, 1,4-bis(triethoxysilyl)benzene (BTEB) and 1,2-bis(triethoxysilyl)ethane (BTEE), in mild conditions and in the absence of surfactant. Hybrid materials show both high surface areas (200-360 m²/g) and pore volumes (0.3 cm³/g), even after calcination. These materials were tested in the degradation of rhodamine 6G (R6G) as well as in the partial oxidation of propene, showing excellent photocatalytic activity, especially after the calcination of the samples. The sintering of nanoparticles during calcination occurs through the co-condensation of Si-OR and Ti-O groups leading to a change in the Ti(IV) coordination as well as to an increase in the concentration of Si-O-Ti bonds. These changes seem to be responsible for the high photocatalytic activity of the calcined materials as compared to the uncalcined samples and the control TiO₂.

6.1. INTRODUCTION

Physically mixed titania-silica materials present the advantages of each component: TiO₂ (an *n*-type semiconductor and an active catalytic support) and SiO₂ (good thermal stability and good mechanical strength). However, titania-silica materials, prepared by co-condensation of several Ti- and Si- containing precursors (mainly alkoxides), have attracted particular attention because they are able to extend their applications through the generation of new catalytic active sites due to the interaction of TiO₂ with SiO₂. Relevant examples are the isomerization and dehydration reactions for acid and oxidation catalysis^[1], respectively. The presence of silica enhances thermal and mechanical stability and maintains the charge balance in the titania framework while preserving its catalytic performance. Moreover, silica and titania precursors are usually commercially available and not expensive.

Silica and titania can be physically mixed (a blend of the two components previously synthesized) or chemically bonded (with the formation of the Ti-O-Si bond). When the interactions are due to chemical bonding, the physico-chemical and reactivity properties of the titania-silica materials are completely different from the individual phases or physical mixtures^[1].

Interestingly, titania-silica materials have been reported to show photocatalytic activity for environmental applications, sometimes improving the performance of the unmodified TiO₂ material^[2-12].

As previously reported^[13-14], besides the insulator character of SiO₂, that leads to an increase in the band gap energy of titania-silica materials, the incorporation of silica in titania enhances, for certain applications, the photocatalytic activity of the semiconductor.

Titania-silica materials can be easily synthesized by co-condensation of silica and titania precursors via sol-gel, usually with the addition of surfactant (CTAB or block

copolymers) which act as templates, to obtain a mesoporous material. Moreover, additional reagents are needed in order to modify the pH or other synthesis conditions to control the hydrolysis rate of both precursors^[3-7], since hydrolysis of titanium alkoxides is significantly faster than that of silicon alkoxides. Using this approach, Davis et al.^[6b] obtained titania-silica materials, chemically bonded, with a Si/Ti molar ratio in the range 0.16-8, which resulted almost four times more active than control TiO₂ for the isomerization reaction of butane. Authors attributed the improvement in the photocatalytic activity to the Brønsted acid sites in the titania-silica materials that were absent on the control TiO₂ prepared by the same methodology^[6]. Recently, Rahmani et.al.^[8] synthesized titania-silica materials via sol-gel with Si/Ti molar ratio in the range 0.05-0.15 obtaining excellent results in the methyl orange photocatalytic bleaching and mineralization. The same reaction was studied by Hilonga et.al.^[9] by using a titania-silica material with Si/Ti molar ratio of 0.2, obtaining a higher degradation rate of the dye with that material as compared to the commercial TiO₂ Degussa P25.

Yang et al.^[10] evaluated two different synthetic approaches to obtain SiO₂-TiO₂ materials. In the first one, the hydrolysis of the titania and silica precursors were separately performed while, in the second one, a pre-hydrolysis of the silica precursor was carried out before adding the titania precursor and the subsequent hydrolysis takes place. In both cases the obtained materials improve the control TiO₂ performance in the photocatalytic water decomposition reaction under UV radiation.

Similarly, titania-organosilica materials have also been prepared by sol-gel using both BTEB and BTEE as organosilica precursors^[11]. The hybrid materials, with BTEB(BTEE)/TBOT molar ratio equal to 0.01 have been tested in the photodegradation of the methylene blue. The reactivity observed in the presence of this hybrid photocatalyst was almost two fold higher than the obtained using the

control TiO₂ (prepared using the same methodology). Unlike our synthesis method, they used a very low Si/Ti ratio, surfactants and acetic or hydrochloric acid to control the rate of the hydrolysis.

In the present work, titania-organosilica materials with high Si/Ti molar ratios (ca. 0.1-0.5) were prepared without adding surfactants or any additional reagents to control the hydrolysis rate of the precursors. These materials were evaluated as photocatalysts in liquid-solid regime for the degradation of the commercial R6G dye, as well as in gas-solid regime, in the propylene epoxidation reaction. Moreover, the ability of these organosilica precursors to act as templates of mesoporous titanias has been also evaluated by calcination of selected samples at 550 °C. Usually, the structure of mesoporous titanias synthesized via sol-gel collapses after calcination^[12] and consequently, the use of BTEB and BTEE as templates has been analyzed through the evaluation of porous properties, thermal stability and photocatalytic activity of the calcined materials.

The titania-silica material should present a strong interaction with cationic substrates, as in the case of R6G, due to the decrease in the isoelectric point of the photocatalysts surface. Anderson et. al^[14] observed a synergistic mechanism in TiO₂-SiO₂ samples that presents a higher photodegradation rate of both R6G and phenol compared with that observed by using the commercial TiO₂ Degussa P25. The photocatalytic degradation of dyes is often used to test the activity of photocatalysts. However, the (photo)adsorption on the titania surface or the dye-sensitizing effect can affect the reactivity results^[15]. Consequently, in the present work, the photocatalytic properties of some selected materials were also tested in gas-solid regime for the epoxidation of propylene.

The partial oxidation of propylene to obtain propylene oxide (PO) is a reaction of paramount importance in the chemical industry. PO is one of the most important

precursors in the industry whose production consumes over 10% of all propene produced. Global propylene capacity was 97.7 Million Metric Tons (MMT) in 2011 against a demand of 80 MMT. The capacity is expected to increase to 119 MMT in 2015 with demand reaching 98 MMT^[16]. The main application of PO is the production of polyether polyols (65%), used for the production of polyurethane foams. It is also used for the production of propene glycol (30%), mainly employed in the production of polyesters, and propene glycol ethers (4%), which are used for a solvents^[17a].

The classical methods to produce PO are based on chlorohydrin and the hydroperoxidation processes^[17]. These reactions show several disadvantages, being the main one the utilization of chlorine to control the hydrolysis rate and the production of hazardous by-products. The epoxidation process using hydrogen peroxide in the presence of methanol and titanosilicalite-1 (TS-1) catalyst^[18] or with O₂ in the presence of Au nanoparticles deposited on modified TS-1^[19] have been also reported. Compared the classical processes, these two methods are advantageous from the environmental point of view; however, they are often carried out at high temperatures and/or pressures. The development of more environmental friendly processes, such as photocatalysis with only O₂, is thus highly desirable.

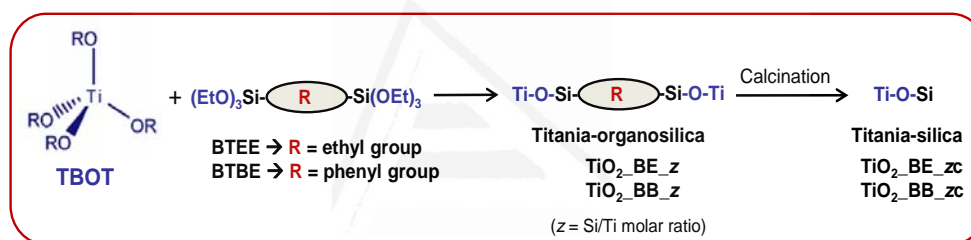
To the best of our knowledge, few papers report the photocatalytic propylene epoxidation with oxygen in mild conditions. From those, it was concluded that metal oxide species, such as TiO₂, can exhibit photocatalytic activity for the partial oxidation of propylene when are highly dispersed on silica, alumina, or zeolites^[20]. Silica, when used as catalyst support, promotes not only catalytic thermal reactions but also photoreactions including photo-oxidation. TiO₂-SiO₂^[21,22] or ZnO-SiO₂^[21] samples prepared at low TiO₂ or ZnO content are active for the propylene partial oxidation in the presence of oxygen at room temperature and low pressure (tested in a batch photocatalytic reactor equipped with a 200 W Xe lamp). The amount of

photoproducted species are quantified by adding the desorbed amount species at 300 °C to the product present in gas-phase^[21,22]. Along this chapter, the photocatalytic activities of the synthesized titania-silica materials will be compared to those already described in previous studies.

6.2. EXPERIMENTAL SECTION

6.2.1. Synthesis of the mesoporous titania-organosilicas

Titania-organosilica materials were synthesized by co-condensation of tetrabutyl orthotitanate (TBOT), with different amounts of two organosilica precursors (0.04-0.25 mol/mol TBOT) by using only water and ethanol as solvents and without the need of surfactants (scheme 6.1). The organosilica precursors used were: an ethyl-organosilane, 1,2-bis(triethoxysilyl)ethane (BTEE, Aldrich 96%), and a benzene-bridged organosilane, 1,4-bis(triethoxysilyl)benzene (BTBE, Aldrich 96%).



Scheme 6.1. Schematic procedure of synthesis of titania-organosilica materials by co-condensation of tetrabutyl orthotitanate (TBOT), with different amounts of two organosilica precursors (0.04–0.25 mol/mol TBOT) by using only water and ethanol as solvents and without the need of surfactants.

Samples were synthesized following the procedure already described in chapter 3. In a typical synthesis, 0.25 g of organosilica precursor was dissolved in absolute ethanol during 10 min under magnetic stirring. Following, 5 g (14.7 mmol) of TBOT was added to the above solution and the mixture was magnetically stirred during 40 min at room temperature. Finally, 123.5 g (6.86 mol) of water was added drop-wise

causing the precipitation of the solid. The mixture was then kept at room temperature during 24 h under vigorous magnetic stirring, followed by a treatment at 80 °C for 24 h in a drying oven. The solid product was washed with water and acetone, successively, filtered and dried in an oven at 100 °C for 8 h.

The molar ratio of the synthesis gel was kept at 1TBOT: x Org: 41.3 EtOH: 467 H₂O, being *Org* the organosilica precursor and x ranging between 0.05 and 0.25 for BTEE precursor and between 0.04 and 0.20 for BTEB precursor. Samples were denoted TiO₂_BE_z and TiO₂_BB_z, for BTEE and BTEB precursors, respectively, where z represents the Si/Ti molar ratio (table 6.1).

The as-synthesized samples were also calcined to analyse the effect of this step on the photocatalytic properties of these new materials. For this purpose, samples were calcined at 550 °C during 5 h (ramp of 2.3 °C/min). Samples were denoted as TiO₂_BE_z_c and TiO₂_BB_z_c.

It should be noted that the titania-organosilica materials were also synthesized using surfactants and no significant differences in their textural properties or in their XRD spectra were observed.

6.2.2. Physico-chemical characterization methods

The incorporation of both organosilica precursors in the titania samples was evaluated by ²⁹Si RMN and FTIR and XPS spectroscopies. XPS technique was used, in the -10 to 2 eV range, to determine the position of the valence band (VB) of the titania materials, while DRUV spectra was used to estimate their band gap. Both techniques (XPS and DRUV) were combined to determine the position of the conduction band (CB) of the titania materials and to estimate the DOS scheme.

XRD analysis was carried out to study the crystalline structure of the titanias. In the same way, TEM was used to investigate the mesoporosity and crystallinity of the materials and to study their morphology.

Porous texture parameters (mesoporosity volume, surface area and pore diameter) were characterized by N₂ adsorption/desorption isotherms at 77 K and the results were analyzed using the software package AUTOSORB.

All the equipment and experimental conditions used are described with more detail in chapter 3.

6.2.3. Photocatalytic activity

6.2.3.1. Liquid-solid regime

The photocatalytic activity of the synthesized materials was evaluated in liquid-solid regime by measuring the absorbance of R6G solutions under UV radiation in a photochemical reactor system (more details in chapter 3). After the bleaching of the solution, monitored by absorbance measurements on a UV-vis spectrophotometer, a total organic carbon analyzer was used in order to determine the TOC content before and after the dye solutions bleaching.

6.2.3.2. Gas-solid regime

The photoreactor designed to operate in the gas-solid regime, was a cylindrical shaped batch type fixed bed Pyrex photoreactor (volume = 100 ml, diameter ≈ 94 mm, height ≈ 15 mm). The photocatalyst (0.2 g) was dispersed as a thin layer inside the photoreactor. In this tightly closed reactor, after purging with pure O₂ during 30 minutes, 5 ml of pure gaseous propylene at standard conditions were injected by means of a gas-tight syringe into the photocatalytic reactor. The propylene initial concentration was 2.1 mM. For all the runs, the reactor, horizontally positioned, was

illuminated from the top inside a SOLARBOX apparatus (CO.FO.ME.GRA.) equipped with a solar simulating lamp (high pressure Xe lamp of 1500 W). The photoreactivity setup is shown elsewhere^[23].

Irradiation started only when steady state conditions were achieved. In the present work, the system was maintained under dark conditions at room temperature to achieve the adsorption equilibrium of the propylene on the photocatalyst surface. During the runs, the irradiance was equal to $1.0 \text{ mW}\cdot\text{cm}^{-2}$ and the temperature inside the reactor was ca. $50 \text{ }^\circ\text{C}$. The runs lasted ca. 2.5 h and the reacting fluid was analyzed by withdrawing gas samples from the photoreactor by means of a gas-tight syringe. Substrate and intermediates concentrations were measured by a gas chromatograph equipped with a HP-1 column and a FID, whereas carbon dioxide was analyzed by a Carboxen column in an HP6890 gas chromatograph equipped with a TCD.

The study of the photocatalytic activity of all titania materials was performed during a pre-doctoral stay in the "Schiavello-Grillone" photocatalysis group of Prof. Palmisano, at the University of Palermo (Italy), under the supervision of Dra. Elisa I. García López.

6.3. RESULTS AND DISCUSSION

6.3.1. Structural and physico-chemical characterization of the as-synthesized titania-organosilica materials

The first step in the characterization of the effectiveness of the synthetic route herein described (see Scheme 6.1) is to evaluate the co-condensation of the benzene- and ethylene-bridged organosilane monomers with the titania precursor and, consequently, their distribution in the final materials. For that purpose, samples were analysed by XRF, FTIR, ^{29}Si NMR and XPS.

Table 6.1. Nomenclature, textural and structural parameters of the titania-organosilica materials prepared with different BTEE (TiO₂_BE) and BTEB (TiO₂_BB) amount, as compared to the control TiO₂.

Sample	Org/ TBOT ^a	Si/Ti ^b	d_p^c (nm)	V_p^d (cm ³ /g)	A_{BET}^e (m ² /g)	$d_{(101)}^{XRD, f}$ (nm)	$D^{XRD, g}$ (nm)	$\Phi^{TEM, h}$ (nm)	
TiO ₂	---	---	---	5.6 (2-9)	0.29	245	0.35	6.4	8.7
TiO ₂ _BE_	0.10	0.05	0.12 (0.10)	4.6 (2-10)	0.33	291	0.35	7.3	8.6
	0.20	0.10	0.17 (0.20)	3.1 (2-7)	0.30	314	0.35	8.9	8.5
	0.50	0.25	0.49 (0.50)	---	0.23	360	0.35	11.6	*
TiO ₂ _BB_	0.08	0.04	0.07 (0.08)	4.6 (2-10)	0.29	280	0.35	6.4	8.4
	0.16	0.08	0.15 (0.16)	3.4 (2-7)	0.29	299	0.35	8.4	8.6
	0.40	0.20	0.37 (0.40)	---	0.20	298	0.35	11.6	*

^aNominal molar ratio between the organosilane precursor (Org) and the titania precursor, TBOT, used during the synthesis. ^bSi/Ti molar ratio determined by XRF measurements. Values in brackets represent the theoretical Si/Ti molar ratio. ^cAverage mesopore diameters estimated from the adsorption branch of the nitrogen isotherm using the BJH method. ^dMesopore volume from the isotherms at relative pressure of 0.95 (see chapter 3). ^eThe BET surface area was estimated by multipoint BET method using the adsorption data in the relative pressure (P/P_0) range of 0.05–0.30. ^fAnatase spacing (d_{101}) calculated using Bragg equation. ^gDomain size of the particle calculated from X-ray diffraction using Scherrer equation. ^hParticle size estimated from TEM images using Gatan software (see chapter 3). *Non determined.

Table 6.1 shows the nomenclature, textural and structural parameters of the mesoporous titania-organosilica materials prepared with different BTEE (TiO₂_BE) and BTEB (TiO₂_BB) amount, as compared to the control titania. XRF measurements (table 6.1, column 3) indicate the organic moieties were fully incorporate in the final material, thus proving the effectiveness of the incorporation route herein proposed.

In order to confirm the presence of the Si-O-Ti bonds in the hybrid titania materials, the samples were firstly analysed by FTIR (see figure 6.1).

FTIR spectra of the BTEE precursor and an organosilica xerogel synthesized using only BTEE precursor in the same conditions that those used for titania-based samples, for comparison purposes, are shown in figure 6.1a.

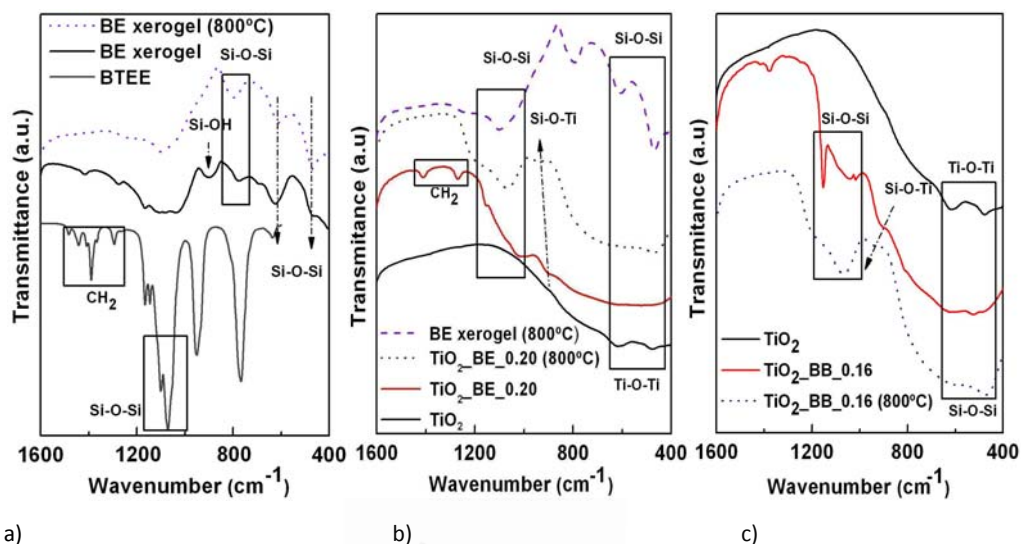


Figure 6.1. FTIR spectra of the titania-organosilica materials as-synthesized and treated at 800°C (b, c) in comparison with the FTIR spectra of an organosilica xerogel (BE xerogel sample) synthesized using only BTEE precursor in the same conditions that those used for titania-based samples (a).

The spectrum of the BE xerogel shows the peaks characteristics of Si-O-Si bonds: asymmetric and symmetric stretching vibrations at 1105 cm^{-1} and 780 cm^{-1} , respectively, symmetric stretching vibrations at ca. 621 cm^{-1} , and bending modes of the Si-OH and Si-O-Si at around 903 and 472 cm^{-1} , respectively^[24-26].

The spectra of the $\text{TiO}_2\text{-BE}_0.20$ and $\text{TiO}_2\text{-BB}_0.16$ samples are shown in figure 6.1b and 6.1c, respectively. The bands around 940 cm^{-1} , typically used to confirm the presence of Ti-O-Si bonds in hybrid titano-silica materials, overlap with those corresponding to Si-OH bending mode^[24,27,28]. Vibrations in the range of $1000\text{-}1210\text{ cm}^{-1}$ are characteristic of the Si-O-Si asymmetric stretching mode, indicating self-condensation of some organosilanes units during the sol-gel reaction, as further

confirmed by XPS (see below). Similarly, bands below 750 cm^{-1} are due to the Ti-O-Ti asymmetric stretching mode, at 617 and 473 cm^{-1} . There is a strong overlapping between Ti-O-Ti with Si-O-Si vibrations. To avoid this, both the BE xerogel and the titania-based samples were treated at $800\text{ }^\circ\text{C}$ ($\text{TiO}_2\text{_BE_0.20}$ and $\text{TiO}_2\text{_BB_0.16}$). In case of the BE xerogel, the bands due to the presence of Si-OH disappear after treatment at $800\text{ }^\circ\text{C}$ while the bands associated with Si-O-Si remain practically unmodified. On the contrary, in the case of $\text{TiO}_2\text{_BE}$ a shift from 905 to 940 cm^{-1} can be clearly observed in the spectrum of $\text{TiO}_2\text{_BE_0.20}$ and $\text{TiO}_2\text{_BB_0.16}$ samples after treatment at $800\text{ }^\circ\text{C}$, thus indicating the hetero-condensation of Si-O-Ti was well performed (figures 6.1b-c).

In addition to the bands characteristics of Ti-O-Si bonds, there are also bands at 1272 and 1440 cm^{-1} due to the C-H deformation vibration $\delta(\text{CH}_2)$ in $\text{TiO}_2\text{_BE_0.20}$ as well as C-H stretching of phenyl groups at ca. 3100 cm^{-1} and aromatic ring vibrations $\delta(\text{CH})$ at 1600 and 1400 cm^{-1} in $\text{TiO}_2\text{_BB_0.16}$ spectra. These bands disappear after the treatment at $800\text{ }^\circ\text{C}$. These experiments confirm the existence of phenyl and ethane groups in the titania-based materials before calcination^[29].

The best tool to elucidate the connectivity of silicon atoms in the titania-organosilica materials is ^{29}Si NMR. Figure 6.2a shows the ^{29}Si NMR spectra of $\text{TiO}_2\text{_BE_0.20}$ sample in comparison with the BE organosilica xerogel. As expected, the spectrum of the BE xerogel shows a broad signal characteristic of the T^m $[\text{RC-Si}(\text{OSi})_m(\text{OH})_{3-m}]$ sites of organosilica materials^[30]. The deconvolution of these peaks lead to four individual signals: T^3 , $\delta = -85.8\text{ ppm}$; T^2 , $\delta = -76.6\text{ ppm}$; T^1 , $\delta = -69.0\text{ ppm}$, and T^0 , $\delta = -56.0\text{ ppm}$; that can be assigned to the ethylene fragments of the BTEE precursor^[30]. The ratio between the different signals is $T^3: T^2: T^1: T^0 = 27: 43: 25: 5$, being the T^3/T^2 ratio around 0.63 , which points out the low degree of framework crosslinking under the synthetic conditions used and also the low amount of Si-OH

groups. No signals corresponding to Q^n species, $[\text{Si}(\text{OSi})_n(\text{OH})_{4-n}]$, can be observed indicating that all the silicon atoms are covalently bonded to carbon atoms^[30].

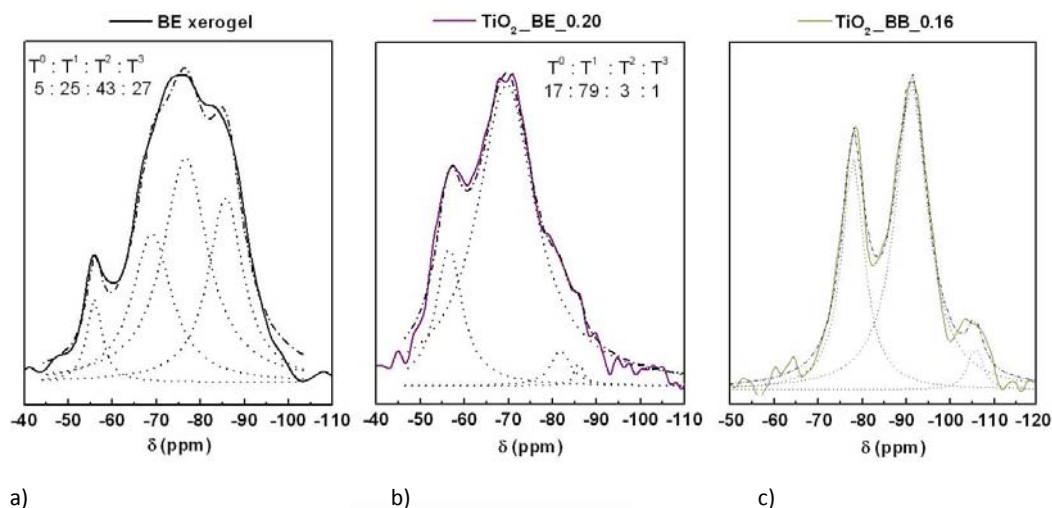


Figure 6.2. ^{29}Si NMR spectra of a BE organosilica xerogel prepared under the same conditions than hybrid titania-organosilica samples (a), and the titania-organosilica $\text{TiO}_2\text{-BE}_0.20$ (b) and $\text{TiO}_2\text{-BB}_0.20$ (c).

The ^{29}Si NMR spectrum of $\text{TiO}_2\text{-BE}_0.20$ sample is very similar to that corresponding to the BE organosilica xerogel, showing the four T^m peaks at: T^3 , $\delta = -86.0$ ppm; T^2 , $\delta = -81.2$ ppm; T^1 , $\delta = -69.6$ ppm, and T^0 , $\delta = -56.6$ ppm (figure 6.3b). In this case, the ratio between the different signals is $T^3:T^2:T^1:T^0 = 1:3:79:17$, being the T^3/T^2 ratio around 0.33. Taking into account both the FTIR and XPS results (figure 6.1 and 6.3), the T^m signals can be also attributed to $[\text{RC-Si}(\text{OSi})_m(\text{OTi})_{3-m}]$, as it has been previously reported for Zr or Ti incorporation in silica materials^[31], which could explain the high ratio of T^0 species as $[\text{RC-Si}(\text{OTi})_a(\text{OH})_{3-a}]$. Thus, the BE titania-organosilica exhibits a higher fraction of incompletely cross-linked T^1 and T^0 framework, as previously observed for other titania-silica aerogels^[24] and titania-silica

oxides prepared by condensation of titania and silica precursors in absence of surfactant^[6,32] with no evidence for the presence of Si-C bonds during the sol-gel synthesis.

The ²⁹Si NMR spectrum of TiO₂_BB_0.16 sample (figure 6.2c), however, shows two signals at -78.8 ppm and -91.6 ppm. The area of the small peak, which appears around -110 ppm, is lower than 4% and thus we consider of minor importance. Inagaki et al.^[33] first reported the use of the BTEB precursor for the synthesis of a PMO by using a cationic surfactant in alkaline conditions, where T³ and T² signal appeared around -80.7 ppm and -71.6 ppm, respectively. The second resonance, around -91.7 ppm, can be attributed to Q² [(OH)₂Si(OSi)₂] sites^[25], suggesting a partial Si-C bond cleavage during the sol-gel synthesis. Similar features were observed by Fan et al.^[11] for a mesoporous titania modified with a lower amount of BTEB precursor.

In fact, no Q^m signals were observed for the organosilica xerogels synthesized under these conditions. Smith et al.^[34] showed that titanium act as a network former in TiO₂-ZrO₂-SiO₂ sol-gel materials and the Q^m signals can be associated with corresponding mTi, where species with *m* next-nearest-neighbour titanium have a negligible effect on the shift. This affirmation is supported by calculations made on Ti-substituted silicalite by Ricchiardi and Sauer^[35], who observed that the isotropic chemical shift of 1 next-nearest-neighbour titanium atom is only around 1 ppm. Thus the Q^m signal could also be due to titanium being part of the network and not only to Si-C cleavage during the sol-gel process.

Surface characterization of samples was performed by XPS measurements. Figure 6.3 shows XPS spectra of the TiO₂_BE_0.20 and TiO₂_BB_0.16 materials in comparison with the control TiO₂. Spectra in the Ti 2p region of all samples shows two signals at around 458 eV and 464 eV, typical of Ti(IV) in TiO₂, that are usually

related to Ti_{Oh} sites as with anatase, while no signals corresponding to Ti_{Td} sites at 460.5 and 466.2 eV have been found (figure 6.3a)^[36].

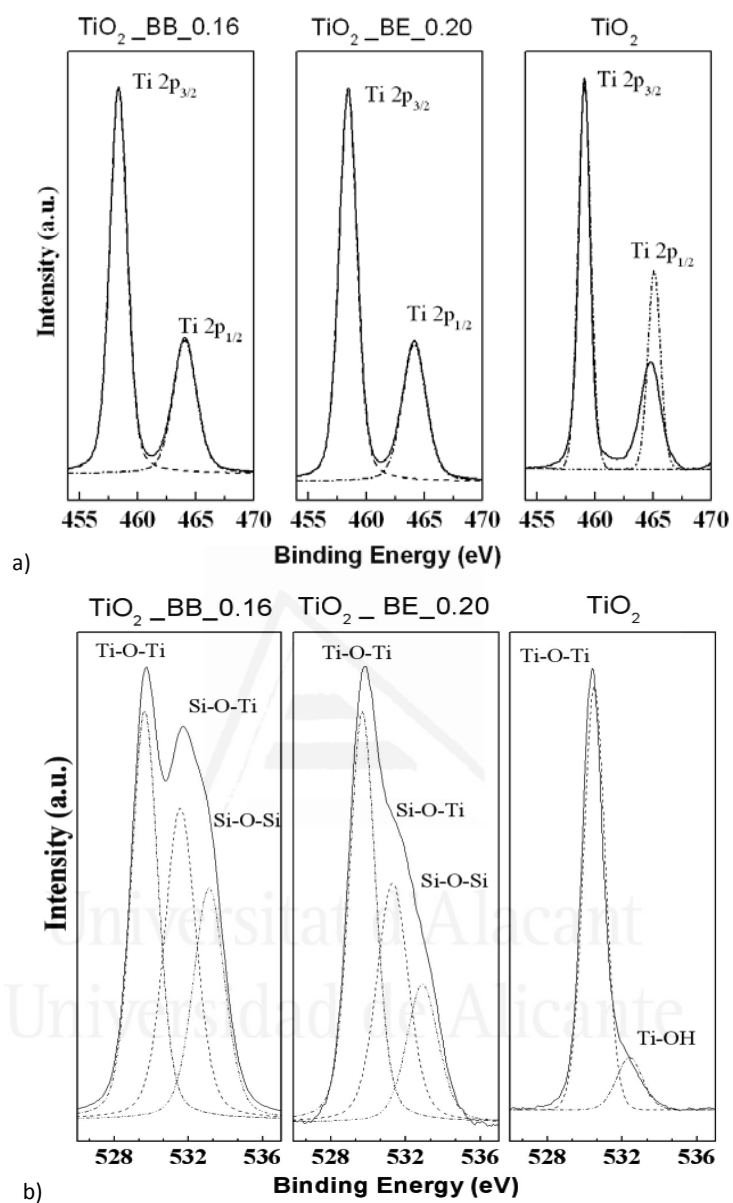


Figure 6.3. XPS spectra in the Ti2p (a) and O1s (b) regions of $\text{TiO}_2_{\text{BE}_0.20}$ and $\text{TiO}_2_{\text{BB}_0.16}$ samples as compared with those corresponding to control TiO_2 .

The O1s XPS spectra of all samples show significant differences (figure 6.3b). The control TiO₂ sample shows the typical O²⁻ peak associated to Ti-O-Ti bonds of titania at 530.4 eV and a small peak (15% of the area of the total) at 532 eV which can be attributed to Ti-OH species^[37]. Titania-organosilica samples, however, show three peaks at around 529 eV, 531 eV and 533 eV, which have been assigned to Ti-O-Ti, Ti-O-Si and Si-O-Si species, respectively^[31,38]. Probably, there would be a small contribution of Ti-OH species since the control titania showed a peak at around 532.5 eV. Unfortunately, that peak couldn't be identified after trying to fit the fourth individual peaks of this region, probably due to its small contribution. The relative ratios of the surface species were estimated from the areas under the Lorentzian curves to be Ti-O-Ti: Ti-O-Si: Si-O-Si = 47.2: 33.4: 19.3 and 38.7: 35.1: 26.2 for TiO₂_BE_0.20 and TiO₂_BB_0.16, respectively, which supports the co-condensation of titania and organosilica precursors, as stated by FTIR and NMR measurements.

The XRD spectra of these new titania materials (figure 6.4) indicate anatase structure with its typical angles ($2\theta = 25.3^\circ, 37.8^\circ, 48.05^\circ$ and 54.5°) and a $d_{101} = 0.35$ nm^[39,40], with a distorted network for the highest organosilane precursor content, as previously reported for BTEB and BTEE-titania based systems^[11]. The broad XRD peaks indicate that the as-synthesized materials are composed of nanoparticles, whose corresponding particle size determined using the Scherrer equation is in the 6-10 nm range (table 6.1). A slightly increase in the crystalline domain was observed in the hybrid materials, when compared to the control TiO₂, in good agreement with the decrease in the interparticular diameter determined from adsorption measurement (entry d_p in table 6.1).

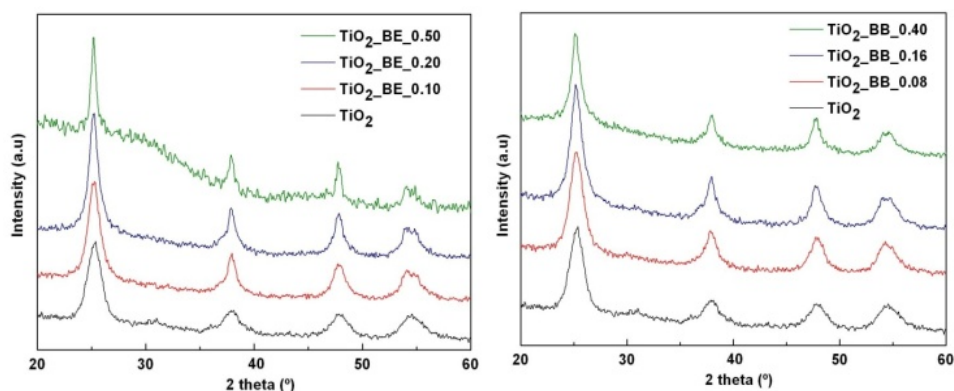


Figure 6.4. XRD patterns of the titania-organosilica materials prepared with different amount of: BTEE precursor, $\text{TiO}_2\text{-BE}$ samples (left) and BTEB precursor, $\text{TiO}_2\text{-BB}$ samples (right). XRD spectra are shifted for clarity.

The accessibility of the reactive sites is a key parameter for catalytic applications and it is related to the porosity presented in the samples. The porosity of a material is directly proportional to its surface area and therefore to the accessibility of the reactive sites. It should be remembered that all samples herein described are synthesized without the use of surfactants. Except for those materials with the higher Si/Ti content, all the materials show Type IV isotherms with a similar shape, indicative of their mesoporous nature, as confirmed by TEM (figure 6.6, table 6.1).

The textural properties of both organosilica precursors are similar to those of the control titania. In fact, the pore diameter decreases with the organosilica incorporation in line with the increase of the crystalline domain size, determined by XRD (table 6.1). These results support the incorporation of the organosilane components in the titania framework and not between the titania nanoparticles because the increase of the crystalline domain are related with the co-condensation of both precursors and the formation of the Ti-O-Si bond, instead of the typical Ti-O-Ti, thus proving the effectiveness of the synthetic route herein proposed and the

potential catalytic activity of these materials. However, for the highest organosilane precursor content (samples $\text{TiO}_2\text{-BE}_0.50$ and $\text{TiO}_2\text{-BB}_0.40$), the isotherms do not show the hysteresis loop at intermediate relative pressures and the total volume is lower than for the other titania-organosilica materials. In $\text{TiO}_2\text{-BE}_0.50$ and $\text{TiO}_2\text{-BB}_0.40$ samples, the content of the organosilica precursor is extremely high, BE/ TiO_2 and BB/ TiO_2 mass ratios ca. 100%, in agreement with the distorted XRD spectra and the absence of surfactant during the synthesis process and TEM analysis (figure 6.6e).

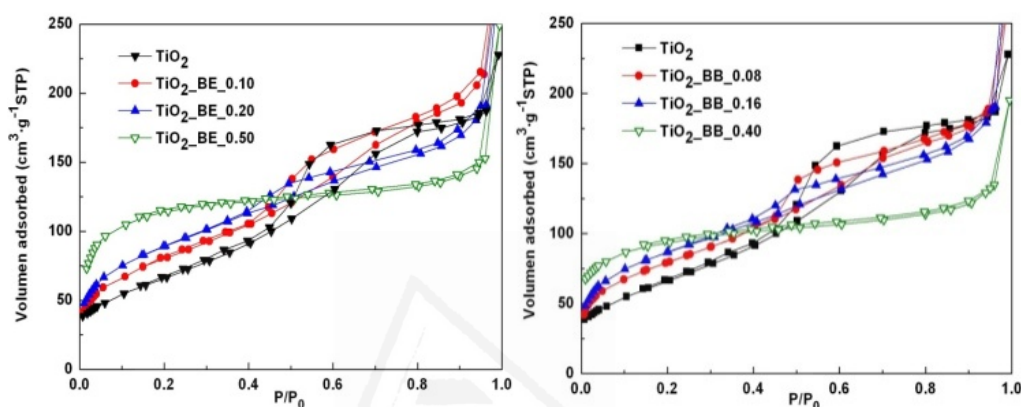


Figure 6.5. Representative adsorption/desorption isotherms at 77K of titania-organosilica materials prepared with different amount of: BTEE precursor (left), $\text{TiO}_2\text{-BE}$ samples and BTEB precursor (right), $\text{TiO}_2\text{-BB}$ samples.

TEM analysis of the titania-organosilicas with low-middle organosilica precursor content clearly confirm the crystalline structure of these materials and their nanoparticle morphology with an average size of 6.4-11.6 nm (figure 6.6). However, those samples with highest organosilane precursor content (samples $\text{TiO}_2\text{-BE}_0.50$ and $\text{TiO}_2\text{-BB}_0.40$) nanoparticles are significantly agglomerated, which is in agreement with their isotherms, being not possible to determine the particle size by TEM (figure 6.6e).

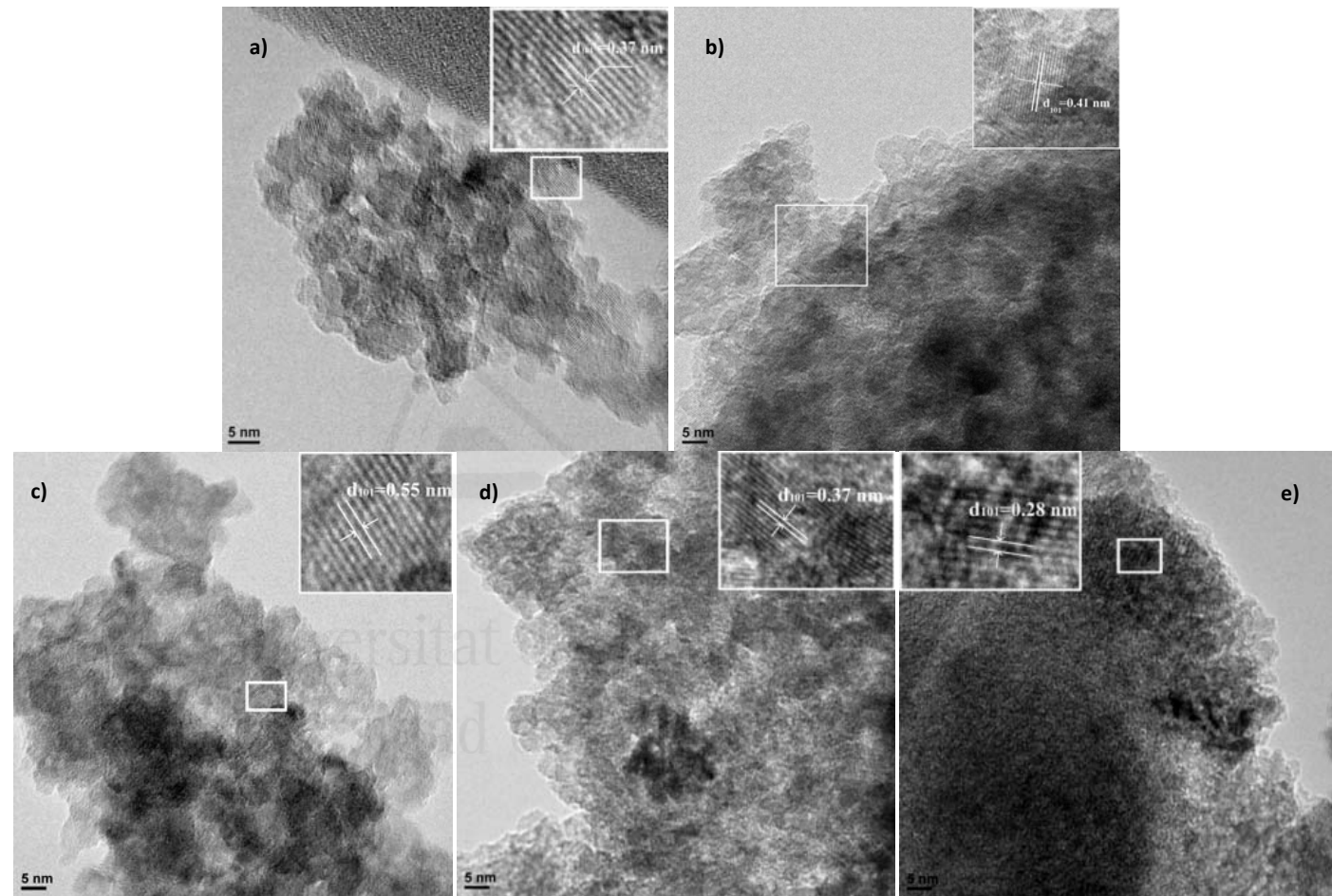


Figure 6.6. Representative TEM micrographs of control TiO_2 (a), $\text{TiO}_2_{\text{BB}_0.16}$ (b) and TiO_2_{BE} samples: $\text{TiO}_2_{\text{BE}_0.10}$ (c) $\text{TiO}_2_{\text{BE}_0.20}$ (d) and $\text{TiO}_2_{\text{BE}_0.50}$ (e). Scale bar = 5 nm.

6.3.2. Structural and physico-chemical changes after calcination

After calcination, control titania as well as titania-organosilane with the highest silica content collapse as evidenced by the significant reduction in N_2 uptake capacity at 77K (figure 6.7), indicating the low thermal stability of these samples. Accordingly, the BET areas of these samples decrease from ca. 250-300 m^2/g (before calcination) to 55-150 m^2/g (after calcination) (compare table 6.1 and table 6.2). This is similar to what was previously observed for other titania-silica composites synthesized without using surfactant^[9,41].

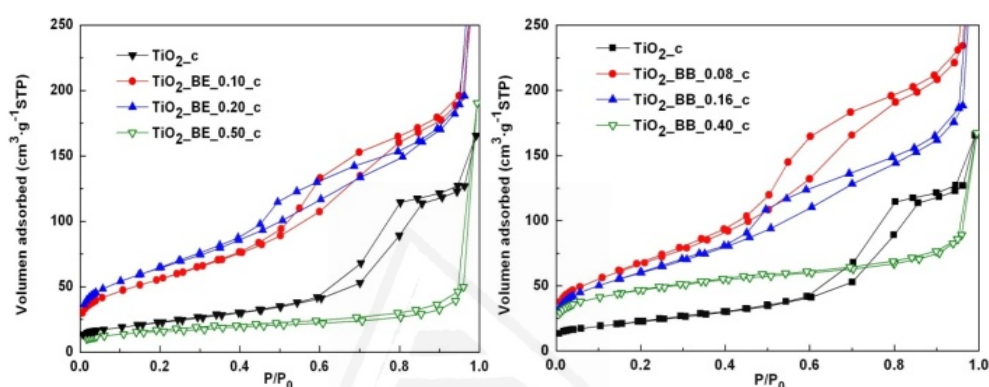


Figure 6.7. Representative adsorption/desorption isotherms at 77K of calcined titania-organosilica materials: $TiO_2_BE_c$ (left) and $TiO_2_BB_c$ materials (right).

Loryuenyong et al.^[12] analysed the effect of calcination temperature on synthesized mesoporous titania nanoparticles synthesized by sol-gel, using ethanol as solvent.

These authors observed a significant collapse of the pore structure and an increase of particle size of the titania nanoparticles after calcination of titania a 500 °C^[12], due to sintering with the consequent decrease in BET area. Surprisingly, titania-organosilica samples with Si/Ti molar ratios between 0.08 and 0.20, are

thermally stable up to 550 °C, in spite of the calcination of the organic fragments, with only a slightly decrease in the textural parameters of the as-synthesized samples (compare table 6.1 and table 6.2). Although the organosilica precursors decompose at lower temperatures (BTEE at 280 °C and BTEB at 400 °C), experiments were carried out at 550 °C to evaluate if the titania-organosilicas crystalline structure would be transformed from the anatase to the rutile phase.

Table 6.2. Nomenclature, textural and structural parameters of the calcined titania-organosilica materials prepared with different BTEE (TiO₂_BE) and BTEB (TiO₂_BB) amount, as compared to the control TiO₂.

Sample		d_p^a (nm)	V_p^b (cm ³ /g)	A_{BET}^c (m ² /g)	$d_{101}^{XRD, d}$ (nm)	$D^{XRD, e}$ (nm)	$\Phi^{TEM, f}$ (nm)
TiO ₂ _c	---	8.8 (5-19)	0.20	82	0.35	13.1	17.2
TiO ₂ _BE_	0.10c	6.0 (2-11)	0.30	204	0.35	8.0	**
	0.20c	4.6 (2-10)	0.30	232	0.35	10.3	11.1
	0.50c	*	0.07	55	0.35	12.0	**
TiO ₂ _BB_	0.08c	6.0 (2-10)	0.36	245	0.35	7.1	**
	0.16c	4.6 (2-10)	0.29	217	0.35	9.8	12.1
	0.40c	*	0.13	155	0.35	10.1	**

^aAverage mesopore diameters were estimated from the adsorption branch of the nitrogen isotherm using the BJH method. ^bPore volume from the isotherms at relative pressure of 0.95 (see chapter 3). ^cThe BET surface area was estimated by multipoint BET method using the adsorption data in the relative pressure (P/P_0) range of 0.05–0.30. ^dAnatase spacing (d_{101}) calculated using Bragg equation. ^eDomain size of the particle calculated from X-ray diffraction using Scherrer equation. ^fParticle size estimated from TEM images using Gatan software. *Pore size distribution is too broad to determine an average pore size value. **Non determined.

The anatase structure with its typical angles and the d_{101} spacing around 0.35 nm is maintained after calcination of all samples (table 6.2, figure 6.8). A XRD shoulder appears at $2\theta = 31^\circ$, the area of which is too small to perform any calculations, that is

related to the (121) peak of brookite phase forming during the calcination at 550 °C, as previously reported^[42,43], associated with an increase in the particle size. The results suggest both that the incorporation of the organosilane precursor stabilizes the titania network and a threshold of organosilane precursor exists equivalent to Si/Ti molar ratio of ca. 0.2 under the synthetic conditions herein employed.

As expected, domain size increases after calcination. Interestingly, both the crystalline domain size as well as the particle size, determined by TEM, for calcined control titania are higher than those determined for the titania-organosilica samples (table 6.2), which could play an important role in the photocatalytic properties of these new materials.

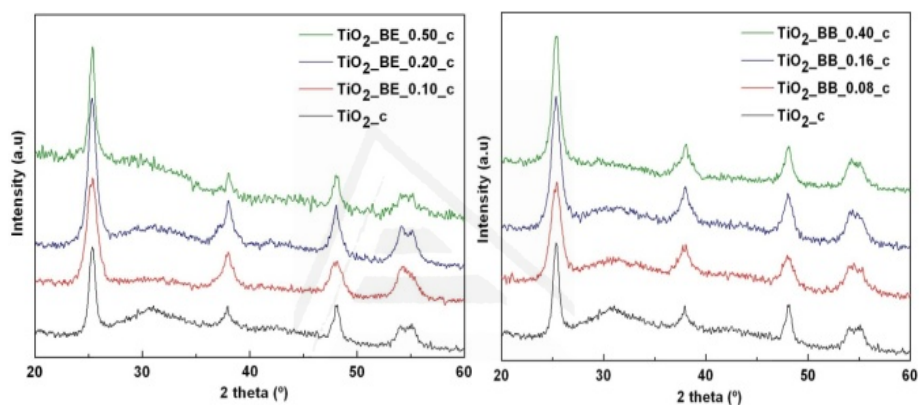


Figure 6.8. XRD patterns of calcined titania-organosilica materials: TiO₂_BE_c (left) and TiO₂_BB_c materials (right). XRD spectra are shifted for clarity.

Surface analysis of calcined samples by XPS is shown in figure 6.9. Spectra in the Ti 2p region of the calcined control tio₂ (figure 6.9a, bottom) shows the two signals associated to Ti(IV) species in octahedral coordination at 458.9 and 464.6 ev. In the case of titania-organosilica calcined samples, however, there are three signals at ca. 458 ev, 460 ev and 465 ev, being the ratio between the areas 20:50:30 and 10:60:30

for BE and BB_based titania, respectively (figure 6.9a, middle-top). Peak at at 460 eV is assigned to t_{td} sites^[36]. So, XPS results suggest that there is a change of ca. 50% of Ti(IV) surface species coordination after calcination. As previously reported, the displacement of the peak at 465 eV at higher binding energies could be attributed to both, a higher interaction between the titania and silica components and to a change in the Ti(IV) coordination^[9,41b].

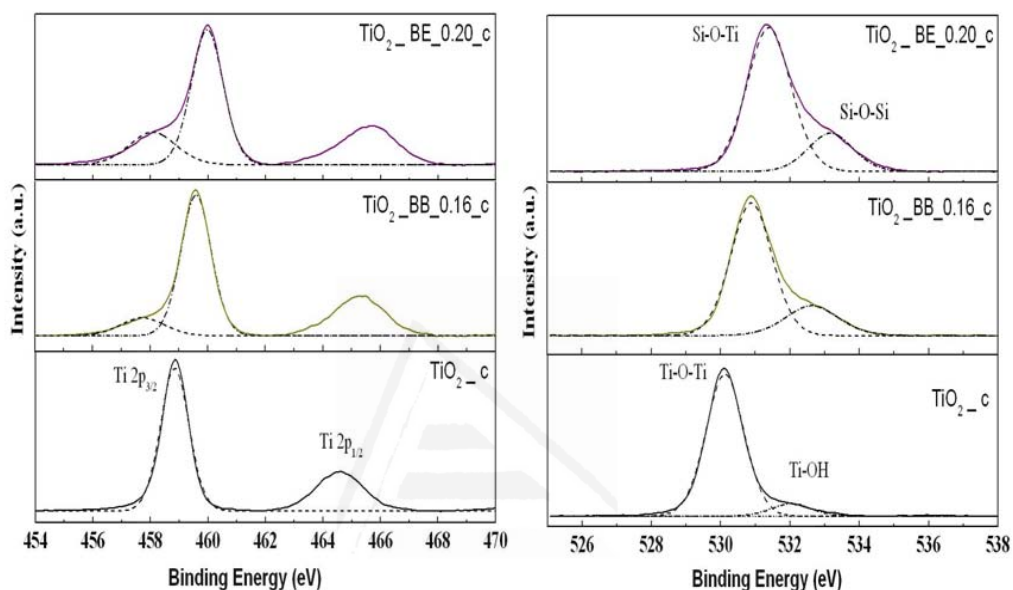


Figure 6.9. XPS spectra in the Ti2p (left) and O1s (right) regions of calcined $TiO_2_{BE_0.20}$ and $TiO_2_{BB_0.16}$ samples as compared with those corresponding to control TiO_2 after calcination.

Similarly, O1s peaks in XPS spectra shift from 530.1 eV (Ti-O-Ti bond) and 532.0 eV (Ti-OH bond) in calcined TiO_2 , to 530.9 (531.4) eV and 532.6 (533.2) eV for BB (BE) based titania (figure 6.9b). Usually, Ti-O-Ti, Ti-O-Si and Si-O-Si species appear at 529 eV, 531 eV and 533 eV, respectively^[31,38], but there is an initial shift of Ti-O-Ti peak up to 530 eV in our calcined control titania which makes difficult to determine if the

main O1s peak in BE and BB_based materials is due to Ti-O-Ti or Ti-O-Si. Kim et al.^[9] obtained similar Ti2p and O1s XPS spectra for titania-silica composites with Si/Ti molar ratio of 0.2, similar of those herein employed, attributing the O1s peaks to the strong interaction between the silica and titania components with no presence of Ti-O-Ti at the surface.

Guo et. al.^[41b] also obtained similar results for titania-silica composites prepared from wollastonite and titanium sulphate in the absence of any surfactant. These results are consistent with the different reactivity of titania and organosilica precursors during the hydrolysis and condensation reactions in the sol-gel process, being the hydrolysis of the titania precursor much faster than that corresponding to silica precursor^[24].

As concluded from our NMR studies, as-synthesized titania-organosilica samples showed a low degree of framework crosslinking and a higher fraction of incompletely cross-linked T¹ and T⁰ framework. So the calcination process could help the BE and BB precursors to reach a higher degree of framework crosslinking. It is well known that Si is preferentially located on the surfaces of Ti-rich mixed oxides^[6]. This suggests that the sintering of anatase nanoparticles during calcination occurs through the reaction between the superficial Si-OR and Si-OH groups condensed with the Ti-O bonds during calcination having a strong interaction between silica and titania components, which seems to be even higher in case of titania-BTEE samples, probably due to the lower volume of ethylene chains in comparison to the phenylen ones of BTEB.

6.3.3. Optical properties

DRUV spectra of all the samples showed an abrupt decrease in the reflectance at the wavelength corresponding to the band gap energy. For the quantitative estimation of the band-gap, the reflectance data were converted into the equivalent

absorption coefficient using the Kubelka-Munk formalism, as it was described in chapter 3. For band gap calculations $F(R) = (F(R') \cdot h\nu)^x$ vs $(h\nu)$ plots for titania-organosilica samples before and after calcination are shown in figure 6.10a and 6.11a, respectively.

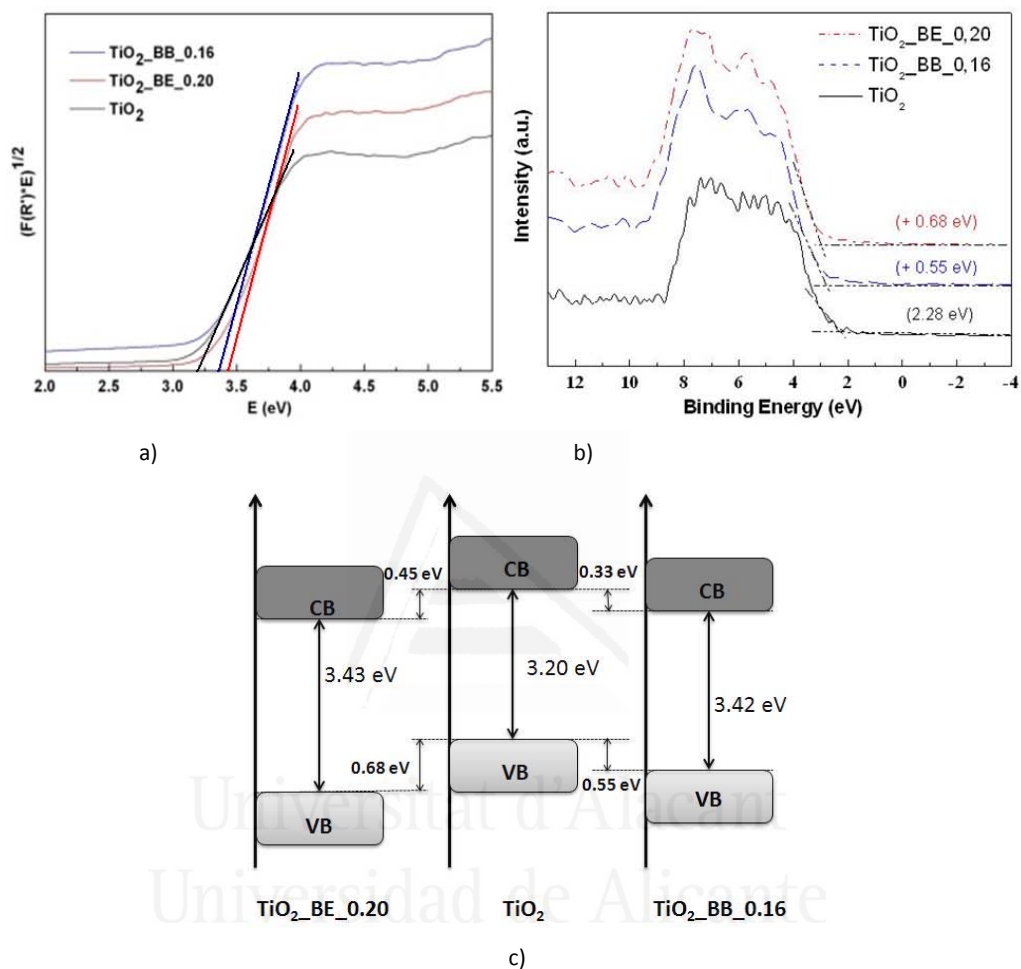


Figure 6.10. Plot of the transformed Kubelka-Munk function versus the energy of light adsorbed (a), valence band XPS spectra (b) and schematic illustration of the DOS (c) of as-synthesized titania-organosilica nanoparticles as compared with the control TiO_2 .

Since TiO₂ is considered an indirect semiconductor, the value for x is $\frac{1}{2}$ and as previously reported^[42, 44-47], the intercept of the tangent to $F(R)$ vs $h\nu$ plot gives a good estimation of the band gap energy for these materials. The maximum of the VB determined from the XPS spectra in the valence band region was used for drawing the density of states (DOS scheme) shown in figure 6.10c. In figure 6.10b, titania XPS spectra show the edge of the maximum energy at about 2.28 eV, slightly higher than for other titania samples^[37a]. As expected, the band gap of the hybrid titania-organosilica samples increases up to 3.42–3.43 eV due to the presence of the insulating Si atoms^[48].

Table 6.3. Band gap energies (E_g), pseudo-first order kinetic constant values (k') and regression coefficients (R) of the R6G degradation reaction under UV radiation for the as-synthesized titania-organosilica catalysts as compared with control titania, TiO₂.

Sample	E_g (eV)	$k' \cdot 10^3, {}^a$ (min ⁻¹)	R^{*b}	$k'/k'_{TiO_2}{}^c$	%Conversion ^d			
					1h	2h	3h	
TiO ₂	---	3.24	7.2 ± 1.9 (6.3)	0.9897	---	31.1	52.8	67.7
TiO ₂ _BE_	0.10	*	4.5 ± 0.5 (5.3)	0.9812	0.6	27.6	47.3	61.7
	0.20	3.43	10.7 ± 2.5 (10.1)	0.9935	1.5	45.7	70.4	83.8
	0.50	*	8.0 ± 2.0 (9.7)	0.9838	1.1	44.6	69.1	82.7
TiO ₂ _BB_	0.08		9.5 ± 1.5 (11.4)	0.9945	1.3	49.8	74.7	87.2
	0.16	3.42	7.9 ± 1.4 (9.7)	0.9963	1.1	44.2	68.8	82.6
	0.40	*	14.5 ± 3.5 (17.8)	0.9892	2.0	65.3	88.1	95.9

^aPseudo-first order rate constant of the degradation of an aqueous solution of R6G obtained as the average of a minimum of three runs. Values in brackets indicate the k' obtained from figure 6.12a and 6.12b. ^bRegression coefficient for the same degradation reaction as paragraph *a*. ^cRatio between the average k' values of the as-synthesized titania-organosilicas and the average k' value determined from the control sample. ^dDegree of conversion (%) achieved by samples after 1 h, 2 h and 3 h of reaction. *Non determined.

However, no significant change in the band gap value is observed when TiO_2 and SiO_2 were physically mixed by grinding^[49]. Furthermore, the use of Si in the synthesized samples also shifted their valence and conduction band edges.

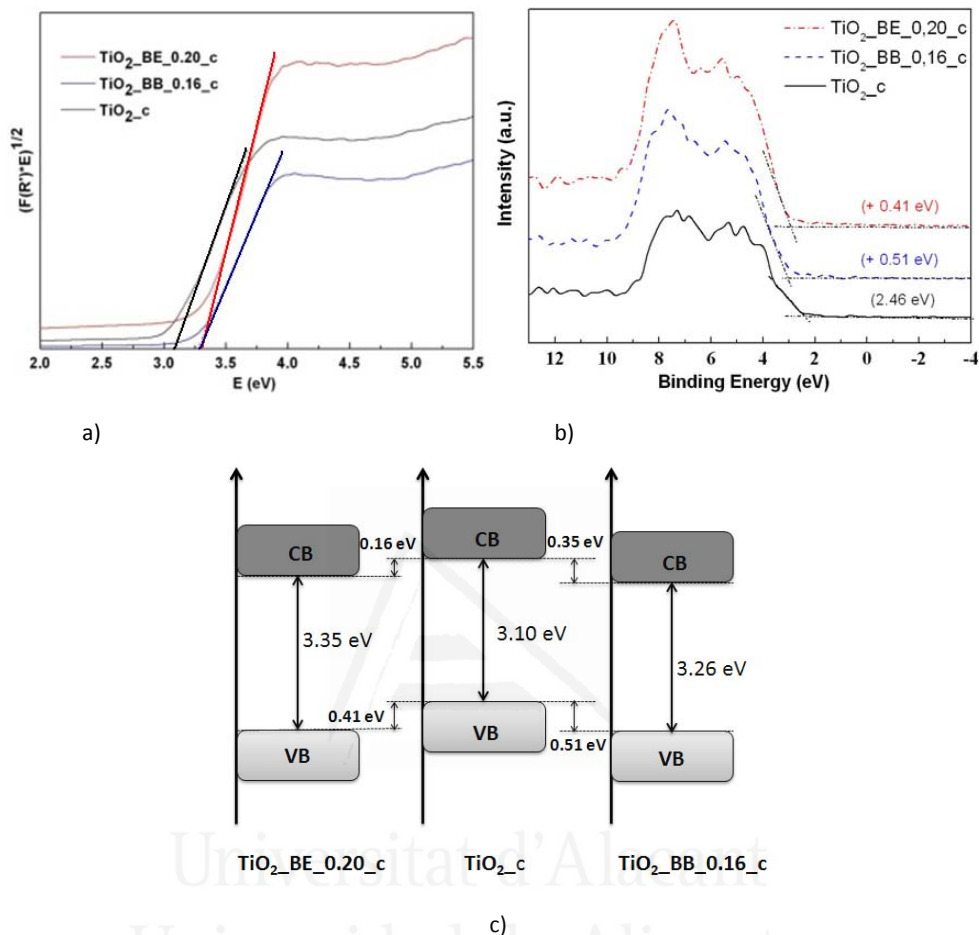


Figure 6.11. Plot of the transformed Kubelka-Munk function versus the energy of light adsorbed (a), valence band XPS spectra (b) and schematic illustration of the DOS (c) of calcined titania-organosilica nanoparticles as compared with calcined TiO_2 nanocrystals.

Both the shift of the band edge positions in the titania-organosilica material and the increase in the band gap of these materials can be attributed to an electronic

interaction through the Si-O-Ti bond^[48]. The valence band maximum energy slightly shifts toward the vacuum level of approximately 0.68 eV and 0.55 eV for BE and BB-based samples, respectively. A schematic illustration of the effect of organosilica incorporation in titania network is shown in figure 6.10c. These anodic band edge shifts were confirmed by XPS measurements.

After calcination, control titania shows a slightly decrease of the band gap energy (table 6.4, figure 6.11), in agreement with the appearance of brookite phase^[50].

The valence and conduction bands of the calcined titania-organosilica materials are shifted, which has been previously associated with a strong electronic interactions between the titania and silica through the surface Si-O-Ti bonds^[48]. As observed by XPS, the main peak in the O1s XPS spectra was related to Si-O-Ti bonds.

Table 6.4. Band gap energies (E_g), pseudo-first order kinetic constant values (k') and regression coefficients (R) of the R6G degradation for the calcined titania-organosilica catalysts as compared with calcined titania sample, $\text{TiO}_2\text{-c}$.

Sample	E_g (eV)	$k' \cdot 10^3, {}^a(\text{min}^{-1})$	R^{*b}	$k'/k'_{\text{TiO}_2}{}^c$	%Conversion ^d			
					1h	2h	3h	
$\text{TiO}_2\text{-c}$	---	3.10	6.3 ± 1.24 (5.8)	0.9790	---	29.6	50.3	64.9
$\text{TiO}_2\text{-BE-}$	0.10c	3.27	29.5 ± 7.7 (26.9)	0.9981	4.7	80.2	96.1	99.2
	0.20c	3.35	25.7 ± 7.4 (27.3)	0.9928	4.1	80.8	96.3	99.3
	0.50c	3.30	21.0 ± 8.0 (26.6)	0.9982	3.5	79.8	95.9	99.2
	0.08c	3.28	14.3 ± 3.2 (15.1)	0.9921	2.3	59.8	83.8	93.4
$\text{TiO}_2\text{-BB-}$	0.16c	3.26	30.5 ± 6.6 (30.3)	0.9941	4.8	83.7	97.4	99.6
	0.40c	3.22	20.3 ± 1.8 (18.8)	0.9954	3.2	67.5	89.5	96.6

^aPseudo-first order rate constant of the degradation of an aqueous solution of R6G obtained as the average of a minimum of three runs. Values in brackets indicate the k' obtained from figure 6.12c and 6.12d. ^bRegression coefficient for the same degradation reaction as paragraph *a*. ^cratio between the average k' values of the as-synthesized titania-organosilicas and the average k' value determined from the control sample. ^dDegree of conversion (%) achieved by samples after 1 h, 2 h and 3 h of reaction.

However, in the calcined titania-organosilica samples, the valence and conduction bands shifts are smaller than in the as-synthesized samples, which can be tentatively related to the change in Ti(IV) coordination on the surface of the material. This possibility is supported by XPS, which confirm the coordination change in Ti(IV) and the increase in crystal size.

6.3.4. Liquid-solid regime photocatalytic activity of the as-synthesized and calcined titania-organosilica samples

The as-synthesized samples showed a similar photocatalytic activity in the R6G degradation reaction under UV radiation than the control titania (figure 6.12a-b and table 6.3). In the case of the calcined samples, the catalytic activity of titania-organosilicas is enhanced 2-5 times when is compared with the control titania $\text{TiO}_2\text{-c}$ (figure 6.12c and d).

The total bleaching of the dye takes place after ca. 3 h of irradiation in the case of hybrid titanias against the more than 12h needed for the control sample. TOC measurements carried out the solutions before and after irradiation in the presence of the catalysts showed a partial degradation of the total organic dissolved carbon (up to ca. 50%) at least when the dye was totally bleached.

It is difficult to establish the relationship between the different photoactivity of the various samples with their structural and physico-chemical features, especially when a dye is the substrate to degrade because of the interaction between the dye and titania. Indeed, when a dye is irradiated in the presence of a photocatalyst, along with the classical photocatalytic process, a photo-adsorption of the dye on the titania surface followed by a dye sensitization can occur^[51]. The photo-adsorption of the dye, unfortunately is difficult to quantify and could affect the photoactivity. Probably,

in the samples herein described, the photo-adsorption of the R6G on the titania-silica photocatalysts could be significantly.

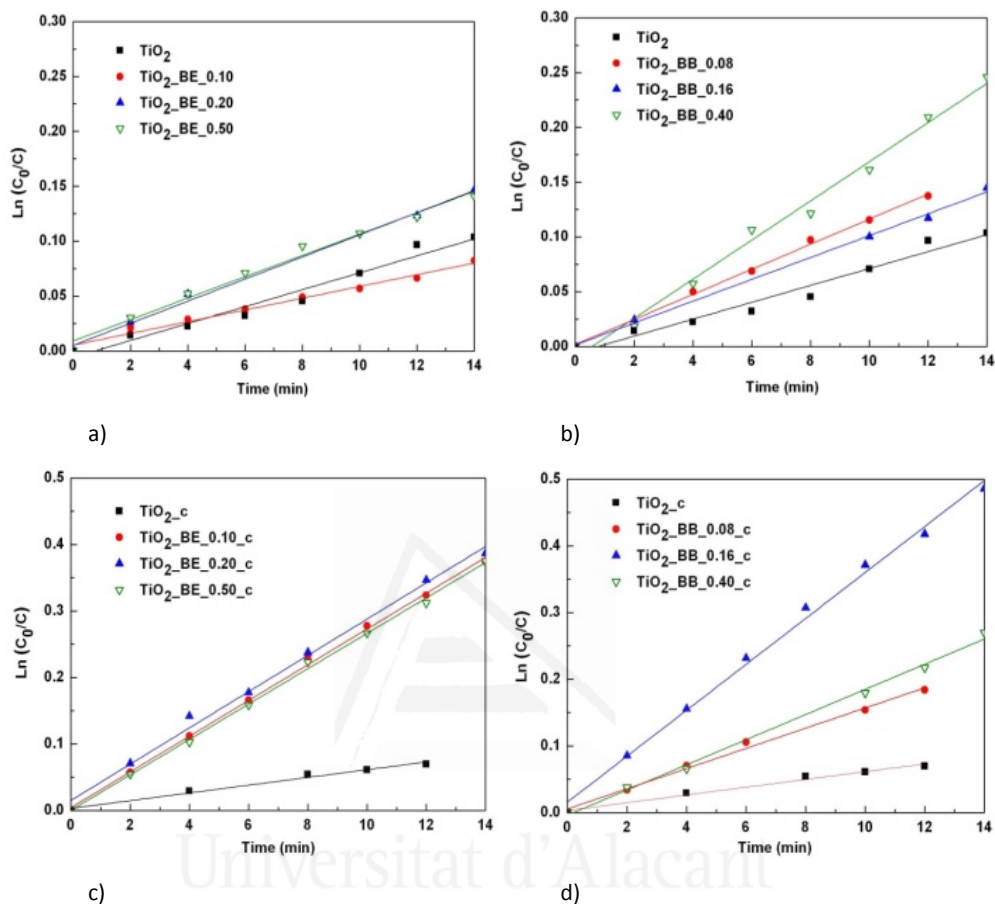


Figure 6.12. $\ln(C_0/C)$ vs. irradiation time for the as-synthesized catalysts, $\text{TiO}_2\text{-BE}$ (a) and $\text{TiO}_2\text{-BB}$ (b) and for the calcined photocatalysts, $\text{TiO}_2\text{-BE}_c$ (c) and $\text{TiO}_2\text{-BB}_c$ (d).

The incorporation of Si into TiO_2 structure causes an increase in the band gap energy of the titania-silica materials due to a modification in the electronic structure of these materials. These new electronic properties are in agreement with

the formation of a Ti-O-Si bond. This insight can justify the enhancement of the photocatalytic activity observed for the calcined hybrid titania-organosilica with respect to both uncalcined samples as well as the control TiO₂ sample. NMR and XPS results show that the formation of the Ti-O-Si bond is higher in the titania-organosilica samples after calcination which could explain the high photocatalytic properties of these materials.

Although the mechanism remains still unclear, the change in the electronic properties as well as the predominance of Ti-O-Si bonds, with Ti in both Oh and Td coordination, leads to an increment of the effective positive charge on Ti atoms, which could be responsible of the enhancement of the photocatalitical properties^[13,14].

6.3.5. Gas-solid regime photocatalytic activity of the calcined titania-organosilica samples

Taking into account the great results obtained with the calcined titania-silica materials in the R6G degradation reaction under UV radiation, the photocatalytic activity of these materials was also evaluated for the partial oxidation reaction of propylene to yield propylene oxide (PO). Blank reactivity experiments were performed under the same experimental conditions used for the photo-reactivity runs but in the absence of photocatalyst, oxygen or light. No reactivity was observed in each one of these cases, that it was concluded that the contemporary presence of O₂, catalyst, and irradiation was needed for the occurrence of propylene oxidation process.

Three selected samples were tested: the TiO₂_BE_0.20_c, the TiO₂_BB_0.16_c, and the control TiO₂_c. No adsorption of propylene was observed in any of the

samples, indeed after the equilibration time, the experimental measurement of the initial propylene concentration coincides with the nominal initial amount.

The photocatalytic reaction proceeded, in any case, with the formation of the following species: propylene oxide (PO), acetaldehyde (AA), acetone (AC), propionaldehyde (PA) (figure 6.13). Carbon dioxide was also obtained as final oxidation product. The formation of these species was already reported for the photocatalytic propene partial oxidation using V-Ti/MCM-41 as photocatalyst^[52].

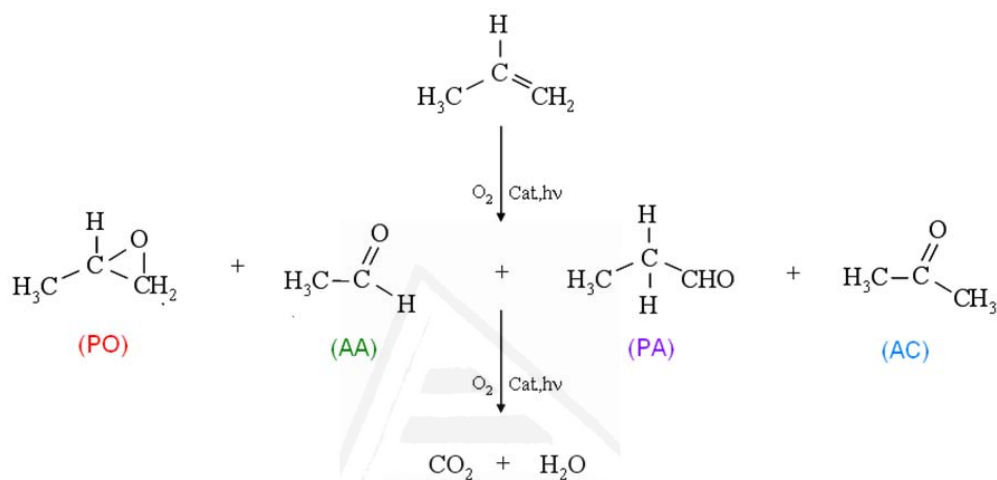


Figure 6.13. Reaction pathway of photocatalytic propene partial oxidation in the presence of the studied photocatalysts and UV radiation. Molecules in brackets are identified intermediate products.

The evolution of the products reported in figure 6.14 suggests that propylene was oxidized with the subsequent formation of (PO), (AA), (AC) and (PA). Consequently, four different types of active sites should exist on the catalyst. During the formation of (AA), methanol should also be formed albeit this species was not revealed probably because it was quickly oxidized to CO_2 .

Figure 6.14 shows that the behaviour of the three catalysts versus the partial oxidation of propylene was different. By using $\text{TiO}_2\text{_{BB}_0.16_c}$ as a catalyst, propylene oxide was the only intermediate observed during the first minutes of irradiation.

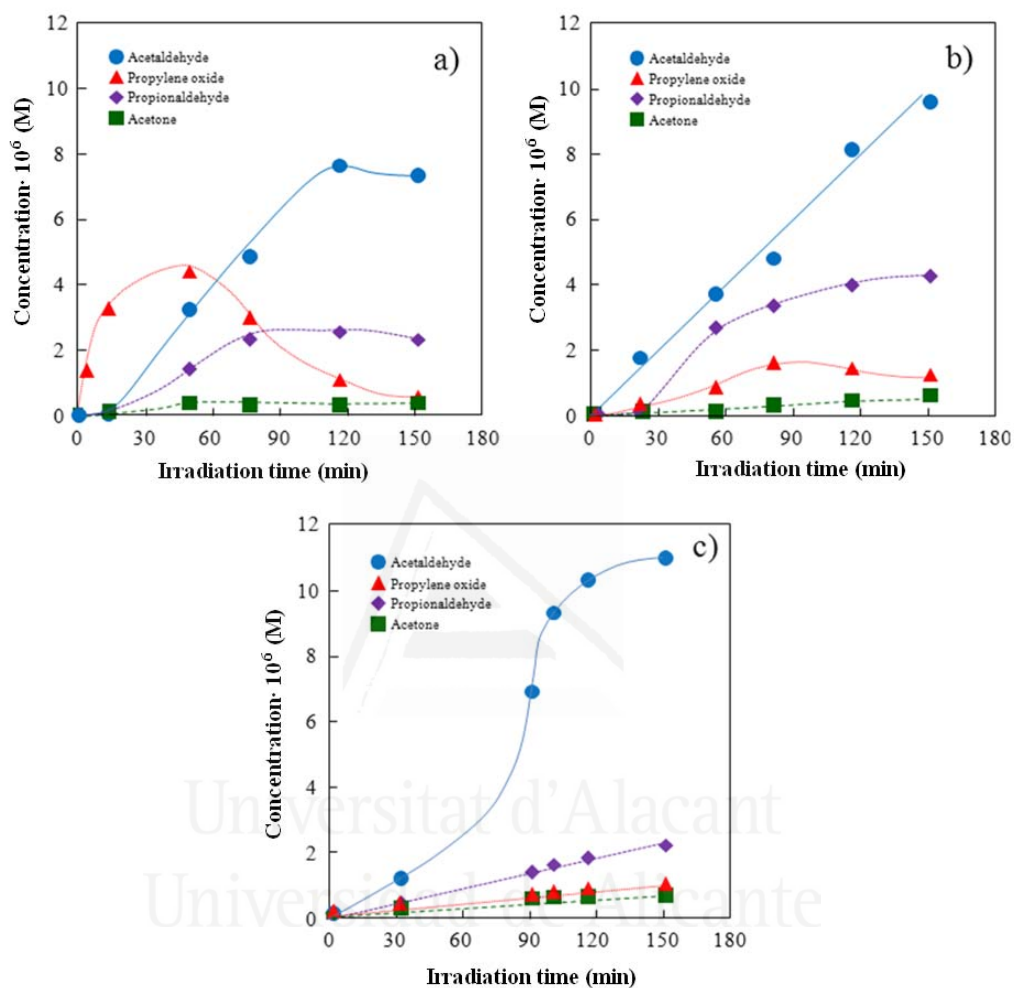


Figure 6.14. Evolution of acetaldehyde (blue), propylene oxide (red), acetone (green), and propionaldehyde (violet) during the irradiation time for runs carried out in the presence of: $\text{TiO}_2\text{_{BB}_0.16_c}$ (a), $\text{TiO}_2\text{_{BE}_0.20_c}$ (b) and control TiO_2_c (c).

On the contrary, for the other two samples, especially for the control $\text{TiO}_2\text{-c}$, the amount of propylene oxide formed was much less significant. Figure 6.14a also shows that acetaldehyde concentration increased during the 150 min of the run, reaching a maximum after ca. 120 min when $\text{TiO}_2\text{-BB}_0.16\text{-c}$ was used as photocatalysts. The evolution of propionaldehyde was very similar in the presence of the two titania-organosilica samples, whereas the formation of acetone was in any case very scarce.

The different evolution of the four products, particularly concerning the formation of propylene oxide and propionaldehyde, can be related to the presence of Ti-O-Si bonds in the titania-organosilica samples. Indeed, as already reported, the presence of silica in the photocatalyst is beneficial for the partial photo-oxidation of propylene oxide^[22]. Anyway, the selectivity to propylene oxide was ca. 36 % after 2 minutes of reaction with a 0.2 % propylene conversion in the presence of $\text{TiO}_2\text{-BB}_0.16\text{-c}$. These results are very interesting because, even if the conversion is low, no other intermediates were detected at this reaction stage.

It is worth reminding that the current experimental reaction conditions are extremely soft (green) corresponding to a solar irradiation device working at atmospheric pressure. The best results reported in literature^[22] are obtained at low pressure by considering the total amount of PO both in the gas-phase and that adsorbed on the catalysts surface.

After that Murata et al.^[22], in order to desorb the propylene oxide, heated the batch reactor at 573 K with the possible occurrence of a further catalytic reaction. Figure 6.14 shows that by increasing the irradiation time the amount of PO increase reaching a maximum after ca. 45 minutes of irradiation for the $\text{TiO}_2\text{-BB}_0.16\text{-c}$ sample (PO selectivity of 20 % and propylene conversion of 1.0 %). For higher irradiation time the amount of PO decreases (figura 6.14). On the other hand, when

TiO₂_BE_0.20_c was used as photocatalyst the evolution of PO was different even if the maximum was very similar.

In this case, the higher selectivity towards PO was only 1.4 % at 5.5% propylene conversion. The lower selectivity observed by using the TiO₂_BE_0.20_c catalyst can be due to the higher content of Ti. Indeed, as already reported, a lower loading of Ti favours the selectivity towards PO^[21,22]. Nijhuis et.al prepared TiO₂-SiO₂^[21,22] and ZnO-SiO₂^[21] samples with low amounts of TiO₂ and ZnO and confirmed that they were active for the propylene partial oxidation in the presence of oxygen and at room temperature (the photocatalyst bed achieved ca. 50 °C) and low pressure (30 torr oxygen and 15 torr propylene) in a batch photocatalytic reactor equipped with a 200 W Xe lamp. TiO₂-SiO₂ catalysts achieve a PO selectivity of 60% with a propylene conversion of 4.4%. In the case of ZnO-SiO₂ catalysts, the PO selectivity was 34% with a propylene conversion of 8.6%.

As far as the control TiO₂_c sample is concerned, the PO selectivity was always very low because the most abundant intermediate was always acetaldehyde. In this case the maximum propylene conversion observed after 2.5 h of irradiation was 8.5%.

6.5. CONCLUSIONS

A series of catalytically active anatase titania-organosilica nanoparticles were prepared by co-condensation of a titania precursor, TBOT, with different organosilica precursors, using mild conditions and in absence the surfactants. Co-condensation of both precursors and the subsequent Ti-O-Si bond formation have been confirmed by NMR, FTIR, and XPS, indicating that the organic moieties were incorporated in the structure of the titania.

Textural characterization of samples after calcination proves the high thermal stability of hybrid samples with low-middle organosilica precursor content, despite the absence of surfactant, due to a template effect created by the organosiliceous precursor incorporated.

The change in optical properties of these materials is probably associated to the change in Ti(IV) coordination due to the high proportion of Si-O-Ti bonds after calcination.

The photocatalytic degradation of R6G dye was carried out in liquid-solid regime by using both control TiO₂ and titania-organosilica photocatalysts. Photoreactivity experiments show that the dye degradation rate is up to 3-4 times higher when the calcined hybrid samples are used relative to both uncalcined samples and control TiO₂, probably associated to the change in the electronic structure of these samples.

The partial oxidation of propylene, carried out in gas-solid regime, shows that the hybrid materials are more efficient than the control TiO₂ in the formation of propylene oxide (TiO₂_BB_0.16_c 4 times better and TiO₂_BE_0.20_c two times). In particular, the catalyst TiO₂_BB_0.16_c showed in the first minutes of irradiation a high selectivity to PO.

6.6. REFERENCES

- [1] X. Gao, I.E. Wachs, *Catal. Today*, 1999, **51**, 233.
- [2] a) H. Park, Y. Park, W. Kim W. Choi, *J. Photochem. Photobiol. C* 2013, **15**, 1; b) H.E. Byrne, D.W. Mazyck, *J. Hazard. Mat.*, 2009, **170**, 915.
- [3] Y. Zhao, L. Xu, Y. Wang, C. Gao, D. Liu, *Catal. Today*, 2004, **93**, 583.
- [4] H. Chu, Y. Wan, D. Zhao, *Catal. Today*, 2009, **148**, 19.
- [5] C. Xie, Z. Xu, Q. Yang, B. Xue, Y. Du, J. Zhang, *Mat. Sci. & Eng. B*, 2004, **112**, 34.

- [6] a) Z.F. Liu, R.J. Davis, *Chem. Mater.*, 1997, **9**, 2311; b) Z.F. Liu, J. Tabora, R.J. Davis, *J. Catal.*, 1994, **149**, 117.
- [7] R.A. Aziz, L. Sopyan, *Indian J. Chem.*, 2009, **48A**, 951.
- [8] E. Rahmani, A. Ahmadpour, M. Zebarjad, *Chem. Eng. J.*, 2011, **174**, 709.
- [9] A. Hilonga, J.K. Kim, P.B. Sarawade, H.T. Kim, *Powder Tech.*, 2009, **196**, 286.
- [10] T. Nguyen, O. Yang, *Catal. Today*, 2003, **87**, 69.
- [11] X. Liu, J. Guo, L. Xiao, J. Fan, *Chem. Commun.*, 2010, **46**, 6729.
- [12] V. Loryuenyong, K. Angamnuaysiri, *Ceram. Int.*, 2012, **38**, 2233.
- [13] a) X. Gao, I.E. Wachs, *Catal. Today*, 1999, **51**, 233; b) J. Robertson, K. Xiong, S.J. Clark, *Thin solid films*, 2006, **496**, 1; c) A. Jaroenworuluck, N. Pijarn, N. Kosachan, R. Stevens, *Chem. Eng. J.*, 2012, **181**, 45; d) A. Mahyar, A. Behnajady, N. Modirshahla, *Indian J. Chem.*, 2010, **49A**, 1593.
- [14] a) C. Anderson, A.J. Bard, *J. Phys. Chem.*, 1995, **99**, 9882; b) C. Anderson, A.J. Bard *J. Phys. Chem.*, 1997, **101**, 2611.
- [15] S. Kim, W. Choi, *J. Phys. Chem B*, 2005, **109**, 5143.
- [16] Chemicals & Petrochemicals Manufacturer's Association of India, "Propylene" (<http://cpmaindia.com/propylene>) (Accessed on July 2014)
- [17] a) T.A. Nijhuis, M. Makkee, J.A. Moulijn, B.M. Weckhuysen, *Ind. Eng. Chem. Res.*, 2006, **45**, 3447; b) S.B. Shin, D. Chadwick, *Ind. Eng. Chem. Res.*, 2010, **49**, 8125.
- [18] G. Wu, Y. Wang, L. Wang, W. Feng, H. Shi, Y. Lin, T. Zhang, X. Jin, S. Wang, X. Wu, P. Yao, *Chem. Eng. J.*, 2013, **215-216**, 306.
- [19] J. Huang, T. Takei, H. Ohashi, M. Haruta, *Appl. Catal. A*, 2012, **435-436**, 115.
- [20] A. Maldotti, A. Molinari, R. Amadelli, *Chem. Rev.*, 2002, **102**, 3811.
- [21] H. Yoshida, C. Murata, T. Hattori, *J. Catal.*, 2000, **194**, 364.
- [22] C. Murata, H. Yoshida, J. Kumagai, T. Hattori, *J. Phys. Chem. B*, 2003, **107**, 4364.

- [23] a) V. Nguyen, J.C.S Wu, H. Bai, *Chem. Eng. J.*, 2012, **179**, 285; b) V. Nguyen, J.C.S Wu, H. Bai, *Catal. Comm.*, 2013, **33**, 57.
- [24] C. Beck, T. Mallat, T. Bürgi, A. Baiker, *J. Catal.*, 2001, **204**, 428.
- [25] N. Hao, Y. Yang, H. Wang, P.A. Webley, D. Zhao, *J. Coll. Int. Sci.*, 2010, **346**, 429.
- [26] M. Cornelius, F. Hoffmann, M. Fröba, *Chem. Mater.*, 2005, **17**, 6674.
- [27] X. Gao, E. Wachs, *Catal. Today*, 1999, **51**, 233.
- [28] A.N. Murashkevich, A.S. Lavitskaya, T.I. Barannikova, I.M. Zharskii, *J. Appl. Spectrosc.*, 2008, **75**, 730.
- [29] a) G. Zhu, Q. Yang, D. Jiang, J. Yang, L. Zhang, Y. Li, C. Li, *J. Chromat. A*, 2006, **1103**, 257; b) O. Muth, C. Schellbach, M. Fröba, *Chem. Commun.*, 2001, **2032-2033**; c) M. Llusar, G. Monros, C. Roux, J.L. Pozzo, C. Sanchez, *J. Mater. Chem.*, 2003, **13**, 2505.
- [30] N. Linares, A.E. Sepúlveda, J.R. Berenguer, E. Lalinde, J. Garcia-Martinez, *Microp. Mesop. Mater.*, 2012, **158**, 300.
- [31] V. Degirmenci, O. F. Erdem, O. Ergun, A. Yilmaz, D. Michel, D. Uner, *Top Catal.*, 2008, **49**, 204.
- [32] K.L. Walther, A. Wokaun, B.E. Handy, A. Baiker, *J. Non Cryst. Solids*, 1991, **134**, 47.
- [33] S. Inagaki, S. Guan, T. Ohsuna, O. Terasaki, *Nature*, 2002, **416**, 304.
- [34] P.N. Gunawidjaja, M.A. Holland, G. Mountjoy, D.M. Pickup, R.J. Newport, M.E. Smith, *Solid State Nucl. Magne. Reson.* 2003, **23**, 88.
- [35] G. Ricchiardi, J. Sauer, *Phys. Chem.*, 1999, **15**, 181.
- [36] Y. Fu, H. Du, S. Xhang, W. Huang, *Mater. Sci. Eng. A*, 2005, **403**, 25.
- [37] a) X. Chen, L. Liu, P.Y. Yu, S.S. Mao, *Science*, 2011, **331**, 746; b) E. McCafferty, J.P. Wightman, *Surf. Interface Anal.*, 1998, **26**, 549.
- [38] a) X. Zhang, F. Zhang, K.Y. Chan, *App. Catal. A-Gen.*, 2005, **284**, 193; b) D.H. Kang, G.U. Park, H.H. Lee, M.S. Ahn, H.Y. Park, *J. Ceram. Proc. Res.*, 2012, **13**, 78.

- [39] V. Etacheri, M.K. Seery, S.J. Hinder, S.C. Pillai, *Inorg. Chem.*, 2012, **51**, 7164.
- [40] a) C.D. Valentin, G. Pacchioni, A. Selloni, *Chem. Mater.*, 2005, **17**, 6656; b) D. Valentin, E. Finazzi, G. Pacchioni, A. Selloni, S. Livraghic, M.C. Paganini, E. Giamello, *Chem. Phys.*, 2007, **339**, 44; c) W. Mao, H. Ma, B. Wag, *J. Hazard. Mater.*, 2009, **167**, 707.
- [41] a) V. Loryuenyong, K. Angamnuaysiri, J. Sukcharoenpong, A. Suwannasri, *Ceram. Int.*, 2012, **38**, 2223; b) S. Ren, X. Zhao, L. Zhao, M. Yuan, Y. Yu, Y. Guo, Z. Wang, *J. Solid State Chem.*, 2009, **182**, 312.
- [42] D. Reyes-Coronado, G. Rodriguez-Gattorno, M.E. Espinosa-Pesqueira, C. Cab, R. Coss, G. Oskam, *Nanotechnology*, 2008, **19**, 14605.
- [43] J. Yu, J.C. Yu, W. Ho, M.K. Leung, B. Cheng, G. Zhang, X. Zhao, *Appl. Cat. A: Gen.*, 2005, **255**, 309.
- [44] P. Kubelka, *J. Opt. Soc. Am.*, 1948, **38**, 448.
- [45] S. Valencia, J.M. Marin, G. Restrepo, *Open Mater. Sci. J.*, 2010, **4**, 9.
- [46] N. Serpone, D. Lawless, and R. Khairutdinov, *J. Phys. Chem.*, 1995, **99**, 16646.
- [47] L. Zhao, J. Yu, *J. Coll. Int. Sci.*, 2006, **304**, 84.
- [48] M. Gärtner, V. Dremov, P. Müller, H. Kisch, *Chem. Phys. Chem.*, 2005, **6**, 714.
- [49] G. Lassaletta, A. Fernandez, J.P. Espinos, A.R. Gonzalez-Felipe, *J. Phys. Chem.*, 1995, **99**, 1484.
- [50] M. Landmann, E. Rauls, W.G Schmidt, *J.Phys.: Condens. Matter.*, 2012, **24**, 195503.
- [51] H. Park, Y. Park, W. Kim, W. Choi, *J. Photochem. Photobiol. C: Photochem. Rev.*, 2013, **15**, 1.
- [52] V. Nguyen, J. C.S. Wu, H. Bai, *Catalysis Comm.*, 2013, **33**, 57.

VII. General conclusions and future lines



Universitat d'Alacant
Universidad de Alicante

VII. General conclusions and future lines

This chapter summarizes the research work, discusses the results obtained and highlights the main findings presented in previous chapters. Some future research directions are suggested, which could provide the next steps towards exploring the potential applications for these novel titania-based materials.

Universitat d'Alicant
Universidad de Alicante

7.1. GENERAL CONCLUSIONS

Nowadays, the depletion of fossil fuels and the environmental problems associated with their use as energy sources are encouraging the research towards other energy models, both renewable and sustainable. In this context, photocatalysts that could work using visible light offer an excellent alternative to traditional forms of chemical activation. The advantages of photocatalysis are both clear and significant: they avoid the use of toxic and environmentally hazardous materials, such as heavy metals, strong oxidant/reducing chemicals, and reduce our dependence on fossil fuels. However, two main technical challenges still limit the wide applications of photocatalysts: the narrow light-response range and the low separation probability of the photoinduced electron-hole pairs in the most stable semiconductor photocatalysts.

During the research work herein presented, a new alternative to control the band gap of crystalline semiconductors by the incorporation of organic molecules in their structure has been investigated. The fine tuning of the semiconductor's band gap will expand the application range of these materials to the visible spectrum (45% of the total solar energy) opening up the possibility of using sunlight to activate these photocatalysts.

Aware of the limitations of the current methods to improve the visible-light response of titanias and the new opportunities offered by Sol-Gel Coordination Chemistry, the proposed solution is based on the use of organic moieties which can act as ligands to coordinate with Ti(IV) in titanium alkoxides to form a Ti(IV) coordination compound as the first step for the synthesis of the new photocatalysts. The second step is the hydrolysis at room temperature of these coordination compounds to form a gel. This gel is then crystallized into the anatase phase. By using this methodology, the organic moieties are incorporated into the anatase framework acting as crystal disruptors. The synthesis parameters were

optimized to obtain mesoporous anatase nanoparticles with anatase structure and BET areas of c.a. 300 m²/g, without a surfactant and in mild conditions, by using only water and ethanol as solvents.

The incorporation of different functionalities such as: organic compounds, organosilica precursors and metal complexes into the framework of the titania material proved the effectiveness of the proposed synthetic route.

So, a facile and low cost synthetic methodology for stable and visible light-activated photocatalysts with controlled band gap and enhanced photocatalytic activity has been established in this PhD thesis. This promising strategy would open the door to further development of self-cleaning surfaces, such as outside walls and roads which autonomously remove air pollutants; solar cells with much higher efficiency, and the possibility of obtaining H₂ from H₂O, using only sunlight as an activator.

All the synthesized materials have been fully characterized by means the following physico-chemical characterization techniques. Thus, EA, TG and ICP-OES measurements were used to determine the yield of incorporation of the different functionalities. Chemical composition of the materials was analysed by NMR, FTIR and XPS. XRD was used to confirm the anatase structure of the photocatalyst and to determine the crystallite size, while the morphology and nanoparticle size of the titania materials was analyzed by TEM. Porosity of samples was analysed by adsorption/desorption isotherms of N₂ at 77K. Band gap was determined by DRUV and XPS measurements in the VB region was used to estimate the position of the VB. So, the combination of both techniques allowed us the construction of the DOS scheme. Finally, the photocatalytic activity of the materials was evaluated in the degradation reaction of R6G under UV and visible light, followed by UV-vis spectroscopy and a TOC analyzer.

7.1.1. Incorporation of different organic compounds

In chapter 4, hybrid organotitanias with anatase structure and reduced band gap have been synthesized. The titanias synthesized in this chapter have been obtained by complexing two different organic compounds, DHP and PPD, with the Ti(IV) atom and the further hydrolysis of the precursor, TBOT, obtaining coloured mesoporous organotitanias without the concurrence of surfactants.

The homogeneous incorporation of the organic moieties into the structure of mesoporous titania was confirmed by EA, FTIR, TGA and XPS analyses, with incorporation yields up to 86 %, which indicates the effectiveness of this synthetic route. Their properties include good textural properties with high surface BET areas (250-300 m²/g), narrow pore size distribution and a similar particle size in all materials. An enhancement in their optical properties over the titania control was obtained.

While these materials are pale-yellow solids for DHP, in the case of PPD this method yields black titanias, due to the partial oxidation of the diamine, conferring this material the optical property of being active in the visible range of the electromagnetic spectrum, providing a novel direction for the development of new photocatalysts active under solar light.

This titania is one of the few black titanias reported so far and it is the first time that this material has been synthesized in mild conditions and with such a reduced cost (an increase of only 0.6% with respect to the control titania). This black titania, thanks to a remarkable reduction of its band gap (from 3.20 eV to 2.74 eV), is able to absorb in the whole solar spectrum. This new photocatalyst exhibited enhanced photocatalytic activity under visible light in the rhodamine 6G degradation reaction even after several recycling tests confirming its stability. This material constitutes the only example of the use of polymetallic titanium alkoxides as organotitania precursors for the synthesis of stable and visible light active titanias.

7.1.2. Incorporation of metal complexes

A Ru(II) complex with terminal carboxylic groups, similar to the commercial dye N3 widely used as molecular antenna in DSSCs, was incorporated into the framework of the mesoporous titania nanoparticles by the formation of a covalent bond between the carboxylic groups of the ligands and the titania precursor previous to the hydrolysis of the precursor. This novel strategy allows the homogeneous incorporation of the Ru(II) complex within the anatase structure of the titania, probably, modifying it, with a high yield of incorporation, as further confirmed by ICP, FTIR and XPS measurements.

The novel hybrid material (TiO₂_IS) has similar textural properties in comparison to the control titania, thus corroborating the incorporation of the Ru(II) complex not only in the surface, as it happens in the sample synthesized by the grafting of this complex on the surface of a previously synthesized titania (TiO₂_G sample), but also in the structure of the titania.

The hybrid Ru(II) complex titania material shows a significant reduction of its band gap, making this material active in the visible range. Indeed, the band gap has decreased significantly for the TiO₂_IS sample while it remains constant for the sample TiO₂_G. In addition, the range in which TiO₂_IS is active has been extended from the UV to visible range, thus improving its photocatalytic properties and enabling a better use of solar light.

Both hybrid titanias have been tested by the photocatalytic degradation reaction of R6G under both UV radiation and visible light. The results herein described showed that the R6G degradation rate is faster, both UV and visible light, for the TiO₂_IS sample in comparison to TiO₂_G and control titania.

Emphasis is given to the existence of an effective protection of the Ru(II) complex in the TiO₂_IS titania sample, preventing their loss and maintaining the

effectiveness of this material after several cycles of reuse. It can be associated with a higher protection of the Ru(II) complex inside the titania structure, which gets a better overlap between the LUMO of the Ru(II) complex and the CB of the titania. Furthermore, the position of the Ru(II) complex into the titania structure can be related with a reduction of the electron-hole recombination rate in this hybrid material.

7.1.3. Incorporation of organosilica precursors

In chapter 6, a series of highly catalytically active anatase titania-organosilica nanoparticles were prepared by the hydrolysis and co-condensation of a titanium precursor, TBOT, with two different organosilica precursors: 1,4-bis(triethoxysilyl) benzene (BTEB) and 1,2-bis(triethoxysilyl) ethane (BTEE), using mild conditions, in absence of surfactants. Co-condensation of both precursors has been confirmed by NMR, FTIR, and XPS as well as the Ti-O-Si bond formation, characteristic of these materials.

Besides the organosilica precursor content, all samples have high BET surface areas indicating the mesoporous nature of these samples and confirming the incorporation of the organosilane components in the titania framework and not between the titania nanoparticles. Textural characterization of samples after calcination proves the high thermal stability of the samples with low-middle organosilica precursor content, despite the absence of surfactant, which is probably associated to the change in surface Ti(IV) coordination and the Si-O-Ti bonds increase after calcination.

The photocatalytic degradation of R6G was carried out in a liquid-solid regime by using both the control TiO₂ and titania-organosilica photocatalysts. Photoreactivity experiments showed that the R6G degradation rate was faster by using the calcined hybrid samples on respect to both uncalcined samples and

control TiO₂, probably related to the change in the electronic structure of these samples.

The application of these hybrid materials in photocatalysis, particularly in the partial oxidation of propylene, carried out in gas-solid regime, shows that the hybrid titania-silica materials are more efficient than control TiO₂ in the formation of propylene oxide.


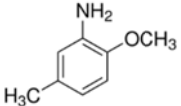
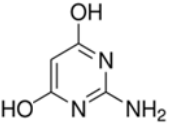
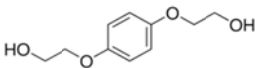
7.2. Future research lines

The results presented herein have proved the effectiveness of the proposed synthetic route to obtain hybrid mesoporous titania materials with organic moieties, metal complexes, and silica precursors homogeneously distributed through the material (in the bulk instead on the surface of titania). The band gap of the hybrid titanias can conveniently be tuned which finally results in a significant increase in the photocatalytic activity of the synthesized materials when used under visible light.

Moving forward, different opportunities will be carried out to explore the potential of both the synthesis of new materials using the strategy herein described, and the applications of these materials as photocatalysts in relevant processes and in dye-sensitized solar cells where the dye will be introduced in the structure instead of anchored on the surface of the metal oxide.

With regard to the materials which incorporate organic moieties described in chapter 4, different organic compounds containing bidentate or bridge N and/or O ligands able to coordinate the Ti(IV) atom in the titania precursor will be introduced into the mesoporous material by the described methodology (see Table 7.1). Special emphasis should be placed on bidentate amines which are known because of their dark color under oxidation to improve the visible-light response of titanias.

Table 7.1. Some of the bidentate or bridge N and/or O ligands suggested as crystal disruptors.

Hydroquinone	2-methoxy-5-methylaniline	2-amino-4,6-dihydroxypyrimidine	hydroquinone bis(2-hydroxyethyl) ether
			

Ligands containing di-, tri- and tetracarboxylic acids (such as oxalic acid, terephthalic acid, benzene-1,3,5-tricarboxylic acid or diphenyl-4,4'-dicarboxylic acid) with increased size will be used to establish the role of crystal disruptor size in tuning the band gap of these new materials by comparing the morphological, textural and structural properties with the optical and photocatalytic properties.

Finally, another family of compounds with potential interest are thiophene-based conductor compounds containing N and O ligands, such as 1-(thiophene-2-carbonyl)-piperidine-4-carboxylic acid or thiophene-3-carbonyl chloride, that can also be investigated as alternative crystal disruptors in this research line.

Our methodology implies traditional strategies, such as covalent grafting are not able to use the organic compounds as crystal disruptors. Thus, a comparison between structural, electronic and photocatalytic properties of the materials obtained by both, traditional strategies versus the proposed one, will help to elucidate the role of the crystal disruptors on the band gap tuning of these novel materials.

The key findings of chapter 5 is the development of a hybrid Ru(II) complex-titania material through the incorporation of the Ru(II) dye N3, widely used as molecular antenna in DSSCs, but with a band gap much lower than that obtained by traditional grafting of the dye on the titania surface. However, besides this well-

known dye, other Ru(II)-based complexes can also be synthesized with ligands such as 2,2'-bipyridine-4,4'-dicarboxylic acid. These compounds are widely used in chemiluminescent reactions. In addition, iridium complexes containing cyclometalated ligands are known to be stable luminescent systems thus the substitution of one cyclometalated ligand with a phosphine with terminal carboxylic acid groups could achieve both coordination with the Ti (IV) atom and the luminescent properties. Similarly, Cu(I) complexes are good candidates for these purposes. For this reason, another of the future research lines that will be explored in the future is the incorporation of those complexes into the titania framework and the study of the optical properties of the final materials in both DSSC and photoluminescent devices.

Regarding the potential applications of our materials, these are the three directions suggested for future work: NO_x degradation, self-cleaning properties and PV solar cells.

a) NO_x degradation measurements:

The main goal of chapter 4 is to expand the absorption spectra of titanias to the visible range. Coloured titanias, as the black one described in chapter 4 (TiO₂-PPD) are able to use the whole solar spectrum. So, they are ideal candidates to be used in outdoor applications. For that reason, TiO₂-PPD samples as well as ones synthesized by using the bidentate amines, which are known because of their dark color under oxidation, will be evaluated as photocatalysts in the NO_x degradation reaction (DeNO_x process). The process is very simple, the black titania is exposed to a known amount of NO_x in a flow reactor cell illuminated by a 300 W lamp (emitting in UV and visible-near IR range). By using a commercial NO analyzer based on chemiluminescence, able to simultaneously measure NO and NO₂ concentrations NO_x (NO_x = NO+NO₂) conversions can be easily evaluated. The

photonic efficiency should be also determined, a parameter that is required for the rigorous design and scaling-up of photocatalytic reactors in order to accomplish a commercial application of photocatalytic technologies. The condition reactions will be as similar as possible to the ISO standard associated to photocatalytic materials produced for air purification ISO 22197-1:200735. Finally, the amount of NO adsorbed in the titania surface and the surface composition, NH_3 , NO, NO_2 as well as NO_3^- evolution can be followed by XPS (surface composition) or chromatography (NO_3^-).

Our black titania TiO_2 -PPD-b has recently been tested at the Technological Institute of Construction AIDICO (Spain) showing outstanding NO_x degradation values with high selectivity towards nitrates (80% versus 25% of control titania). The next step is to evaluate its photocatalytic activity in NO_x degradation when tested on a road.

b) Self-cleaning properties: In a similar way, visible light active titanias can also be evaluated as surface additives for self-cleaning properties in different materials (walls, kitchen surfaces, etc.). The self-cleaning properties of these materials can be evaluated easily evaluated using the ISO test 27448:2009 conditions, a standard method for self-cleaning performance of semiconductor photocatalytic materials based on water contact angle measurements. In this test, an organic material (oleic acid, $\text{C}_{18}\text{H}_{34}\text{O}_2$) is applied and the change in the wettability of the semiconductor substrate, as measured via its water droplet contact angle, is then monitored as a function of UVA irradiation time. When the contact angle is lower than 5° , the measurement is finished and the value of the contact angle and the time taken to achieve it are reported.

c) PV solar cell tests: The metal complex-containing titania materials described in chapter 5 will be evaluated as alternative photocatalysts in solar cells. The main goal of this research is to evaluate both the activity and stability of traditional dye, such N3 in titanias introduced in two different ways: 1) by conventional grafting on

the surface of the metal oxide and 2) by incorporation in its structure, as described in chapter 5. The superior activity and reusability of our novel materials in the test reactions discussed already are the basis of our expectation to get better more resistant solar cells. For this purpose, titania films will be prepared by spin coating of titania suspensions previously ultrasonicated in an adequate solvent, such as isopropanol. If non-homogeneous films would obtain, it is proposed to perform the synthesis of the hybrid materials using isopropanol (or any other low boiling point solvent) as solvent. The second approach could be the use of low temperature spray pyrolysis for the preparation of the titania-based films. Standard iodine-based electrolyte with additives and platinum-based counter electrodes will be used in the devices and the performance of the solar cells will be measured. This work has been recently begun in collaboration with Dr. R. Costa, from the Friedrich-Alexander University (Germany). Preliminary results indicated a performance similar to the commercial solar cells, probably related to the carrier diffusion. So, two approaches are proposed in order to increase the contact between nanoparticles and, consequently, to improve the diffusion between them: i) the sintering at low temperature of the titania nanoparticles and ii) the hydrolysis of a small amount of TBOT over the already synthesized hybrid materials to connect the nanoparticles. After the refinement of the solar cell preparation, the effect of the disruptor amount on the cell performance should be investigated.

Universidad de Alicante

Annex



Universitat d'Alacant
Universidad de Alicante

ANNEX 1. LIST OF ABBREVIATIONS

T	Absolute temperature
AA	Acetaldehyde
AC	Acetone
E1	Adsorption heat of the monolayer
E2	Adsorption heat for subsequent layers of E1
AlKα	Al monochromatic microbeam
n^a	Amount of adsorbed gas
n^a_m	Amount of gas adsorbed in the monolayer
d₍₁₀₁₎^{XRD}	Anatase spacing (d ₁₀₁) calculated by Bragg
d₍₁₀₁₎^{TEM}	Anatase spacing (d ₁₀₁) calculated by TEM
H₀	Applied magnetic field
σ^*	Antibonding orbital
BJH	Barret, Joyner and Halenda method
C	BET constant related to the heat of adsorption of the monolayer
σ	Bonding orbital
E_g	Band gap
θ	Bragg angle
BET	Brunauer, Emmett and Teller method
E_{Binding}	Binding energy of the electron
r_k	Capillary radius
CB	Conduction band
CuKα	Cu monochromatic microbeam
DOS	Density orbital state
K	Dimensionless shape factor
D^{XRD}	Domain size of the particle calculated from X-ray diffraction using Scherrer equation
ϕ^{TEM}	Domain size of the particle estimated by TEM
DSSCs	Dye-sensitized nano-structured solar cell
e⁻-h⁺	Electron-hole pair
EA	Elemental analysis
ΔE	Energy difference
E_{Photon}	Energy of the X-ray photons
FTIR	Fourier transform infrared spectroscopy
FID	Flame ionization detector
ν	Frequency
R	Gas constant
GC	Gas chromatography

OH[·]	Hydroxyl radicals
HOMO	Highest occupied molecular orbital
H	Hours
ICP-OES	Inductively coupled plasma optical emission spectrometry
IC	Inorganic carbon
d_{hkl}	Inter-plane distance
E_{Kinetics}	Kinetic energy of the electron measured by the instrument
$F(R')$	Kubelka-munk function
B	Line at half the maximum intensity in radians
LUMO	Lowest unoccupied molecular orbital
MgKα	Mg monochromatic microbeam
V_p	Mesopore volume
MB	methylene blue
Vol	Molar volume of liquid nitrogen
NMR	Nuclear magnetic resonance
Ph.D	Philosophiae Doctor
h	Planck's constant
d_p	Pore diameter
r_p	Pore radius
PA	Propionaldehyde
H^+	Protons
k'	Pseudo-first order rate constant of the degradation of an aqueous solution of R6G
P/P_0	Relative pressure of gas
R'	Reflectance value obtained directly from the spectrophotometer
R^*	Regression coefficient for the degradation of an aqueous solution of R6G
R6G	Rhodamine 6G
θ	Scattering angle
D	Size of the ordered crystalline domains
β	State of maximum energy
α	State of minimum energy
A_{BET}	Superficial area (BET)
ϕ	Surface tension of liquid nitrogen
TiO₂	Titanium dioxide
SSTi	Technical Services
TBOT	Tetrabutyl orthotitanate
TCD	Thermal conductivity detector
TGA	Thermogravimetric analysis

t	Thickness of the absorbed layer
TC	Total carbon
TOC	Total organic carbon
TEM	Transmission electronic microscopy
UV-vis	UV-vis spectroscopy
UV	Ultraviolet
UA	University of Alicante
VB	Valence band
N	Value representing the order of the diffraction peak
λ	Wavelength
ϕ	Work function of the spectrometer
XRD	X-ray diffraction
XRF	X-ray fluorescence
XPS	X-ray photoelectron spectroscopy
DHP	4,6-dihydroxypyrimidine
PPD	<i>p</i> -phenylenediamine
BTEB	1,4-bis(triethoxysilyl) benzene
BTEE	1,2-bis(triethoxysilyl) ethane



Universitat d'Alacant
Universidad de Alicante

ANNEX 2: LIST OF FIGURES**Chapter 2: Introduction**

- Figure 2.1.** Extrinsic semiconductors: (a) *p*-type, gallium-doped silicon and (b) *n*-type, arsenic-doped silicon (adapted from ref. 2b).
- Figure 2.2.** Molecular orbital diagram for the hydrogen molecule (left, adapted from ref.4) and band formation of molecular orbitals (right, adapted from ref.5)
- Figure 2.3.** Scheme of a semiconductor energy band diagram where VB is the valence band edge, CB the conduction band edge and E_g the band gap (adapted from ref.3).
- Figure 2.4.** Representative crystalline structures of the three polymorphs of TiO₂: brookite (a), anatase (b) and rutile (c)^[9].
- Figure 2.5.** Representative octahedron of brookite (a), anatase (b) and rutile (c) crystalline structures where A, B and R represents the distances between the different ions (adapted from ref.21).
- Figure 2.6.** Molecular orbital bonding structure for anatase TiO₂ (adapted from ref.26c).
- Figure 2.7.** Synthesis options by sol-gel process^[59].
- Figure 2.8.** TiO₂ photocatalysis applications (adapted from ref. 68).
- Figure 2.9.** TiO₂ water splitting process.
- Figure 2.10.** Schematic illustration of TiO₂ applications as a pigment (adapted from ref.80).

Chapter 3: Experimental Procedures

- Figure 3.1.** Representation of cohesive forces: in a solid (a) and in a solid where a gas has been adsorbed (b)^[6].
- Figure 3.2.** Wavelengths in the electromagnetic spectrum^[13].
- Figure 3.3.** Schematic illustration about how diffuse reflectance works.
- Figure 3.4.** Schematic illustration of the nuclear spins in absence of magnetic field (left) and under a magnetic field (right).
- Figure 3.5.** Types of interference when crystalline solids are exposed to X-Rays: constructive (a) and destructive (b).
- Figure 3.6.** Bragg's law of diffraction: illustration of how X-rays interact with crystal lattice. Two-dimensional description of the X-ray reflection beam from two parallel crystalline planes separated by a distance d_{hkl} .
- Figure 3.7.** Representation of the different phenomena that can result from the excess of energy when a sample is irradiated with a X radiation.
- Figure 3.8.** Irradiated surface with a source of high-energy photons that causes the emission of electrons (left) and photon which imparts its energy to an electron of an internal electronic level (right) (adapted from ref. 34).

- Figure 3.9.** Transmission electron microscope used in SSTi (UA).
- Figure 3.10.** Emission spectrum for the medium pressure mercury lamp used in these photocatalytic reactions of rhodamine 6G^[47]
- Figure 3.11.** Image of the photochemical reactor system of the Molecular Nanotechnology Lab (UA), equipped with a 125W medium-pressure Hg lamp and a UV sonde, that allows to monitor *in-situ* reactions.
- Figure 3.12.** Schematic diagram showing TOC measurement.

Chapter 4: Incorporation of organic compounds in the framework of mesoporous titania

- Figure 4.1.** Comparison of the colour of control titania, a pale yellow titania (TiO₂-DHP-b) and a black titania (TiO₂-PPD-b).
- Figure 4.2.** FTIR spectra of organotitanias (12 wt% organic compounds), as compared with the control TiO₂ and the organic compounds. The bands characteristics of the incorporation of the organic compounds are denoted by arrows.
- Figure 4.3.** N1s XPS spectra of hybrid TiO₂-DHP-b and TiO₂-PPD-b organotitanias (left) and O 1s XPS spectra (right) of hybrid TiO₂-PPD-b organotitania as compared with those of control TiO₂.
- Figure 4.4.** Ti 2p XPS spectra of the synthesized organotitanias (left) and Ti 2p XPS spectra of the TiO₂-PPD_b, before (hydrolysis) and after the crystallization (right) as compared with those of control TiO₂.
- Figure 4.5.** Nitrogen adsorption/desorption isotherms at 77 K of TiO₂-DHP (left) and TiO₂-PPD (right) organotitanias, as compared to control TiO₂.
- Figure 4.6.** Normalized XRD patterns of the TiO₂-DHP (left) and TiO₂-PPD (right) organotitanias, as compared to control TiO₂.
- Figure 4.7.** TEM images of: TiO₂ (a), TiO₂-DHP-a (b), TiO₂-DHP-b (c), TiO₂-DHP-c (d), TiO₂-PPD-a (e) and TiO₂-PPD-b (f). Spacing of lattice image was determined by using Gatan software and, in all cases, corresponds to 101-spacing of anatase crystalline phase.
- Figure 4.8.** Valence band XPS spectra (a) and plot of the transformed Kubelka-Munk function versus the energy of light adsorbed (b). Schematic illustration of the DOS (c) of the organotitania TiO₂-DHP-b and TiO₂-PPD-b samples as compared with the control TiO₂.
- Figure 4.9.** Oxidative process of the organic compound *p*-phenylenediamine (PPD).
- Figure 4.10.** UV-vis absorption spectra of the degradation reaction of an aqueous solution of R6G (5·10⁻⁵ M) under UV radiation using as photocatalysts: TiO₂ (a), TiO₂-DHP-b (b) and TiO₂-PPD-b(c).
- Figure 4.11.** Photographs of the different samples taken along the degradation reaction of an aqueous solution of R6G (5·10⁻⁵ M) under UV radiation using TiO₂-PPD-b as photocatalysts.
- Figure 4.12.** N-deethylation reaction of R6G to rhodamine^[29].

- Figure 4.13.** Representation of the proposed photocatalytic mechanism for the rodhanime 6G degradation reaction using TiO₂-DHP and TiO₂-PPD titania as photocatalysts.
- Figure 4.14.** Representation of the pseudophotocatalytic constant (k') of the of the organotitania samples: TiO₂-DHP-b and TiO₂-PPD-b as compared with control titania, TiO₂, in the degradation reaction of an aqueous solution of R6G ($5 \cdot 10^{-5}$ M) under UV radiation (left). Cycling tests under the same conditions (right).
- Figure 4.15.** Representation of the pseudophotocatalytic constant (k') of TiO₂-DHP-b and TiO₂-PPD-b as compared with control titania, in the degradation reaction of an aqueous solution of R6G ($5 \cdot 10^{-5}$ M) under visible light (left). Cycling tests under the same conditions (right).
- Figure 4.16.** UV-vis absorption spectra of the degradation reaction of an aqueous solution of R6G ($5 \cdot 10^{-5}$ M) under visible light using as photocatalysts: TiO₂ (a), TiO₂-DHP-b (b) and TiO₂-PPD-b (c).
- Figure 4.17.** Variation of the concentration along the time in the photodegradation reaction of aqueous solutions of R6G ($5 \cdot 10^{-5}$ M) by TiO₂-PPD-b in the absence or presence of different scavengers (¹PrPH or TEOA, $5 \cdot 10^{-2}$ M) under visible light.

Chapter 5: Incorporation of Ru(II) complex in the framework of mesoporous titania

- Figure 5.1.** Chemical structure of the Ru(II) complex *cis-bis(isothiocyanato) bis(2,2'-bipyridyl-4,4'-dicarboxylate ruthenium(II))*.
- Figure 5.2.** Absorption spectra of the Ru(II) complex *cis-Bis(isothiocyanato) bis(2,2'-bipyridyl-4,4'-dicarboxylato ruthenium(II))*.
- Figure 5.3.** ¹H RMN spectra of the Ru(II) complex *cis-Bis(isothiocyanato) bis(2,2'-bipyridyl-4,4'-dicarboxylato ruthenium(II))*.
- Figure 5.4.** FTIR spectra of the synthesized Ru(II) complex *cis-Bis(isothiocyanato) bis(2,2'-bipyridyl-4,4'-dicarboxylato ruthenium(II))*.
- Figure 5.5.** FTIR spectra of the ruthenium titania materials: TiO₂_IS (c), TiO₂_G (d) as compared with the FTIR spectra of the Ru(II) complex (a) and control TiO₂ (b).
- Figure 5.6.** XPS spectra in the Ti2p (left) and O1s (right) regions of TiO₂_IS and TiO₂_G samples as compared with control TiO₂.
- Figure 5.7.** Representative nitrogen adsorption isotherms (left) and XRD patterns (right) for the materials with the Ru(II) complex, TiO₂_IS and TiO₂_G as compared to the control mesoporous titania TiO₂.
- Figure 5.8.** Representative TEM images of the materials with the Ru(II) complex: TiO₂_IS (a) and TiO₂_G (b) as compared with control TiO₂ (c).

- Figure 5.9.** Valence band XPS spectra (a), plot of the transformed Kubelka-Munk function versus the energy of light adsorbed (b) and schematic illustration of the DOS (c) of the Ru(II) complex titania materials as compared with the control TiO₂.
- Figure 5.10.** UV-vis absorption spectra of the degradation reaction of an aqueous solution of R6G (5·10⁻⁵ M) under UV radiation using as photocatalysts: TiO₂ (a), TiO₂_IS (b) and TiO₂_G (c).
- Figure 5.11.** Representation of the pseudophotocatalytic constant (*k'*) of the TiO₂_IS and TiO₂_G samples as compared with control TiO₂, in the degradation reaction of an aqueous solution of R6G (5·10⁻⁵ M) under UV radiation (left). Cycling tests under the same conditions (right).
- Figure 5.12.** Schematic representation of the injection electrons from the dye to the titania materials in the synthesized samples.
- Figure 5.13.** UV-vis absorption spectra of the degradation reaction of an aqueous solution of R6G (5·10⁻⁵ M) under visible light using as photocatalysts: TiO₂ (a), TiO₂_IS (b) and TiO₂_G (c).
- Figure 5.14.** Representation of the pseudophotocatalytic constant (*k'*) of the TiO₂_IS and TiO₂_G samples as compared with control TiO₂, in the degradation reaction of an aqueous solution of R6G (5·10⁻⁵ M) under visible light (left). Cycling tests under the same conditions (right).
- Figure 5.15.** Variation of the concentration along time in the photodegradation reaction of aqueous solutions of R6G (5·10⁻⁵ M) by TiO₂_IS in the absence or presence of different scavengers ¹PrOH or TEOA, 5·10⁻²M) under visible light.

Chapter 6: Incorporation of organosilica precursors in the framework of mesoporous titania

- Figure 6.1.** FTIR spectra of the titania-organosilica materials as-synthesized and treated at 800°C (b, c) in comparison with the FTIR spectra of an organosilica xerogel (BE xerogel sample) synthesized using only BTEE precursor in the same conditions that those used for titania-based samples (a).
- Figure 6.2.** ²⁹Si NMR spectra of a BE organosilica xerogel prepared under the same conditions than hybrid titania-organosilica samples (a) the titania-organosilica TiO₂_BE_0.20 (b) and TiO₂_BB_0.20 (c).
- Figure 6.3.** XPS spectra in the Ti2p (a) and O1s (b) regions of TiO₂_BE_0.20 and TiO₂_BB_0.16 samples as compared with those corresponding to control TiO₂.
- Figure 6.4.** XRD patterns of the titania-organosilica materials prepared with different amount of: BTEE precursor, TiO₂_BE samples (left) and BTEB precursor, TiO₂_BB samples. XRD spectra are shifted for clarity (right).

- Figure 6.5.** Representative adsorption/desorption isotherms at 77K of titania-organosilica materials prepared with different amount of: BTEE precursor (left), TiO₂_BE samples and BTEB precursor (right), TiO₂_BB samples.
- Figure 6.6.** Representative TEM micrographs of control TiO₂ (a), TiO₂_BB_0.16 (b) and TiO₂_BE samples: TiO₂_BE_0.10, (c) TiO₂_BE_0.20 (d) and TiO₂_BE_0.50 (e). Scale bar = 5 nm.
- Figure 6.7.** Representative adsorption/desorption isotherms at 77K of calcined titania-organosilica materials: TiO₂_BE_c (left) and TiO₂_BB_c materials (right).
- Figure 6.8.** XRD patterns of calcined titania-organosilica materials: TiO₂_BE_c (left) and TiO₂_BB_c materials (right). XRD spectra are shifted for clarity.
- Figure 6.9.** XPS spectra in the Ti2p (left) and O1s (right) regions of calcined TiO₂_BE_0.20 and TiO₂_BB_0.16 samples as compared with those corresponding to control TiO₂ after calcination.
- Figure 6.10.** Plot of the transformed Kubelka-Munk function versus the energy of light adsorbed (a), valence band XPS spectra (b) and schematic illustration of the DOS (c) of as-synthesized titania-organosilica nanoparticles as compared with the control TiO₂.
- Figure 6.11.** Plot of the transformed Kubelka-Munk function versus the energy of light adsorbed (a), valence band XPS spectra (b) and schematic illustration of the DOS (c) of calcined titania-organosilica nanoparticles as compared with calcined TiO₂ nanocrystals.
- Figure 6.12.** Ln (C₀/C) vs. irradiation time for the as-synthesized catalysts, TiO₂_BE (a) and TiO₂_BB (b) and for the calcined photocatalysts, TiO₂_BE_c (c) and TiO₂_BB_c (d).
- Figure 6.13.** Reaction pathway of photocatalytic propene partial oxidation in the presence of the studied photocatalysts and UV radiation. Molecules in brackets are identified intermediate products.
- Figure 6.14.** Evolution of acetaldehyde (blue), propylene oxide (red), acetone (green), and propionaldehyde (violet) during the irradiation time for runs carried out in the presence of: TiO₂_BB_0.16_c (a), TiO₂_BE_0.20_c (b) and control TiO₂_c (c).

ANNEX 3: LIST OF SCHEMES

Chapter 2: Introduction

- Scheme 2.1.** Scheme of the mechanism produced by the electron-hole pair^[6] (adaptated from ref.6).
- Scheme 2.2.** Schematic TiO₂ photoexcitation mechanism (left) and primary steps in the photocatalysis mechanism of TiO₂ under UV radiation (right) (adapted from ref.24).
- Scheme 2.3.** Schematic electron-hole recombination in a TiO₂ nanoparticle (adapted from ref.34).
- Scheme 2.4.** Different strategies for improving TiO₂ photoactivity.
- Scheme 2.5.** Reaction steps in the formation of a titania network by sol-gel process^[567].
- Scheme 2.6.** Novel strategy for synthesise TiO₂ with the functionalities incorporated into its structure (left) and VB and CB position in the titania and novel titania materials (right)^[62].
- Scheme 2.7.** NREL's latest chart of best research-cell efficiencies^[74].
- Scheme 2.8.** Scheme of a possible and future large-scale H₂ production via water splitting^[79].

Chapter 4: Incorporation of organic compounds in the framework of mesoporous titania

- Scheme 4.1.** Synthesis methodology to incorporate the organic compounds: a) 4,6-dihydroxypyrimidine (DHP) and b) *p*-phenylenediamine (PPD) in the mesoporous titania.

Chapter 5: Incorporation of RU(II) complex in the framework of mesoporous titania

- Scheme 5.1.** Energetic schema of a dye sensitized solar cell where S⁰ is the initial state, S* the excited state and the S⁺ the oxidated state of the dye (adapted from ref.1)
- Scheme 5.2.** Schematic diagram of the Grätzel solar cell (adapted from ref.12)
- Scheme 5.3.** Schematic diagram of the most common covalent anchoring groups for surface modification of TiO₂ photocatalyst (adapted from ref.25)
- Scheme 5.4.** Synthesis methodology to incorporate the Ru(II) complex by the *in-situ* methodology (TiO₂_IS)^[28].
- Scheme 5.5.** Ru(II) complex covalently bonded to the titania surface by *grafting*(TiO₂_G).

Chapter 6: Incorporation of organosilica precursors in the framework of mesoporous titania

Scheme 6.1. Schematic procedure of synthesis of titania-organosilica materials by co-condensation of tetrabutyl orthotitanate (TBOT), with different amounts of two organosilica precursors (0.04–0.25 mol/mol TBOT) by using only water and ethanol as solvents and without the need of surfactants.



Universitat d'Alacant
Universidad de Alicante

ANNEX 4: LIST OF TABLES**Chapter 2: Introduction**

Table 2.1. Physical and structural properties of the three common polymorphs of TiO₂^[13].

Chapter 4: Incorporation of organic compounds in the framework of mesoporous titania

Table 4.1. Nomenclature of the organotitanias synthesized indicating the name and chemical formula of the incorporated organic compound as well as the nominal and experimental organic compound content.

Table 4.2. Textural and structural parameters of the mesoporous organotitania materials synthesized as compared to the control titania.

Table 4.3. Constant values of the photocatalytic activity under UV radiation, regression coefficients and conversions at different times of the organotitania samples as compared with the control TiO₂.

Table 4.4. Constant values of the photocatalytic activity under visible light, regression coefficients and conversions at different times of the organotitania samples as compared with control TiO₂.

Chapter 5: Incorporation of Ru(II) complex in the framework of mesoporous titania

Table 5.1. Textural and structural parameters of the mesoporous titania materials with the Ru (II) complex, as compared to the control titania

Table 5.2. Constant values of the photocatalytic activity under UV radiation, regression coefficients and conversions at different times of the titanias with the Ru (II) complex as compared with the control titania, TiO₂

Table 5.3. Constant values of the photocatalytic activity under UV radiation, regression coefficients and conversions at different times of the titanias with the Ru(II) complex as compared with the control titania, TiO₂.

Chapter 6: Incorporation of organosilica precursors in the framework of mesoporous titania

Table 6.1. Nomenclature, textural and structural parameters of the titania-organosilica materials prepared with different BTEE (TiO₂_BE) and BTEB (TiO₂_BB) amount, as compared to the control TiO₂.

Table 6.2. Nomenclature, textural and structural parameters of the calcined titania-organosilica materials prepared with different BTEE (TiO₂_BE) and BTEB

Table 6.3. (TiO₂_BB) amount, as compared to the control TiO₂. Band gap energies (E_g), pseudo-first order kinetic constant values (k') and regression coefficients (R) of the R6G degradation reaction under UV radiation for the as-synthesized titania-organosilica catalysts as compared with control titania, TiO₂.

Table 6.4. Band gap energies (E_g), pseudo-first order kinetic constant values (k') and regression coefficients (R) of the R6G degradation for the calcined titania-organosilica catalysts as compared with calcined titania sample, TiO₂_c.

Chapter 7: Conclusions and future lines

Table 7.1. Some of the bidentate or bridge N and/or O ligands suggested as crystal disruptors.



Universitat d'Alacant
Universidad de Alicante

The main objective of this Ph.D. Thesis is to tune the band gap of titania through the incorporation of different moieties into the structure of the anatase network. The novel synthesis methodology involves the hydrolysis and co-condensation of a titania precursor in the presence of organic compounds, organosilica precursors and metallic complexes. The contribution of this Ph.D. Thesis is that the proposed incorporation strategy allows for an efficient control of the band gap of titania, extending its application to visible light, an important goal in the way to cheaper more efficient photocatalysts and solar cells.



Universitat d'Alacant
Universidad de Alicante